

Title	Synthesis and characterisation of self-seeded germanium and germanium tin nanowires
Authors	Garcia-Gil, Adrià
Publication date	2021-09-06
Original Citation	Garcia-Gil, A. 2021. Synthesis and characterisation of self-seeded germanium and germanium tin nanowires. PhD Thesis, University College Cork.
Type of publication	Doctoral thesis
Rights	© 2021, Adrià Garcia-Gil. - <a href="https://creativecommons.org/licenses/by-nc-nd/4.0/">https://creativecommons.org/licenses/by-nc-nd/4.0/</a>
Download date	2025-04-05 19:59:31
Item downloaded from	<a href="https://hdl.handle.net/10468/12464">https://hdl.handle.net/10468/12464</a>



**UCC**

**University College Cork, Ireland**  
Coláiste na hOllscoile Corcaigh

Ollscoil na hÉireann, Corcaigh  
**National University of Ireland, Cork**



**Synthesis and Characterisation of Self-Seeded Germanium  
and Germanium Tin Nanowires**

Thesis presented by

**Adrià Garcia Gil**

for the degree of

**Doctor of Philosophy**

**University College Cork**

**School of Chemistry**

Head of School: Dr Humphrey Moynihan

Supervisors: Prof. Justin D. Holmes and Dr Subhajit Biswas

2021



*Als avis,*  
*Isabel, Lluís, Margarita i Pepe.*





## Table of Contents

<b>Declaration.....</b>	<b>iii</b>
<b>Acknowledgements.....</b>	<b>iv</b>
<b>List of publications.....</b>	<b>vii</b>
<b>Abstract.....</b>	<b>ix</b>
<b>A Review of Self-Seeded Germanium Nanowires: Synthesis, Growth Mechanisms and Potential Applications ..... 1</b>	
1.1. Introduction .....	2
1.2. Germanium Nanowires Growth Mechanisms .....	7
1.2.1. Primary Growth Paradigms for the Nanowire Growth .....	7
1.2.2. Why Self-Seeded growth: Disadvantages of Catalytic Ge Nanowire Growth .....	12
1.3. Self-Seeded Germanium Nanowires Synthesis Methods .....	15
1.3.1. Bottom-Up Synthesis of Self-Seeded Germanium Nanowires .....	16
1.4. Growth Mechanism for Self-Seeded Ge Nanowires .....	36
1.4.1. Nanoparticle Seeds .....	36
1.4.2. Proposed Growth Mechanism for Self-Seeded Germanium Nanowires ..	39
1.5. Growth of Self-Seeded Ge Nanowire Alloys .....	48
1.6. Potential Applications of Self-Seeded Germanium Nanowires .....	51
1.6.1. Self-Seeded Ge Nanowires in Li-Ion Battery .....	52
1.6.2. Self-Seeded Ge Nanowires in Other Applications .....	55
1.7. Conclusions and Outlook .....	58
1.8. Thesis Summary .....	59
1.9. References .....	61
<b>Carbonaceous Germanium Nanowires and their Application as Highly-efficient Lithium-ion Battery Anodes .....86</b>	
2.1. Abstract .....	87
2.2. Introduction .....	88

2.3. Experimental .....	91
2.4. Results and Discussion .....	94
2.5. Conclusions .....	112
2.6. Appendix .....	113
2.7. References .....	121
<b>Exploring the Tetragonal (ST12) Germanium Phase in One-dimensional (1D)</b>	
<b>Nanostructures .....</b>	<b>129</b>
3.1. Abstract .....	130
3.2. Introduction .....	131
3.3. Experimental .....	134
3.4. Results and Discussion .....	136
3.5. Conclusions .....	152
3.6. Appendix .....	153
3.7. References .....	161
<b>Batch-produced self-seeded Germanium-Tin Alloy Nanowires as Highly</b>	
<b>Efficient Li-Ion Battery Anodes.....</b>	<b>167</b>
4.1. Abstract .....	168
4.2. Introduction .....	169
4.3. Experimental .....	172
4.4. Results and Discussion .....	174
4.5. Conclusions .....	192
4.6. Appendix .....	194
4.7. References .....	199
<b>Conclusions and Future Outlook.....</b>	<b>206</b>

## **Declaration**

Adrià Garcia Gil, hereby certifies that the work I am submitting is my own and has not been submitted for another degree, either at University College Cork or elsewhere. All external references and sources are acknowledged and identified within the contents.

## **Acknowledgements**

I really can't believe this moment has finally arrived. So many years denying any intention to participate in this madness of being 4 years fully dedicated to research. And now, I wouldn't trade it for anything. Firstly, and most important thanks to Prof. Justin Holmes and Dr Subhajit Biswas. Prof. Justin gave me the possibility 5 years ago to start this trip and I just can't express with words my deepest gratitude for this opportunity. Your support along with improvements and guidance in the course of this project has helped me to improve and grow not only as a student but also as a person. I have always blessed your straight-talking character when I was lost, even if I didn't know I was. Thanks for your patience and your jokes at the worst moments, I couldn't have done it without you. And talking about patience, no one had more patience with me than Dr Subhajit Biswas, who was always there when needed. You always showed me the bright side of every situation and opened my mind in terms of how research has to be faced. I apologise for every WhatsApp message I have sent you on the weekends, during your holidays or late in the evenings, even though you were always there to reply to them. Your knowledge and leadership both in the lab and in the office were invaluable for the project progress and improvement. Thanks for pointing the right direction and supporting me even when I decided not to take it.

I also want to thank the rest of the MCAG group. Special mention to Alex, my partner in crime; Eadaoin, cause she always has a smile on her face; Fionan, the handyman; Jessica Doherty, the Queen; Karzan, keep always being so joyful my Kurdish friend; Mai, innocent and so hard worker; and last but not least Shane, he was always there for a coffee and a small talk to forget about it all. Thanks to Vojislav Krstić and Maria Kolečnik-Gray for their patience, support and guidance when I did my stage at their

facilities in Erlangen (Germany). I would like to have a few words for Tina and Denis from the apparatus store and Kasia, Clare, Niamh and all the secretaries who have always been there to solve our little dramas. In Kane Building I have met very interesting people but I can't mention them all. However, among all, I want to thank Gerard Pareras because he has always been there. He became one of my pillars for both research and personal life. Thanks for insisting me on taking part in the Handball team, it has been a great experience and I have learned team sports can create great bonds with people. Thanks for sharing all those moments with me, the good ones when partying and wasting time doing nothing, but also to listen to me on all the bad ones. You always made me laugh in the end. During this adventure in Ireland, my flatmates and the "Little Napoli" group have always been at my side and helped me to forget about work and enjoy my free time here in Ireland. Can't mention them all, but special thanks to Emmanuele Galluccio for his loyalty and attitude both at work and in the pub.

And this links it with my family, since Eloi, my brother, was one of these flatmates for almost a year. *A vosaltres, mama i papa, no puc dir res més que gràcies. Gràcies per tot el que m'heu ensenyat, per tot el que m'heu aguantat i per tot el que heu lluitat per mi. Si sóc res es sobretot gracies a vosaltres. I a tu Eloi, qué t'haig de dir? Doncs que gràcies per tot el que m'has ensenyat i m'ensenyas cada dia, per demostrar-me que es pot veure el món des d'un altre prisma, de que es poden fer les coses diferents i que, tot i així, tot pot funcionar. Em sento molt afortunat de haver-te tingut al meu costat durant part d'aquest viatge i espero compartir-ne molts més amb tu. No m'agradaria acabar sense dedicar unes paraules als amics i professors de l'escola, com el Jordi, la Mònica, el Cristian i els Carles; ni tampoc a amics i professors de la*

*Universitat, com el Daniel, l'Ivan, l'Arnau o la Maria. Gràcies de tot cor, per què sense tots vosaltres i la manera que m'heu fet veure els estudis, la química i la vida, no seria aquí on sóc. Gràcies per encara ser al meu costat. Finalment, i potser la persona més important en aquest viatge per Irlanda, gràcies a tu Sílvia. Em quedo sense paraules quan penso en tot el que hem viscut aquests anys. Venir a Irlanda amb tu, més enllà del doctorat, va ser la millor decisió que podria haver prè i no me'n penediré mai. Fa més de 5 anys que et conec i sembla que això tot just acaba de començar. Gràcies per tots els moments super guays aquí i allà, ja fos viatjant o quedant-nos mirant Netflix al llit. Gràcies pels somriures i les celebracions quan les coses anaven bé i pel suport quan les coses semblava que es torçaven més del compte. Gràcies per tot el que m'ensenyas cada dia i per ensenyar-me a ser una mica millor persona cada dia. Gràcies per haver-me acompanyat en aquesta aventura que mai vaig pensar que iniciaria. Gràcies també per tot el que vindrà. Ara només queda el triar el proper destí, i gaudir les alegries i aventures que allà ens esperen. M'acompanyes?*

## List of publications

### Based on the research presented in this thesis:

**Garcia-Gil, A.;** Biswas, S.; Holmes, J. D. A Review of Self-Seeded Germanium Nanowires: Synthesis, Growth Mechanisms and Potential Applications. *Nanomaterials* **2021**, *11*, 2002.

**Garcia-Gil, A.;** Biswas, S.; McNulty, D.; Roy, A.; Raha, S.; Trabesinger, S.; Nicolosi, V.; Singha, A.; Holmes, J. D. Single-step Synthesis of Carbonaceous Germanium Nanowires and their Application as Highly-efficient Lithium-Ion Battery Anodes. Submitted May 2021.

**Garcia-Gil, A.;** Biswas, S.; Roy, A.; Saladukh, D.; Raha, S.; Conroy, M.; Nicolosi, V.; Singha, A.; Holmes, J. D. Exploring the Novel Tetragonal (ST12) Germanium Phase in Nanowires. Submitted June 2021.

**Garcia-Gil, A.;** Biswas, S.; McNulty, D.; Roy, A.; Ryan, K. M.; Nicolosi, V.; Holmes, J. D. Batch-produced self-seeded Germanium-Tin Alloy Nanowires as Highly Efficient Li-Ion Battery Anodes. Submitted August 2021.

### Conference contributions and talks

**Garcia-Gil, A.;** Biswas, S.; Holmes, J. D. High-quality Seedless Group IV nanowires: Synthesis and Characterisation. I HRS NanoNet Annual Workshop, 5-7 September 2018, Bad Gottleuba, Germany.



**Garcia-Gil, A.**; Biswas, S.; Holmes, J. D. Single-pot synthesis of metal-free group IV semiconductor nanowires. NanoNet International Conference, 8-11 October 2019, Dresden, Germany.

### **Other contributions**

Wang, L.; Pei, J.; Cong, Z.; Zou, Y.; Sun, T.; Davitt, F.; **Garcia-Gil, A.**; Holmes, J. D.; O'Driscoll, C. M.; Rahme, K.; Guo, J., Development of anisamide-targeted PEGylated gold nanorods to deliver epirubicin for chemo-photothermal therapy in tumor-bearing mice. *Int. J. Nanomedicine*. **2019**, 14, 1817.

Doherty, J.; Biswas, S.; Galluccio, E.; Broderick, C. A.; **Garcia-Gil, A.**; Duffy, R.; O'Reilly, E. P.; Holmes, J. D. Progress on Germanium–Tin Nanoscale Alloys. *Chem. Mater.* **2020**, 32, 4383.

Raha, S.; Singha, A.; Srivastava D.; Karttunen A. J.; **Garcia-Gil, A.**; Biswas, S.; Holmes, J. D. ST12 Germanium Nanowire: Identification and Study by Raman Spectroscopy and DFT Calculations. Submitted June 2021.

## Abstract

Li-ion batteries are important energy storage devices today, powering a range of electrical equipment from mobile phones to electric vehicles. Most commercial Li-ion battery anodes are made from carbon-based materials which limit their improvement of total battery capacity, energy density and cycle life performance because of the relatively low specific charge capacity of carbon. Group IV semiconductors, particularly Ge and GeSn, are a promising alternative to conventional carbon-based electrodes: especially in niche energy storage applications like small high-tech devices. In this thesis, I describe a cost-effective and simple method for synthesising Ge and GeSn nanowires, with potential application as anode materials in Li-ion batteries. A single-pot, solvothermal-like synthetic method, employing supercritical solvent conditions, was used to grow self-seeded group IV nanowires, without the need for traditional metal catalysts or templating agents. My approach permitted the growth of thin ( $\sim 10$  nm) and highly crystalline nanowires of carbon-coated cubic Ge (C-Ge), metastable tetragonal ST12 Ge and GeSn, from commercially available precursors at moderate reaction temperatures, between 330 and 490 °C. Photoluminescence studies carried out on tetragonal ST12 Ge nanowires suggested they possessed a fundamental direct bandgap of  $\sim 0.64$  eV. Both C-Ge and GeSn nanowires were directly grown onto Ti current collectors and evaluated as potential anodes for Li-ion batteries. C-Ge nanowires demonstrated exceptional performance, displaying a high specific charge value of  $> 1200$  mA h g<sup>-1</sup> after 500 cycles at 0.2 C, while GeSn alloy nanowires also displayed an impressive specific charge capacity of 1127 mA h g<sup>-1</sup> after 150 cycles at 0.2 C. The growth mechanisms for each set of nanowires are also described in detail in the thesis. Similarities in growth mechanisms were observed between nanowires grown using the single-step approach and previously reported solution-phase studies.

# Chapter 1

## A Review of Self-Seeded Germanium Nanowires: Synthesis, Growth Mechanisms and Potential Applications

Data from this chapter was submitted for publication in June 2021. Consequently, sections of the chapter such as the abstract and introduction may contain repeating concepts and paragraphs.

Garcia-Gil, A.; Biswas, S.; Holmes, J. D., ‘A Review of Self-Seeded Germanium Nanowires: Synthesis, Growth Mechanisms and Potential Applications’. *Nanomaterials* **2021**, *11*, 2002.

## 1.1. Introduction

The discovery of the semiconducting behaviour in materials, by Alessandro Volta in the 18<sup>th</sup> century, settled an inconceivable breakthrough in the technological progress that was going to be developed in the next centuries.<sup>1</sup> Later on, in the years that followed the visionary work of Wagner and Ellis in the 1960s,<sup>2</sup> several semiconductor compounds were successfully synthesised, including the widely popular Si and Ge structures.<sup>3,4</sup> As stated by Moore's Law,<sup>5</sup> the semiconductor industry had no choice but to follow a continuous drive towards device miniaturisation for greater integration in electronic devices. Moore's prediction has been used as a guide for long-term planning and to set targets for research and development in electronics. Thanks to developments in nanoscale materials and devices, we are now embarking on a nanotechnology time in history. The *leitmotiv* which powers the investigation of nanoscale materials is the captivating new chemical and physical properties exhibited when compared to their analogous bulk material.<sup>6</sup> Particularly, some of the significantly size-dependent features are the physical, electrical and optical properties.<sup>7-9</sup> These materials are gathered in a range of structures such as zero-dimensional (0D) (quantum dots)<sup>10</sup>, one-dimensional (1D) (nanorods,<sup>11</sup> nanotubes,<sup>12</sup> nanobelts<sup>13</sup> and nanowires<sup>14</sup>), two-dimensional (2D) (nanofilms,<sup>15</sup> nanodisks,<sup>16</sup> nanoplates<sup>17</sup> and nanosheets<sup>18</sup>) and three-dimensional (3D) (assemblies of nanocrystals<sup>19</sup> and nanocomposites<sup>20</sup>).

The revolution on 1D nanomaterials started with Haraguchi *et al.*<sup>21</sup> who achieved the first device fabricated from 1D nanostructures, back in 1992. The semiconductor nanowires of small diameters make them attractive for potential quantum confinement effects, while their unconstrained lengths make it easy to integrate them into already

existing devices. This escalated the interest for 1D nanostructures in all kinds of potential applications (photocatalysts,<sup>22</sup> magnetic storage media,<sup>23</sup> nanoscale sensors,<sup>24</sup> optical devices,<sup>25</sup> solar cells,<sup>26</sup> liquid crystal devices<sup>27</sup> *etc.*). In particular, research into group IV semiconductor nanowires has been of high interest since the beginning of the 2000s.<sup>28</sup> Within group IV elements, silicon has been the material of choice for the microelectronics industry due to its abundance on the Earth's crust (and cost-effective as a consequence), non-toxic nature and chemical stability.<sup>29</sup> As well, it presents high carrier mobility and optimum structural and electrical characteristics of the Si/SiO<sub>2</sub> interface, all advantageous features for different electronic, optoelectronic, and energy applications. Thus, a key requirement is to research materials compatible with well-developed Si-based industrial technology. Although the first transistor, made in the 40s,<sup>30,31</sup> was made using Ge, its lower natural abundance (and higher price as a consequence) and less stable external oxide layer forced the industry to replace it with Si.<sup>32</sup> However, the current development of high-*k* dielectric materials have boosted the research on synthetic protocols applied to Ge nanostructures formation, and nanowires in particular.<sup>33,34</sup>

Germanium exhibits superior features to Si such as a superior charge carrier transport due to lower effective mass of electrons and holes,<sup>35</sup> and presents quantum confinement effects at larger dimensions (Bohr radius of 24.3 nm and 4.9 nm for Ge and Si, respectively).<sup>36–39</sup> Also, germanium displays a smaller indirect bandgap of 0.66 eV (at 300 K) with a very small difference with the direct bandgap (~ 140 meV) compared to Si (1.11 eV with the large direct-indirect bandgap difference of 2.4 eV at 300 K). Fortunately, the similarities in crystal structure between Si and Ge simplified the development of bottom-up synthetic techniques and catalytic growth procedures

to obtain high quality Ge nanostructures, and nanowires in particular.<sup>40</sup> This synthetic progress has been profited not only in nanoelectronic devices,<sup>41–43</sup> but also in other applications fields such as solar energy conversion,<sup>44,45</sup> memory applications,<sup>46</sup> biological nanosensors,<sup>47,48</sup> catalysis,<sup>49</sup> nanoelectromechanical systems<sup>50</sup> and energy storage<sup>51,52</sup>.

Germanium, along with carbon, silicon and tin, can form many allotropes besides graphite and diamond cubic (dc), and a relatively easy synthetic path has been found for most of them. Over the years, however, germanium allotropes have mainly been obtained by pressure induction.<sup>53</sup> It is well established that when germanium, both amorphous or diamond-cubic forms (see Figure 1.1a), is placed in a diamond anvil cell (DAC) under a reasonable amount of pressure (above 10 GPa), a new metallic  $\beta$ -Sn structure (I4<sub>1</sub>/amd) arises due to a phase transformation.<sup>53,54</sup> It is worth mentioning that this transformation is uplifted to pressures above 17 GPa at the nanoscale.<sup>55</sup> Yet, upon pressure release at room temperature, germanium does not follow a reverse structural sequence. Instead, the appearance of a tetragonal phase (see Figure 1.1b) (also called ST12-Ge or Ge-III, which contains 12 atoms per unit cell in the space group P4<sub>3</sub>2<sub>1</sub>2 – D<sup>8</sup><sub>4–</sub>) or a body centred cubic structure (also called BC8, which slowly changes to the hexagonal diamond crystal structure), both sometimes mixed with dc-Ge form, have been reported.<sup>53,54</sup> Hydrostaticity and shear-stress factors have been suggested as the main parameters for phase selection.<sup>56</sup> Through this process, and also over higher pressures, dc-Ge undergoes a series of structural transitions, which have been the subject of a large number of theoretical and experimental studies.<sup>54,57,58</sup> A considerable effort has been made to simulate and characterize the different properties conferred to most of these different polymorphs presented by germanium, and

hypothetical metastable structures of germanium, such as Pbam-24,<sup>59</sup> P42/ncm,<sup>60</sup> or P6522,<sup>61</sup> have been predicted to possess better energetic stabilities in comparison with diamond cubic phase. Among all the crystalline Ge allotropes, nearly none of them is stable at room temperature and ambient pressure, yet ST12-Ge has been reported to be kinetically stable at ambient conditions.<sup>62</sup> ST12-Ge (see Figure 1.1b) is based on a tetrahedral structure with 12 atoms per unit cell arranged to form fivefold, sixfold and sevenfold rings. Hence, it is expected to be a semiconductor and has attracted special attention due to its potential in electronic and energy storage applications. Also, comparisons with theoretical calculations carried out for ST12-Silicon point that doped ST12-Ge may act as a superconductor at low temperatures.<sup>63</sup>

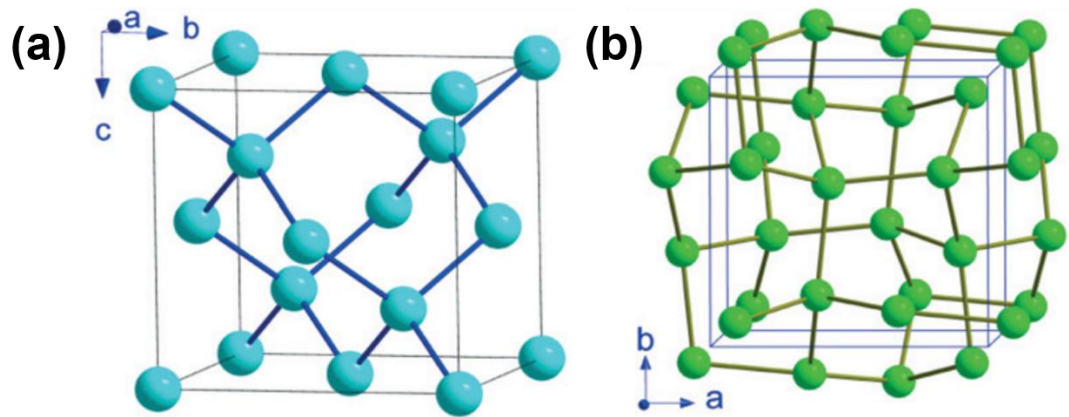


**Figure 1.1.** Crystal structures of germanium. (a) Germanium in the diamond cubic-type structure with the  $Fd\bar{3}m$  space group. (b) The metastable tetragonal ST12 structure with the  $P4_32_12$  space group.<sup>64</sup>

Ge nanowires have been produced using a wide variety of synthetic protocols most of which are based on the vapour-liquid-solid (VLS) or VLS-like mechanisms. These approaches are based on a three-phase system (growth media, seed particle and nanowire/substrate support) where nanowire growth occurs. The nature of the selected nucleation seed (external or self-seeded) plays a crucial role in nanowire growth

development. However, even though some external catalyst seeds may present synthetic advantages, they might also diffuse and incorporate into the structure of nanowires. This phenomenon might lead to impurity incorporation into the nanowire structure and a significant modification of the semiconducting properties of the nanowires. Catalyst-free and self-seeded growth approaches have demonstrated to be able to obtain competitive nanowire growth rates and narrow diameter distribution without affecting the chemical and physical nature of the resultant nanomaterial.

Among all applications for the self-seeded Ge nanowires, energy storage, lithium-ion batteries (LIB) in particular, have raised a vast interest.<sup>65,66</sup> Semiconductor nanowires are very attractive for LIBs due to the good electronic conduction, the short Li-ion diffusion distance, and the high surface contact area with battery electrolytes.<sup>65,67</sup> LIBs have been accepted as the pre-eminent energy storage technology for portable electronic devices due to several presented advantages such as high energy/power density, long life and eco-friendly features.<sup>68,69</sup> However, state-of-the-art LIBs still do not meet the demands of high-performance requirements in the current market, *i.e.* electric vehicles, and germanium is one of the most promising candidates for the next-generation LIBs. Features of germanium such as the theoretical specific capacity of 1624 mA h g<sup>-1</sup> (for Li<sub>22</sub>Ge<sub>5</sub>), the high electrical conductivity (10<sup>4</sup> times higher than that of Si), the high Li-ion diffusivity (400 times greater than that of Si) and a volumetric capacity of 7366 Ah L<sup>-1</sup> place germanium (and its alloys or composites) in a privileged position to replace common graphite as a future anode for LIBs.<sup>65,70–72</sup>

In this chapter, I evaluate synthetic methods and growth mechanisms for self-seeded Ge nanowires growth. Section 2 introduces the general growth mechanisms for both



externally-seeded and self-seeded Ge nanowire growth and the most popular catalysts employed. Section 3 reviews synthetic methods employed to grow Ge nanowires without any externally added metallic seed, with the focus on the self-seeded bottom-up approaches. Section 4 focus on the growth mechanisms applied for self-seeded Ge nanowire production. Section 5 examines the growth of self-seeded Ge nanowire alloys with a special focus on GeSn alloy. Finally, I will discuss the application for self-seeded Ge nanowires, in particular in a lithium-ion battery application.

## **1.2. Germanium Nanowires Growth Mechanisms**

### **1.2.1. Primary Growth Paradigms for the Nanowire Growth**

Ge nanowires can be synthesised using a wide variety of synthetic protocols, most of which are based on the three-phase VLS mechanism and its derivatives such as vapour-solid-solid (VSS), solution-liquid-solid (SLS) or supercritical fluid-solution-solid (SFLS) growth paradigms. Less popular growth mechanisms, such as the vapour-solid (VS) mechanism and oxide-assisted growth (OAG) mechanism, have also been explored for Ge nanowire growth. Although other growth mechanisms have also been used for nanowires synthesis like solvent-vapour, epitaxial growth or solid-liquid-solid mechanism, this section will only focus on the most used growth mechanisms for Ge nanowires, which are also relevant in understanding the seedless and self-seeded growth mechanisms of nanowires. A brief discussion on the different bottom-up growth mechanisms involving seed/catalyst, *e.g.* VLS, VSS) or no participation of seed, *e.g.* VS, OAG, is presented in this section.

Generally, the names attributed to growth mechanisms tend to be quite self-explanatory and are derived from the physical states of the phases involved. Some of

the growth methods, *e.g.* VLS, VSS, SLS, SFLS, differ only in the reaction media, but the growth mechanism is otherwise identical. The initial word, such as “vapour”, “solution” or “supercritical fluid” refers to the medium where the reaction is going to take place and the source of the reaction material. The second word, “liquid” or “solid”, indicates the state of the catalyst seed or droplet at the reaction temperature. The last word refers to the substrate and the single-crystal nanowires formed, where the growth takes place. Successful implementation of these growth mechanisms requires the precursor species to be delivered and reach a catalyst droplet (liquid or solid), where supersaturation and nucleation, and finally crystallisation into a solid nanowire structure will take place. A generalisation for the different growth mechanisms is that the growth rate at the seed-crystal solid interface is faster than the growth rate at any of the other interfaces. This point will be discussed in detail in later sections.

While the catalyst for the VLS growth of Ge nanowires is in the liquid state, the catalyst for VSS growth is at a temperature below the melting point, in the solid state. The state of the catalyst is assumed to be at a temperature below its melting point (or eutectic point of the mixture) based on bulk phase diagrams.<sup>73</sup> However, at the nanoscale a modification in the phase diagram (or melting point of the nanoscale seed) may occur and a shift of the metal-semiconductor eutectic towards lower temperature may lead to attribution to a wrong growth mechanism.<sup>74–76</sup> Likewise, the eutectic point shift might differ between materials with the same-sized nanoparticles.<sup>77,78</sup> The state of the seed can also influence nanowire growth. For example, a reduction in the growth rate of nanowires via VSS growth, by an order of magnitude compared to the VLS growth under identical growth conditions, has been identified.<sup>79</sup> This is

attributed to weaker surface reactivity (lower eutectic point) and lower diffusivity through the solid droplet compared to the growth with the liquid nanoparticle.

Solution-based (SLS<sup>80</sup> and SFLS<sup>81</sup>) synthesis mechanisms are analogous variants of the VLS mechanism, although conducted in solution or solvent dispersions. Solution-based mechanisms are a promising approach for the mass production of nanomaterials with excellent controls of the composition and morphology. They are usually conducted in the presence of coordinating solvents, which help in tuning the growth kinetics and passivating the generated structures. These mechanisms present some clear advantages over other widely used mechanisms. Narrow size distributions (diameter as small as 5 nm) and the crystallinity could be achieved at much lower growth temperatures (usually 200-350 °C) compared to vapour-phase growth.<sup>81,82</sup> Better control over the nanowire morphology and crystallinity was achieved via flow-through solution-based process compared to a batch growth process.<sup>81-83</sup> Nevertheless, a clear challenge that still exists is the significant amount of carbonaceous by-products formed during the reaction, which often limits reaction yields and contaminates the resulting nanowires. Although, this issue has been used as an advantage for battery applications and will be discussed later.

An SFLS growth mechanism, in particular, is achieved when the solvent is at a temperature and pressure beyond its critical point. Above the critical point, the vapour and liquid coexist and a single-phase fluid with intermediate properties is generated which presents a unique density, low viscosity, high diffusivity and low surface tension.<sup>84</sup> These particular properties allow significant synthetic tunability by varying temperature and/or pressure, acquiring desired gas-like or liquid-like conditions.

Growth under these conditions provides: (i) higher chemical flexibility, (ii) dispersion of bigger nanoparticle seeds, (iii) precursors solubilisation at higher concentrations than usual and (iv) growth under high temperatures in a solution phase by increasing the boiling point of the solvent. The yield of the nanowires from SFLS growth is surprisingly high, extended up to milligram quantities of different single crystal nanowires.<sup>85–87</sup> The main flaws of the SFLS growth are the possible nanoparticle seed agglomeration and coarsening leading to broad nanowire diameter distributions.<sup>84</sup> Additionally, nanowire nucleation and growth take place at a higher rate than VLS growth ( $\mu\text{m min}^{-1}$  in SFLS while  $\text{nm min}^{-1}$  in VLS), which is often too fast for quantitative analysis of growth kinetics and mechanics. At the same time, the sequential introduction of precursors or concentration adjustments are much more limited, which restricts the synthesis of axial heterostructures.<sup>88</sup>

The vapour-solid (VS) growth mechanism is one of the most widely employed mechanisms for the general growth of nanomaterials. This mechanism is a catalyst-free (unseeded) mechanism, which means it does not require the presence of a third party to act as a nucleation point. Instead, VS growth only involves two phases and growth occur directly from the vapour-phase source species condensing to the crystalline solid-phase nanostructure. The required growth temperature for this mechanism is higher than in other catalytic methods due to the absence of an energetically favoured catalytic point (the seed). This mechanism is mainly governed by the temperature and pressure of the reaction and the nature of the surface where the deposition takes place. The main advantage of this method is the absence of any contamination resulting from parts of the seed becoming trapped in the crystalline structure of the nanowires. Ge nanowires produced via a VS mechanism are generally

free from stacking faults and metal contamination and can be more efficient light emitters than the seeded, *e.g.* Ni seeded, nanowires.<sup>89,90</sup>

Oxide assisted growth (OAG) is another mechanism employing high temperature as the main driving force for nanowire growth. In this process, instead of a metal or metalloid catalyst seed, oxides play a key role in the nucleation and growth of the nanowires. High yield and high purity nanowires with preferential growth directions, uniform diameters can be obtained through OAG.<sup>91</sup> While nanowire diameter is limited by the seed diameter in VLS-like growth, in the OAG very narrow diameter (even  $\sim 1$  nm) can be achieved by careful control of gas flow and substrate temperature.<sup>92</sup> Another important advantage is the use of simple elemental and oxide powders as precursors, avoiding poisonous and flammable precursor gases such as silane or germane. However, the main drawbacks are the high-reaction temperature required (enough to vaporise the precursors under vacuum) and the unavoidable oxide shell growth, which must be removed before implementation in electrical or optical devices. In a conventional OAG process, the first step consists of thermal evaporation of a mixture of the material and its oxide. Despite the high temperatures used, most of the solid source materials may not sublime in a regular atmosphere, thus high-vacuum conditions are required. Reactive oxide clusters (a mixture of Ge and  $\text{GeO}_x$ ) are also formed and deposited while generating some bonding with the substrate itself and limiting the mobility across the surface. As a result, non-bonded and highly reactive atoms present in the cluster are exposed to the vapour phase. Oxides play an important role here in the formation of intermediate catalyst-seed-like clusters.<sup>93–95</sup> Initial clusters may act as nuclei for absorption of additional clusters or other vapour species, serving as a driving force for nanowire growth.<sup>96,97</sup> In this process, oxygen

atoms are desorbed from the clusters during crystallisation, inducing the diffusion of the oxygen to the surface and producing a chemically inert oxide sheath.<sup>98</sup>

### **1.2.2. Why Self-Seeded growth: Disadvantages of Catalytic Ge Nanowire Growth**

As pioneered by Wagner and Ellis,<sup>2</sup> metal-catalyst based techniques have become the most commonly employed for growing 1D semiconductor nanostructures. The catalytic particle assisting the growth becomes the crucial point of the overall growth process. This is not only because the size of the particle determines the diameter of the nanowires, but also, the catalyst position on the substrate may dictate nanowire placement.<sup>99,100</sup> Seeded growth involving a metal catalyst is based on the idea that the energy barrier required for a given material to nucleate heterogeneously onto a pre-existing seed is lower than the necessary activation energy to induce, homogeneously, self-nucleation.<sup>165</sup>

#### **1.2.2.1. Different Catalyst Type and their Effect on Physical Properties of Nanowires**

Au is the most extensively studied catalyst for Ge nanowire growth. Some of the main reasons for it to be considered the standard catalyst are its low toxicity, chemical stability when exposed to air, the low vapour pressure at high temperatures and simple processing. Although Au forms a low-temperature eutectic with Ge (361 °C)<sup>101</sup>, there are certain disadvantages associated with using the metal, which had led to the screening of other elements and alloys as catalytic seeds for Ge nanowire growth. The catalysts used for Ge nanowire growth are generally categorised into three groups:<sup>102</sup> (i) type A, *i.e.* Au, Ag and Al, with simple binary phase diagrams and high eutectic solubility (> 10 % of Ge in the eutectic alloy), (ii) type B, *i.e.* In Sn and Bi, with also

simple binary phase diagrams but low eutectic solubility (typically < 1 % of Ge in the eutectic alloy) and (iii) type C, *i.e.* Fe, Ni and Cu, germanide forming catalysts which result in complex binary phase diagrams. Due to the high melting point (> 1000 °C), the type C catalyst will generally not be in a liquid state but in solid state to induce VSS growth.<sup>103</sup>

Within type A catalysts, Au, which is an expensive and rare metal, emerges as the predominant catalyst for Ge nanowires, as other type-A metals (Ag or Al) form relatively high temperature eutectics with a high Ge solubility. However, with all catalyst-metal particles used for nanowires growth, the effect of possible metal incorporation into the crystal structure of nanowire can become a critical point for electronic transport. The high diffusion constant of many metals in Ge makes the impurity incorporation process likely to occur during growth.<sup>104</sup> A significant modification of semiconducting properties, *e.g.* bandgap, is produced when the incorporation of  $10^{-7}$  catalyst atoms in the nanowire is surpassed.<sup>105,106</sup> The presence of these impurities not only can introduce deep defect levels in the semiconductor bandgap, making it unfavourable for electronic applications but also negatively affect energy storage applications by inducing irreversible capacity losses in anodes for Li-ion batteries.<sup>107</sup> Although, most deep-level recombination processes and scattering occur from nanowire surface states which may not be altered by the presence of Au in the bulk of the nanowires.<sup>108,109</sup> This is of particular importance for Ge, which displays higher surface-state densities than Si ( $10^{14}$  cm<sup>-2</sup> and  $10^{12}$  cm<sup>-2</sup>, respectively).<sup>110</sup> Selective chemical etching, *e.g.* in *aqua-regia*, has been occasionally used to remove Au present on the surfaces of nanowires, but Au atoms trapped into the nanowire structure during growth might still affect the properties of these nanowires.<sup>111,112</sup>

All these concerns over the use of Au catalysts fuelled the investigation of more suitable catalyst alternatives for the synthesis of semiconductor nanowires, Ge nanowires in particular.<sup>113</sup> Ag, as well as Ag/Au alloys, have shown high efficiency in the growth of Ge nanowires.<sup>114</sup> Al is also presented as one of the critical seed-metals as it creates low-level traps in the Ge nanowire structure<sup>115</sup> and also acts as a p-type dopant.<sup>116</sup> However, the sensitivity and high reactivity of Al with oxygen limit its usage in most synthetic setups, requiring demanding oxide removal steps. For type-B catalysts, the diffusion of the seed into the nanowire structure might be seen as an advantage since the presence of those elements can act as dopants. However, the solubility of Ge in these metals or metalloids is usually low ( $< 1\%$ ) which might lead to meta-stable structures when high incorporation ratios are achieved.<sup>117</sup> Zn is the least interesting one within this group because it can introduce electron traps (like type A catalysts) but despite this, good quality nanowires have been obtained with Zn.<sup>118</sup> Cd and Tl are not very suitable for Ge nanowire growth due to the droplet-nanowire system surface tension, a crucial element in nanowire growth. Group III, *i.e.* Ga<sup>119</sup> and In<sup>120</sup>, IV, *i.e.* Sn<sup>121</sup> and Pb<sup>122</sup> and V, *i.e.* Sb<sup>40</sup> and Bi<sup>123</sup>, elements are much more interesting as seed materials due to their low eutectic temperatures while having potential doping capacities as both, n-type and p-type dopants. Type C catalysts, *e.g.* Cu<sup>124</sup> and Ni<sup>125</sup>, are of particular interest due to their compatibility with group IV materials, and thus, potential integration in the CMOS (Complementary Metal-Oxide-Semiconductor) industry.<sup>126</sup> As type B catalysts are promising due to their doping capacity, type C materials have become popular due to their promising ability to be used in microelectronic applications where properties like high conductivity and high-quality crystal structures are required. However, oxidation of these catalysts could be



an issue along with the slow nanowire growth rate and germanide phase formation, which may limit their application.

### **1.3. Self-Seeded Germanium Nanowires Synthesis Methods**

Ge nanowires are commonly fabricated by either top-down or bottom-up processes. Each of the approaches presents intrinsic advantages and limitations and may be adopted under the appropriate circumstances. In the semiconductor industry, since its onset in 1959, top-down approaches, optical lithography or photolithography, was utilised to fabricate nanowires.<sup>127</sup> Photolithography involves several steps, comprising material removal from bulk samples through local etching and deposition processes, to build up a nanowire structure. This technique has been able to design and produce nanowires with dimensions down to the 10 nm range.<sup>128</sup> Top-down methods also include electron beam and focused ion-beam lithography, both less present at the industrial-scale production. The main drawback presented by photolithography is the surface roughness of nanowires generated which may result in considerable diameter variability. Rough surfaces are also susceptible to increase surface scattering. Additionally, top-down processing also has a limitation in achieving engineered nanostructures such as heterostructure and alloys.

In contrast, bottom-up techniques present a high degree of freedom in combining materials to construct very complex structures through self-assembly. After the first demonstration of bottom-up nanowire synthesis in 1964<sup>2</sup>, this method became the most common path to obtain any anisotropic growth at the nanoscale. A wide range of bottom-up approaches have been developed, and most of them are well-known for the formation of high yields of small-diameter nanowires while maintaining low costs

of production. However, usage of external catalysts for nanowire growth lead to metal incorporation in the nanowire atomic structure which critically alters the semiconducting properties of the nanostructures (discussed in detail in Section 1.2). Another potential drawback for bottom-up growth is the precise placement with high regularity over large surface areas, as required for integrated circuits. This section will review the synthetic methods widely used for Ge nanowire growth, with a special focus on the self-seeded approaches.

### **1.3.1. Bottom-Up Synthesis of Self-Seeded Germanium Nanowires**

Bottom-up techniques have the potential to outperform the limits and functionalities of top-down strategies controlling morphology, composition and structure within a narrow distribution range. Within bottom-up synthetic approaches, different explored routes can be classified as (i) vapour-phase growth, (ii) solution-based growth and (iii) growth techniques using templates.

The standard process for both vapour-phase and solution-based techniques can be described by three simple steps. Initially, a gaseous Ge precursor (originally gas or volatilised liquid) is introduced into the system. An inert carrier gas such as Ar is employed to transport the precursor in the reaction chamber, providing an oxygen-free environment. The supplied gaseous precursor (either in molecular or atomic form) gathers around the nanoparticle seed (either in solid or liquid phase) deposited over a substrate. This is followed by the decomposition of the precursor molecules on the surface of the nanoparticle seed, as well as adsorption and diffusion of the Ge atoms into the nanoparticle seed. Finally, when supersaturation is reached in the seed particle, preferential precipitation occurs as a single-direction elongation (usually at

the interface between the seed and the substrate) to form one-dimensional structures. Most often, this deposition process is thermally driven, but several other perturbation processes (growth enhancement by laser<sup>129</sup>, X-Ray,<sup>130</sup> microwave<sup>131</sup>) have also been described.

The three-phase bottom-up Ge nanowire growth may also be achieved without the use of an external catalyst. Ge itself plays an important role in the formation and growth of Ge nanowires via a self-seeding mechanism in a VLS paradigm. This is usually achieved when *in situ* Ge nucleation seeds form, requiring no pre-deposited nanoparticle seeds or films of Ge, generating nanowires. A more detailed analysis of the self-seeded growth of Ge nanowire will be discussed in Section 4.

#### **1.3.1.1. Vapour-Phase Growth of Self-Seeded Nanowires**

Within the vapour-phase growth group of techniques, chemical vapour deposition (CVD) and physical vapour deposition (PVD) can be distinguished. While PVD is based on physical mechanisms to deposit nanomaterials, CVD relies on chemical reactions to obtain different nanostructures.

***PVD growth of self-seeded nanowires.*** In PVD growth, a solid precursor transforms into vapour using a laser or high-power electrical tools. Once transferred into the reaction chamber, the vaporised material is adsorbed on the substrate or nanoparticles yielding to the growth of desired material, thus not relying on any chemical process. This growth method has advantages not only as an eco-friendly technique but also when growing extremely hard and corrosion-resistant materials because of their high-temperature laser-ablation resistance. However, the main flaw for its scalability is the

high cost due to the slowness of the process and the intense heating and cooling procedures required.

Oblique angle deposition (OAD), utilising the epitaxy of a growth substrate is one of the simplest examples of PVD. Epitaxial growth refers to atoms nucleated and grown on a single-crystal face ordered in a relative orientation to a substrate. This technique bases its capacity of growing nanowires only on the appropriate selection of a substrate crystal orientation, the temperature and precursor evaporation rate, and the control of the deposition angles.<sup>132</sup> Taking advantage of the possible crystallographic correlation between the single crystal substrate and the crystal structure of the nanowires (lattice matching), a predominant growth orientation is achieved.<sup>35</sup> Nanowire growth can also be produced when there is a large lattice mismatch between a nanowire and substrate material.<sup>133</sup> The relative substrate-deposit orientation depends on the structure of the crystal planes in contact and the atomic interactions across the interface, although, a mask layer, *i.e.* SiO<sub>x</sub>, is often used to allow growth on specific areas of a substrate.<sup>134</sup> Growth takes place at a very slow rate on low-surface-energy side facets, as no catalyst seeds are used and the process is only controlled by temperature, which significantly limits its tunability.<sup>135,136</sup> However, a drawback of this technique is the formation of kinked nanowires.<sup>137,138</sup> Electron beam melting (EBM) is an analogous technique based on the use of suitable substrates to control the alignment and crystal orientation of nanowires. A detailed study about self-seeded Ge nanowire growth by OAD was published by Li *et al.*<sup>139</sup>, the first and only attempt to grow pure Ge nanowires by OAD. Different substrate temperatures were screened, under an optimised flux angle and deposition rate variables, and long and self-standing nanowires were obtained at a temperature around 330 °C. As the nanowires did not display a straight morphology

with smooth surfaces (see SEM images in Figures 1.2a and 1.2b), details on mean diameter, diameter variation and length of the nanowires were not disclosed. The crystallinity of the nanowires was confirmed by Raman spectroscopy and X-Ray diffraction (XRD), obtaining the highest crystallinity for samples grown at a high temperature (330 °C). Transmission electron microscopy (TEM) (see Figures 1.2c and 1.2d) further validated the presence of amorphous Ge at 130 °C, polycrystalline Ge at 230 °C and highly crystalline structures growing in the (110) direction at a temperature of 330 °C. Thermal stability tests were also performed, presenting Ge nanowires with excellent structural cohesion below 500 °C. At 500 °C nanowires started to melt and aggregate together, and above 580 °C they were all melted and aggregated as particles.

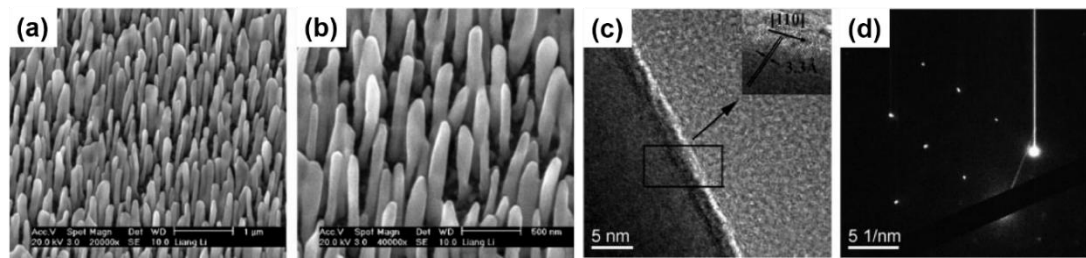


**Figure 1.2.** (a), (b) Scanning electron microscopy (SEM) images of the Ge nanostructures deposited at a substrate temperature of 330 °C with a flux angle of 87° and a deposition rate of between 0.1 - 0.2 Å s<sup>-1</sup>. Scale bar of (a): 1 μm and the magnified image of (b) the scale bar is: 500 nm. (c), (d) High-resolution TEM (HRTEM) images and selected-area electron diffraction (SAED) patterns of Ge nanowires fabricated at a temperature of 330 °C.<sup>139</sup>

**CVD growth of nanostructures.** In CVD growth, a vapour-phase chemical reaction takes place close to the surface of the substrate, which is maintained at the growth temperature during the whole deposition period. Depending on the processing conditions, CVD can be classified as metal-organic CVD, low-pressure CVD, plasma-

assisted CVD, hot-wall CVD, *etc.* As a widely studied technique, and probably the most popular for nanowire growth, CVD allows the formation of a variety of nanomaterials from a vast number of material sources. CVD is based on a near-equilibrium process, which grants a firm control over the composition, dimension, location, and morphology of the desired nanomaterial, as well as the impurity concentration and distribution (*in situ* doping). CVD as a method for growing semiconductor nanowires has advantages or disadvantages that mainly depend on the reaction temperature used. For example, working at low temperatures ( $< 600\text{ }^{\circ}\text{C}$ ) makes CVD more compatible with Si processing, so any innovation is more likely to be used for industrial applications.<sup>140</sup> At temperatures  $< 600\text{ }^{\circ}\text{C}$ , narrow and uniform diameter nanowires, along with highly-crystal and well-faceted structures are achievable. *In situ* doping processes are also more readily accomplished, allowing facile tuning of nanowire properties.<sup>141,142</sup> However, there is a wider choice of precursors when working at high temperatures ( $> 700\text{ }^{\circ}\text{C}$ ), which also allows a greater degree of freedom to vary growth conditions (temperature and pressure). The main concern with using high temperatures is the aggregation and Ostwald ripening processes suffered by the nanoparticle seeds due to the surface diffusion. These effects result in large seed particles formation, which inhibits the formation of uniform diameter distributions. In this regard, self-seeded bottom-up grown carbon-capped seeds formed *in situ* has an advantage over the common metal-assisted CVD growth via the VLS technique. The main drawbacks of the popular CVD technique are the numerous control variables to consider when designing an experiment and the use of harmful gases and/or precursors.

***Self-seeded nanowire growth by CVD.*** Kim *et al.*<sup>143</sup> used a hydrogen-terminated patterned Si substrate surface as a reactive surface to accommodate the growth of Ge nanowires in a common CVD setup. The use of the GeH<sub>4</sub> precursor mixed with H<sub>2</sub> gases yielded highly dense growth of nanowires (see Figures 1.3a and 1.3b) with aspect ratios above 10<sup>3</sup>.<sup>143</sup> The same precursor was utilised to evaluate the effect of X-rays in Ge nanowire growth in a CVD reaction.<sup>130</sup> Ge nanowires with high aspect ratios, lengths up to 20 µm, and a high degree of kinking were produced at a low synthesis temperature of 300 °C. Aggregated spheroids or amorphous hydrogenated Ge were not found in the samples,<sup>144,145</sup> and the nanowires obtained were highly kinked (see Figures 1.3c and 1.3d). Broad diffraction peaks determined by XRD pointed towards low crystallinity in the nanowire samples, further confirmed by the TEM observation of a small yield of amorphous Ge (a-Ge) phase. Dřínek *et al.*<sup>146</sup> utilised alternative commercial precursors such as (GeMe<sub>3</sub>)<sub>2</sub> for the Ge nanowire growth without the presence of any additional catalysts. A growth temperature of 490 °C led to the formation of high-quality Ge nanowires on substrates such as Ta, SiO<sub>x</sub> and W. While kinking was absent in the nanowires (see Figure 1.3e) bending of the nanowires was observed (see Figure 1.3f) which may inhibit their application in electronic/optoelectronic devices. The same authors experimented with other Ge precursors, such as (SiMe<sub>3</sub>)<sub>3</sub>GeH, in a single-step CVD approach which created unusual nanowire morphologies, such as core-shell Ge-Si/C nanowires (see Figure 1.3g).<sup>147</sup> A Ge core with a variable diameter between 5 - 40 nm was coated by a two-layer shell of Si and C (see Figure 1.3h) with a total thickness of 5 to 20 nm. The shell part was constituted by an inner coating of 5 nm Ge crystallites in an amorphous body, surrounded by a completely amorphous outer coating. These Ge nanowires with an outer diameter up to 100 nm (core and shell) generally presented a crystalline Ge core

growing along the [110] direction, exhibiting a single crystal Ge structure without any defect.<sup>147</sup>

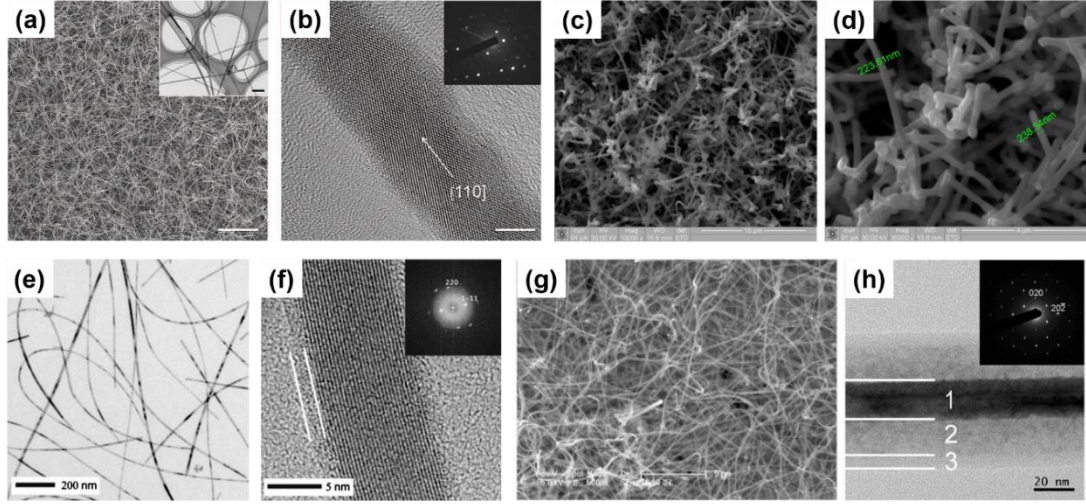


**Figure 1.3.** (a) SEM image showing high-density, uniform Ge nanowires grown from a planar thin SiO<sub>x</sub> film on a Si surface; scale bar: 3 μm. Inset: a TEM image of the Ge nanowires, scale bar: 100 nm. (b) A lattice-resolved TEM image of a single-crystal Ge nanowire. The arrow highlights the nanowire axis, which corresponds to the  $\langle 110 \rangle$  direction; scale bar: 5 nm. Inset: the corresponding diffraction pattern (ED).<sup>143</sup> (c), (d) SEM images of Ge nanowire products deposited on the lower surface of a quartz substrate. Specific diameters of nanowire frames are reported in (d).<sup>130</sup> (e) Bright-field TEM image of Ge nanowires prepared on a stainless steel AISI 310 substrate. (f) HRTEM observations of Ge nanowire elongated along the [110] direction prepared on a stainless steel AISI 310 substrate (the amorphous germanium oxide shell is indicated).<sup>146</sup> (g) SEM observations of the sample annealed at 700 °C. (h) HRTEM observations of a single Ge nanowire from a sample annealed at 700 °C. Nanowire elongated along the (110) plane, electron diffraction of Ge along [101] as an inset (1-core, 2-inner jacket, 3-outer jacket).<sup>147</sup>

CVD (as well as PVD) processes can accommodate thermal evaporation of solid Ge precursors for Ge nanowire growth; a simple and scalable process which does not require hazardous or toxic precursors but powder or solid pellets. Typically, the thermal evaporation technique requires the use of a very high temperature ( $> 938$  °C,



corresponding to Ge melting point), although the evaporation temperature can be lowered ( $\sim 700\text{ }^{\circ}\text{C}$ ) with the use of metal catalyst seeds.<sup>37,148–150</sup> Wu *et al.*<sup>151</sup> first attempt to grow self-seeded Ge nanowires by the thermal evaporation of Ge powder at a temperature of  $1050\text{ }^{\circ}\text{C}$ , under a flowing Ar/H<sub>2</sub> atmosphere for 2.5 hours. Very poor-quality Ge nanorods (see Figure 1.4a), with diameters ranging from between 20 to 200 nm and lengths up to 5  $\mu\text{m}$ , were obtained with a mixture of crystalline and amorphous structure (see Figure 1.4b). However, the nanorods produced showed a mixture of tetragonal, cubic and amorphous Ge structures, including a combination of these morphologies in single nanorods. GeO<sub>2</sub> has also been used as an alternative solid precursor, as it can be reduced *in situ* by H<sub>2</sub> at high reaction temperatures.<sup>152,153</sup> The crystallinity of the Ge nanowires produced can be tuned to be either amorphous, polycrystalline or single crystalline, by modifying the substrate temperature and/or evaporation rate. Wu *et al.*<sup>154</sup> used the GeO<sub>2</sub> precursor to synthesise self-seeded Ge nanostructures under H<sub>2</sub> flow at a temperature of  $1100\text{ }^{\circ}\text{C}$  ( $727 - 627\text{ }^{\circ}\text{C}$  in the deposition zone). Different 1D structure morphologies (such as straight nanowires, sphere-capped nanowires and tapered nanowires) were obtained along the substrate length, each corresponding to a different growth temperature (see Figure 1.4c). Uniform nanowire morphology was obtained at the coolest deposition area of the substrate ( $645\text{ }^{\circ}\text{C}$ ) where Ge nanowires with diameters ranging between 20 to 120 nm, lengths between 0.5-10  $\mu\text{m}$ , and smooth surfaces and very few structural defects were produced (see Figure 1.4d). An amorphous shell of between 1-7 nm in thickness was also observed on the surfaces of these nanowires. Other research groups also utilised GeO<sub>2</sub> as a precursor for growing Ge nanowires, combined with H<sub>2</sub> and various hydrocarbon molecules, *e.g.* methane, acetylene and ethanol, to achieve self-seeded core-shell 1D nanostructures (shells composed of carbon).<sup>152,153,155</sup> These carbon-

based self-seeded Ge nanowires were shown to be useful for energy storage applications such as anode materials for Li-ion batteries.<sup>152,153,155</sup>

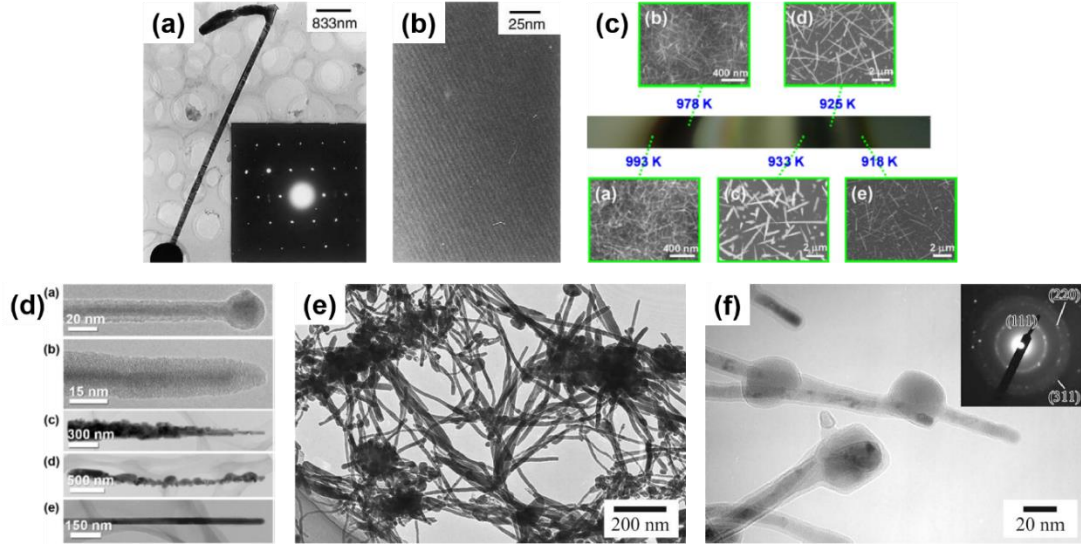


**Figure 1.4.** (a), (b) TEM image and a SAED pattern (inset) along the (101) direction and a lattice fringe image (HREM) of single-crystal Ge (high-pressure phase) nanorods.<sup>151</sup> (c) Optical micrographs of an as-synthesised nanowire specimen grown on a Si substrate; (a-e) the corresponding temperatures and SEM images of the as-synthesised nanostructures in different regions. (d) TEM images, corresponding to (c), of Ge nanostructures from (a-e), respectively.<sup>154</sup> (e) TEM image of deposits obtained at a Ge content of 40 at.% and an Ar pressure of 0.1 MPa and (f) TEM image of nanowires and their tip parts in deposits, and inset: corresponding SAED pattern.<sup>156</sup>

**Other vapour phase growth of self-seeded Ge nanowires.** The laser ablation technique was first used to synthesis semiconductor nanowires in 1998<sup>157</sup> and since then has been combined with both CVD and PVD approaches to grow nanowires.<sup>158-160</sup> Laser ablation involves irradiating the source material with a laser to generate a vapour flux, which is then carried by an inert gas to a heated substrate. The laser generates a local temperature of up to 5000 °C within few nanoseconds, allowing ablation of the source materials, regardless of their binding energies.<sup>161</sup> While the high temperatures required (> 800 °C) limit its scalability for industrial

production, this approach is suitable for the rapid growth of nanowires; growth rate in the range of  $\mu\text{m min}^{-1}$ . Nanowire composition also be easily tuned by varying the source target. Self-seeded crystalline Ge nanowires, coated with a carbon shell, have been obtained using a laser ablation CVD setup.<sup>156</sup> As-obtained Ge nanowires (see Figure 1.4e) exhibited diameters of between 8 - 35 nm with lengths up to  $\sim 1 \mu\text{m}$ . Covalent bonding between the Ge core and C shell was found to prevent oxidation of the nanowires (see Figure 1.4f).

Electric arc discharge evaporation techniques are considered very promising approaches for growing semiconductor nanowires. These techniques create concentrated atomic flows of the precursor, resulting in high yields of nanowires that can often be structural tuned. The approach is based on a two-electrode setup, usually a cathode of carbon or tungsten and an anode of the source material of interest. A mixture of gases is also required to enhance and quench the reaction, as well as a background gas (inert gas) which is ionised to generate a plasma (serving as the reactive point). Synthesising Ge nanostructures via arc discharge presents serious challenges due to Ge low melting and boiling points (938 and 2850 °C, respectively) and a fairly high electrical resistivity at room temperature (40  $\Omega \text{ cm}$  in bulk Ge with less than  $10^{13}$  impurity atoms per  $\text{cm}^3$ ).<sup>162</sup> High electrical resistivity creates problems when the electric arc ignition takes place, which is not suitable for the transmission of large currents.<sup>163,164</sup> However, promising results have recently been achieved for the growth of 1D Ge nanostructures (see Figure 1.5a) without the involvement of any foreign metal catalysts. Catalyst-free Ge structures with a mean diameter in the order of  $1 \mu\text{m}$  and lengths from  $100 \mu\text{m}$  to  $1 \text{ mm}$  was achieved via arc-discharge CVD.<sup>165</sup> Even though some tapering of the nanowires was detected, the nanowires presented a

smooth surface (see Figure 1.5b) with the presence of small Ge nanocrystal spheres at their ends. The crystallinity of these nanowires was not confirmed through structural characterisation.

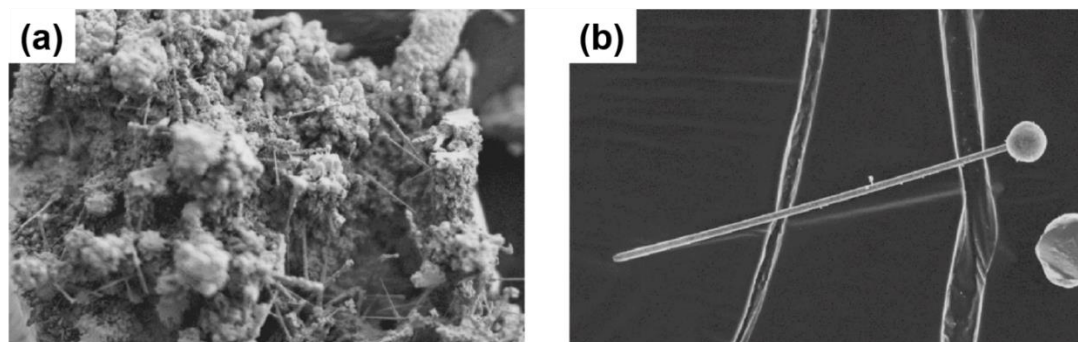


**Figure 1.5.** (a) SEM image of a sample at  $\times 700$  magnification and (b) the image of an individual Ge nanotube at  $\times 5000$  magnification.<sup>165</sup>

#### 1.3.1.2. Solution-Phase Growth of Self-Seeded Ge Nanowires

Nanowire growth can also take place in a liquid medium. Solution-phase growth methods usually guarantee a high production yield of nanowires, while exhibiting less control over the nanowire growth process compared to easily tuneable CVD methods.<sup>11,166</sup> In this section I have also included a discussion on the synthesis of Ge nanowires in supercritical fluid (SCF) solvents.

SCF synthesis of nanowires was first reported in 1993<sup>167</sup> and, even though this method requires a pressurised system and suitable reaction vessels, it can be considered a fast-growth technique.<sup>161</sup> In this approach, the generation of a liquid-vapour coexistence state depends on the pressure applied (or self-induced by the system), as well as the supercritical temperature of the organic solvent (usually solvents with  $< 300$  °C boiling points).<sup>168</sup> SCFs are interesting growth media as they offer a wider reaction temperature range than usual traditional solution-based techniques.<sup>169</sup> The ability to

tune both temperature and pressure parameters can be utilised to promote the solubility, mobility (high diffusivity) and reactivity of precursors; by governing solvent properties such as viscosity, polarity, dielectric constant and heat capacity.<sup>170</sup> The interactions of the solvent with the precursors, intermediates, and by-products can also profoundly modify the reaction equilibrium and kinetics.<sup>102</sup>

A great advantage of solution-based techniques is their continuous nature which allows them to be scale-up for industrial purposes. The first report of self-seeded growth of Ge nanowires by a solvent-mediated process was back in 1993, using an SCF setup.<sup>167</sup> Heath and LeGoues<sup>167</sup> reported the high-pressure reduction of  $\text{GeCl}_4$  and phenyl- $\text{GeCl}_3$  in hexane at 275 °C for a period of between 2-8 days, in a batch setup. The diamond cubic structure of the Ge nanowires was confirmed by XRD and FTIR (Fourier-Transform Infrared Spectroscopy) analysis showed the surface of the nanowires to be terminated with hydrocarbons, oxygen and chlorine. Although the yield of nanowires was low (between 5 - 10 %), TEM imaging (see Figure 1.6a) showed nanowires with diameters between 7 and 30 nm and lengths up to 10  $\mu\text{m}$ . The self-seeded Ge nanowires (see Figure 1.6b) exhibited a high density of stacking faults parallel to the crystal growth direction, (111) plane in this case, and the faults were present along the entire lengths of the nanowires. The same authors also used a self-tailored Ge precursor to hinder aggregation and coarsening of Ge nanoparticles during the self-seed growth of nanowires.<sup>171</sup> Hexakis(trimethylsilyl)digermane,  $\text{Ge}_2(\text{TMS})_6$ , was used (dissolved in toluene) with a continuous-flow setup at growth temperatures of between 300-500 °C and a pressure of 17 MPa. Seedless sub-10 nm Ge nanowires of excellent quality were obtained with a characteristic core-shell morphology (see Figure 1.6c). The crystalline cores of the nanowires consisted of pure dc-Ge with

diameters ranging from between 6.3 to 9.4 nm (depending on the growth temperature) and the shell was found to be mostly an amorphous matrix largely composed of Si and C with some polycrystalline Ge nanoparticles (see Figure 1.6d). While the amorphous shell has a non-uniform thickness, the core diameter remained uniform along the length of the nanowires. The relationship between reaction temperature and diameter distribution was also studied. In particular, a model was developed to describe the nanowire formation stages (nucleation, coalescence and Ostwald ripening) to explain the influence of growth temperature on the diameter of the seedless Ge nanowires produced.<sup>172</sup>

Hydrothermal synthesis is a specific variant of the SCF technique, where the solvent used is supercritical H<sub>2</sub>O. The technique is very flexible and offers a unique scenario to preparing high-quality Ge nanowires at relatively lower temperatures using a simple and cost-effective process.<sup>173</sup> Another advantage is the use of a non-toxic and eco-friendly solvent, H<sub>2</sub>O, in contrast with the other solution-based techniques.<sup>174,175</sup> Hydrothermal techniques have brought excellent results in the self-seeded growth of Ge nanowires. In a simple batch setup using Ge powder and distilled water in a reaction kettle, crystalline Ge nanowires were produced after 6 hours at temperatures between 450-470 °C under stirring.<sup>170</sup> The nanowires produced displayed smooth surfaces and straight morphologies, with no spherical seeds at the tips of the nanowires (see Figure 1.6e). TEM observations of the nanowires suggested a rectangular cross-section (see Figure 1.6f) with a mean diameter of 50 nm (ranging from 10 to 150 nm) and a single crystal structure of tetragonal ST12-Ge. Although, this particular crystallinity was only confirmed by TEM and no other characterisation techniques, *e.g.* Raman spectroscopy or XRD, were used to corroborate the result. Such an

interesting outcome in terms of achieving a novel metastable phase of Ge is of high interest and more detailed characterisation would have been required to verify the crystal structure and phase of these nanowires.

Another high-yield nanowire production method is ‘solution-phase synthesis’.<sup>11</sup> Here, the growth environment is not a supercritical fluid, rather an organic solvent at ambient pressure. This technique probably represents one of the most simple methods for growing nanowires, as nanostructures can be produced without the need for complex and high-cost equipment or high vacuum systems.<sup>80,176</sup> Growth of Ge nanowires in liquid-phase is usually conducted in high boiling point (HBP) solvents, with boiling points typically above 400 °C, *e.g.* squalane, and squalene.<sup>177</sup> This group of organic solvents permits Ge nucleation in a non-pressurised system, facilitating Ge precursor decomposition and nanowire growth.<sup>178,179</sup> A large number of studies on the solution-phase synthesis of Ge nanowire have focussed on self-seeded approaches for nanowire growth.<sup>171,180</sup> Colloidal synthetic approach has been used for the growth of nanocrystals and nanorods in HBP solvents. This approach has also profited from the use of surfactants to grow 1D nanostructures.<sup>181</sup> In this case, surfactants are used to selectively passivate certain facets of the evolving nanocrystal to allow growth along a certain direction, forming nanowires. The solution-phase growth of Ge generally requires reaction temperatures to be high enough to thermally decompose Ge organometallic precursors and to successfully nucleate Ge under these growth conditions.

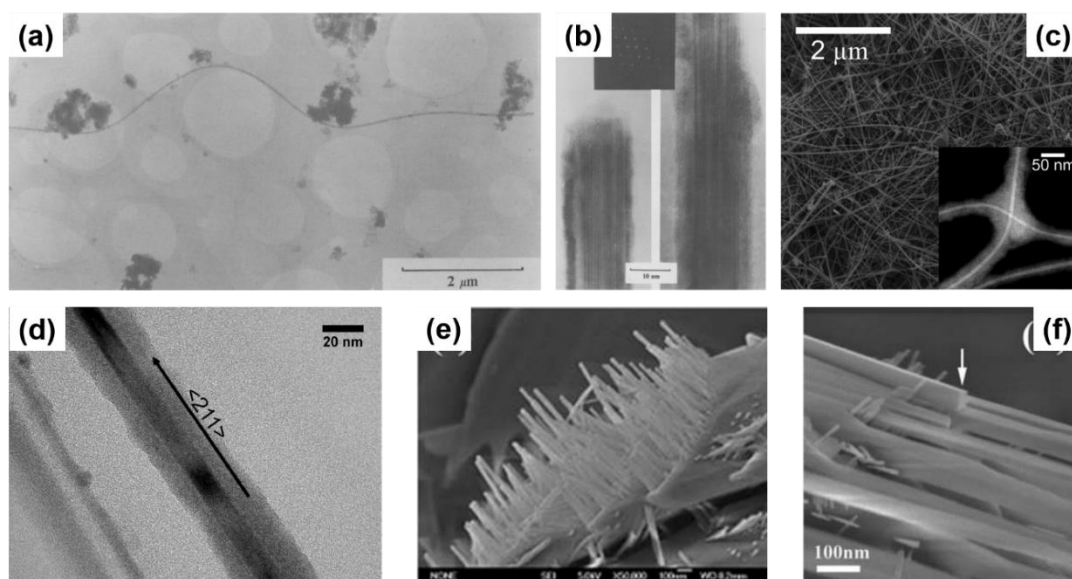


**Figure 1.6.** (a) TEM image of a 10  $\mu\text{m}$  long, 18 nm diameter, single-crystal Ge nanowire. The islands of material scattered throughout the micrograph consist primarily of bunches of Ge nanodots. (b) TEM image of the tip (left) and a central portion of an 18 nm diameter, 650 nm long Ge nanowire. At the top left is an ED pattern of the wire, indicating that the wire is a diamond lattice single crystal oriented along its  $[011]$  zone axis. Visible in the micrographs are a set of  $\{200\}$  and  $\{111\}$  lattice planes, running diagonally across the diameter, and a second set of  $\{111\}$  planes, running parallel to the wire axis. Note the faults which traverse the length of the wire.<sup>167</sup> (c) SEM images of the Ge nanowires. Inset is a High-angle annular-dark-field STEM (HAADF-STEM) micrograph of Ge nanowires synthesised at 400  $^{\circ}\text{C}$ , clearly displaying the core-shell morphology. Including shell, the nanowires shown are 20-50 nm in diameter, while the cores are 8-10 nm in diameter and show good uniformity along the wires. (d) TEM image of a nanowire synthesised at 500  $^{\circ}\text{C}$ , showing the distinct core-shell morphology. The image was obtained along the  $\langle 111 \rangle$  zone axis of the Ge nanowire.<sup>171</sup> (e) Field-emission SEM images of Ge nanowire arrays and (f) the SEM of a sectional view of Ge nanowires.<sup>170</sup>

Zaitseva *et al.*<sup>180</sup> presented a detailed study on the influence of reaction pressure and solvent type on the growth of self-seeded Ge nanowires. Ge nanowire formation from the Ge precursor tetraethylgermane (TEG) at a temperature of  $\sim 400$   $^{\circ}\text{C}$  and pressure  $\leq 5$  MPa was compared to reactions performed under vacuum and ambient pressure



conditions. In both scenarios, HBP solvents, *i.e.* trioctylamine and squalene and low boiling point (LBP) solvents, *i.e.* hexane and toluene were screened. The best yields of Ge nanowires, up to nearly 100 %, were obtained when reactions took place under pressure in HBP solvents. The use of LBP solvents led to substantially lower yields of Ge nanowires which were mixed with isometric amorphous particles. LBP solvents were not able to produce Ge nanowires in reasonable yields at ambient pressure, at least with the TEG precursor. The choice of self-tailoring a Ge precursor to achieve the desired reactivity under certain reaction conditions has also been explored using different nanowire synthesis techniques. Ge *et al.*<sup>80</sup> reported an effective Ge precursor for growing highly crystalline Ge nanowires known as TOG, with the molecular formula  $[(\text{CH}_3(\text{CH}_2)_7\text{CH}=\text{CH}(\text{CH}_2)_7\text{CH}_2\text{NH}_2)_4\text{Ge}]^{4+} \cdot (\text{Cl}^-)_4$ . These self-seeded nanowires were produced in a three-neck round-bottom flask at a reaction temperature of 360 °C for 4 hours using tri-*n*-octylamine as the solvent. Straight and slightly curved Ge nanowires with diameters between 50 - 70 nm and lengths between 10 and 20 µm were observed (see Figure 1.7a). A direct correlation between the amount of precursor used and the mean diameter of the nanowires obtained was determined. Amorphous-like Ge nanoparticles, with diameters < 7 nm, were observed in the amorphous-carbon coating surrounding the nanowires (C-Ge nanowires) (see Figure 1.7b). In another report, Gerung *et al.*, synthesising self-seeded Ge nanowires from new  $\text{Ge}^{2+}$  precursor, *i.e.*  $\text{Ge}(2,6\text{-OC}_6\text{H}_3(\text{C}(\text{CH}_3)_3)_2)$ .<sup>176</sup> Although crystalline, the nanowires formed displayed kinked and tapered structures with diameter distributions between 15 and 25 nm and lengths ranging from 100 nm to 10 µm could be found in the samples (see Figure 1.7c). The use of commercially available Ge precursors has been widely used by several research groups to grow self-seeded Ge nanowires. Barrett *et al.*<sup>177</sup> used the commercially available precursor diphenylgermane (DPG),

under reflux, to grow high-yields of long ( $> 10\ \mu\text{m}$ ), untapered Ge nanowires with diameters ranging between 7 and 15 nm (see Figure 1.7d). All of the nanowires synthesised had diamond-cubic crystal structures, with the majority of nanowires displaying a [111] crystal growth direction and about 20 % exhibiting a [112] growth orientation (see Figure 1.7e and 1.7f), consistent with previous reports.<sup>176</sup> A more detailed study on the growth of self-seeded Ge nanowires using the DPG precursor in HBP solvents at a temperature of 420 °C was reported by Geaney *et al.*<sup>182</sup>, with an in-depth analysis of the different morphologies obtained (see Figure 1.7g). Straight, defect-free and single crystal Ge nanowires, with diameters ranging between 7 and 20 nm, were found to constitute the majority of the samples. However, around 5 % of nanowires presented lateral and longitudinal stacking faults, which originated during the nucleation process. The lateral defects were found to run parallel to the growth direction for  $\langle 111 \rangle$  oriented nanowires, while the nanowires where the growth occurs in the  $\langle 112 \rangle$  direction, the defects keep appearing on the (111) type plane to alleviate the stress. Kinked and very abrupt angular kinked (“wormlike”) nanowires, with diameters between 15 - 40 nm, were found at a higher reaction temperature (450 °C).<sup>182</sup>

Electrochemical deposition of self-seeded nanowires can also be classified as a solvent (electrolyte) based growth method. Electrochemical deposition is a versatile and cost-effective technique for Ge nanowire production. This technique presents a unique combination of several advantages, such as low operation temperatures (mostly at room temperature), simple setup, ease of scalability (widely present in current large-scale production), tunability and environmental friendliness.<sup>183–185</sup> Even though this technique can eliminate the requirements of a catalyst seed, long, kink-free and single

crystal Ge nanowires with the potential to be used in different applications are still a challenge.<sup>186</sup>

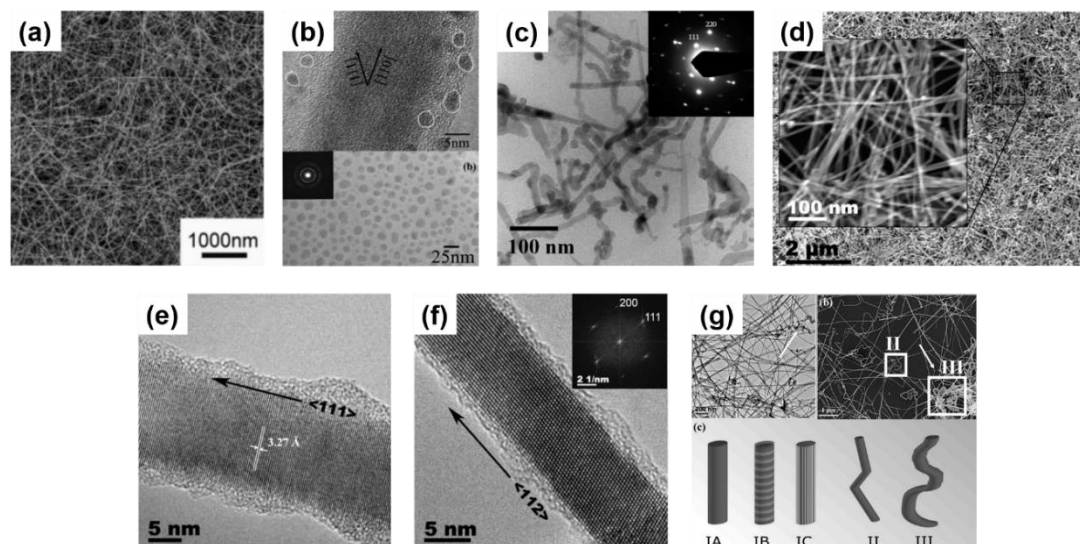


**Figure 1.7.** (a) SEM image of C-Ge nanowires produced by thermal decomposition of  $1.8 \times 10^{-4}$  mole of TOG at 360 °C for 4 h. (b) Upper image: HRTEM image showing amorphous-like Ge nanoparticles (marked by circles) with diameters below 7 nm on the surface of one C-Ge nanowire after refluxing for 4 h. Lower image: TEM image for C-Ge nanoparticles with sizes between 10-15 nm from the solidification of larger L-Ge droplets in the sample after 1 h reflux. The inset SAED shows the diamond-type (cubic-structured) Ge.<sup>80</sup> (c) Ge nanowires (inset, typical SAED pattern).<sup>176</sup> (d) SEM image of nanowires with magnified image inset. (e, f) HRTEM images of nanowires exhibiting (111) and (112) growth directions, respectively. The interplanar spacing of 3.27 angstroms for the (111) nanowire is shown in (e) while an indexed FFT is shown in (f).<sup>177</sup> (g) Top-left TEM image of straight Ge nanowires synthesised using squalene as the HBS. Most of the nanowires can be seen to be straight and untapered, while the arrow highlights a small area of kinked nanowires. Top-right SEM image of increasingly kinked nanowires synthesised in squalene with specific nanowire types highlighted. The schematic at the bottom depicts the five different types of nanowires discussed within the text; IA: straight, defect-free nanowires, IB: laterally faulted nanowires, IC: longitudinally faulted nanowires, II: angular nanowires and III: more complex, wormlike kinked nanowires.<sup>182</sup>

Chi *et al.*<sup>187</sup> proposed an electrochemical setup to deposit Ge nanowires onto indium tin oxide (ITO) glass substrates. The unusual morphology obtained (choral-like structures of Ge nanowires) (see Figure 1.8a and 1.8b) displayed an amorphous structure by TEM observation, although XRD and Raman suggested the formation of a crystalline Ge phase. Subsequently, Hao *et al.*<sup>52</sup> presented encouraging results with a simple two-step electrochemical method. After elementary Ge nanoparticle formation by ionic liquid electrodeposition, samples were annealed at 500 °C in an Ar atmosphere to generate Ge nanowires. The as-obtained nanowires (see Figure 1.8c and 1.8d) displayed diameters of between 100-200 nm and lengths of 2-3 µm, with no tapering or branching, but with a certain degree of kinking and surface roughness.

#### **1.3.1.3. Templated Growth of Unseeded Ge Nanowires**

Templated growth techniques are often used to define the position and growth direction of semiconductor nanowires, without the need for catalytic metal seeds. These techniques have been investigated to grow Ge nanowires in high densities with controlled placement and alignment.

Templated growth of semiconductor nanowires can be achieved by depositing material into nanochannels formed within a substrate or membrane. A commonly used nanoporous membrane for templating nanowires is anodised aluminium oxide (AAO).<sup>189,190</sup> AAO templates not only allow the formation of vertically aligned arrays of nanowires but also allow control over nanowire diameters. The best methods for depositing metals and semiconductors in the channels of AAO to form nanowires include electrodeposition,<sup>191</sup> CVD<sup>192</sup> and epitaxial growth<sup>192</sup>.

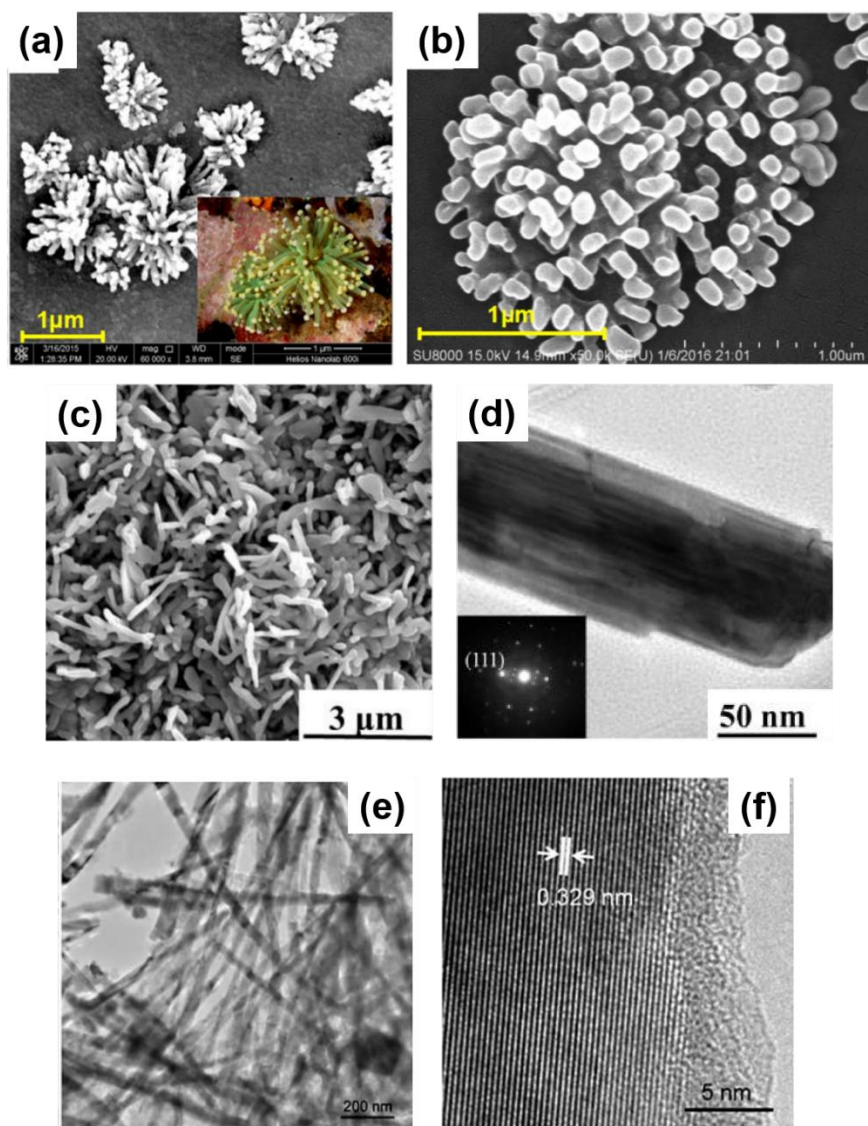


**Figure 1.8.** (a) and (b) SEM images of electrodeposited Ge with UV irradiation on ITO at different potentials: (a) at  $-1.300$  V, (b) at  $-1.325$  V.<sup>187</sup> (c) SEM images of Ge films obtained from  $1.5$  M  $\text{AlCl}_3$  +  $0.1$  M  $\text{GeCl}_4$ /[EMIm] $\text{Tf}_2\text{N}$  after annealing at  $500$  °C for  $2$  h in Ar. (d) TEM image and SAED pattern of Ge nanowires.<sup>52</sup> (e, f) Regions of darker contrast correspond to elemental Ge while outer walls with lighter contrast are oxide layers of  $4$  to  $8$  nm thickness. Surface roughness is observed on the Ge nanowires in high-resolution imaging (f).<sup>188</sup>

Yang and Veinot also successfully formed Ge nanowires by thermally reducing  $\text{GeO}_2$  sol-gels within the pores of AAO membranes.<sup>188</sup> The sol-gel was thermally reduced at  $600$  °C in an atmosphere of Ar/ $\text{H}_2$  for  $5$  hours to generate Ge nanowires to minimise

carbon contamination.<sup>193</sup> Temperature and time were the two main variables used to control nanowire growth which led to the formation of Ge nanowires with tailorable diameters and lengths, between 30 - 300 nm and 2 - 7  $\mu\text{m}$  respectively (see Figure 1.8e and 1.8f).<sup>194</sup> Sol-gels are formed by condensing a suspension of colloidal particles (the sol) to yield a gel and the technique has evolved into a general and powerful approach for producing a range of nanostructures.<sup>195</sup> Sol-gel synthesis has also been combined with other synthetic steps to produce nanowires. Template-aided synthesis combined with electrophoretic deposition, or reductive thermal processing, have also proved to be efficient for Ge nanowire growth. Key parameters for tuning the properties of sol-gel derived nanostructures are pH, oxidation state and temperature.<sup>196</sup>

## **1.4. Growth Mechanism for Self-Seeded Ge Nanowires**

### **1.4.1. Nanoparticle Seeds**

As self-seeded growth of Ge nanowires typically involves the formation of *in situ* Ge nanoparticle seeds. Similar to the VLS growth of nanowires, the self-seeded growth of semiconductor nanowires involves three components: (i) the precursor dispersed in a media (supply phase), (ii) the seed particle (collector phase) and (iii) the nanowire (crystalline solid phase).<sup>197</sup> The presence of the nanoparticles at the tips of nanowires is dependent on a balance between the vapour-nanoparticle, vapour-substrate/nanowire and nanoparticle-substrate/nanowire interfacial energies.<sup>198</sup> These three junctions combine in a singular area commonly known as a three-phase boundary (TPB), and this trijunction is where nanowire growth occurs (see Figure 1.9). For growth to take place, the first step prior to nucleation of the nanowire is the delivery of molecular or atomic precursors to the seed particle. This transport may happen through vapour, solution or a supercritical fluid phase. This process is known as

‘accommodation’ and can be split into two different steps: (i) adsorption of the precursor adatom onto the seed particle/media interface and (ii) incorporation of the precursor adatom into the new crystalline solid phase. The incorporation of atoms into a nanowire structure may also occur via diffusion of adatoms along its sidewalls, via a VS mechanism.<sup>199</sup> When the molecule decomposition process to liberate adatoms takes place, both in the nucleating seed or along a nanowire’s sidewall, the organic ligands in the precursors may form volatile by-products. These organic substituents, which might be as simple as a hydrogen atom, may interact with the seed or the nanowire surface promoting surface passivation which may reduce the energy and the reactivity of the surface<sup>200,201</sup>; surface passivation can significantly mitigate VS interfacial growth.<sup>202</sup> Surfactants can also be used in both solution- and vapour-mediated processes to promote the preferential growth of certain facets.<sup>203,204</sup> By utilising three-phase growth and surfactants, uncommon sidewall facet can become stable, allowing modification of the growth direction. Surface facet development during growth may dictate the axial crystallographic alignment of the wires.<sup>205,206</sup> This is due to the chemical potential reduction of the incorporated adatoms during growth is correlated with the sidewall facet planes and their surface energies.<sup>205,207</sup> This is especially valid for very small nanowires, where the surface energy of the exposed facets becomes much more relevant and may govern the wire into a particular orientation.<sup>205,208</sup>

Axial growth of semiconductor nanowires occurs when the concentration of the reactive species, *e.g.* Ge atoms, reaches supersaturation in the seed particles. The point of supersaturation largely depends on the thermodynamics of the system, however, kinetic factors such as precursor diffusion and incorporation frequency are also

relevant.<sup>209</sup> The generation of crystal building blocks followed by the aggregation of one another to form seed nuclei is generally known as the nucleation step.<sup>197</sup> Growth will then occur when accommodating more precursor in the drop is no longer thermodynamically favourable.<sup>197</sup>

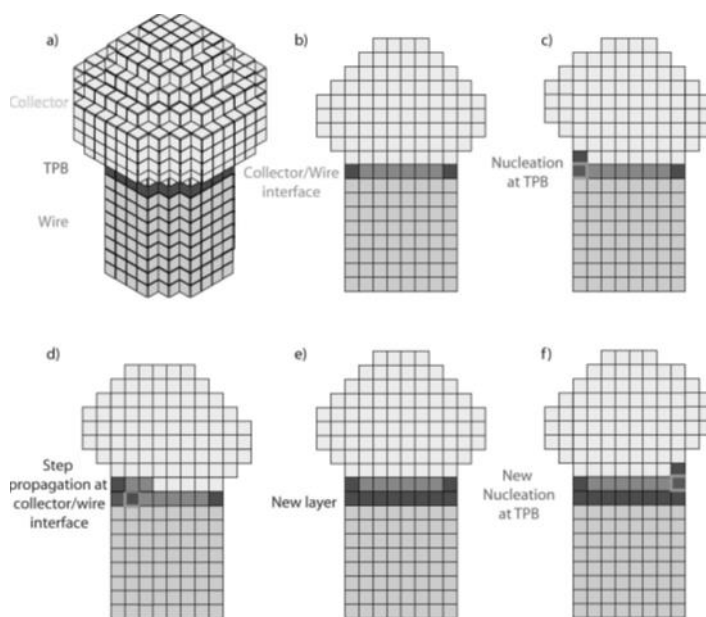


**Figure 1.9.** Illustration of preferential interface nucleation, birth and spread growth of a nanowire. (a) 3D depiction of a wire illustrating that the TPB as a dark line on the circumference of the collector/crystal interface. (b) 2D cross-section of the wire depicted in (a). (c) Nucleation at the TPB with the TPB being displaced in the growth direction. (d) Step propagation at the collector/crystal interface. (e) The new layer is completely formed. (f) Nucleation at a different site.<sup>197</sup>

A key parameter which significantly influences self-seeded nanowire growth is the diffusion of the seeds (Ge in this case) on the surface of a substrate before the nucleation of the nanowires. This diffusion may promote coarsening and Ostwald ripening effect<sup>210</sup>, leading to the formation of bigger nanoparticle seeds and broadening of nanowire diameter distributions.<sup>211</sup> Factors such as adatom diffusion along the sidewalls of nanowires<sup>212</sup> and diffusion and coarsening of the nucleation seed during self-seeded nanowire growth may also lead to tapered nanowires.<sup>212</sup> Other



critical factors which can influence crystal structure, the crystal growth direction and the tapering of the nanowires include the wettability and contact angle between the initial seed nanoparticles with the substrate, and later with the nanowire growth face.<sup>213–217</sup> The volume and phase of nanoparticle seeds should also remain unchanged during nanowire growth to minimise crystal defects such as kinking.<sup>218–222</sup> The growth temperature and precursor partial pressure (precursor concentration) are the main variables that can be used to modify parameters such as contact angle, seed volume *etc.*, in a fixed system.<sup>223</sup>

#### **1.4.2. Proposed Growth Mechanism for Self-Seeded Germanium Nanowires**

Generally accepted growth mechanisms for Ge nanowires, including self-seeded nanowire, have been described in Section 2.1. A vast consensus can be found on the growth pathway for metal/metalloid seeded Ge nanowires. Thus, when literature refers to any conventional three-phase bottom-up growth, *e.g.* VLS, VSS, SFLS *etc.*, no additional explanation is usually required to justify the growth of the Ge nanowires. However, no standardised mechanism has been found to justify the formation of Ge catalytic seeds and self-seeded Ge nanowire growth. Conventional growth paradigms, *e.g.* VLS, VSS, can participate to direct 1D growth with the self-formed seeds of a growth material (described in section 4.1). However, one of the important criteria is the initial creation of Ge in nanoparticles form which nanowires grow. The self-seeded growth of 1D nanostructures does not involve any foreign metals, metalloids and oxides. The only involvement of third-party material in any self-seeded and unseeded growth of Ge nanowires is for OAG, where oxides, *i.e.* GeO<sub>x</sub>, are believed to assist in 1D growth. The growth mechanism for OAG has been previously discussed in detail in Section 2.1.

However, in most of the self-seeded growth processes, no third party catalyst is intentionally added into the reaction. The VS growth mechanism can explain some aspects of self-seeded nanowire growth, but it is inadequate or incomplete for most cases. Generally, most of the self-seeded Ge nanowire literature extensively propose a growth mechanism to explain novel growth behaviour observed in experiments. Thus, it is not possible to represent the self-seeded growth of Ge nanowires by a single growth mechanism. In this section, I will summarise and group all of the suggested growth mechanisms for self-seeded Ge nanowire growth. I will also try to establish a common link between these growth mechanisms in an attempt to standardise self-seeded growth processes.

***Growth mechanisms of self-seeded growth by vapour phase methods.*** Within the group of vapour-phase grown self-seeded Ge nanowires, several mechanisms have been proposed. Among these, classical VS growth was proposed to be mainly responsible for self-seeded growth of Ge nanowires, as reported by Kim *et al.*<sup>143</sup> in 2009 and Wu *et al.*<sup>154</sup> in 2010. Kim *et al.* achieved nanowire growth via a CVD setup using GeH<sub>4</sub> as a precursor.<sup>143</sup> They did not attribute the self-catalysed nanowire growth to a VLS mechanism<sup>224</sup> but instead, proposed that the initial growth seeds that nucleated nanowires, in a thermodynamically preferred direction (see Figure 1.10a), were derived from the etching of the hydrogen-terminated silicon oxide wafer. Higher densities of nanowires were observed on activated regions of the substrate (see Figure 1.10b). In another report, Wu *et al.*<sup>154</sup> proposed a mixture of OAG and VS growth mechanisms using GeO<sub>2</sub> as a precursor for the self-seeded growth of Ge nanowires. In the coldest substrate reaction zone (645 °C), participation of both VS and OAG

growth produced Ge nanowires at high densities.<sup>98</sup> Whereas, in the hottest substrate zone (720 °C) nanowires were produced by OAG combined with self-catalytic VLS growth.<sup>225</sup> The nanowires present in the hottest area of the substrate showed a spherical shape on their tips due to the formation of a liquid droplet, which lead to nanowire growth via a self-catalytic VLS mechanism. A similar self-seeded VLS growth mechanism was also observed for the growth of tin oxide nanostructures.<sup>226,227</sup>

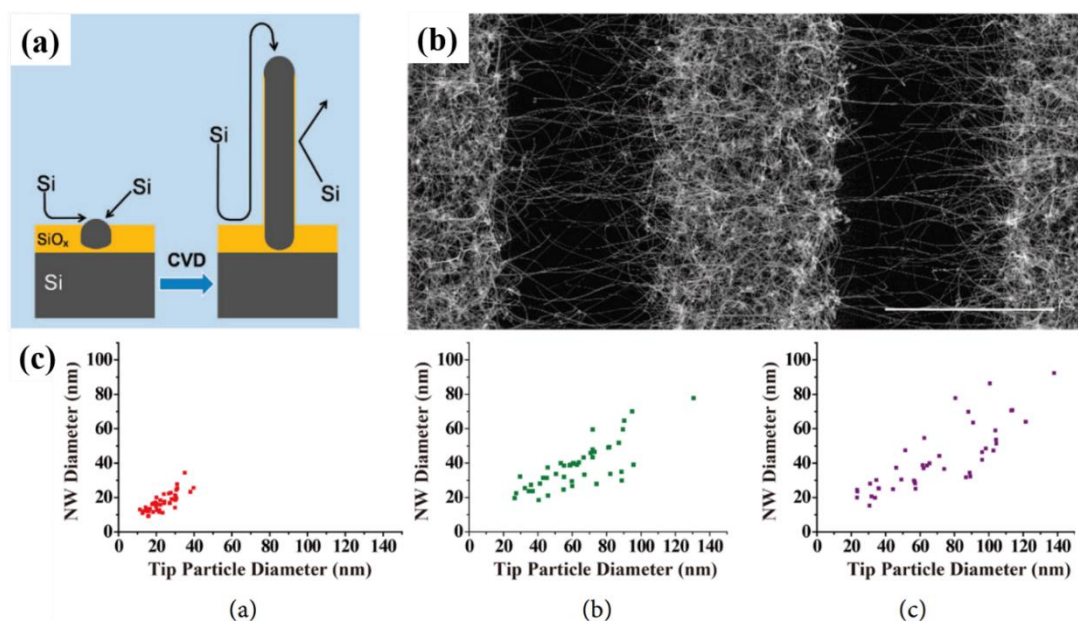


**Figure 1.10.** (a) A schematic for the proposed catalyst-free Si nanowire growth model. (b) SEM image of metal-free Si nanowires grown on a patterned substrate; scale bar 10 μm. The growth substrate was photolithographically patterned using a silicon (100) wafer with a 50 nm oxide layer. The selected area was chemically etched to remove oxide layers and treated with ultrapure water at 100 °C to generate the reactive SiO<sub>x</sub> surface.<sup>143</sup> (c) Plots of nanowire diameter versus tip nanoparticle diameter obtained at (c).a) 0.1; (c).b) 0.5; and (c).c) 0.9 MPa.<sup>156</sup>

Demaria *et al.*<sup>130</sup> used an X-ray-assisted CVD technique to grow self-seeded Ge nanowires. The influence of the X-rays (voltage of 250 kV and current of 10 mA which corresponds to an absorbed dose rate of  $5 \times 10^3 \text{ Gy h}^{-1}$ ) and reaction temperature

(300 °C) on nanowire growth were explored. While the temperature was essential for the growth of any nanostructure, X-rays were deemed to be a growth enhancer; due to a lower yield of nanowires in their absence. Radiolytic activation was believed to accelerate the dehydrogenation of the Ge precursor ( $\text{GeH}_4$  in this case). Although the energy of the X-rays was probably not high enough to target the bonds directly, it might have excited core electrons and reshuffled the electron distribution.<sup>228</sup> A thin amorphous layer of Ge was also observed on the substrates which was also assumed to participate in nanowire nucleation. An oversimplification might lead us to conclude that the nuclei formation was caused by naturally activated sites on the substrate (as previously reported by Kim *et al.*<sup>143</sup>) or oriented heteroepitaxy (as previously reported by Li *et al.*<sup>139</sup>). However, massive  $\text{H}_2$  formation due to X-ray dehydrogenation and the substantial presence of the  $\text{H}_2$  near the substrate is hypothesised as the reason for nanowires to nucleate.  $\text{H}_2$  interacts with the thin Ge amorphous layer, blocking the surface and leaving few dangling Ge atoms available to act as nuclei to promote the formation of Ge nanowires.

Laser ablation of Ge and C powder can also lead to the formation of Ge nanowires.<sup>156</sup> The presence of spherical shapes at the tips of nanowires and the strong correlations between nanoparticle diameters and nanowire diameters points towards the participation of *in situ* formed nanoparticles as catalytic seeds for the nanowire growth (see Figure 1.10c). The formation of Ge/C liquid droplets was proposed for nanowire growth, analogous to the  $\text{SiO}_x$  nanowire formation from  $\text{SiO}_x$  nanoparticles.<sup>229</sup> Ge and C precipitates from the liquid droplet and a phase separation between Ge and C generate the Ge-C core-shell nanowire structures. Similar growth mechanisms were suggested by several other groups for self-seeded Ge nanowire growth.<sup>152,153,155</sup> In

these methods the GeO<sub>2</sub> precursor was intentionally mixed with a hydrocarbon gas (methane, acetylene and ethanol respectively) to obtain Ge-C core-shell nanowires.

Most of the self-seeded nanowire growths via vapour phase approaches have been obtained on inert growth substrates, *i.e.* no chemical or reactive role was played by a substrate. Substrates only accommodate catalytic droplets (Ge nanoparticles in this case) for further nanowire growth. Dřínek *et al.*<sup>146</sup> screened a series of substrates such as stainless steel, Fe, Mo, Ta, W and SiO<sub>2</sub> at a reaction temperature of 490 °C, with (GeMe<sub>3</sub>)<sub>2</sub> as the Ge precursor, to evaluate the role of the substrates in self-seeded Ge nanowire growth. Even though Fe, Mo and Ta form intermetallic phases with Ge, only Fe does it at the reaction temperature of 490 °C, while the others form at temperatures of ~ 700 and 600 °C respectively.<sup>230</sup> W and SiO<sub>2</sub> do not present any intermetallic alloy with Ge.<sup>230</sup> Considering the required necessity of adhesion and limited mobility of the precursor atoms until they anchor at a specific surface site to form a nucleus nanocrystal, Dřínek *et al.*<sup>146</sup> proposed the physicochemical properties of the substrate surface (such as defects, imperfections and present impurities) as the decisive feature for nanowire formation. However, the presence of the methyl groups during precursor decomposition was not considered. Raman peaks corresponding to amorphous and graphite carbon were found, even though no strong Ge-C interaction was detected by FTIR. The presence of the organic ligands on the substrate may have helped nuclei formation for nanowire growth.<sup>156</sup> In this case, the carbonaceous material might have played a special role in assisting initial droplet stabilisation. The carbonaceous structures on the substrate seem crucial for self-seeded nanowire growth over inert substrates.<sup>151</sup> Wu and Tao proposed a VLS growth mechanism, without any in-depth analysis of the nanowire formation mechanism in the presence of

carbonaceous compounds.<sup>151</sup> The presence of spherical tips at the end of the nanorods, which appear to be eutectic droplets, was indicative of a self-seeded VLS process aided by the presence of carbonaceous compounds.

Mathur *et al.*<sup>231</sup> also explored the growth mechanism of Ge nanowires grown on Fe substrates. No evidence of spherical seeds was found at the tips of the nanowires, unlike those reported by Dřínek *et al.*<sup>146</sup> for Ge nanowire growth with the same Fe substrates. Recently, Dřínek *et al.*<sup>147</sup> have also reported the formation of core-shell Ge-Si/C nanowires in the absence of external catalytic seeds. Additionally, no spherically shaped nanoparticles were observed at the tip of the nanowires, thus a process similar to an OAG mechanism was proposed. Dřínek *et al.*<sup>147</sup> describe that while starting the reaction from tris(trimethylsilyl)germane,  $(\text{Si}(\text{CH}_3)_3)_3\text{GeH}$ , a series of reactions in the vicinity of the substrate surface led to the formation of germane-like structures, with the presence of Si and C. Similar nanostructures were previously formed with a very similar precursor in a supercritical setup.<sup>171</sup> The initiation of the growth was triggered by Ge-Si/C droplets formed on high energy defects, or imperfection sites, on the substrates, which participate to generate seed-free core-shell Ge-Si/C nanowires.

***Growth mechanisms of self-seeded growth by solution-phase methods.*** A more generalised nanowire growth mechanism has been proposed for self-seeded nanowire growth in solvents compared to vapour. Growth under supercritical conditions is included in this section to simplify the understanding of the rationale. The majority of self-seeded Ge nanowires grown in the solution phase have taken place in organic solvents using metalorganic precursors. Heath and LeGoues presented the first report

of self-seeded Ge nanowire growth in 1993.<sup>167</sup> Taking account of the limited characterisation techniques available at that time for an in-depth analysis of the growth mechanism, various possible explanations were considered by the authors. Essentially, the importance of the organic ligands of the precursors was elucidated. When using  $\text{GeCl}_4$  as a precursor Ge nanoparticles were obtained, while nanowires were only produced using phenyl- $\text{GeCl}_3$  as a precursor. The phenyl group shows a high tendency to polymerise and in combination with HBP solvents can form catalytic droplets, which act as sinks for Ge atoms, ideal for the self-seeded growth of Ge nanowires.

Zaitseva *et al.*<sup>180</sup> laid the groundwork by proposing a general growth mechanism for the self-seeded growth of Ge nanowires which was useful in explaining subsequent research on the self-seeded growth of Ge nanowires in the solvent phase. They proposed the formation of an organic droplet, analogous to the liquid catalyst seed used in VLS growth, which aids the growth of self-seeded nanowires. When working close to the boiling point of the solvent, small drops of condensed solvent act as a sink for precursor vapour molecules (TEG in this case), similar to the role Au plays in the conventional VLS growth of nanowires.<sup>232</sup> Ge incorporates into the organic droplet, and when saturated, crystallises over a substrate, to initiate nanowire growth. Organic radicals released during the precursor decomposition might also polymerise and catalyse further precursor decomposition.<sup>233</sup> Barrett *et al.*<sup>177</sup> presented their results with the commercially available Ge precursor DPG in HBP solvents. They proposed a similar mechanism of nanowire growth as described by Zaitseva *et al.*<sup>180</sup>, except they proposed the formation of germane gas due to the decomposition of DPG during the reaction. There is no in-depth study on how different Ge organo-metallic precursors

might affect the nanowire growth process, but similar outcomes seem to be obtained using commercially available precursors. The dependence of nanowire diameter on the size of the organic droplets was confirmed by substrate screening, *i.e.* Pyrex, quartz and ITO.<sup>177</sup>

Ge *et al.*<sup>80</sup> described a new synthetic pathway to explain the growth of Ge nanowires from the self-tailored precursor  $[(\text{CH}_3(\text{CH}_2)_7\text{CH}=\text{CH}(\text{CH}_2)_7\text{CH}_2\text{NH}_2)_4\text{Ge}]^{4+}(\text{Cl}^-)_4$  (TOG). Decomposition of the precursor (see Figure 1.11), initiated the formation of liquid Ge droplets on the surface of the substrates. At a critical size, the liquid droplets solidify and act as catalytic seeds for nanowire formation. The growth direction was likely controlled by preferable plane crystallisation, (110) in this case. Although not discussed by the authors, some role may be played by the organic solvent or organic ligands released during precursor decomposition step on nanowire growth. Gerung *et al.*<sup>176</sup> also described the formation of Ge nanowires from the precursor  $\text{Ge}(\text{2,6-OC}_6\text{H}_3(\text{C}(\text{CH}_3)_3)_2)_2$  (germanium 2,6-dibutylphenoxide,  $\text{Ge}(\text{DBP})_2$ ). They introduced two viable growth mechanisms: (i) a self-seeding VLS mechanism and (ii) a self-assembly mechanism. The first mechanism, agreeing with Zaitseva *et al.*<sup>180</sup> description, was supported by the presence of a spherical shaped seed at the end of the nanowires which shared a common crystallographic structure with the nanowire. However, the second mechanism was also put forward due to the observance of aggregates of smaller rods near the tip of the nanowires, which suggests a continued recrystallization process of these aggregates extending the length of the nanowires, as also described for Ag.<sup>234</sup>



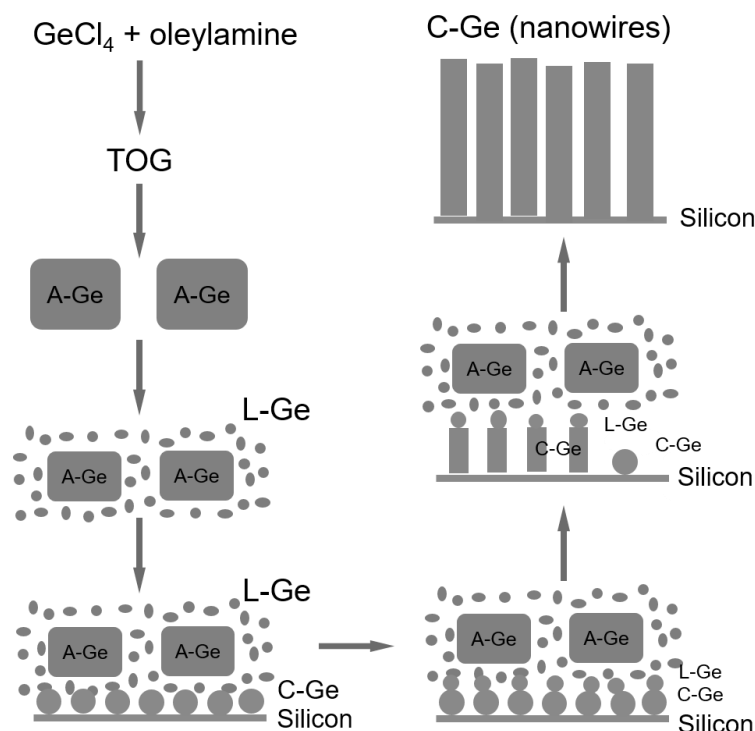


**Figure 1.11.** Schematic illustration for the formation of C-Ge nanowires during the decomposition of TOG in TOA solution at 360 °C.<sup>80</sup>

More complex self-seeded Ge nanowire formation mechanisms occur when precursors are used that include Si atoms within the structures. Hobbs *et al.*<sup>171</sup> obtained core-shell Ge-Si/C nanowires in a supercritical LBP solvent (toluene). The precursor used by Hobbs *et al.* liberated the Ge atoms prior to the Si species, which immediately formed the initial Ge nuclei.<sup>80,235</sup> The liberated trimethylsilyl groups from the precursor formed a matrix which accommodated molten Ge nanoparticles preventing them from aggregating. These droplets acted as nucleation seeds for Ge nanowire formation. The amorphous shell (composed of Si, Ge, C and O), which passivated the surfaces of the Ge nanowires formed, was not directly involved in the formation of the nanowires beyond nanoparticle stabilisation. This was elucidated by screening different reaction temperatures. Hobbs *et al.*<sup>171</sup> described in detail some in-between reaction mechanisms to predict the whole reaction pathway for self-seeded nanowire

growth. Another interesting growth mechanism for the self-seeded Ge nanowires was proposed with H<sub>2</sub>O as a solvent, under supercritical conditions.<sup>170</sup> Lin *et al.*<sup>170</sup> described in detail the reactions of Ge (Ge powder as a precursor) in combination with water ions, to nucleate self-seeded Ge nanowires. An analogous method to the OAG mechanism was described with subtle but crucial differences. Here, both H<sup>+</sup> and OH<sup>-</sup> ions played an important role, not only on the phase separation but also on the redox reaction in the initial droplet, while phase separation only occurs at the growth tip via the OAG mechanism.

### 1.5. Growth of Self-Seeded Ge Nanowire Alloys

Group IV alloy semiconductor nanowires are attractive due to the ability for bandgap manipulation in these materials, and application in photonics, optoelectronics and nanoelectronics devices. For example, with a Sn concentration of ~ 9 at.%, GeSn shows a transition to a direct bandgap material from an indirect bandgap Ge. Among the reported Ge alloys, such as GeSn,<sup>131</sup> SiGe,<sup>236</sup> SiGeSn,<sup>237,238</sup> *etc.*, only GeSn nanowires have been successfully grown to date through a self-seed growth mechanism.<sup>131</sup> Adding  $\alpha$ -Sn (grey tin, a Sn allotrope with diamond cubic structure) into the Ge lattice results in an energy difference between the  $\Gamma$ - and L-valleys ( $\Delta E_{\Gamma-L}$ ) decreases as the Sn content increases, leading to the formation of a direct bandgap material at between 6 - 10 at.% Sn content. A key challenge with synthesising GeSn is the low equilibrium solubility of Sn in Ge (< 1 at.%) and the tendency for Sn to segregate at high temperatures,<sup>239</sup> which can be controlled in nanowires by manipulating growth kinetics.

There are numerous recent reports<sup>240</sup> on synthesising GeSn nanomaterials due to their potential application in fields such as electronics,<sup>241</sup> optoelectronics<sup>242</sup> and energy

storage<sup>243</sup> (see Figure 1.12). GeSn nanowires have been principally grown to date using pre-synthesised metal catalytic seeds, such as Au,<sup>244</sup> AuAg,<sup>243</sup> AuSn<sup>245</sup> and Sn<sup>121</sup> nanoparticles. Barth *et al.*<sup>131</sup> were the first to report the formation of self-seeded GeSn nanowires; formed by heating bis[*N,N*-bis(trimethylsilyl)amido]tin(II) and bis[*N,N*-bis(trimethylsilyl)amido]Ge(II) precursors dispersed in dodecylamine in a microwave. One of the main advantages of microwave heating was that a uniform temperature distribution was achieved throughout the dodecylamine solvent.<sup>246,247</sup> Additionally, GeSn nanowires could be obtained at relatively low reaction temperatures, *e.g.* 230 °C, within minutes. The GeSn nanowires synthesised displayed a mean diameter of 190 ( $\pm$  30) nm with Sn incorporation of up to 12.4 ( $\pm$  0.7) at.% of Sn. Despite their high Sn content, the GeSn nanowires were crystalline, corresponding to a dc-Ge structure. All of the nanowires synthesised had a bent morphology, which was attributed to the growth kinetics and the solution stirring rate during the growth, which might have created disturbance on the triple-phase boundary at the nanowire growth front.<sup>248</sup>

Seifner *et al.*<sup>249</sup> reported an in-depth analysis of the growth pathway involved in the self-seeded growth of GeSn, as previously described by Barth *et al.*<sup>131</sup>. They described the *in situ* formation of different Ge-rich and Sn-rich heterocubanes as the first step in the formation of GeSn nanowires. Those heterocubanes behave as intermediate molecules which would facilitate the growth through a classical SLS mechanism, which is divided in 3 stages such as nucleation, elongation and termination (see Figure 1.13).

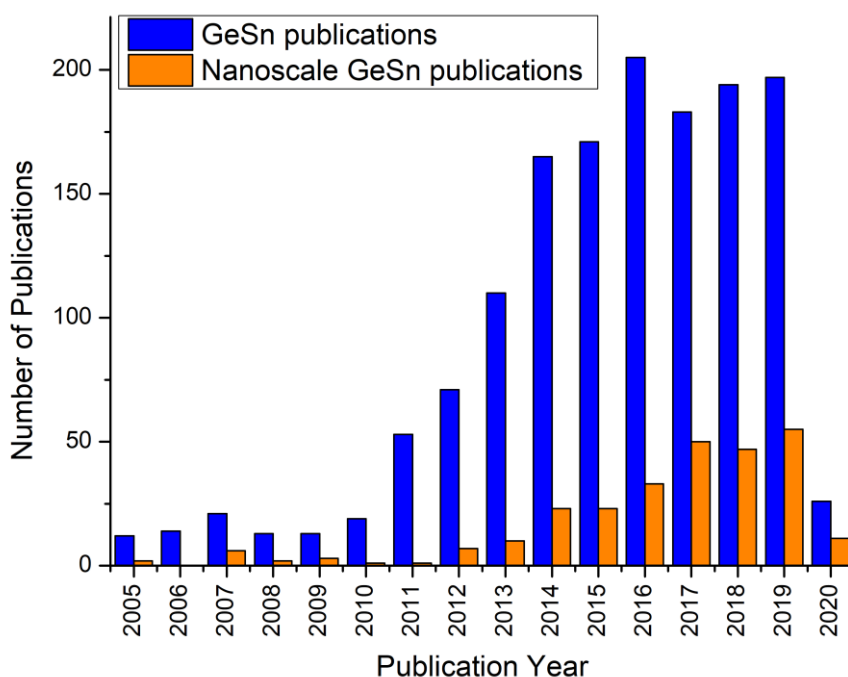


**Figure 1.12.** Google Scholar results for publications on GeSn per calendar year.<sup>240</sup>

SLS mechanism is usually described through two differentiated steps (nucleation and elongation), although the third extra step in this described growth mechanism was associated with long reaction periods where the Sn-rich seeds at the tips of the nanowires were finally consumed as long as not enough Sn and Ge containing precursor is available anymore. This third step leads to the formation of nanowires with coned-shaped tails, as observed with other growth methods.<sup>250</sup> More recent, Seifner *et al.*<sup>251</sup> also reported the formation of GeSn at lower temperature and higher Sn incorporation by using a very similar microwave-assisted growth method. A growth temperature as low as 140 °C was successfully used to obtain GeSn nanorods with a Sn content of up to 28 at.%. These globular-shaped GeSn nanorods displayed a diameter distribution ranging between 50 and 250 nm.

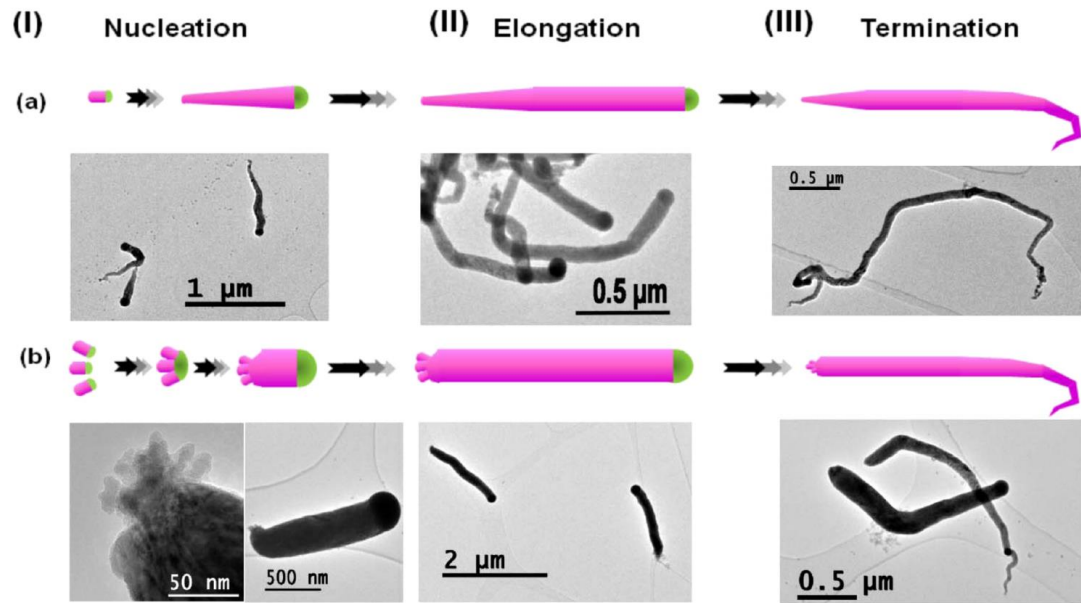


**Figure 1.13.** Schematic representation of the three growth stages for  $\text{Ge}_{1-x}\text{Sn}_x$  nanowire formation and TEM images to illustrate the structural features (Ge in purple; Sn in green). (a) Describes the growth via homogeneous nucleation with diameter expansion and accumulation of Sn at the growth front. (b) Represents the pre-nucleation of  $\text{Ge}_{1-x}\text{Sn}_x$  nanowires by an additional heat treatment and nucleus formation via oriented attachment leading to a quickly settling nanowire diameter at the nucleation (I) stage. The elongation (II) is a phase where the nanowire grows along its axis with a constant diameter due to constant Sn supply and consumption caused by incorporation in the Ge matrix. The termination (III) includes shrinkage in nanowire diameter and the consumption of the tin growth seed.

### 1.6. Potential Applications of Self-Seeded Germanium Nanowires

Many potential applications of self-seeded Ge nanowires are related to their semiconductor character, especially in energy storage devices such as Li-ion battery anodes. A sub-section dedicated to the potential application of self-seeded Ge nanowires in Li-ion batteries is given below.

### 1.6.1. Self-Seeded Ge Nanowires in Li-Ion Battery

LIBs, compared with metal hydride, lead-acid and alkaline batteries, represent a state-of-the-art energy storage technology.<sup>252,253</sup> However, advancements in commercial LIBs (generally based on  $\text{LiCoO}_2$  and graphite/carbonaceous electrodes) are still required to better their longevity and improve their environmental sustainability, as well as their safety in some applications.<sup>254</sup> Li-ion batteries are a type of rechargeable battery based on the movement of the lithium ions from the negative electrode to the positive electrode through an electrolyte during discharge, and the inverse process when charging. During the battery usage (discharge), an oxidation reaction at the cathode produces simultaneously lithium ions and electrons. Lithium ions move through the electrolyte while electrons move through the electric circuit. At the anode, the reduction occurs when electrons react with lithium ions to incorporate them into the solid structure.

Lithium cobalt oxide ( $\text{LiCoO}_2$ ), lithium iron phosphate ( $\text{LiFePO}_4$ ) and lithium manganese oxide ( $\text{LiMn}_2\text{O}_4$ ) are the most commonly used cathodes in commercially available LIBs.<sup>255</sup> The electrolyte is typically a mixture of organic compounds mixed with lithium salts. Pure lithium is highly reactive because it reacts vigorously with water. Thus, it is avoided for commercial use and, instead, non-aqueous gel polymer electrolytes are a much safer alternative.<sup>256</sup> Most commercial LIBs employ carbonaceous anodes, which provide low reversible capacities ( $372 \text{ mA h g}^{-1}$  for graphite) due to the formation of  $\text{LiC}_6$ , and thus there is a demand for an alternative anode material with a higher energy density and longer life cycles, such as Ge nanowires.<sup>257–259</sup> Albeit the high cost of Ge compared to the rest of the group IV elements, the exceptional diffusivity of Li ions in Ge ( $6.51 \times 10^{-12} \text{ cm}^2 \text{ s}^{-1}$  at room

temperature which is 400 times faster than Si,<sup>260</sup> a value estimated from the value obtained by Fuller and Severiens of germanium diffusivity at 360 °C of  $2.14 \times 10^{-7} \text{ cm}^2 \text{ s}^{-1}$  by using the empirical equation for the diffusion coefficient),<sup>261</sup> its high theoretical specific capacity ( $1624 \text{ mA h g}^{-1}$ ),<sup>262</sup> high volumetric capacity ( $7360 \text{ mA h cm}^{-3}$ )<sup>262</sup> and high electrical conductivity (100 times higher than Si)<sup>263</sup>, make it a potential material for replacing carbon as an anode material.

Nanowire structures grant efficient electron transport in the axial direction, high interfacial contact and short Li-ion diffusion distances, as well as accommodating electrode volume changes during repeated cycling.<sup>12</sup> Likewise, reducing the diameter of nanowires results in improving electrochemical performance as cracking and pulverisation is significantly reduced.<sup>264</sup> Bottom-up, self-seeded Ge nanowires (Section 1.3) grown directed onto conductive substrates as a 3D porous mesh of entangled nanowires can act as ideal anodes for LIBs. There is no requirement for binders and/or conductive materials, which add extra weight, inhibit ion transport and degrade the electrical conductivity, unlike with conventional electrodes. The addition of external carbonaceous layers or the incorporation of earth-abundant (cost-effective) metal into the germanium crystalline structure has the purpose to improve mechanical stability and electrochemical performance. However, the challenge remains to determine the critical dimensions and morphologies of nanowires to reduce pulverisation upon repeated cycling of the LIB.<sup>265</sup> The simple fabrication of nanowires is unable to guarantee the structural integrity of Ge anodes, due to the aggregation and large volume changes suffered by the nanowires upon cycling of a LIB. To relieve this volume change, while improving cyclability, several porous materials, such as carbonaceous (amorphous carbon,<sup>266</sup> carbon nanotubes<sup>267</sup> and

graphene<sup>268</sup>) or oxide coatings,<sup>269</sup> have been tested as ‘volume buffer’ materials with Ge based anodes.

***Carbon coated Ge nanowires as anode for LIBs.*** Amorphous carbon has been shown to form a coating on Ge nanowires grown via metal-organic precursor, self-seeded approaches. In LIBs this amorphous carbon coating can be beneficial due to the formation of a conductive, compact outer layer on the surface of Ge nanowires. This not only accommodates any volume expansion during cycling but also assists in the formation of a stable solid electrolyte interface (SEI) layer, which is a key factor for the long-time performance of lithium-ion batteries. Additionally, although the final state of Ge lithiation is usually considered to be  $\text{Li}_{15}\text{Ge}_4$ , some authors have pointed to the influence the carbon-coating in Ge electrodes has on the formation of  $\text{Li}_{22}\text{Ge}_5$ <sup>270</sup> or  $\text{Li}_{17}\text{Ge}_4$ <sup>271</sup> phases. The appearance of this range of alloys is caused by the state of cycling of the anode materials such as crystallinity, dimensions, and surface/interface conditions,<sup>272</sup> and rate and depth of lithiation,<sup>272</sup> which modify the kinetics of the different phase transformations into several stable and metastable Li-Ge structures (i.e.  $\text{Li}_7\text{Ge}_2$ ,  $\text{Li}_9\text{Ge}_4$ ,  $\text{Li}_{15}\text{Ge}_4$  or  $\text{Li}_{22}\text{Ge}_5$ ).<sup>273,274</sup>

The most significant data highlighting the positive benefits of using self-seeded Ge/C nanowires in LIBs were obtained by Liu *et al.*<sup>275</sup>, who synthesised  $\text{GeO}_x/\text{C}$  nanowires and reduced them to Ge/C nanowires under a  $\text{H}_2$  atmosphere at high temperatures to form highly efficient anodes; resulting in porous Ge nanowire structure anode which was ideal for accommodating Li-ion. The specific reversible capacity (calculated only by the mass of pure Ge) obtained at 5 C (Coulomb of electric charge) was  $877 \text{ mA h g}^{-1}$  (see Figure 1.14a). Although remarkable capacity retention was



observed after 50 cycles, longer testing times would be needed to demonstrate the stability of the electrodes. Hao *et al.*<sup>52</sup> have also tested catalyst-free Ge nanowires for the anode in LIBs with similar results. While using a loading density of their electrode of 0.3 mg per cm<sup>2</sup>, the samples showed a capacity of 620 mA h g<sup>-1</sup> at 5 C (see Figure 1.14b). An abrupt drop in the charge and discharge capacities identified in the first few cycles was due to SEI layer formation. After 20 cycles, Coulombic efficiency reached values over 98 % and good capacity retention was observed after 200 cycles (see Figure 1.14a and 1.14b). Other interesting results using C-Ge nanowires as anodes in LIBs were reported by Sun *et al.*<sup>155</sup> In their study Ge nanowires coated by multilayer-graphite tubes exhibited a reversible capacity of 515 mA h g<sup>-1</sup> at a current density of 5 C (see Figure 1.14c). Although stability tests were only undertaken for 100 cycles, great capacity retention was obtained for the nanowires. In another report, Choi *et al.*<sup>152</sup> presented very poor results for catalyst-free carbon-sheathed Ge nanowires with a specific capacity below 260 mA h g<sup>-1</sup> at a rate of 5 C (see Figure 1.14d).

### 1.6.2. Self-Seeded Ge Nanowires in Other Applications

***Self-seeded Ge nanowires in semiconducting devices.*** In order to see the effect of metal-free growth on the nanowire performance, Connaughton *et al.*<sup>276,277</sup> presented two reports analysing the conductivity displayed by core-shell Ge-Si/C nanowires. Two types of nanowire were produced by tuning the growth temperature and reaction time, with comparably contrasting electrical properties. The first type of nanowires was produced via a single-step synthetic process, where the nanowires had a greater presence of Ge nanocrystals in their amorphous shell. Another type of nanowires produced by annealing in a two-step synthetic process had a lower amount of Ge

nanocrystals presence in their amorphous shells. Both nanowires showed greater electrical conductivity, one order of magnitude higher than the conductivity of bulk Ge.<sup>278</sup> Ge nanowires grown via the single-step displayed a p-type behaviour with low conductance values when compared with nanowires grown via the two-step process. The conductance values presented non-linearity and hysteresis, varying around 25 nS, which is indicative of memristance.<sup>279,280</sup> Nanowires grown via the two-step process, with a lower amount of crystalline Ge present in the amorphous shell, displayed linear and higher conductance values, with no field effect present. These nanowires displayed quasi-metallic behaviour compared with degenerately doped Ge (doping density of from  $10^{19} \text{ cm}^{-3}$  onwards), due to the absence of field effect and the high conductivity displayed.<sup>281–283</sup> Nanowires grown via a two-step process displayed resistivity values that rapidly decreased with nanowire diameter, from 40 nm to 20 nm. This observation was explained by the quantum behaviour of the charge carriers at small diameters (below Bohr radius  $\approx 24 \text{ nm}$ ).<sup>37</sup> The versatile behaviour of the nanowires with slightly different structural features satisfies the requirement of both conduction-channel and source- and drain-components for nanoscale semiconductor devices.

***Self-seeded Ge nanowires for field emission.*** Ge nanowires could be used as potential field emitters, and some self-seeded Ge nanowires have been screened for this application. Comparison of the emission properties between different Ge nanowire samples is difficult due to their different morphologies, which affects the geometric enhancement factor  $\beta$ ; which describes how electric fields are affected by geometry and surface.

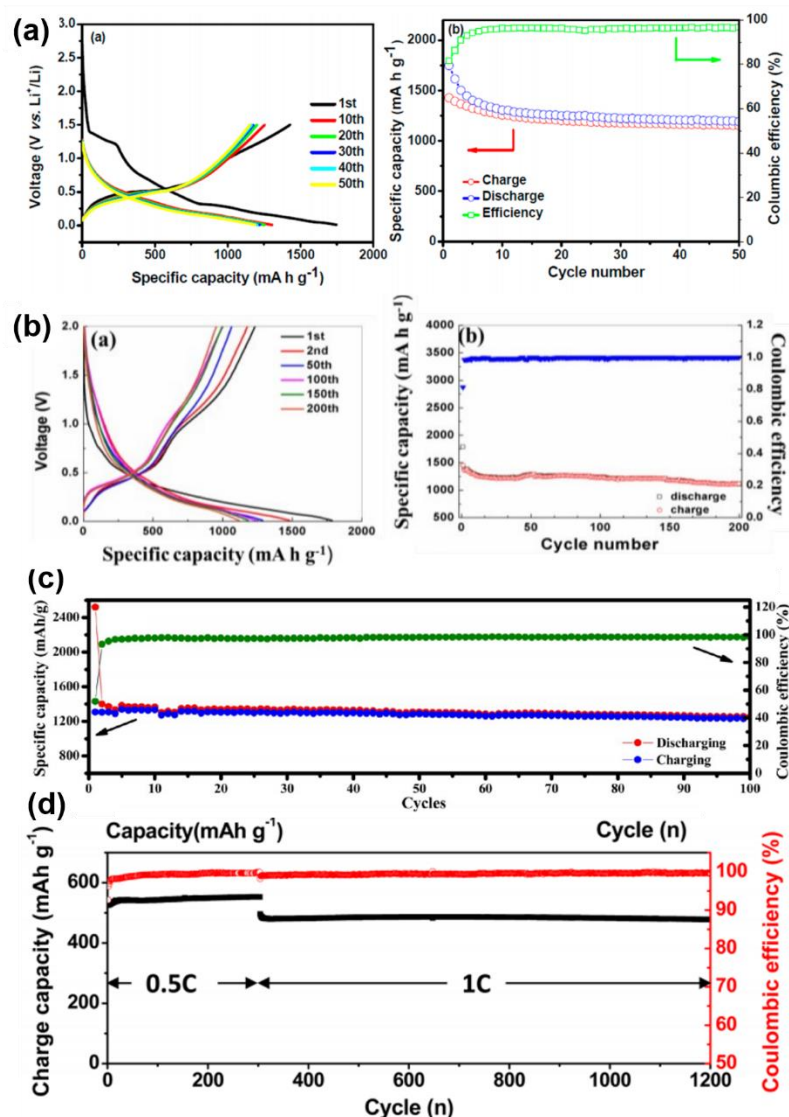


**Figure 1.14.** (a) Electrochemical performances of Ge/C composite nanowires with fully and homogeneously carbon encapsulation: (a) a) voltage profiles of Ge/C composite nanowires after 1, 10, 20, 30, 40, and 50 cycles between 0.01 and 1.5 V at a charge/discharge rate of 0.2 C. (a),b) The plot of specific capacity and Coulombic efficiency of (a),a) as a function of cycle number.<sup>275</sup> (b) a) Galvanostatic charge-discharge profiles for different cycles of Ge nanowires at 0.1 C. (b) b) Cycling performance and Coulombic efficiency of Ge nanowires at 0.1 C.<sup>52</sup> (c) LIB cyclic stability test and rate performance of the composite, 100 cycles capacity measurement.<sup>155</sup> (d) Cyclic stability test of the C-Ge nanowire electrodes obtained at the 0.5 and 1 C rate.<sup>152</sup>

Wu *et al.*<sup>154</sup> reported VS-grown Ge nanowires (diameter around 60 nm) with a turn-on field (applied field to draw an emission current density of 100 nA cm<sup>-2</sup>) of 4.6 V μm<sup>-1</sup>. Li *et al.*<sup>139</sup>, instead, obtained a turn-on voltage of 8.5 V μm<sup>-1</sup> for the Ge nanowires grown by OAG. The turn-on field improved to 7.6 V μm<sup>-1</sup> at 1 μA cm<sup>-2</sup> when the nanowire sample was annealed at a temperature of 550 °C.

There are also a few other innovative applications of self-seeded Ge nanowires. For example, they are used as bio-regenerative and cell proliferation materials, particularly in mammalian cells.<sup>284</sup>

## **1.7. Conclusions and Outlook**

The aim of this chapter is to outline and benchmark synthesis methods and described growth mechanisms for self-seeded Ge nanowires. Advances reported in the last two decades has drastically enhanced the possibility of application of self-seeded Ge nanowires in a wide variety of fields. While Si has been, almost from the very beginning, the material of choice for the microelectronics industry, graphite (carbon) has played the same role in the LIB industry. Predictions indicate that the dependence on microelectronics and LIBs will continue to expand and new materials will be required to fulfil the performance demanded by consumers. Ge nanowires, in general, present numerous advantages which place them as a genuine alternative in many application fields. Self-seeded Ge nanowires represent a novel material which can overcome impurity issues associated with metal-catalysed Ge nanowires, while displaying competitive nanowire growth rates, narrow-diameter distributions and comparable morphologies.

This chapter summarises progress in the bottom-up growth and mechanisms of self-seeded Ge nanowires, also examining the applications fields of greater interest. A considerable number of growth methods were detailed. The various growth methods discussed are quite distinct, and the question of which method suits best mainly depends on the application. Most of the approaches described generate meshes of entangled nanowires, which may require a subsequent positioning and assembly step for some applications. A lack of in-place fabrication methods, that is, the synthesis of nanowires at specific positions on a substrate is still a challenge which needs to be overcome. Success would allow bottom-up growth approaches to directly compete with the top-down fabrication methods, in terms of controllability, reliability and size variability. Understanding the growth mechanisms behind the self-seeded growth of Ge nanowires still needs to be understood in more detail. Nevertheless, connections have been found between the different approaches reported in the literature. Solution-phase methods share many commonalities and the presence of organic ligands (carbonaceous structures) and their decomposition pathways seem to play a vital role in the growth of self-seeded Ge nanowires. Vapour-phase methods, however, still show a lack of connection and deeper exploration and more detailed studies are required. Among all the described applications, energy storage, and LIBs in particular is seen as promising application area for self-seeded Ge nanowires.

### **1.8. Thesis Summary**

This thesis focuses on my contribution to the growth of Ge and GeSn nanowires via a self-seeded approach. Chapter 2 describes a simple one-pot solvothermal (supercritical) growth of carbonaceous Ge (C-Ge) nanowires that were subsequently tested as an anode material in Li-ion batteries. These nanowires were grown in

supercritical toluene without any metal catalysts at reaction temperatures between 380-490 °C, using a commercially sourced Ge precursor (diphenylgermane). The nanowires displayed high specific charge values ( $> 1200 \text{ mA h g}^{-1}$  after 500 cycles) and remarkable stable capacity retention when used as an anode material. Chapter 3 details the fabrication of tetragonal ST12-Ge nanowires via a one-step, bottom-up synthetic process in supercritical toluene. The growth of the ST12 phase of Ge nanowires was studied and the crystalline phase was characterised in-depth. The ST12-Ge nanowire allotrope was studied for the first time by photoluminescence, where the nanowires displayed intense light emission and evidence of a direct bandgap. Finally, Chapter 4 describes the fabrication of high aspect ratio ( $> 440$ ) GeSn nanowires using a simple, catalyst-free, solvothermal-like (supercritical) growth method. GeSn nanowires were grown with mean Sn concentrations between 3.1 to 10.2 at.%. The nanowires with the lowest Sn content (3.1. at.%) were evaluated as a potential anode material for Li-ion batteries; demonstrating high capacity retention of  $\sim 90 \%$  from the 10<sup>th</sup> to the 100<sup>th</sup> cycles while maintaining a specific capacity value of  $1127 \text{ mA h g}^{-1}$  after 150 cycles.

## 1.9. References

- (1) Busch, G. Early History of the Physics and Chemistry of Semiconductors-from Doubts to Fact in a Hundred Years. *Eur. J. Phys.* **1989**, *10* (4), 254–264.
- (2) Wagner, R. S.; Ellis, W. C. Vapor-Liquid-Solid Mechanism of Single Crystal Growth. *Appl. Phys. Lett.* **1964**, *4* (5), 89–90.
- (3) Givargizov, E. I. Fundamental Aspects of VLS Growth. *Vap. Growth Ep.* **1975**, 20–30.
- (4) Bootsma, G. A.; Gassen, H. J. A Quantitative Study on the Growth of Silicon Whiskers from Silane and Germanium Whiskers from Germane. *J. Cryst. Growth* **1971**, *10* (3), 223–234.
- (5) Moore, G. E. Cramming More Components onto Integrated Circuits. *IEEE Solid-State Circuits Soc. Newsl.* **2009**, *11* (3), 33–35.
- (6) Alivisatos, A. P. Semiconductor Clusters, Nanocrystals, and Quantum Dots. *Science* **1996**, *271* (5251), 933–937.
- (7) Kalyuzhny, G.; Murray, R. W. Ligand Effects on Optical Properties of CdSe Nanocrystals. *J. Phys. Chem. B* **2005**, *109* (15), 7012–7021.
- (8) Sutter, E. A.; Sutter, P. W. Size-Dependent Phase Diagram of Nanoscale Alloy Drops Used in Vapor - Liquid - Solid Growth of Semiconductor Nanowires. *ACS Nano* **2010**, *4* (8), 4943–4947.
- (9) Li, L. S.; Hu, J.; Yang, W.; Alivisatos, A. P. Band Gap Variation of Size- and Shape-Controlled Colloidal CdSe Quantum Rods. *Nano Lett.* **2001**, *1* (7), 349–351.
- (10) Hendrickx, N. W.; Franke, D. P.; Sammak, A.; Kouwenhoven, M.; Sabbagh, D.; Yeoh, L.; Li, R.; Tagliaferri, M. L. V.; Virgilio, M.; Capellini, G.; Scappucci, G.; Veldhorst, M. Gate-Controlled Quantum Dots and Superconductivity in Planar Germanium. *Nat. Commun.* **2018**, *9* (1), 2835.
- (11) Chockla, A. M.; Harris, J. T.; Korgel, B. A. Colloidal Synthesis of Germanium Nanorods. *Chem. Mater* **2011**, 23.
- (12) Park, M. H.; Cho, Y.; Kim, K.; Kim, J.; Liu, M.; Cho, J. Germanium Nanotubes Prepared by Using the Kirkendall Effect as Anodes for High-Rate Lithium Batteries. *Angew. Chemie - Int. Ed.* **2011**, *50* (41), 9647–9650.
- (13) Vaughn, D.; Sun, D.; Levin, S. M.; Biacchi, A. J.; Mayer, T. S.; Schaak, R. E. Colloidal Synthesis and Electrical Properties of GeSe Nanobelts. *Chem. Mater.*

- 2012**, 24 (18), 3643–3649.
- (14) Seifner, M. S.; Sistani, M.; Porrati, F.; Di Prima, G.; Pertl, P.; Huth, M.; Lugstein, A.; Barth, S. Direct Synthesis of Hyperdoped Germanium Nanowires. *ACS Nano* **2018**, 12 (2), 1236–1241.
  - (15) Liang, X.; Zhang, Q.; Lay, M. D.; Stickney, J. L. Growth of Ge Nanofilms Using Electrochemical Atomic Layer Deposition, with a Bait and Switch Surface-Limited Reaction. *J. Am. Chem. Soc.* **2011**, 133 (21), 8199–8204.
  - (16) Aslan, E. Germanium Hollow Nanodisk Resonator for Magnetic Dipole Decay Rate Enhancement in Near-Infrared. *Microw. Opt. Technol. Lett.* **2021**, 63 (1), 279–285.
  - (17) Wang, Q.; Kang, S. Z.; Li, X.; Yang, Y. W.; Qin, L.; Mu, J. A Facile Preparation of Crystalline GeS<sub>2</sub> Nanoplates and Their Photocatalytic Activity. *J. Alloys Compd.* **2015**, 631, 21–25.
  - (18) Yu, H.; Helbich, T.; Scherf, L. M.; Chen, J.; Cui, K.; Fässler, T. F.; Rieger, B.; Veinot, J. G. C. Radical-Initiated and Thermally Induced Hydrogermylation of Alkenes on the Surfaces of Germanium Nanosheets. *Chem. Mater.* **2018**, 30 (7), 2274–2280.
  - (19) Zhong, C.; Wang, J. Z.; Gao, X. W.; Wexler, D.; Liu, H. K. In Situ One-Step Synthesis of a 3D Nanostructured Germanium-Graphene Composite and Its Application in Lithium-Ion Batteries. *J. Mater. Chem. A* **2013**, 1 (36), 10798–10804.
  - (20) Cui, G.; Gu, L.; Zhi, L.; Kaskhedikar, N.; Van Aken, P. A.; Müllen, K.; Maier, J. A Germanium-Carbon Nanocomposite Material for Lithium Batteries. *Adv. Mater.* **2008**, 20 (16), 3079–3083.
  - (21) Haraguchi, K.; Katsuyama, T.; Hiruma, K.; Ogawa, K. GaAs P-n Junction Formed in Quantum Wire Crystals. *Appl. Phys. Lett.* **1992**, 60 (6), 745–747.
  - (22) Weng, B.; Liu, S.; Tang, Z. R.; Xu, Y. J. One-Dimensional Nanostructure Based Materials for Versatile Photocatalytic Applications. *RSC Adv.* **2014**, 4 (25), 12685–12700.
  - (23) Whitney, T. M.; Jiang, J. S.; Searson, P. C.; Chien, C. L. Fabrication and Magnetic Properties of Arrays of Metallic Nanowires. *Science* **1993**, 261 (5126), 1316–1319.
  - (24) Favier, F.; Walter, E. C.; Zach, M. P.; Benter, T.; Penner, R. M. Hydrogen Sensors and Switches from Electrodeposited Palladium Mesowire Arrays.



- Science* **2001**, 293 (5538), 2227–2231.
- (25) Arpin, K. A.; Mihi, A.; Johnson, H. T.; Baca, A. J.; Rogers, J. A.; Lewis, J. A.; Braun, P. V. Multidimensional Architectures for Functional Optical Devices. *Adv. Mater.* **2010**, 22 (10), 1084–1101.
  - (26) Li, L.; Zhai, T.; Bando, Y.; Golberg, D. Recent Progress of One-Dimensional ZnO Nanostructured Solar Cells. *Nano Energy* **2012**, 1 (1), 91–106.
  - (27) Mohamed, M. S.; Hameed, M. F. O.; El-Okr, M. M.; Obayya, S. S. A. Characterization of One Dimensional Liquid Crystal Photonic Crystal Structure. *Optik (Stuttg.)* **2016**, 127 (20), 8774–8781.
  - (28) Yang, P.; Yan, R.; Fardy, M. Semiconductor Nanowire: Whats Next? *Nano Lett.* **2010**, 10 (5), 1529–1536.
  - (29) Saga, T. Advances in Crystalline Silicon Solar Cell Technology for Industrial Mass Production. *NPG Asia Mater.* **2010**, 2 (3), 96–102.
  - (30) Shockley, W.; Pearson, G. L.; Haynes, J. R. Hole Injection in Germanium-Quantitative Studies and Filamentary Transistors. *Bell Syst. Tech. J.* **1949**, 28 (3), 344–366.
  - (31) Bardeen, J.; Pfann, W. G. Effects of Electrical Forming on the Rectifying Barriers of N- and p-Germanium Transistors. *Phys. Rev.* **1950**, 77 (3), 401–402.
  - (32) Huang, J.; Chim, W. K.; Wang, S.; Chiam, S. Y.; Wong, L. M. From Germanium Nanowires to Germanium–Silicon Oxide Nanotubes: Influence of Germanium Tetraiodide Precursor. *Nano Lett.* **2009**, 9 (2), 583–589.
  - (33) Xiang, J.; Lu, W.; Hu, Y.; Wu, Y.; Yan, H.; Lieber, C. M. Ge/Si Nanowire Heterostructures as High-Performance Field-Effect Transistors. *Nature* **2006**, 441 (7092), 489–493.
  - (34) Maity, N. P.; Maity, R.; Thapa, R. K.; Baishya, S. Image Force Effect on Tunneling Current for Ultra Thin High-K Dielectric Material Al<sub>2</sub>O<sub>3</sub> Based Metal Oxide Semiconductor Devices. *J. Nanoelectron. Optoelectron.* **2015**, 10 (5), 645–648.
  - (35) Nguyen, P.; Ng, H. T.; Meyyappan, M. Growth of Individual Vertical Germanium Nanowires. *Adv. Mater.* **2005**, 17 (5), 549–553.
  - (36) Maeda, Y.; Tsukamoto, N.; Yazawa, Y.; Kanemitsu, Y.; Masumoto, Y. Visible Photoluminescence of Ge Microcrystals Embedded in SiO<sub>2</sub> Glassy Matrices. *Appl. Phys. Lett.* **1991**, 59 (24), 3168–3170.
  - (37) Gu, G.; Burghard, M.; Kim, G. T.; Düsberg, G. S.; Chiu, P. W.; Krstic, V.;

- Roth, S.; Han, W. Q. Growth and Electrical Transport of Germanium Nanowires. *J. Appl. Phys.* **2001**, *90* (11), 5747–5751.
- (38) Greytak, A. B.; Lauhon, L. J.; Gudixsen, M. S.; Lieber, C. M. Growth and Transport Properties of Complementary Germanium Nanowire Field-Effect Transistors. *Appl. Phys. Lett.* **2004**, *84* (21), 4176–4178.
- (39) Bruno, M.; Palummo, M.; Marini, A.; Del Sole, R.; Olevano, V.; Kholod, A. N.; Ossicini, S. Excitons in Germanium Nanowires: Quantum Confinement, Orientation, and Anisotropy Effects within a First-Principles Approach. *Phys. Rev. B - Condens. Matter Mater. Phys.* **2005**, *72* (15), 153310.
- (40) Sun, X.; Calebotta, G.; Yu, B.; Selvaduray, G.; Meyyappan, M. Synthesis of Germanium Nanowires on Insulator Catalyzed by Indium or Antimony. *J. Vac. Sci. Technol. B Microelectron. Nanom. Struct.* **2007**, *25* (2), 415–420.
- (41) Lu, W.; Lieber, C. M. Semiconductor Nanowires. *J. Phys. D. Appl. Phys.* **2006**, *39* (21).
- (42) Jia, C.; Lin, Z.; Huang, Y.; Duan, X. Nanowire Electronics: From Nanoscale to Macroscale. *Chem. Rev.* **2019**, *119* (15), 9074–9135.
- (43) Bayani, A. H.; Dideban, D.; Voves, J.; Moezi, N. Investigation of Sub-10nm Cylindrical Surrounding Gate Germanium Nanowire Field Effect Transistor with Different Cross-Section Areas. *Superlattices Microstruct.* **2017**, *105*, 110–116.
- (44) Tian, B.; Kempa, T. J.; Lieber, C. M. Single Nanowire Photovoltaics. *Chem. Soc. Rev.* **2009**, *38* (1), 16–24.
- (45) Yu, Z.; Zhang, X.; Zhang, H.; Huang, Y.; Li, Y.; Zhang, X.; Gan, Z. Improved Power Conversion Efficiency in Radial Junction Thin Film Solar Cells Based on Amorphous Silicon Germanium Alloys. *J. Alloys Compd.* **2019**, *803*, 260–264.
- (46) Jung, Y.; Nam, S. W.; Agarwal, R. High-Resolution Transmission Electron Microscopy Study of Electrically-Driven Reversible Phase Change in Ge<sub>2</sub>Sb<sub>2</sub>Te<sub>5</sub> Nanowires. *Nano Lett.* **2011**, *11* (3), 1364–1368.
- (47) Cui, Y.; Wei, Q.; Park, H.; Lieber, C. M. Nanowire Nanosensors for Highly Sensitive and Selective Detection of Biological and Chemical Species. *Science* **2001**, *293* (5533), 1289–1292.
- (48) Blond, P.; Bevernaegie, R.; Troian-Gautier, L.; Lagrost, C.; Hubert, J.; Reniers, F.; Raussens, V.; Jabin, I. Ready-to-Use Germanium Surfaces for the

- Development of FTIR-Based Biosensors for Proteins. *Langmuir* **2020**, *36* (40), 12068–12076.
- (49) Wei, T.; Pei, L. Z.; Lin, N. Ce Doped Germanium Dioxide Nanowires and Solar Light Photocatalytic Performance. *e-Journal Surf. Sci. Nanotechnol.* **2016**, *14* (0), 4–8.
  - (50) Ziegler, K. J.; Lyons, D. M.; Holmes, J. D.; Ertz, D.; Polyakov, B.; Olin, H.; Svensson, K.; Olsson, E. Bistable Nanoelectromechanical Devices. *Appl. Phys. Lett.* **2004**, *84* (20), 4074–4076.
  - (51) McNulty, D.; Biswas, S.; Garvey, S.; O'Dwyer, C.; Holmes, J. D. Directly Grown Germanium Nanowires from Stainless Steel: High-Performing Anodes for Li-Ion Batteries. *ACS Appl. Energy Mater.* **2020**, *3* (12), 11811–11819.
  - (52) Hao, J.; Yang, Y.; Zhao, J.; Liu, X.; Endres, F.; Chi, C.; Wang, B.; Liu, X.; Li, Y. Ionic Liquid Electrodeposition of Strain-Released Germanium Nanowires as Stable Anodes for Lithium Ion Batteries. *Nanoscale* **2017**, *9* (24), 8481–8488.
  - (53) Zhao, Z.; Zhang, H.; Kim, D. Y.; Hu, W.; Bullock, E. S.; Strobel, T. A. Properties of the Exotic Metastable ST12 Germanium Allotrope. *Nat. Commun.* **2017**, *8*, 1–8.
  - (54) Wang, J.-T.; Chen, C.; Mizuseki, H.; Kawazoe, Y. Kinetic Origin of Divergent Decompression Pathways in Silicon and Germanium. *Phys. Rev. Lett.* **2013**, *110* (16), 165503.
  - (55) Sapelkin, A. V.; Karavanskii, V. A.; Kartopu, G.; Es-Souni, M.; Luklinska, Z. Raman Study of Nano-Crystalline Ge under High Pressure. *Phys. status solidi* **2007**, *244* (4), 1376–1380.
  - (56) Coppari, F.; Chervin, J. C.; Congeduti, A.; Lazzeri, M.; Polian, A.; Principi, E.; Di Cicco, A. Pressure-Induced Phase Transitions in Amorphous and Metastable Crystalline Germanium by Raman Scattering, x-Ray Spectroscopy, and Ab Initio Calculations. *Phys. Rev. B - Condens. Matter Mater. Phys.* **2009**, *80* (11), 1–9.
  - (57) Mujica, A.; Needs, R. J. First-Principles Calculations of the Structural Properties, Stability, and Band Structure of Complex Tetrahedral Phases of Germanium: ST12 and BC8. *Phys. Rev. B* **1993**, *48* (23), 17010–17017.
  - (58) Boucherif, A.; Radescu, S.; Arès, R.; Mujica, A.; Mélinon, P.; Machon, D. Metastable States in Pressurized Bulk and Mesoporous Germanium. *J. Phys. Chem. C* **2018**, *122* (20), 10929–10938.

- (59) Mujica, A.; Pickard, C. J.; Needs, R. J. Low-Energy Tetrahedral Polymorphs of Carbon, Silicon, and Germanium. *Phys. Rev. B - Condens. Matter Mater. Phys.* **2015**, *91* (21), 214104.
- (60) Zhao, Z.; Tian, F.; Dong, X.; Li, Q.; Wang, Q.; Wang, H.; Zhong, X.; Xu, B.; Yu, D.; He, J.; Wang, H. T.; Ma, Y.; Tian, Y. Tetragonal Allotrope of Group 14 Elements. *J. Am. Chem. Soc.* **2012**, *134* (30), 12362–12365.
- (61) Pickard, C. J.; Needs, R. J. Hypothetical Low-Energy Chiral Framework Structure of Group 14 Elements. *Phys. Rev. B - Condens. Matter Mater. Phys.* **2010**, *81* (1), 014106.
- (62) Bundy, F. P.; Kasper, J. S. A New Dense Form of Solid Germanium. *Science* **1963**, *139* (3552), 340–341.
- (63) Malone, B. D.; Sau, J. D.; Cohen, M. L. Ab Initio Survey of the Electronic Structure of Tetrahedrally Bonded Phases of Silicon. *Phys. Rev. B - Condens. Matter Mater. Phys.* **2008**, *78* (3), 035210.
- (64) Morozova, N. V.; Korobeinikov, I. V.; Abrosimov, N. V.; Ovsyannikov, S. V. Controlling the Thermoelectric Power of Silicon-Germanium Alloys in Different Crystalline Phases by Applying High Pressure. *CrystEngComm* **2020**, *22* (33), 5416–5435.
- (65) Xiao, X.; Li, X.; Zheng, S.; Shao, J.; Xue, H.; Pang, H. Nanostructured Germanium Anode Materials for Advanced Rechargeable Batteries. *Adv. Mater. Interfaces* **2017**, *4* (6), 1600798.
- (66) Kennedy, T.; Brandon, M.; Ryan, K. M. Advances in the Application of Silicon and Germanium Nanowires for High-Performance Lithium-Ion Batteries. *Adv. Mater.* **2016**, *28*, 5696–5704.
- (67) Chan, C. K.; Zhang, X. F.; Cui, Y. High Capacity Li Ion Battery Anodes Using Ge Nanowires. *Nano Lett.* **2008**, *8* (1), 307–309.
- (68) Yang, C.; Chen, J.; Ji, X.; Pollard, T. P.; Lü, X.; Sun, C. J.; Hou, S.; Liu, Q.; Liu, C.; Qing, T.; Wang, Y.; Borodin, O.; Ren, Y.; Xu, K.; Wang, C. Aqueous Li-Ion Battery Enabled by Halogen Conversion–Intercalation Chemistry in Graphite. *Nature* **2019**, *569* (7755), 245–250.
- (69) Zheng, M.; Tang, H.; Hu, Q.; Zheng, S.; Li, L.; Xu, J.; Pang, H. Tungsten-Based Materials for Lithium-Ion Batteries. *Adv. Funct. Mater.* **2018**, *28* (20), 1707500.
- (70) Liu, D.; Liu, Z. jiao; Li, X.; Xie, W.; Wang, Q.; Liu, Q.; Fu, Y.; He, D. Group

- IVA Element (Si, Ge, Sn)-Based Alloying/Dealloying Anodes as Negative Electrodes for Full-Cell Lithium-Ion Batteries. *Small* **2017**, *13* (45), 1702000.
- (71) Tang, W.; Liu, Y.; Peng, C.; Hu, M. Y.; Deng, X.; Lin, M.; Hu, J. Z.; Loh, K. P. Probing Lithium Germanide Phase Evolution and Structural Change in a Germanium-in-Carbon Nanotube Energy Storage System. *J. Am. Chem. Soc.* **2015**, *137* (7), 2600–2607.
- (72) Wu, S.; Han, C.; Iocozzia, J.; Lu, M.; Ge, R.; Xu, R.; Lin, Z. Germanium-Based Nanomaterials for Rechargeable Batteries. *Angew. Chemie - Int. Ed.* **2016**, *55* (28), 7898–7922.
- (73) Ganji, S. Nanowire Growths, and Mechanisms of These Growths for Developing Novel Nanomaterials. *J. Nanosci. Nanotechnol.* **2018**, *19* (4), 1849–1874.
- (74) Tatsumi, Y.; Hirata, M.; Shigi, M. Characteristics of Whisker Growth in Amorphous Silicon. *Jpn. J. Appl. Phys.* **1979**, *18* (12), 2199–2206.
- (75) Weber, L. Equilibrium Solid Solubility of Silicon in Silver. *Metall. Mater. Trans. A Phys. Metall. Mater. Sci.* **2002**, *33* (4), 1145–1150.
- (76) Wacaser, B. A.; Reuter, M. C.; Khayyat, M. M.; Wen, C. Y.; Haight, R.; Guha, S.; Ross, F. M. Growth System, Structure, and Doping of Aluminum-Seeded Epitaxial Silicon Nanowires. *Nano Lett.* **2009**, *9* (9), 3296–3301.
- (77) Thombare, S. V.; Marshall, A. F.; McIntyre, P. C. Kinetics of Germanium Nanowire Growth by the Vapor-Solid-Solid Mechanism with a Ni-Based Catalyst. *APL Mater.* **2013**, *1* (6), 061101.
- (78) Mohammad, S. N. General Hypothesis and Shell Model for the Synthesis of Semiconductor Nanotubes, Including Carbon Nanotubes. *J. Appl. Phys.* **2010**, *108* (6), 064323.
- (79) Kodambaka, S.; Tersoff, J.; Reuter, M. C.; Ross, F. M. Germanium Nanowire Growth below the Eutectic Temperature. *Science* **2007**, *316* (5825), 729–732.
- (80) Ge, M.; Liu, J. F.; Wu, H.; Yao, C.; Zeng, Y.; Fu, Z. D.; Zhang, S. L.; Jiang, J. Z. Synthesis of Germanium Nanowires. *J. Phys. Chem. C* **2007**, *111* (30), 11157–11160.
- (81) Hanrath, T.; Korgel, B. A. Supercritical Fluid-Liquid-Solid (SFLS) Synthesis of Si and Ge Nanowires Seeded by Colloidal Metal Nanocrystals. *Adv. Mater.* **2003**, *15* (5), 437–440.
- (82) Lu, X.; De La Mata, M.; Arbiol, J.; Korgel, B. A. Colloidal Silicon-Germanium

Nanorod Heterostructures. *Chem. Mater.* **2017**, *29* (22), 9786–9792.

- (83) Lu, X.; Hanrath, T.; Johnston, K. P.; Korgel, B. A. Growth of Single Crystal Silicon Nanowires in Supercritical Solution from Tethered Gold Particles on a Silicon Substrate. *Nano Lett.* **2003**, *3* (1), 93–99.
- (84) Savage, P. E.; Gopalan, S.; Mizan, T. I.; Martino, C. J.; Brock, E. E. Reactions at Supercritical Conditions: Applications and Fundamentals. *AIChE J.* **1995**, *41* (7), 1723–1778.
- (85) Hanrath, T.; Korgel, B. A. Nucleation and Growth of Germanium Nanowires Seeded by Organic Monolayer-Coated Gold Nanocrystals. *J. Am. Chem. Soc.* **2002**, *124* (7), 1424–1429.
- (86) Davidson, F. M.; Schricker, A. D.; Wiacek, R. J.; Korgel, B. A. Supercritical Fluid-Liquid-Solid Synthesis of Gallium Arsenide Nanowires Seeded by Alkanethiol-Stabilized Gold Nanocrystals. *Adv. Mater.* **2004**, *16* (7), 646–649.
- (87) Davidson, F. M.; Wiacek, R.; Korgel, B. A. Supercritical Fluid-Liquid-Solid Synthesis of Gallium Phosphide Nanowires. *Chem. Mater.* **2005**, *17* (2), 230–233.
- (88) Laocharoensuk, R.; Palaniappan, K.; Smith, N. A.; Dickerson, R. M.; Werder, D. J.; Baldwin, J. K.; Hollingsworth, J. A. Flow-Based Solution-Liquid-Solid Nanowire Synthesis. *Nat. Nanotechnol.* **2013**, *8* (9), 660–666.
- (89) Chèze, C.; Geelhaar, L.; Brandt, O.; Weber, W. M.; Riechert, H.; Münch, S.; Rothmund, R.; Reitzenstein, S.; Forchel, A.; Kehagias, T.; Komninou, P.; Dimitrakopoulos, G. P.; Karakostas, T. Direct Comparison of Catalyst-Free and Catalyst-Induced GaN Nanowires. *Nano Res.* **2010**, *3* (7), 528–536.
- (90) Chèze, C.; Geelhaar, L.; Jenichen, B.; Riechert, H. Different Growth Rates for Catalyst-Induced and Self-Induced GaN Nanowires. *Appl. Phys. Lett.* **2010**, *97* (15), 153105.
- (91) Zhang, Y. F.; Tang, Y. H.; Wang, N.; Yu, D. P.; Lee, C. S.; Bello, I.; Lee, S. T. Silicon Nanowires Prepared by Laser Ablation at High Temperature. *Appl. Phys. Lett.* **1998**, *72* (15), 1835–1837.
- (92) Wang, N.; Tang, Y.; Zhang, Y.; Lee, C.; Lee, S. Nucleation and Growth of Si Nanowires from Silicon Oxide. *Phys. Rev. B - Condens. Matter Mater. Phys.* **1998**, *58* (24), R16024–R16026.
- (93) Xie, T.; Jiang, Z.; Wu, G.; Fang, X.; Li, G.; Zhang, L. Characterization and Growth Mechanism of Germanium Nitride Nanowires Prepared by an Oxide-

- Assisted Method. *J. Cryst. Growth* **2005**, 283 (3–4), 286–290.
- (94) Zhang, R. Q.; Chu, T. S.; Cheung, H. F.; Wang, N.; Lee, S. T. Mechanism of Oxide-Assisted Nucleation and Growth of Silicon Nanostructures. *Mater. Sci. Eng. C* **2001**, 16 (1–2), 31–35.
  - (95) Zhang, Y. F.; Tang, Y. H.; Lam, C.; Wang, N.; Lee, C. S.; Bello, I.; Lee, S. T. Bulk-Quantity Si Nanowires Synthesized by SiO Sublimation. *J. Cryst. Growth* **2000**, 212 (1), 115–118.
  - (96) Lee, S. T.; Wang, N.; Zhang, Y. F.; Tang, Y. H. Oxide-Assisted Semiconductor Nanowire Growth. *MRS Bull.* **1999**, 24 (8), 36–42.
  - (97) Zhang, Y.; Tang, Y.; Wang, N.; Lee, C.; Bello, I.; Lee, S. Germanium Nanowires Sheathed with an Oxide Layer. *Phys. Rev. B - Condens. Matter Mater. Phys.* **2000**, 61 (7), 4518–4521.
  - (98) Zhang, R. Q.; Lifshitz, Y.; Lee, S. T. Oxide-Assisted Growth of Semiconducting Nanowires. *Adv. Mater.* **2003**, 15 (7–8), 635–640.
  - (99) Jun, Y. W.; Choi, J. S.; Cheon, J. Shape Control of Semiconductor and Metal Oxide Nanocrystals through Nonhydrolytic Colloidal Routes. *Angew. Chemie - Int. Ed.* **2006**, 45 (21), 3414–3439.
  - (100) Cozzoli, P. D.; Pellegrino, T.; Manna, L. Synthesis, Properties and Perspectives of Hybrid Nanocrystal Structures. *Chem. Soc. Rev.* **2006**, 35 (11), 1195–1208.
  - (101) Lieber, C. M.; Wang, Z. L. Functional Nanowires. *MRS Bull.* **2007**, 32 (2), 99–108.
  - (102) Schmidt, V.; Wittemann, J. V.; Senz, S.; Gösele, U. Silicon Nanowires: A Review on Aspects of Their Growth and Their Electrical Properties. *Adv. Mater.* **2009**, 21 (25–26), 2681–2702.
  - (103) Noor Mohammad, S. For Nanowire Growth, Vapor-Solid-Solid (Vapor-Solid) Mechanism Is Actually Vapor-Quasisolid-Solid (Vapor-Quasiliquid-Solid) Mechanism. *J. Chem. Phys.* **2009**, 131 (22), 224702.
  - (104) Allen, J. E.; Hemesath, E. R.; Perea, D. E.; Lensch-Falk, J. L.; Li, Z. Y.; Yin, F.; Gass, M. H.; Wang, P.; Bleloch, A. L.; Palmer, R. E.; Lauhon, L. J. High-Resolution Detection of Au Catalyst Atoms in Si Nanowires. *Nat. Nanotechnol.* **2008**, 3 (3), 168–173.
  - (105) Moutanabbir, O.; Isheim, D.; Blumtritt, H.; Senz, S.; Pippel, E.; Seidman, D. N. Colossal Injection of Catalyst Atoms into Silicon Nanowires. *Nature* **2013**, 496 (7443), 78–82.

- (106) Chen, W.; Yu, L.; Misra, S.; Fan, Z.; Pareige, P.; Patriarche, G.; Bouchoule, S.; Cabarrocas, P. R. I. Incorporation and Redistribution of Impurities into Silicon Nanowires during Metal-Particle-Assisted Growth. *Nat. Commun.* **2014**, *5*, 1–7.
- (107) Chockla, A. M.; Bogart, T. D.; Hessel, C. M.; Klavetter, K. C.; Mullins, C. B.; Korgel, B. A. Influences of Gold, Binder and Electrolyte on Silicon Nanowire Performance in Li-Ion Batteries. *J. Phys. Chem. C* **2012**, *116* (34), 18079–18086.
- (108) Xie, P.; Hu, Y.; Fang, Y.; Huang, J.; Lieber, C. M. Diameter-Dependent Dopant Location in Silicon and Germanium Nanowires. *Proc. Natl. Acad. Sci. U. S. A.* **2009**, *106* (36), 15254–15258.
- (109) Calarco, R.; Marso, M.; Richter, T.; Aykanat, A. I.; Meijers, R.; Hart, A. V.D.; Stoica, T.; Luth, H. Size-Dependent Photoconductivity in MBE-Grown GaN - Nanowires. *Nano Lett.* **2005**, *5* (5), 981–984.
- (110) Kingston, R. H. Review of Germanium Surface Phenomena. *J. Appl. Phys.* **1956**, *27* (2), 101–114.
- (111) Simanullang, M.; Wisna, G. B. M.; Usami, K.; Cao, W.; Kawano, Y.; Banerjee, K.; Oda, S. Undoped and Catalyst-Free Germanium Nanowires for High-Performance p-Type Enhancement-Mode Field-Effect Transistors. *J. Mater. Chem. C* **2016**, *4* (22), 5102–5108.
- (112) Goldthorpe, I. A.; Marshall, A. F.; McIntyre, P. C. Synthesis and Strain Relaxation of Ge-Core/Si-Shell Nanowire Arrays. *Nano Lett.* **2008**, *8* (11), 4081–4086.
- (113) Gouveia, R. C.; Kamimura, H.; Munhoz, R.; Rodrigues, A. D.; Leite, E. R.; Chiquito, A. J. Germanium Nanowires Grown Using Different Catalyst Metals. *Mater. Chem. Phys.* **2016**, *183*, 145–151.
- (114) Wittemann, J. V.; Münchgesang, W.; Senz, S.; Schmidt, V. Silver Catalyzed Ultrathin Silicon Nanowires Grown by Low-Temperature Chemical-Vapor-Deposition. *J. Appl. Phys.* **2010**, *107* (9), 096105.
- (115) Wang, Y.; Schmidt, V.; Senz, S.; Gösele, U. Epitaxial Growth of Silicon Nanowires Using an Aluminium Catalyst. *Nat. Nanotechnol.* **2006**, *1* (3), 186–189.
- (116) Schmidt, V.; Wittemann, J. V.; Gösele, U. Growth, Thermodynamics, and Electrical Properties of Silicon Nanowires. *Chem. Rev.* **2010**, *110* (1), 361–388.



- (117) Dayeh, S. A.; Chen, R.; Ro, Y. G.; Sim, J. Progress in Doping Semiconductor Nanowires during Growth. *Mater. Sci. Semicond. Process.* **2017**, *62*, 135–155.
- (118) Chung, S. W.; Yu, J. Y.; Heath, J. R. Silicon Nanowire Devices. *Appl. Phys. Lett.* **2000**, *76* (15), 2068–2070.
- (119) Seifner, M. S.; Sistani, M.; Zivadinovic, I.; Bartmann, M. G.; Lugstein, A.; Barth, S. Drastic Changes in Material Composition and Electrical Properties of Gallium-Seeded Germanium Nanowires. *Cryst. Growth Des.* **2019**, *19* (5), 2531–2536.
- (120) Aghazadeh Meshgi, M.; Biswas, S.; McNulty, D.; O'Dwyer, C.; Alessio Verni, G.; O'Connell, J.; Davitt, F.; Letofsky-Papst, I.; Poelt, P.; Holmes, J. D.; Marschner, C. Rapid, Low-Temperature Synthesis of Germanium Nanowires from Oligosilylgermane Precursors. *Chem. Mater.* **2017**, *29* (10), 4351–4360.
- (121) Mullane, E.; Kennedy, T.; Geaney, H.; Dickinson, C.; Ryan, K. M. Synthesis of Tin Catalyzed Silicon and Germanium Nanowires in a Solvent-Vapor System and Optimization of the Seed/Nanowire Interface for Dual Lithium Cycling. *Chem. Mater.* **2013**, *25* (9), 1816–1822.
- (122) Seifner, M. S.; Pertl, P.; Bernardi, J.; Biswas, S.; Holmes, J. D.; Barth, S. Lead-Supported Germanium Nanowire Growth. *Mater. Lett.* **2016**, *173*, 248–251.
- (123) Heitsch, A. T.; Fanfair, D. D.; Tuan, H. Y.; Korgel, B. A. Solution-Liquid-Solid (SLS) Growth of Silicon Nanowires. *J. Am. Chem. Soc.* **2008**, *130* (16), 5436–5437.
- (124) Geaney, H.; Bree, G.; Stokes, K.; Collins, G. A.; Aminu, I. S.; Kennedy, T.; Ryan, K. M. Enhancing the Performance of Germanium Nanowire Anodes for Li-Ion Batteries by Direct Growth on Textured Copper. *Chem. Commun.* **2019**, *55* (54), 7780–7783.
- (125) Yan, C.; Higgins, J. M.; Faber, M. S.; Lee, P. S.; Jin, S. Spontaneous Growth and Phase Transformation of Highly Conductive Nickel Germanide Nanowires. *ACS Nano* **2011**, *5* (6), 5006–5014.
- (126) Richards, B. T.; Gaskey, B.; Levin, B. D. A.; Whitham, K.; Muller, D.; Hanrath, T. Direct Growth of Germanium and Silicon Nanowires on Metal Films. *J. Mater. Chem. C* **2014**, *2* (10), 1869–1878.
- (127) Xia, Y.; Whitesides, G. M. Soft Lithography. *Angew. Chemie Int. Ed.* **1998**, *37* (5), 550–575.
- (128) Manfrinato, V. R.; Zhang, L.; Su, D.; Duan, H.; Hobbs, R. G.; Stach, E. A.;

- Berggren, K. K. Resolution Limits of Electron-Beam Lithography toward the Atomic Scale. *Nano Lett.* **2013**, *13* (4), 1555–1558.
- (129) Hu, J.; Liu, K.; Ma, T.; Wei, Y.; Chen, J.; Li, Z. Zn<sub>2</sub>GeO<sub>4</sub> Nanowires Synthesized by Dual Laser-Hydrothermal Method for Deep-Ultraviolet Photodetectors. *Opt. Laser Technol.* **2021**, *140*, 106946.
- (130) Demaria, C.; Arrais, A.; Benzi, P.; Boccaleri, E.; Antoniotti, P.; Rabezzana, R.; Operti, L. A Catalyst-Free Synthesis of Germanium Nanowires Obtained by Combined X-Ray Chemical Vapour Deposition of GeH<sub>4</sub> and Low-Temperature Thermal Treatment Techniques. *Bull. Mater. Sci.* **2016**, *39* (2), 499–507.
- (131) Barth, S.; Seifner, S.; Bernardi, J. Microwave-Assisted Solution–Liquid–Solid Growth of Ge<sub>1</sub>-XS<sub>n</sub> Nanowires with High Tin Content. *Chem. Commun.* **2015**, *51* (61), 12282–12285.
- (132) Markov, I.; Stoyanov, S. Mechanisms of Epitaxial Growth. *Contemp. Phys.* **1987**, *28* (3), 267–320.
- (133) Tomioka, K.; Motohisa, J.; Hara, S.; Fukui, T. Control of InAs Nanowire Growth Directions on Si. *Nano Lett.* **2008**, *8* (10), 3475–3480.
- (134) Mohan, P.; Motohisa, J.; Fukui, T. Controlled Growth of Highly Uniform, Axial/Radial Direction-Defined, Individually Addressable InP Nanowire Arrays. *Nanotechnology* **2005**, *16* (12), 2903–2907.
- (135) Mandl, B.; Stangl, J.; Mårtensson, T.; Mikkelsen, A.; Eriksson, J.; Karlsson, L. S.; Bauer, G.; Samuelson, L.; Seifert, W. Au-Free Epitaxial Growth of InAs Nanowires. *Nano Lett.* **2006**, *6* (8), 1817–1821.
- (136) Mandl, B.; Stangl, J.; Hilner, E.; Zakharov, A. A.; Hillerich, K.; Dey, A. W.; Samuelson, L.; Bauer, G.; Deppert, K.; Mikkelsen, A. Growth Mechanism of Self-Catalyzed Group III-V Nanowires. *Nano Lett.* **2010**, *10* (11), 4443–4449.
- (137) Adhikari, H.; Marshall, A. F.; Chidsey, C. E. D.; McIntyre, P. C. Germanium Nanowire Epitaxy: Shape and Orientation Control. *Nano Lett.* **2006**, *6* (2), 318–323.
- (138) Dayeh, S. A.; Wang, J.; Li, N.; Huang, J. Y.; Gin, A. V.; Picraux, S. T. Growth, Defect Formation, and Morphology Control of Germanium-Silicon Semiconductor Nanowire Heterostructures. *Nano Lett.* **2011**, *11* (10), 4200–4206.
- (139) Li, L.; Fang, X.; Chew, H. G.; Zheng, F.; Liew, T. H.; Xu, X.; Zhang, Y.; Pan, S.; Li, G.; Zhang, L. Crystallinity-Controlled Germanium Nanowire Arrays:

- Potential Field Emitters. *Adv. Funct. Mater.* **2008**, *18* (7), 1080–1088.
- (140) Yuan, F. W.; Yang, H. J.; Tuan, H. Y. Seeded Silicon Nanowire Growth Catalyzed by Commercially Available Bulk Metals: Broad Selection of Metal Catalysts, Superior Field Emission Performance, and Versatile Nanowire/Metal Architectures. *J. Mater. Chem.* **2011**, *21* (36), 13793–13800.
  - (141) Dayeh, S. A.; Picraux, S. T. Direct Observation of Nanoscale Size Effects in Ge Semiconductor Nanowire Growth. *Nano Lett.* **2010**, *10* (10), 4032–4039.
  - (142) Tutuc, E.; Chu, J. O.; Ott, J. A.; Guha, S. Doping of Germanium Nanowires Grown in Presence of PH<sub>3</sub>. *Appl. Phys. Lett.* **2006**, *89* (26), 263101.
  - (143) Kim, B.-S.; Koo, T.-W.; Lee, J.-H.; Kim, D. S.; Jung, Y. C.; Hwang, S. W.; Choi, B. L.; Lee, E. K.; Kim, J. M.; Whang, D. Catalyst-Free Growth of Single-Crystal Silicon and Germanium Nanowires. *Nano Lett.* **2009**, *9* (2), 864–869.
  - (144) Arrais, A.; Benzi, P.; Bottizzo, E.; Demaria, C. Characterization of Hydrogenated Amorphous Germanium Compounds Obtained by X-Ray Chemical Vapor Deposition of Germane: Effect of the Irradiation Dose on Optical Parameters and Structural Order. *J. Appl. Phys.* **2007**, *102* (10), 104905.
  - (145) Arrais, A.; Benzi, P.; Bottizzo, E.; Demaria, C. Correlations among Hydrogen Bonding Configuration, Structural Order and Optical Coefficients in Hydrogenated Amorphous Germanium Obtained by x-Ray-Activated Chemical Vapour Deposition. *J. Phys. D: Appl. Phys.* **2009**, *42* (10), 105406.
  - (146) Dřínek, V.; Fajgar, R.; Klementová, M.; Šubrt, J. Deposition of Germanium Nanowires from Hexamethyldigermane: Influence of the Substrate Pretreatment. *J. Electrochem. Soc.* **2010**, *157* (10), K218.
  - (147) Dřínek, V.; Šubrt, J.; Klementová, M.; Rieder, M.; Fajgar, R. From Shelled Ge Nanowires to SiC Nanotubes. *Nanotechnology* **2009**, *20* (3).
  - (148) Shen, G.; Chen, D. One-Dimensional Nanostructures for Photodetectors. *Recent Pat. Nanotechnol.* **2010**, *4* (1), 20–31.
  - (149) Li, C. B.; Usami, K.; Muraki, T.; Mizuta, H.; Odal, S. The Impacts of Surface Conditions on the Vapor-Liquid-Solid Growth of Germanium Nanowires on Si (100) Substrate. *Appl. Phys. Lett.* **2008**, *93* (4), 041917.
  - (150) Pecora, E. F.; Irrera, A.; Artioni, P.; Boninelli, S.; Bongiorno, C.; Spinella, C.; Priolo, F. Heteroepitaxial Growth and Faceting of Ge Nanowires on Si(111) by Electron-Beam Evaporation. *Electrochem. Solid-State Lett.* **2010**, *13* (5), K53.
  - (151) Wu, X.; Tao, Y. Synthesis of Crystalline and Amorphous Germanium

- Nanorods. *Mater. Res. Bull.* **2002**, 37 (13), 2179–2183.
- (152) Choi, S.; Kim, J.; Hwang, D. Y.; Park, H.; Ryu, J.; Kwak, S. K.; Park, S. Generalized Redox-Responsive Assembly of Carbon-Sheathed Metallic and Semiconducting Nanowire Heterostructures. *Nano Lett.* **2016**, 16 (2), 1179–1185.
  - (153) Cumbul Altay, M.; Eroglu, S. Catalyst-Free Chemical Vapor Deposition of Ge Wires from Readily Available Precursors. *Mater. Lett.* **2020**, 278, 128385.
  - (154) Wu, H. C.; Hou, T. C.; Chueh, Y. L.; Chen, L. J.; Chiu, H. T.; Lee, C. Y. One-Dimensional Germanium Nanostructures-Formation and Their Electron Field Emission Properties. *Nanotechnology* **2010**, 21 (45).
  - (155) Sun, Y.; Jin, S.; Yang, G.; Wang, J.; Wang, C. Germanium Nanowires-in-Graphite Tubes via Self-Catalyzed Synergetic Confined Growth and Shell-Splitting Enhanced Li-Storage Performance. *ACS Nano* **2015**, 9 (4), 3479–3490.
  - (156) Hatano, K.; Asano, Y.; Kameda, Y.; Koshio, A.; Kokai, F. Formation of Germanium-Carbon Core-Shell Nanowires by Laser Vaporization in High-Pressure Ar Gas without the Addition of Other Metal Catalysts. *Mater. Sci. Appl.* **2017**, 08 (12), 838–847.
  - (157) Morales, A. M.; Lieber, C. M. A Laser Ablation Method for the Synthesis of Crystalline Semiconductor Nanowires. *Science* **1998**, 279 (5348), 208–211.
  - (158) Tang, Y. H.; Zhang, Y. F.; Wang, N.; Shi, W. S.; Lee, C. S.; Bello, I.; Lee, S. T. Si Nanowires Synthesized from Silicon Monoxide by Laser Ablation. *J. Vac. Sci. Technol. B Microelectron. Nanom. Struct.* **2001**, 19 (1), 317–319.
  - (159) Shi, W.; Zheng, Y.; Peng, H.; Wang, N.; Lee, C. S.; Lee, S. T. Laser Ablation Synthesis and Optical Characterization of Silicon Carbide Nanowires. *J. Am. Ceram. Soc.* **2000**, 83 (12), 3228–3230.
  - (160) Shi, W. S.; Zheng, Y. F.; Wang, N.; Lee, C. S.; Lee, S. T. Synthesis and Microstructure of Gallium Phosphide Nanowires. *J. Vac. Sci. Technol. B Microelectron. Nanom. Struct.* **2001**, 19 (4), 1115.
  - (161) Mohammad, S. N. Nanomaterials Synthesis Routes. In *Springer Series in Materials Science*; Springer Science and Business Media Deutschland GmbH, 2020; Vol. 307, pp 13–26.
  - (162) Fritzsche, H. Electrical Properties of Germanium Semiconductors at Low Temperatures. *Phys. Rev.* **1955**, 99 (2), 406–419.

- (163) Saifutdinov, A. I.; Fairushin, I. I.; Kashapov, N. F. Analysis of Various Scenarios of the Behavior of Voltage–Current Characteristics of Direct-Current Microdischarges at Atmospheric Pressure. *JETP Lett.* **2016**, *104* (3), 180–185.
- (164) Saifutdinov, A. I.; Timerkaev, B. A.; Ibragimov, A. R. Numerical Simulation of Temperature Fields in a Direct-Current Plasma Torch. *Tech. Phys. Lett.* **2018**, *44* (2), 164–166.
- (165) Timerkaev, B. A.; Kaleeva, A. A.; Timerkaeva, D. B.; Saifutdinov, A. I. Synthesizing Germanium Nanotubes in an Electric Arc Plasma. *Russ. J. Phys. Chem. A* **2020**, *94* (3), 613–617.
- (166) Heitsch, A. T.; Hessel, C. M.; Akhavan, V. A.; Korgel, B. A. Colloidal Silicon Nanorod Synthesis. *Nano Lett.* **2009**, *9* (8), 3042–3047.
- (167) Heath, J. R.; LeGoues, F. K. A Liquid Solution Synthesis of Single Crystal Germanium Quantum Wires. *Chem. Phys. Lett.* **1993**, *208* (3–4), 263–268.
- (168) Shah, P. S.; Hanrath, T.; Johnston, K. P.; Korgel, B. A. Nanocrystal and Nanowire Synthesis and Dispersibility in Supercritical Fluids. *J. Phys. Chem. B* **2004**, *108* (28), 9574–9587.
- (169) Subramaniam, B.; McHugh, M. A. Reactions in Supercritical Fluids—a Review. *Ind. Eng. Chem. Process Des. Dev.* **1986**, *25* (1), 1–12.
- (170) Lin, L. W.; Tang, Y. H.; Chen, C. S.; Xu, H. F. Self-Assembled Single Crystal Germanium Nanowires Arrays under Supercritical Hydrothermal Conditions. *CrystEngComm* **2010**, *12* (10), 2975–2981.
- (171) Hobbs, R. G.; Barth, S.; Petkov, N.; Zirngast, M.; Marschner, C.; Morris, M. A.; Holmes, J. D. Seedless Growth of Sub-10 Nm Germanium Nanowires. *J. Am. Chem. Soc.* **2010**, *132* (39), 13742–13749.
- (172) Lotty, O.; Hobbs, R.; O'Regan, C.; Hlina, J.; Marschner, C.; O'Dwyer, C.; Petkov, N.; Holmes, J. D. Self-Seeded Growth of Germanium Nanowires: Coalescence and Ostwald Ripening. *Chem. Mater.* **2013**, *25* (2), 215–222.
- (173) Siskin, M.; Katritzky, A. R. Reactivity of Organic Compounds in Hot Water: Geochemical and Technological Implications. *Science* **1991**, *254* (5029), 231–237.
- (174) Pei, L. Z.; Zhao, H. S.; Tan, W.; Yu, H. Y.; Chen, Y. W.; Fan, C. G.; Zhang, Q. F. Smooth Germanium Nanowires Prepared by a Hydrothermal Deposition Process. *Mater. Charact.* **2009**, *60* (11), 1400–1405.
- (175) Pei, L. Z.; Zhao, H. S.; Tan, W.; Yu, H. Y.; Chen, Y. W.; Wang, J. F.; Fan, C.

- G.; Chen, J.; Zhang, Q. F. Low Temperature Growth of Single Crystalline Germanium Nanowires. *Mater. Res. Bull.* **2010**, *45* (2), 153–158.
- (176) Gerung, H.; Boyle, T. J.; Tribby, L. J.; Bunge, S. D.; Brinker, C. J.; Han, S. M. Solution Synthesis of Germanium Nanowires Using a Ge<sup>2+</sup> Alkoxide Precursor. *J. Am. Chem. Soc.* **2006**, *128* (15), 5244–5250.
- (177) Barrett, C. A.; Geaney, H.; Gunning, R. D.; Laffir, F. R.; Ryan, K. M. Perpendicular Growth of Catalyst-Free Germanium Nanowire Arrays. *Chem. Commun.* **2011**, *47* (13), 3843–3845.
- (178) Zaitseva, N.; Dai, Z. R.; Grant, C. D.; Harper, J.; Saw, C. Germanium Nanocrystals Synthesized in High-Boiling-Point Organic Solvents. *Chem. Mater.* **2007**, *19* (21), 5174–5178.
- (179) Chockla, A. M.; Korgel, B. A. Seeded Germanium Nanowire Synthesis in Solution. *J. Mater. Chem.* **2009**, *19* (7), 996–1001.
- (180) Zaitseva, N.; Harper, J.; Gerion, D.; Saw, C. Unseeded Growth of Germanium Nanowires by Vapor-Liquid-Solid Mechanism. *Appl. Phys. Lett.* **2005**, *86* (5), 1–3.
- (181) Milliron, D.; Hughes, S. M.; Cui, Y.; Manna, L.; Li, J.; Wang, L. W.; Alivisatos, A. P. Colloidal Nanocrystal Heterostructures with Linear and Branched Topology. *Nature* **2004**, *430* (6996), 190–195.
- (182) Geaney, H.; Dickinson, C.; Weng, W.; Kiely, C. J.; Barrett, C. A.; Gunning, R. D.; Ryan, K. M. Role of Defects and Growth Directions in the Formation of Periodically Twinned and Kinked Unseeded Germanium Nanowires. *Cryst. Growth Des.* **2011**, *11* (7), 3266–3272.
- (183) Penner, R. M. Mesoscopic Metal Particles and Wires by Electrodeposition. *J. Phys. Chem. B* **2002**, *106* (13), 3339–3353.
- (184) Therese, G. H. A.; Kamath, P. V. Electrochemical Synthesis of Metal Oxides and Hydroxides. *Chem. Mater.* **2000**, *12* (5), 1195–1204.
- (185) Gavrilov, S. A.; Dronov, A. A.; Gavrilin, I. M.; Volkov, R. L.; Borgardt, N. I.; Trifonov, A. Y.; Pavlikov, A. V.; Forsh, P. A.; Kashkarov, P. K. Laser Crystallization of Germanium Nanowires Fabricated by Electrochemical Deposition. *J. Raman Spectrosc.* **2018**, *49* (5), 810–816.
- (186) Fahrenkrug, E.; Gu, J.; Jeon, S.; Veneman, P. A.; Goldman, R. S.; Maldonado, S. Room-Temperature Epitaxial Electrodeposition of Single-Crystalline Germanium Nanowires at the Wafer Scale from an Aqueous Solution. *Nano*

*Lett.* **2014**, *14* (2), 847–852.

- (187) Chi, C.; Hao, J.; Yang, Y.; Liu, S.; Liu, X.; Ma, X.; Liu, X.; Zhao, J.; Li, Y. Template-Free Growth of Coral-like Ge Nanorod Bundles via UV-Assisted Ionic Liquid Electrodeposition. *J. Mater. Sci. Mater. Electron.* **2018**, *29* (16), 14105–14110.
- (188) Yang, Z.; Veinot, J. G. C. Size-Controlled Template Synthesis of Metal-Free Germanium Nanowires. *J. Mater. Chem.* **2011**, *21* (41), 16505–16509.
- (189) Jessensky, O.; Müller, F.; Gösele, U. Self-Organized Formation of Hexagonal Pore Arrays in Anodic Alumina. *Appl. Phys. Lett.* **1998**, *72* (10), 1173–1175.
- (190) Lange, F.; Ernst, O.; Teubner, T.; Richter, C.; Schmidbauer, M.; Skibitzki, O.; Schroeder, T.; Schmidt, P.; Boeck, T. In-Plane Growth of Germanium Nanowires on Nanostructured Si(001)/SiO<sub>2</sub> Substrates. *Nano Futur.* **2020**, *4* (3), 1–8.
- (191) Bandyopadhyay, S. Spin Transport in Nanowires Synthesized Using Anodic Nanoporous Alumina Films. *Multilayer Thin Film. - Versatile Appl. Mater. Eng.* **2020**.
- (192) Shimizu, T.; Xie, T.; Nishikawa, J.; Shingubara, S.; Senz, S.; Gösele, U. Synthesis of Vertical High-Density Epitaxial Si(100) Nanowire Arrays on a Si(100) Substrate Using an Anodic Aluminum Oxide Template. *Adv. Mater.* **2007**, *19* (7), 917–920.
- (193) Henderson, E. J.; Seino, M.; Puzzo, D. P.; Ozin, G. A. Colloidally Stable Germanium Nanocrystals for Photonic Applications. *ACS Nano* **2010**, *4* (12), 7683–7691.
- (194) Henderson, E. J.; Hessel, C. M.; Veinot, J. G. C. Synthesis and Photoluminescent Properties of Size-Controlled Germanium Nanocrystals from Phenyl Trichlorogermane-Derived Polymers. *J. Am. Chem. Soc.* **2008**, *130* (11), 3624–3632.
- (195) Brinker, C. J.; Scherer, G. W. *Sol-Gel Science: The Physics and Chemistry of Sol-Gel Processing*; Elsevier Inc., 2013.
- (196) Li, X.; Zhang, H.; Chi, F.; Li, S.; Xu, B.; Zhao, M. Synthesis of Monocrystalline Composite Oxides La<sub>1-x</sub>Sr<sub>x</sub>Fe<sub>1-y</sub>Co<sub>y</sub>O<sub>3</sub> with the Perovskite Structure Using Polyethylene Glycol-Gel Method. *Mater. Sci. Eng. B* **1993**, *18* (3), 209–213.
- (197) Wacaser, B. A.; Dick, K. A.; Johansson, J.; Borgström, M. T.; Deppert, K.; Samuelson, L. Preferential Interface Nucleation: An Expansion of the VLS

- Growth Mechanism for Nanowires. *Adv. Mater.* **2009**, *21* (2), 153–165.
- (198) Ek, M.; Filler, M. A. Atomic-Scale Choreography of Vapor-Liquid-Solid Nanowire Growth. *Acc. Chem. Res.* **2018**, *51* (1), 118–126.
- (199) Owen, J. H. G.; Miki, K.; Bowler, D. R.; Goringe, C. M.; Goldfarb, I.; Briggs, G. A. D. Gas-Source Growth of Group IV Semiconductors: II. Growth Regimes and the Effect of Hydrogen. *Surf. Sci.* **1997**, *394* (1–3), 91–104.
- (200) Sivaram, S. V.; Shin, N.; Chou, L. W.; Filler, M. A. Direct Observation of Transient Surface Species during Ge Nanowire Growth and Their Influence on Growth Stability. *J. Am. Chem. Soc.* **2015**, *137* (31), 9861–9869.
- (201) Gentile, P.; Solanki, A.; Pauc, N.; Oehler, F.; Salem, B.; Rosaz, G.; Baron, T.; Den Hertog, M.; Calvo, V. Effect of HCl on the Doping and Shape Control of Silicon Nanowires. *Nanotechnology* **2012**, *23* (21).
- (202) Leitsmann, R.; Bechstedt, F. Surface Influence on Stability and Structure of Hexagon-Shaped III-V Semiconductor Nanorods. *J. Appl. Phys.* **2007**, *102* (6), 063528.
- (203) Wang, C.; Murphy, P. F.; Yao, N.; McIlwrath, K.; Chou, S. Y. Growth of Straight Silicon Nanowires on Amorphous Substrates with Uniform Diameter, Length, Orientation, and Location Using Nanopatterned Host-Mediated Catalyst. *Nano Lett.* **2011**, *11* (12), 5247–5251.
- (204) Voigtländer, B.; Zinner, A.; Weber, T.; Bonzel, H. P. Modification of Growth Kinetics in Surfactant-Mediated Epitaxy. *Phys. Rev. B* **1995**, *51* (12), 7583–7591.
- (205) Schmidt, V.; Senz, S.; Gösele, U. Diameter-Dependent Growth Direction of Epitaxial Silicon Nanowires. *Nano Lett.* **2005**, *5* (5), 931–935.
- (206) Wu, Y. S.; Bagchi, S.; Garg, S.; Singh, N.; Tsai, T. Controlled Growth and Structures of Molecular-Scale Silicon Nanowires. *Nano Lett.* **2004**, *4* (3), 433–442.
- (207) Wang, Y.; Ryu, S.; McIntyre, P. C.; Cai, W. A Three-Dimensional Phase Field Model for Nanowire Growth by the Vapor-Liquid-Solid Mechanism. *Model. Simul. Mater. Sci. Eng.* **2014**, *22* (5).
- (208) Cui, Y.; Lauhon, L. J.; Gudiksen, M. S.; Wang, J.; Lieber, C. M. Diameter-Controlled Synthesis of Single-Crystal Silicon Nanowires. *Appl. Phys. Lett.* **2001**, *78* (15), 2214–2216.
- (209) Krogstrup, P.; Yamasaki, J.; Sørensen, C. B.; Johnson, E.; Wagner, J. B.;



- Pennington, R.; Aagesen, M.; Tanaka, N.; Nygård, J. Junctions in Axial III - V Heterostructure Nanowires Obtained via an Interchange of Group III Elements. *Nano Lett.* **2009**, *9* (11), 3689–3693.
- (210) Slezák, J.; Ondřejček, M.; Chvoj, Z.; Cháb, V.; Conrad, H. Surface Diffusion of Au on Si(111): A Microscopic Study. *Phys. Rev. B - Condens. Matter Mater. Phys.* **2000**, *61* (23), 16121–16128.
- (211) Koto, M.; Marshall, A. F.; Goldthorpe, I. A.; McIntyre, P. C. Gold-Catalyzed Vapor-Liquid-Solid Germanium-Nanowire Nucleation on Porous Silicon. *Small* **2010**, *6* (9), 1032–1037.
- (212) Hannon, J. B.; Kodambaka, S.; Ross, F. M.; Tromp, R. M. The Influence of the Surface Migration of Gold on the Growth of Silicon Nanowires. *Nature* **2006**, *440* (7080), 69–71.
- (213) Dubrovskii, V. G. Development of Growth Theory for Vapor-Liquid-Solid Nanowires: Contact Angle, Truncated Facets, and Crystal Phase. *Cryst. Growth Des.* **2017**, *17* (5), 2544–2548.
- (214) Colombo, C.; Spirkoska, D.; Frimmer, M.; Abstreiter, G.; Fontcuberta I Morral, A. Ga-Assisted Catalyst-Free Growth Mechanism of GaAs Nanowires by Molecular Beam Epitaxy. *Phys. Rev. B - Condens. Matter Mater. Phys.* **2008**, *77* (15), 155326.
- (215) Sutter, E.; Sutter, P. Phase Diagram of Nanoscale Alloy Particles Used for Vapor-Liquid-Solid Growth of Semiconductor Nanowires. *Nano Lett.* **2008**, *8* (2), 411–414.
- (216) Tang, J.; Maurice, J. L.; Chen, W.; Misra, S.; Foldyna, M.; Johnson, E. V.; Roca i Cabarrocas, P. Plasma-Assisted Growth of Silicon Nanowires by Sn Catalyst: Step-by-Step Observation. *Nanoscale Res. Lett.* **2016**, *11* (1), 455.
- (217) Yu, Z.; Lu, J.; Qian, S.; Misra, S.; Yu, L.; Xu, J.; Xu, L.; Wang, J.; Shi, Y.; Chen, K.; Roca i Cabarrocas, P. Bi-Sn Alloy Catalyst for Simultaneous Morphology and Doping Control of Silicon Nanowires in Radial Junction Solar Cells. *Appl. Phys. Lett.* **2015**, *107* (16), 163105.
- (218) Musin, I. R.; Filler, M. A. Chemical Control of Semiconductor Nanowire Kinking and Superstructure. *Nano Lett.* **2012**, *12* (7), 3363–3368.
- (219) Tian, B.; Xie, P.; Kempa, T. J.; Bell, D. C.; Lieber, C. M. Single-Crystalline Kinked Semiconductor Nanowire Superstructures. *Nat. Nanotechnol.* **2009**, *4* (12), 824–829.

- (220) Hillerich, K.; Dick, K. A.; Wen, C. Y.; Reuter, M. C.; Kodambaka, S.; Ross, F. M. Strategies to Control Morphology in Hybrid Group III-V/Group IV Heterostructure Nanowires. *Nano Lett.* **2013**, *13* (3), 903–908.
- (221) Nebol'sin, V. A.; Shchetinin, A. A. Role of Surface Energy in the Vapor-Liquid-Solid Growth of Silicon. *Inorg. Mater.* **2003**, *39* (9), 899–903.
- (222) Schwarz, K. W.; Tersoff, J. Elementary Processes in Nanowire Growth. *Nano Lett.* **2011**, *11* (2), 316–320.
- (223) Jacobsson, D.; Panciera, F.; Tersoff, J.; Reuter, M. C.; Lehmann, S.; Hofmann, S.; Dick, K. A.; Ross, F. M. Interface Dynamics and Crystal Phase Switching in GaAs Nanowires. *Nature* **2016**, *531* (7594), 317–322.
- (224) Noor Mohammad, S. Self-Catalytic Solution for Single-Crystal Nanowire and Nanotube Growth. *J. Chem. Phys.* **2007**, *127* (24), 244702.
- (225) Peng, H. Y.; Pan, Z. W.; Xu, L.; Fan, X. H.; Wang, N.; Lee, C. S.; Lee, S. T. Temperature Dependence of Si Nanowire Morphology. *Adv. Mater.* **2001**, *13* (5), 317–320.
- (226) Orlandi, M. O.; Leite, E. R.; Aguiar, R.; Bettini, J.; Longo, E. Growth of SnO Nanobelts and Dendrites by a Self-Catalytic VLS Process. *J. Phys. Chem. B* **2006**, *110* (13), 6621–6625.
- (227) Chen, Y.; Cui, X.; Zhang, K.; Pan, D.; Zhang, S.; Wang, B.; Hou, J. G. Bulk-Quantity Synthesis and Self-Catalytic VLS Growth of SnO<sub>2</sub> Nanowires by Lower-Temperature Evaporation. *Chem. Phys. Lett.* **2003**, *369* (1–2), 16–20.
- (228) Romberg, R.; Heckmair, N.; Frigo, S. P.; Ogurtsov, A.; Menzel, D.; Feulner, P. Atom-Selective Bond Breaking in a Chemisorbed Homonuclear Molecule Induced by Core Excitation: *Class. Phys. Rev. Lett.* **2000**, *84* (2), 374.
- (229) Kobayashi, K.; Kokai, F.; Sakurai, N.; Yasuda, H. Silicon-Catalyzed Growth of Amorphous SiO<sub>x</sub> Nanowires by Laser Vaporization of Si and Si/SiO<sub>2</sub>. *J. Phys. Chem. C* **2013**, *117* (47), 25169–25174.
- (230) Gaudet, S.; Detavernier, C.; Kellock, A. J.; Desjardins, P.; Lavoie, C. Thin Film Reaction of Transition Metals with Germanium. *J. Vac. Sci. Technol. A Vacuum, Surfaces, Film.* **2006**, *24* (3), 474–485.
- (231) Mathur, S.; Shen, H.; Sivakov, V.; Werner, U. Germanium Nanowires and Core-Shell Nanostructures by Chemical Vapor Deposition of [Ge(C<sub>5</sub>H<sub>5</sub>)<sub>2</sub>]. *Chem. Mater.* **2004**, *16* (12), 2449–2456.
- (232) Chernov, A. A. *Modern Crystallography III*; Springer Series in Solid-State

- Sciences; Springer Berlin Heidelberg: Berlin, Heidelberg, 1984; Vol. 36.
- (233) Taylor, H. S.; Jones, W. H. The Thermal Decomposition of Metal Alkyls in Hydrogen-Ethylene Mixtures. *J. Am. Chem. Soc.* **1930**, 52 (3), 1111–1121.
  - (234) Korgel, B. A.; Fitzmaurice, D. Self-Assembly of Silver Nanocrystals into Two-Dimensional Nanowire Arrays. *Adv. Mater.* **1998**, 10 (9), 661–665.
  - (235) Wu, Y.; Yang, P. Melting and Welding Semiconductor Nanowires in Nanotubes. *Adv. Mater.* **2001**, 13 (7), 520–523.
  - (236) Lew, K. K.; Pan, L.; Dickey, E. C.; Redwing, J. M. Vapor-Liquid-Solid Growth of Silicon-Germanium Nanowires. *Adv. Mater.* **2003**, 15 (24), 2073–2076.
  - (237) Wang, L.; Zhang, Y.; Sun, H.; You, J.; Miao, Y.; Dong, Z.; Liu, T.; Jiang, Z.; Hu, H. Nanoscale Growth of a Sn-Guided SiGeSn Alloy on Si (111) Substrates by Molecular Beam Epitaxy. *Nanoscale Adv.* **2021**, 3 (4), 997–1004.
  - (238) Wirths, S.; Buca, D.; Mantl, S. Si-Ge-Sn Alloys: From Growth to Applications. *Prog. Cryst. Growth Charact. Mater.* **2016**, 62 (1), 1–39.
  - (239) Zaima, S.; Nakatsuka, O.; Taoka, N.; Kurosawa, M.; Takeuchi, W.; Sakashita, M. Growth and Applications of GeSn-Related Group-IV Semiconductor Materials. *Sci. Technol. Adv. Mater.* **2015**, 16, 043502.
  - (240) Doherty, J.; Biswas, S.; Galluccio, E.; Broderick, C. A.; Garcia-Gil, A.; Duffy, R.; O'Reilly, E. P.; Holmes, J. D. Progress on Germanium-Tin Nanoscale Alloys. *Chem. Mater.* **2020**, 32 (11), 4383–4408.
  - (241) Gupta, S.; Chen, R.; Magyari-Kope, B.; Lin, H.; Yang, B.; Nainani, A.; Nishi, Y.; Harris, J. S.; Saraswat, K. C. GeSn Technology: Extending the Ge Electronics Roadmap. In *Technical Digest - International Electron Devices Meeting, IEDM*; 2011.
  - (242) Kouvetakis, J.; Menendez, J.; Chizmeshya, A. V. G. TIN-BASED GROUP IV SEMICONDUCTORS: New Platforms for Opto- and Microelectronics on Silicon. *Annu. Rev. Mater. Res.* **2006**, 36, 497–554.
  - (243) Doherty, J.; McNulty, D.; Biswas, S.; Moore, K.; Conroy, M.; Bangert, U.; O'Dwyer, C.; Holmes, J. D. Germanium Tin Alloy Nanowires as Anode Materials for High Performance Li-Ion Batteries. *Nanotechnology* **2020**, 31 (16), 165402.
  - (244) Biswas, S.; Doherty, J.; Saladukha, D.; Ramasse, Q.; Majumdar, D.; Upmanyu, M.; Singha, A.; Ochalski, T.; Morris, M. A.; Holmes, J. D. Non-Equilibrium Induction of Tin in Germanium: Towards Direct Bandgap Ge<sub>1-x</sub>Sn<sub>x</sub>

- Nanowires. *Nat. Commun.* **2016**, 7, 114005.
- (245) Sun, Y. L.; Matsumura, R.; Jevasuwan, W.; Fukata, N. Au-Sn Catalyzed Growth of Ge<sub>1-x</sub>Sn<sub>x</sub> Nanowires: Growth Direction, Crystallinity, and Sn Incorporation. *Nano Lett.* **2019**, 19 (9), 6270–6277.
- (246) Schanche, J. S. Microwave Synthesis Solutions from Personal Chemistry. *Mol. Divers.* **2003**, 7 (2–4), 293–300.
- (247) Muthuswamy, E.; Iskandar, A. S.; Amador, M. M.; Kauzlarich, S. M. Facile Synthesis of Germanium Nanoparticles with Size Control: Microwave versus Conventional Heating. *Chem. Mater.* **2013**, 25 (8), 1416–1422.
- (248) Madras, P.; Dailey, E.; Drucker, J. Kinetically Induced Kinking of Vapor-Liquid-Solid Grown Epitaxial Si Nanowires. *Nano Lett.* **2009**, 9 (11), 3826–3830.
- (249) Seifner, M. S.; Biegger, F.; Lugstein, A.; Bernardi, J.; Barth, S. Microwave-Assisted Ge<sub>1-x</sub>Sn<sub>x</sub> Nanowire Synthesis: Precursor Species and Growth Regimes. *Chem. Mater.* **2015**, 27 (17), 6125–6130.
- (250) Ermez, S.; Jones, E. J.; Crawford, S. C.; Gradečak, S. Self-Seeded Growth of GaAs Nanowires by Metal-Organic Chemical Vapor Deposition. *Cryst. Growth Des.* **2015**, 15 (6), 2768–2774.
- (251) Seifner, M. S.; Hernandez, S.; Bernardi, J.; Romano-Rodriguez, A.; Barth, S. Pushing the Composition Limit of Anisotropic Ge<sub>1-x</sub>Sn<sub>x</sub> Nanostructures and Determination of Their Thermal Stability. *Chem. Mater.* **2017**, 29, 9802–9813.
- (252) Erickson, E. M.; Ghanty, C.; Aurbach, D. New Horizons for Conventional Lithium Ion Battery Technology. *J. Phys. Chem. Lett.* **2014**, 5 (19), 3313–3324.
- (253) Croguennec, L.; Palacin, M. R. Recent Achievements on Inorganic Electrode Materials for Lithium-Ion Batteries. *J. Am. Chem. Soc.* **2015**, 137 (9), 3140–3156.
- (254) Goodenough, J. B.; Park, K. S. The Li-Ion Rechargeable Battery: A Perspective. *J. Am. Chem. Soc.* **2013**, 135 (4), 1167–1176.
- (255) Thackeray, M. M.; Thomas, J. O.; Whittingham, M. S. Science and Applications of Mixed Conductors for Lithium Batteries. *MRS Bull.* **2000**, 25 (3), 39–46.
- (256) Chamaani, A.; Safa, M.; Chawla, N.; El-Zahab, B. Composite Gel Polymer Electrolyte for Improved Cyclability in Lithium-Oxygen Batteries. *ACS Appl. Mater. Interfaces* **2017**, 9 (39), 33819–33826.

- (257) Wu, X. L.; Guo, Y. G.; Wan, L. J. Rational Design of Anode Materials Based on Group IVA Elements (Si, Ge, and Sn) for Lithium-Ion Batteries. *Chem. - An Asian J.* **2013**, 8 (9), 1948–1958.
- (258) Courtney, I. A.; Dahn, J. R. Electrochemical and In Situ X-Ray Diffraction Studies of the Reaction of Lithium with Tin Oxide Composites. *J. Electrochem. Soc.* **1997**, 144 (6), 2045–2052.
- (259) Winter, M.; Besenhard, J. O. Electrochemical Lithiation of Tin and Tin-Based Intermetallics and Composites. *Electrochim. Acta* **1999**, 45 (1), 31–50.
- (260) Liu, X.; Wu, X. Y.; Chang, B.; Wang, K. X. Recent Progress on Germanium-Based Anodes for Lithium Ion Batteries: Efficient Lithiation Strategies and Mechanisms. *Energy Storage Mater.* **2020**, 30, 146–169.
- (261) Graetz, J.; Ahn, C. C.; Yazami, R.; Fultz, B. Nanocrystalline and Thin Film Germanium Electrodes with High Lithium Capacity and High Rate Capabilities. *J. Electrochem. Soc.* **2004**, 151 (5), A698.
- (262) Park, M. H.; Kim, K.; Kim, J.; Cho, J. Flexible Dimensional Control of High-Capacity Li-Ion-Battery Anodes: From 0D Hollow to 3D Porous Germanium Nanoparticle Assemblies. *Adv. Mater.* **2010**, 22 (3), 415–418.
- (263) Lee, H.; Cho, J. Sn<sub>78</sub>Ge<sub>22</sub>@carbon Core-Shell Nanowires as Fast and High-Capacity Lithium Storage Media. *Nano Lett.* **2007**, 7 (9), 2638–2641.
- (264) Deshpande, R.; Cheng, Y. T.; Verbrugge, M. W. Modeling Diffusion-Induced Stress in Nanowire Electrode Structures. *J. Power Sources* **2010**, 195 (15), 5081–5088.
- (265) Lee, S. W.; Ryu, I.; Nix, W. D.; Cui, Y. Fracture of Crystalline Germanium during Electrochemical Lithium Insertion. *Extrem. Mech. Lett.* **2015**, 2 (1), 15–19.
- (266) Li, W.; Zheng, J.; Chen, T.; Wang, T.; Wang, X.; Li, X. One Step Preparation of a High Performance Ge–c Nanocomposite Anode for Lithium Ion Batteries by Tandem Plasma Reactions. *Chem. Commun.* **2014**, 50 (16), 2052–2054.
- (267) Dileo, R. A.; Frisco, S.; Ganter, M. J.; Rogers, R. E.; Raffaele, R. P.; Landi, B. J. Hybrid Germanium Nanoparticle-Single-Wall Carbon Nanotube Free-Standing Anodes for Lithium Ion Batteries. *J. Phys. Chem. C* **2011**, 115 (45), 22609–22614.
- (268) Cheng, J.; Du, J. Facile Synthesis of Germanium-Graphene Nanocomposites and Their Application as Anode Materials for Lithium Ion Batteries.

*CrystEngComm* **2012**, *14* (2), 397–400.

- (269) Li, X.; Yang, Z.; Fu, Y.; Qiao, L.; Li, D.; Yue, H.; He, D. Germanium Anode with Excellent Lithium Storage Performance in a Germanium/Lithium-Cobalt Oxide Lithium-Ion Battery. *ACS Nano* **2015**, *9* (2), 1858–1867.
- (270) Baggetto, L.; Notten, P. H. L. Lithium-Ion (De)Insertion Reaction of Germanium Thin-Film Electrodes: An Electrochemical and In Situ XRD Study. *J. Electrochem. Soc.* **2009**, *156* (3), A169.
- (271) Loaiza, L. C.; Louvain, N.; Fraisse, B.; Boulaoued, A.; Iadecola, A.; Johansson, P.; Stievano, L.; Seznec, V.; Monconduit, L. Electrochemical Lithiation of Ge: New Insights by Operando Spectroscopy and Diffraction. *J. Phys. Chem. C* **2018**, *122* (7), 3709–3718.
- (272) Jung, H.; Allan, P. K.; Hu, Y. Y.; Borkiewicz, O. J.; Wang, X. L.; Han, W. Q.; Du, L. S.; Pickard, C. J.; Chupas, P. J.; Chapman, K. W.; Morris, A. J.; Grey, C. P. Elucidation of the Local and Long-Range Structural Changes That Occur in Germanium Anodes in Lithium-Ion Batteries. *Chem. Mater.* **2015**, *27* (3), 1031–1041.
- (273) Sangster, J.; Pelton, A. D. The Ge-Li (Germanium-Lithium) System. *J. Phase Equilibria* **1997**, *18* (3), 289–294.
- (274) Morris, A. J.; Grey, C. P.; Pickard, C. J. Thermodynamically Stable Lithium Silicides and Germanides from Density Functional Theory Calculations. *Phys. Rev. B - Condens. Matter Mater. Phys.* **2014**, *90* (5), 054111.
- (275) Liu, J.; Song, K.; Zhu, C.; Chen, C. C.; Van Aken, P. A.; Maier, J.; Yu, Y. Ge/C Nanowires as High-Capacity and Long-Life Anode Materials for Li-Ion Batteries. *ACS Nano* **2014**, *8* (7), 7051–7059.
- (276) Connaughton, S.; Hobbs, R.; Lotty, O.; Holmes, J. D.; Krstić, V. Variation of Self-Seeded Germanium Nanowire Electronic Device Functionality Due to Synthesis Condition Determined Surface States. *Adv. Mater. Interfaces* **2015**, *2* (5), 1400469.
- (277) Connaughton, S.; Kolesnik-Gray, M.; Hobbs, R.; Lotty, O.; Holmes, J. D.; Krstić, V. Diameter-Driven Crossover in Resistive Behaviour of Heavily Doped Self-Seeded Germanium Nanowires. *Beilstein J. Nanotechnol.* **2016**, *7* (1), 1284–1288.
- (278) Levitas, A. Electrical Properties of Germanium-Silicon Alloys. *Phys. Rev.* **1955**, *99* (6), 1810–1814.

- (279) Chua, L. O.; Kang, S. M. Memristive Devices and Systems. *Proc. IEEE* **1976**, *64* (2), 209–223.
- (280) Chua, L. O. Memristor—The Missing Circuit Element. *IEEE Trans. Circuit Theory* **1971**, *18* (5), 507–519.
- (281) Meyerhofer, D.; Brown, G. A.; Sommers, H. S. Degenerate Germanium. I. Tunnel, Excess, and Thermal Current in Tunnel Diodes. *Phys. Rev.* **1962**, *126* (4), 1329–1341.
- (282) Sharp, J.; Lee, W. J.; Ploog, K.; Umana-Membreno, G. A.; Faraone, L.; Dell, J. M. A Novel Technique for Degenerate P-Type Doping of Germanium. *Solid. State. Electron.* **2013**, *89*, 146–152.
- (283) Pankove, J. I.; Aigrain, P. Optical Absorption of Arsenic-Doped Degenerate Germanium. *Phys. Rev.* **1962**, *126* (3), 956–962.
- (284) Bezuidenhout, M.; Liu, P.; Singh, S.; Kiely, M.; Ryan, K. M.; Kiely, P. A. Promoting Cell Proliferation Using Water Dispersible Germanium Nanowires. *PLoS One* **2014**, *9* (9), e108006.

# **Chapter 2**

## **Carbonaceous Germanium Nanowires and their Application as Highly-efficient Lithium- ion Battery Anodes**

Data from this chapter was submitted for publication in May 2021. Consequently, sections of the chapter such as the abstract and introduction may contain repeating concepts and paragraphs. I synthesised and performed the elemental and structural analysis of the nanowires reported in this chapter. I co-wrote the paper with SB and JDH and analysed Raman, TEM and electrochemical data obtained from collaborators.

Garcia-Gil, A.; Biswas, S.; McNulty, D.; Roy, A.; Raha, S.; Trabesinger, S.; Nicolosi, V.; Singha, A.; Holmes, J. D., 'Carbonaceous Germanium Nanowires and their Application as Highly-Efficient Lithium-ion Battery Anodes'. Submitted May 2021.



## 2.1. Abstract

Novel materials, new material designs, and simple scalable synthesis are essential for the quest for robust electrodes for lithium-ion (Li-ion) batteries with high specific capacity. Carbon-based nanocomposites could play a key role in integrating group IV semiconducting nanomaterials as efficient anodes into Li-ion batteries. Here we report a simple one-pot growth, resembling the solvothermal growth in supercritical solvent, of carbonaceous germanium (C-Ge) nanowires for use as the anode in Li-ion batteries. C-Ge nanowires were grown in supercritical toluene without any metal catalysts at reaction temperatures between 380-490 °C using diphenylgermane (DPG) as a commercially sourced Ge precursor. The self-seeded nanowires were highly crystalline with an average diameter between 11 to 19 nm, and with high aspect ratios of  $> 10^3$ . The Ge nanowires formed were coated in an amorphous carbonaceous layer, formed from the polymerization and condensation of light carbon compounds generated from the decomposition of DPG during the growth process. These carbonaceous Ge nanowires demonstrated impressive electrochemical performance as an anode material for Li-ion batteries with high specific charge values ( $> 1200 \text{ mA h g}^{-1}$  after 500 cycles) and exceptionally stable capacity retention, specific charges obtained after the 40<sup>th</sup> and 500<sup>th</sup> charges were 1376 and 1224  $\text{mA h g}^{-1}$ , respectively. The specific charge values obtained by the carbonaceous Ge nanowires are very high and greater than most of the specific charge values previously reported for other ‘binder free’ Ge nanowire anode materials. Analysis of differential charge curves revealed that the carbonaceous matrix surrounding the Ge nanowires actively contributes to the total charge storage. The high specific charge values and impressively stable capacity are due to the unique morphology and composition of the nanowires.

## 2.2. Introduction

Group IV materials, especially silicon (Si) and germanium (Ge), continue to gather attention as soon-to-be replacements for graphite as negative electrode materials in energy storage, especially lithium-ion batteries (LIBs), due to the limitations of the traditional carbonaceous electrode materials to meet growing demands.<sup>1,2</sup> Most commercial battery cells still rely on the use of graphite anodes despite their relatively low specific charge ( $372 \text{ mA h g}^{-1}$ )<sup>3</sup>. Group IV semiconductors, particularly Ge, could be a promising alternative to conventional graphite electrodes; especially in niche energy storage applications like small high-tech devices (such as solar cells<sup>4</sup> and nanoscale thermoelectric<sup>5</sup> or electric vehicles<sup>6</sup>); as Ge has a higher theoretical reversible specific charge ( $1600 \text{ mA h g}^{-1}$  for the alloy  $\text{Li}_{22}\text{Ge}_5$ )<sup>7</sup> than graphite. Even though Ge is not as Earth-abundant as Si, it presents several advantages over Si as anode material, such as improved performance at a high charge rate.<sup>8,9</sup> Additionally, Ge is an attractive option due to properties like a higher lithium ions diffusivity, which is about two orders of magnitude higher than that in Si,<sup>10,11</sup> and four orders of magnitude higher electrical conductivity than that of Si.<sup>12</sup>

However, it is generally considered that the main drawback of Li-ion battery anode for both, Si and Ge, is the significant volume expansion and contraction during battery cycling (during lithiation and delithiation), which leads to electrode pulverization after prolonged cycling times, and in turn, to severe capacity fading. This huge volume change (about 230 %)<sup>10</sup> along with the formation of a solid electrolyte interface (SEI) layer during the initial stages of battery cycling, caused by the side reactions on the surface of the electrode, are the main causes for the compromised performance of Ge-based anodes. Yet, the surface composition,

morphology, and composition of the active material is often neglected prior to electrode design, or complex and expensive synthesis steps are added to the overall process to achieve the desired surface morphology.

To overcome the problem of pulverization of Ge (or Si) electrodes and to enhance the cycling stability of Ge electrodes, nanostructuring and various other rational approaches have been reported. Shaping the anode material into nanowire offers a unique solution to the electrode pulverization problem. Nanowires can retain their structural integrity while transitioning from crystalline to amorphous phase during lithiation/delithiation. In addition, nanowires also provide a porous and tunnelled architecture with a high interfacial area in direct contact with the electrolyte, thus increasing the energy density in LIBs.<sup>13,14</sup> Hence, the manufacturing of group IV nanowires, including Ge, for use as anode materials in Li-ion batteries has been widely explored.<sup>15–17</sup> Other strategies to inhibit pulverization of Ge (or Si) materials during the charging/discharging cycles include porous anode materials,<sup>18</sup> alloyed Ge anodes,<sup>19</sup> doping approaches<sup>20</sup> and carbon-encapsulation of Ge nanostructures.<sup>21,22</sup> Designing Ge (or Si) anode materials by combining a carbon-based porous structure (amorphous carbon, graphene, reduced graphene oxide etc.) along with the crystalline nanostructures (i.e. carbonaceous nanostructures) is a possible alternative to graphite anodes for LIBs with high energy densities and long cycling lifetimes.<sup>21,23</sup>

The achievement of the full potential of the one-dimensional (1D) Ge or 1D carbonaceous germanium (C-Ge) nanocomposites in energy storage applications require developments towards simpler and scalable synthetic methods to produce a high yield of nanomaterials at low cost. Different bottom-up paradigms, such as

vapour-liquid-solid (VLS)<sup>24</sup>, vapour-solid-solid<sup>25</sup> and solution-liquid-solid<sup>26</sup> *etc.*, are typically preferred for the 1D growth of phase pure Ge nanostructures via the use of expensive metal or metalloid catalysts, *e.g.* Au, Ag, AuAg *etc.*<sup>27</sup> Nanowire growth using metal seeds is not only more expensive but also can lead to impurity incorporation from the metallic seeds into the nanowire structure, which influences the mechanical and electrical properties of the material, and potentially the capacity of Li-ion cells.<sup>28</sup> On the other hand, the self-seeded growth of Ge nanowires to date has typically involved the use of high-boiling point organic solvents, high reaction temperatures such as 650 - 1000 °C<sup>29</sup> and Ge precursors<sup>30,31</sup>. Additionally, carbon (or carbonaceous compounds) embedding of Ge (or Si) nanostructures, to integrate both elements into a single electrode material, involves ex-situ encapsulation methods<sup>8,32,33</sup> requiring multiple steps and might be difficult to scale up. Numerous efforts involving additional surface chemistry, post-growth calcination, carbon nanotubes, graphite templates and metal nanoparticles as catalysts have been adopted to create ideal group IV based carbon-nanowire nanocomposite materials for use as advanced electrodes in LIBs.<sup>32,34,35</sup>

Here we report a simple yet cutting-edge method to synthesize self-seeded C-Ge nanowires in a batch reaction process. The simple single-step batch synthesis method does not involve any additional catalysts (metal or metalloid) and templates and utilizes a supercritical toluene atmosphere for the nanowire growth and encapsulation with the carbon-based matrix. To the best of our knowledge, this work represents the first solution-phase synthesis of Ge or C-Ge nanowires in a low boiling point solvent (below precursor's decomposition temperature, 280-340 °C)<sup>24,36</sup>, such as toluene, using a commercially-available precursor. The structural and chemical

characteristics of the nanowires were thoroughly analysed for their implementation as anodes in Li-ion batteries. The electrochemical performance of the C-Ge nanowires was evaluated via long-term galvanostatic cycling. The C-Ge nanowires exhibit impressive electrochemical performance in terms of specific charge and capacity retention, demonstrating a reversible capacity of  $> 1200 \text{ mA h g}^{-1}$  after the 500 cycles, close to the theoretical capacity of Ge. Through systematic analysis of differential charge plots (DCPs) from galvanostatic data, we have also presented a detailed insight into how C-Ge nanowire anodes store charge and proposed a hypothesis on why our C-Ge nanowires outperform previously reported Ge nanowire anodes.

### 2.3. Experimental

**Nanowire Synthesis.** Anhydrous toluene 99.8% was purchased from Sigma-Aldrich Co and diphenylgermane (DPG) 95 % was purchased from Fluorochem. These were stored and used under inert conditions ( $\text{O}_2 < 0.1 \text{ ppm}$ ,  $\text{H}_2\text{O} < 0.5 \text{ ppm}$ ) inside a nitrogen-filled glovebox.

Ge-nanowire synthesis was carried out in a single stainless steel reaction cell (5 ml). Prior to synthesis, the reaction cell and connectors were dried under vacuum at  $125^\circ\text{C}$  for 12 h. Reactions were performed at temperatures between  $380$  to  $490^\circ\text{C}$  on Si (100) substrates (native oxide present) of  $0.5 \times 1.5 \text{ cm}$  dimension. The reaction temperature was monitored by a thermocouple connected to the reaction vessel and the pressure was monitored via a pressure gauge, connected to one end of the reaction cell. In general, DPG/toluene (3 ml) was added to the reaction cell (5 ml) and the cell was heated to the desired temperature in a tube furnace for 15 - 150 min. The DPG

concentration was varied between 40 and 120 mM. The filling volume of the reactant solution; *i.e.* filling fraction, was 20, 40, 60 and 80 % of the total reactor's volume (5 ml). The reaction cell was cooled to room temperature after the reaction and disassembled to access the growth substrate. Growth substrates were washed with dry toluene and dried under N<sub>2</sub> flow for further characterisation. For electrochemical testing, the synthesis procedure was repeated with Ti foil instead of Si wafers as substrates, with 40 mM of DPG at an optimal growth temperature of 440 °C.

***Structural and chemical characterisation.*** Samples were imaged using an FEI Quanta FEG 650 scanning electron microscope (SEM) operated at 15 kV. High-Resolution Transmission Electron Microscopy (HRTEM) and High-Resolution Scanning Transmission Electron Microscopy (HRSTEM) imaging were performed on a JEOL 2100 electron microscope operated at 200 kV and an FEI Titan electron microscope, operating at 300 kV. High-angle annular-dark-field scanning-transmission-electron-microscopy (HAADF-STEM) was performed on the FEI Titan electron microscope operated at 300 kV. X-ray Photoelectron Spectroscopy (XPS) spectra were acquired on an Oxford Applied Research Escabase XPS system, equipped with a CLASS VM 100-mm-mean-radius hemispherical electron-energy-analyser with a five-channel detector arrangement in an analysis chamber with a base pressure of  $10 \times 10^{-10}$  mbar. Raman scattering analysis was performed using a Lab RAM HR (Jobin Yvon) spectrometer equipped with a 488 nm laser source and a charge-coupled device (CCD) detector. The laser was focused on the sample using a 100X objective. The laser power was maintained at 0.18 mW throughout the measurement and the data acquisition time was 50 s. Raman scattering analysis was performed on the nanowires using low power (0.18 mW); to avoid laser-induced

heating which can cause structural changes in the nanowires and a red-shift in the Ge-Ge phonon vibration. The Raman spectra for the nanowires was recorded over a wavenumber range between 100 - 2000  $\text{cm}^{-1}$ . The crystal structure of the product was confirmed by X-ray diffraction (XRD) using a Philips X'pert Pro MPD, equipped with a Panalytical Empyrean Cu X-ray tube and a Philips X'celerator detector. Gas chromatography-mass spectroscopy (GC-MS) was performed on an Agilent 6890N GC equipped with a 5973 inert Mass Selective Detector (Agilent Technologies, Waldbronn, Germany). A capillary column HP-5MS [(5%-phenyl)-methylpolysiloxane] Agilent J & W GC column, 30 m, 0.25 mm i.d., coating thickness 0.25  $\mu\text{m}$  was used to separate sample products. Each sample was placed on an auto-sampler (Agilent) and injected at a volume of 1  $\mu\text{L}$  into the GC-MS (Agilent) and the split ratio was 1:10. The GC/MS method consisted of a front inlet temperature of 280  $^{\circ}\text{C}$ , MS transfer line temperature of 280  $^{\circ}\text{C}$ , and the ion source temperature was 230  $^{\circ}\text{C}$ , and the ionization voltage 70 eV. The solvent delay was 4 min. The flow rate of helium through the column was kept at 1.0  $\text{mL min}^{-1}$ . The scan range of the MSD was set from 30  $m/z$  to 350  $m/z$ . MSD Chemstation software (Agilent) (version D.01.02.16) was used to determine the identity of the unknown compounds found within the samples. The individual peaks were identified by comparing their fragmentation pattern with those found in the mass spectral database. Fourier-transform infrared spectroscopy (FTIR) spectra were recorded on an infrared spectrometer (IR 660, Varian) in the range of 400 to 4000  $\text{cm}^{-1}$ .

***Electrochemical testing.*** The electrochemical properties of C-Ge nanowires were investigated in a half-cell configuration against a metallic Li counter electrode (diameter: 13 mm, thickness: 750  $\mu\text{m}$ , Alfa Aesar) in a two-electrode, stainless steel

coin-type cell. The cell was filled with the electrolyte (200  $\mu$ l), consisting of a 1 M solution of lithium hexafluorophosphate salt ( $\text{LiPF}_6$ ) in a 1:1 (v/v) mixture of ethylene carbonate and dimethyl carbonate with 3 wt.% vinylene carbonate as an SEI-forming additive. A Celgard 2400 (diameter: 17 mm, thickness: 25  $\mu$ m) was used as a separator in all electrochemical tests. The samples were tested as-synthesised without further cleaning process, including the surface bonded moieties. The mass loading for all C-Ge nanowire samples was  $\sim 0.1 \text{ mg cm}^{-2}$ . A Mettler Toledo XP2U ultra microbalance was used to determine the mass of C-Ge nanowire material on the Ti foil substrates. No conductive additives or binders were added to the electrodes. Galvanostatic cycling was performed using an Arbin Battery Tester at 0.2 C (1 C = 1384  $\text{mA g}^{-1}$ ) in a potential window of 1.5 - 0.01 V (vs  $\text{Li/Li}^+$ ).

## 2.4. Results and Discussion

***Growth and morphology of the Ge nanowires.*** C-Ge nanowire growth was achieved under a solvothermal-like one-pot growth with supercritical toluene as a solvent without the use of any catalyst or template. Supercritical-fluid reaction conditions were obtained at moderate temperatures without the need for external pressurization of the reaction vessel. The supercritical atmosphere provides ideal conditions for fast precursor decomposition and polymer formation, which is crucial for the self-seeded growth of the carbon-coated Ge nanowires.

Figure 2.1a and 2.1b show representative low and high-magnification SEM images of Ge nanowires grown on a Si (100) substrate at a reaction temperature of 440  $^{\circ}\text{C}$  from a 60 mM solution of DPG in toluene. The low-magnification image clearly shows the formation of a three-dimension porous structure from the interweaving



nanowires, which are several micrometres long, consisting of bundles of individual nanowires. The SEM image in Figure 2.1b, and a higher magnification image shown in the inset, show a core/shell-like feature of the nanowires where brightly contrasted nanowire fibres (bundle consisting of several nanowires) are confined in a dark contrasted matrix material (pointed out in the inset of Figure 2.1b). This dark contrasted matrix can be seen covering all the nanowires in the sample. This contrast difference may arise due to the different electron conductivity of the crystalline core (Ge) and the surrounding amorphous carbonaceous matrix. SEM analysis also confirmed the presence of negligible amounts of spherical aggregates in samples grown at reaction temperatures of 440 °C. Additionally, no spherical (or hemispherical) growth seeds were detected at the tips of the nanowires, which is typically observed with the catalytic bottom-up nanowire growth.

Significantly, the growth of Ge nanowires was also achieved at a very low growth temperature of 380 °C (see Figure A2.1 in Appendix 2.6). SEM analysis showed that nanowires were formed over a range of reaction temperatures and precursor concentrations (see Figure A2.1 in Appendix 2.6). Yields obtained range from 0.18 to 8.74  $\mu\text{g mm}^{-2}$ , depending on the growth temperature and precursor concentration. Synthesis revealed the presence of nanowires in both silicon substrate and the internal walls of the reaction cell, which is consistent with the homogeneous distribution associated with the supercritical fluid atmosphere generated inside the reactor. Considering the dimensions of the reaction cell and the surface of the substrate, the yield varies between ~ 50 % (8.74  $\mu\text{g mm}^{-2}$ ) and ~ 1 % (0.18  $\mu\text{g mm}^{-2}$ ). The presence of carbonaceous structures has been considered in yield calculations and will be further discussed in detail in this section. These values are consistent with the

literature, where have been reported the synthesis of high-yield germanium nanowire with values up to 30 %, <sup>37,38</sup> 40 %<sup>39</sup> and 50 %<sup>26</sup>. A significant amount of spherical nanoparticle aggregates were observed for the samples synthesized at a higher reaction temperature of 490 °C, due to the homogeneous nucleation and aggregation of Ge growth species (see Figure A2.1 in Appendix 2.6). The presence of these spherical aggregates was negligible at lower growth temperatures (380 - 440 °C), most likely due to the slow decomposition rate of DPG at these temperatures.

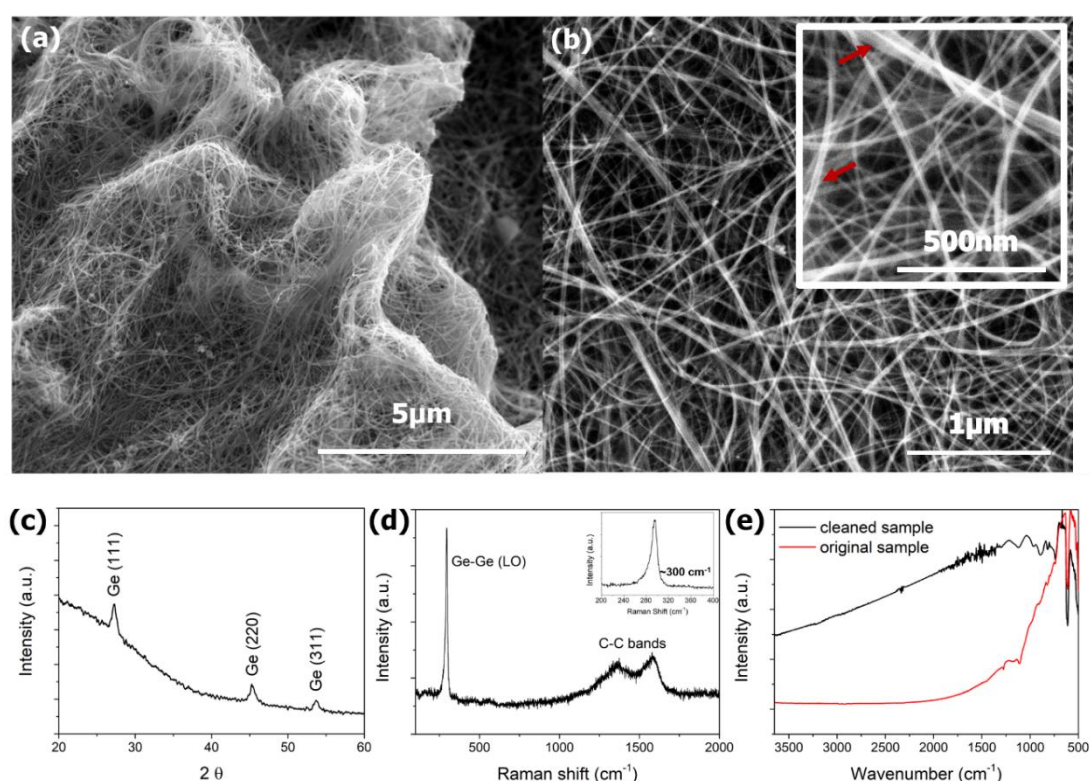


**Figure 2.1.** (a, b) SEM micrographs of Ge nanowires grown from a 60 mM DPG/toluene solution at a temperature of 440 °C. A high-magnification SEM image in the inset of (b) highlights the appearance of a core-shell like morphology in the nanowires (shown by red arrows). (c) XRD pattern of a nanowire sample showing a diamond cubic structure of Ge crystals. (d) Raman spectrum of C-Ge nanowires displaying two vibrational regions, attributed to Ge-Ge LO ( $\sim 300 \text{ cm}^{-1}$  peak) and C-C ( $\sim 1100 - 1800 \text{ cm}^{-1}$ ) modes. Inset of (d) depicts a detail view of the Ge-Ge LO area. (e) FT-IR spectra of the as-grown C-Ge nanowires (red) and the cleaned (with no carbonaceous matrix) Ge nanowires (black) deposited on a Si substrate.

***Structural analysis of Ge nanowires.*** XRD was used to characterize the phase and crystallinity of the nanowires. Figure 2.1c shows a diffraction pattern from a nanowire sample grown from a 60 mM DPG/toluene solution at a reaction temperature of 380 °C and confirms the formation of crystalline Ge. Reflections at 27.4°, 45.4° and 53.8° can be assigned to the (111), (220) and (311) crystallographic planes of the diamond cubic crystal structure of elemental Ge (JCPDS, reference pattern 04-0545), after subtracting the reflection peaks from the Si substrate. All of the nanowire samples grown had the diamond cubic structure of Ge. No crystallinity was associated with the carbon-based matrix. The presence of the carbon-based coating is further verified through TEM analysis, XPS and Raman spectroscopy.

***Chemical & Structural analysis of Ge nanowires and carbon-based matrix.*** Raman Spectroscopy was used for the qualitative assessment of the Ge nanowires, the carbonaceous matrix and their interaction. Raman vibrations in two well-separated regions were observed and attributed to Ge-Ge longitudinal optical (LO) vibration ( $\sim 300 \text{ cm}^{-1}$  peak) and C-C (between 1100 to 1800  $\text{cm}^{-1}$ ) modes (representative Raman spectra is shown in Figure 2.1d). The Raman peak near 300  $\text{cm}^{-1}$  was fitted using Lorentzian functions. The sharp Ge-Ge LO peak at 294  $\text{cm}^{-1}$  was red-shifted compared to the characteristic value for bulk Ge,<sup>27</sup> which could be attributed to a combination of effects, such as phonon confinement, due to the narrow diameter of the nanowires (mean diameter  $\sim 13 \text{ nm}$ )<sup>40</sup> and strain caused by the carbon-based matrix.<sup>41</sup> The observation of C-C Raman modes between 1100 and 1800  $\text{cm}^{-1}$  can be assigned to the characteristic feature of the carbon-based coating around the Ge nanowires.<sup>42,43</sup> A graphitic (G band) at  $\sim 1576 \text{ cm}^{-1}$  is associated with the vibrational

mode  $E_{2g}$  in graphite-like structures and a disordered band (D band) at  $\sim 1356\text{ cm}^{-1}$  can be assigned to disorder-allowed phonon modes.<sup>44</sup>

The chemical and structural characteristics of the darkly contrasted nanowire matrix, as depicted in the SEM image (see Figure 2.1b), and its interaction with the Ge nanowires were analysed by FTIR spectroscopy and XPS. The representative FTIR spectra from the nanowires showed absorption bands at  $\sim 568$ ,  $\sim 610$  and  $\sim 737\text{ cm}^{-1}$  (see Figure 2.1e). These bands have previously been assigned to the stretching modes of C-Ge-C<sup>45</sup>, Ge-C<sup>46</sup> bonds and wagging mode of Ge-H<sub>3</sub><sup>47</sup>, respectively. The FTIR peak at  $\sim 890\text{ cm}^{-1}$  is related to Ge-CH<sub>3</sub> rocking vibrations.<sup>45,48</sup> These data confirm the formation of a carbonaceous structure around the crystalline nanowires due to the presence of peaks at  $\sim 963$  and  $\sim 815\text{ cm}^{-1}$ , corresponding to C=C, as well as  $\sim 890\text{ cm}^{-1}$  which is associated with the presence of CH<sub>3</sub> structure. XPS analysis was performed (see Figure A2.2 in Appendix 2.6) on representative nanowire samples grown at different reaction temperatures (380 and 440 °C) and with a DPG concentration of 60 mM, to study the oxide formation upon exposure of the samples to air. Germanium oxide formation was found due to air exposure of the samples, when stored in ambient atmosphere after a month (8.4 % of GeO and 2.4 % of GeO<sub>2</sub>) and a year (8.3 % of GeO and 17.4 % of GeO<sub>2</sub>). No strong interaction (covalent bonding) between carbon and nanowires surface was found in the C1s spectrum. However, C-C, C=C, C-O and CO<sub>3</sub> bonds were found in the C1s spectrum. The carbonaceous matrix is most likely porous since it does not act as a passivation layer to protect the Ge nanowires from long-term oxidation. Furthermore, the binary phase diagram of C and Ge shows that the formation of solid solutions of C-Ge is not likely at our growth temperature,<sup>49</sup> implying that any carbon formed around the Ge

nanowires is preferably bound by physisorption. Both XPS and FT-IR analysis confirm the presence of carbonaceous materials in the samples and the interaction of the carbon as a physically adsorbed matrix on the surface of the Ge nanowires.

***Structural and crystal quality analysis of nanowires and carbonaceous matrix.*** To determine the structural quality of the Ge nanowires and the characteristics of the carbon-based shell, C-Ge nanowires were investigated by high-resolution TEM (see Figure 2.2). Figure 2.2 shows representative TEM images for nanowires grown at a reaction temperature of 440 °C; nanowires grown at all growth temperatures displayed similar structural quality. Figure 2.2a and 2.2b show bright-field TEM images of the nanowires. A low-contrast coating on the nanowires is visible in these TEM images. This thick (~ 8 - 10 nm) coating is likely to be an amorphous carbonaceous shell. The carbon content detected in the samples (5 to 10 wt.% of samples content) arises from surface bonded moieties and the nanowires shell, and it was estimated from carbonaceous areas present in TEM images (see Figure 2.2a and 2.2b) and subsequently converted to mass. Such low-contrast carbon-based coatings are present in two different kinds of disposition: (i) as free aggregates between the nanowires (see Figure 2.2a), and (ii) as an uneven coating along the nanowire length (see Figure 2.2b). Ge nanowires grown at 440 °C were found to have a mean diameter of 12.2 ( $\pm$  3.0) nm. The mean diameter of the nanowires was found to vary with reaction temperature (see Figure A2.3 in Appendix 2.6), *i.e.* 11.3 ( $\pm$  2.2) nm at 380 °C and 19.7 ( $\pm$ 4.3) nm at 490 °C. Assuming that nanowire growth is self-seeded, higher reaction temperatures provoke a faster precursor decomposition, leading to the nucleation and agglomeration of larger Ge seed nanoparticles, resulting in the growth of larger diameter nanowires. Most of the nanowires observed had length > 4  $\mu$ m,

with very few individual nanowires displaying bending or kinking. Tapered nanowires were also not observed under any growth conditions investigated.

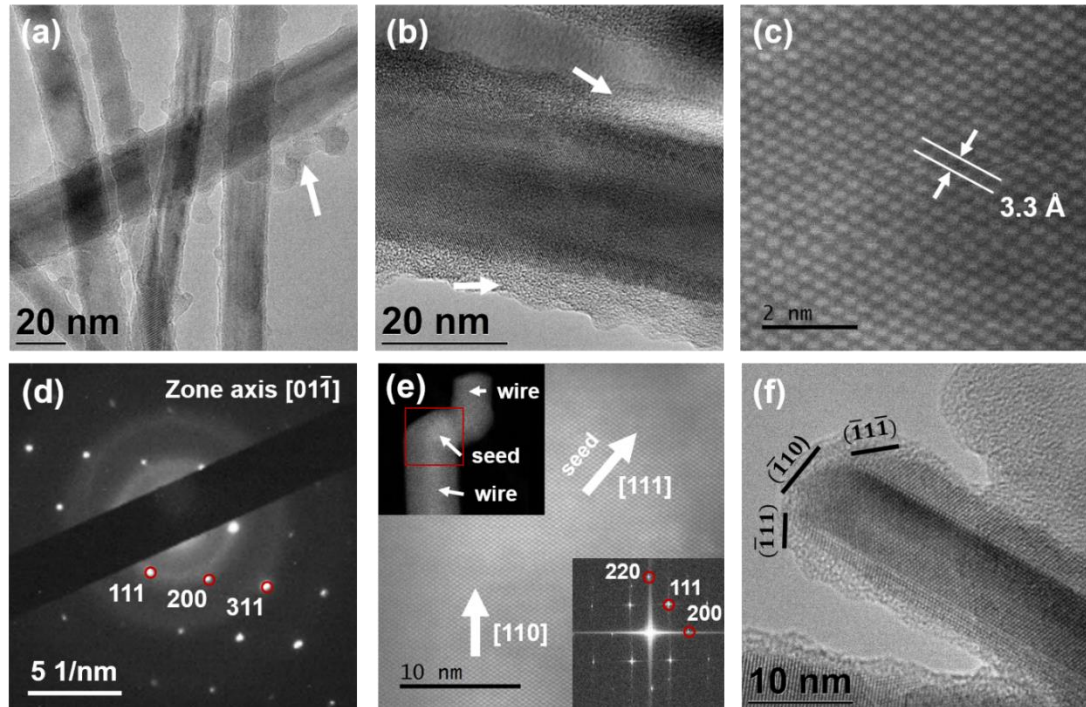


**Figure 2.2.** TEM images of C–Ge nanowires show (a) the discrete deposition of the amorphous C-based layer on the Ge nanowires, and (b) a continuous deposition of the amorphous shell. Some carbon-matrix areas are highlighted with white arrows. (c, d) Lattice-resolved HRTEM image and corresponding SAED pattern of a representative Ge nanowire (diamond cubic crystal structure). (e) HRSTEM image of a Ge seed and nanowire interface with a  $[110]$  growth direction. The red box on the STEM image in the top-left inset represents the magnified area of the main image. Bottom-right inset shows a Fast Fourier Transform (FFT) of the full image. TEM image in (f) shows the faceted termination of a Ge nanowire.

To determine the crystal quality of the nanowires, their morphologies were investigated by HRTEM, HAADF-STEM and selected area electron diffraction (SAED) (see Figure 2.2c-f). HRTEM and HAADF-STEM of Ge nanowires (see Figure 2.2c and 2.2d), revealed their highly crystalline nature. Although localised

defects could be missed, no crystal defects such as longitudinal stacking faults and twinning were found. Defect-free materials allow for long life cycles and are imperative for their use as Li-ion anode materials.<sup>50</sup> HAADF-STEM from the core of the crystalline Ge nanowires revealed an interplanar spacing ( $d$ ) of 0.33 nm (see Figure 2.2c), which is marginally larger than the  $d$  value for bulk diamond Ge crystals of 0.326 nm (JCPDS 04–0545), corresponding to (111) planes of Ge diamond cubic crystal structure. SAED pattern (see Figure 2.2d) corresponds to cubic germanium and the spot pattern indicates that the Ge nanowires are single-crystalline. SAED showed a pseudohexagonal symmetry and the reflections can be assigned to the high-order Laue zone diffraction of {111}, {311} and {200} planes in group IV diamond cubic crystals.

Nanowire growth direction and the seed-nanowire interface were further examined by HRSTEM (see Figure 2.2e). A low-magnification image of a Ge nanowire with a growth seed can be seen in the inset of Figure 2.2e (top-left). A high-magnification image recorded with  $\langle \bar{1}10 \rangle$  zone axis alignment, from the same nanowire, shows seamless growth of the nanowire from the seed. Notably, many of the nanowires analysed displayed an onset of growth in two different directions, from a common nanoparticle seed. However, only one of the growth directions prevailed, increasing to microns in length, while the other end terminated within few nanometres (top-left inset of Figure 2.2e). This can be explained by the initial steps of the nanowire formation mechanism, where the nanoparticles are capped by *in situ* formed polymers which prevent the Ge nanoparticle aggregation. At the same time, the outer area of the nanoparticles interacts more efficiently with the precursor available and thus, the growth in that direction is favoured. A more detailed analysis of the growth

mechanism is given in the following section. The presence of the nanoparticle at the tip of the nanowire points towards a seeded bottom-up mechanism for the onset of the NWs growth.

Nanowires grow along the  $\langle 110 \rangle$  direction (also confirmed from Fast Fourier Transform -FFT- in the inset of Figure 2.2e), as expected for metal-seeded nanowires of this diameter range.<sup>51,52</sup> The crystal structure in both the “seed” and the nanowire segments correspond to the diamond cubic crystal of Ge. No crystallographically different interface was observed between the “seed” and the nanowire segments. However, different crystallographic orientations between the “seed” and the nanowires are also present, as shown in Figure 2.2e, where  $\{111\}$  stacking along the growth orientation is observed in the “seed” segment and the planes in the nanowires are stacked along  $\{110\}$  equivalent directions. The apparent continuity of the similar lattice from the seed to the nanowire confirms the self-seeded; *i.e.* seeded from *in situ* grown Ge nanoparticles; formation of the nanowires. Most of the nanowires were found to exhibit distinctive faceting (see Figure 2.2f), with no defined nanoparticle at any of the ends. This behaviour was previously observed by Lieber *et al.*,<sup>53</sup> where they described preferred  $\langle 110 \rangle$  growth direction in small diameter Si nanowires with a “V-shaped” termination between Au seeds and the wire. The tapered structure consisted of two  $\{111\}$  facets at  $55^\circ$  relative to the  $[110]$  direction, which related to the surface energy of the crystal facets.<sup>54</sup> Faceting is a mechanism which takes place in the initial nanoparticle to adapt to the rounded shape of the nanoscale seed, and thus it translates through the lengths of the nanowire as a faceted structure.<sup>53</sup>



**Growth mechanism of Ge Nanowires.** The growth of the self-seeded nanowires can be explained by a three-phase (source-seed-nanowire) bottom-up growth mechanism. Spontaneous *in situ* formation of Ge seeds and their participation in the nanowire growth is evident from the presence of Ge nanoparticles at the tip of the nanowire (see Figure 2.2e). Although classical round-shape nanoparticles were barely found at the tips, single-crystal faceted structures were always present. The presence of a third-party catalyst seed, such as Au, often acts to enhance precursor decomposition.<sup>26</sup> However, in self-catalytic growth processes, the temperature and the pressure are the factors associated with the initial decomposition of the Ge precursor. Schematic diagrams and TEM images (see Figure 2.3 and Figure A2.4 in Appendix 2.6) outline the different stages of nanowire formation via the supercritical batch synthesis. During “Stage I” of the growth, the Ge precursor (DPG) decomposes to form Ge adatoms, liberating very reactive phenyl groups.<sup>26</sup> GC-MS analysis (see Figure A2.5a in Appendix 2.6) of the reactant solution revealed the by-products of the reaction as diphenylmethane and derivatives (e.g. 2,3'-dimethyl-1,1'-biphenyl, bybenzyl or 1-methyl(4-phenylmethyl)benzene) along with toluene (and derivatives), and tetraphenylgermane. Under supercritical conditions, the phenyl-based long-chain molecules (e.g. diphenylmethane and derivatives) start polymerizing and precipitate over the available surfaces (sample substrate and reactor's walls). tetraphenylgermane, which is associated with the decomposition of the DPG precursor by phenyl redistribution, as previously reported.<sup>26</sup>

The available Ge adatoms aggregate and dissolve into these polymers to form the Ge nanoparticle seeds, capped by the polymers (Stage II of the growth, Figure 2.3 and Figure A2.4a in Appendix 2.6). The *in situ* formed polymeric templates prevent the

Ge nanoparticles from large-scale aggregation and Ostwald ripening and thus the formation of larger spherical particles. Eventually, the Ge nanoparticles exposed at the outer surface of the polymer, act as a nucleating seed for the growth of Ge nanowires (Stage III, Figure 2.3 and Figure A2.4b in Appendix 2.6). Self-seeded growth of Ge nanowires has been previously proposed<sup>24,31</sup> in a “pseudo” VLS like growth with the formation of a liquid organic spherical seed in high-boiling-point solvents. These models account for nanoparticle coalescence at the initial stage of nanowire growth, followed by Ostwald ripening in later growth phases.<sup>31</sup> In our case, the initial formation of Ge nanoparticles in the polymer template (see Figure A2.4a in Appendix 2.6) and the presence of these nanoparticles with symmetric crystal lattices at the tips of the nanowires (see Figure 2.2e and Figure A2.4b in Appendix 2.6), suggests the participation of nanoparticle seed in the growth of single-crystal Ge nanowires. Under our growth conditions, Ge nanoparticles with diameters between ~ 11 and ~ 20 nm should remain in a solid state during the nanowire growth process, due to the negligible bulk Ge melting point (~ 938 °C) depression due to the nanoscale effect at these dimensions.<sup>55</sup> Participation of a solid-state seed is further confirmed by the well-faceted shape of the tip of the nanowires (see Figure 2.2f). The polymeric materials present in the reaction chamber can further precipitate onto the sidewalls of the nanowires to create a carbonaceous coating around the nanowires (see Figure 2.2a and 2.2b). The possibility of nanowire growth in solution, without any substrate, is rejected due to the insignificant quantity of nanowires found in the residual liquid in the reactor after the reaction. Precursor concentration was also not found to play a key role in the quality of the nanowires grown.

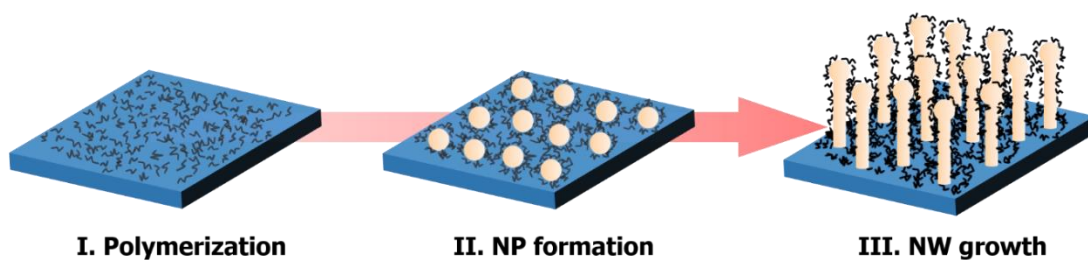


**Figure 2.3.** Illustration of the proposed ‘self-seeded’ nanowire growth mechanism. Stage I corresponds to precursor decomposition and polymerization of the liberated phenyl groups. Stage II consists of aggregation and nanoparticle formation from the available Ge adatoms. Eventually, Stage III represent nucleation and growth of C-Ge nanowires from the outer disposed Ge nanoparticle seeds.

The reaction temperature and loading volume were the two main variables to influence nanowire growth. The autogenic pressure reached in the reaction system depended on the loading volume of the solvent. Temperature and pressure were *in situ* recorded during reactions and the data collected every 5 minutes were further analysed. Both growth constraints were used to calculate the density of the supercritical phase in the reaction cells during the nanowire growth process at each specific reaction time (see Figure A2.5b and A2.5c in Appendix 2.6). A minimum reaction temperature of 350 °C and a volume fraction of 60 % were required to grow Ge nanowires in our set-up; with significant nanowire growth achieved at 380 °C ( $0.35 \mu\text{m mm}^{-2}$ ). At a reaction temperature of 350 °C, toluene was only in a supercritical state (critical temperature ( $T_c$ ) = 293.75 °C and critical pressure ( $P_c$ ) = 598.47 psi, for pure toluene) for only 20 min (see Figure A2.5b and A2.5c in Appendix 2.6). A 60 % filling of the volume fraction with toluene was also found to be ideal for obtaining homogenous nanowires with uniform diameters (see Figures A2.1 and A2.3 in Appendix 2.6). No nanowire growth was achieved with 20 % filling

volume of the reaction cell with toluene. Thus, it can be concluded that the nanowire growth was only successful when a supercritical phase in the toluene solvent was achieved for a considerable time (see Figure A2.3 in Appendix 2.6).

***Electrochemical analysis of C-Ge nanowires.*** To evaluate the electrochemical performance, C-Ge nanowires were grown directly onto Ti foil current collectors. Nanowire growth on the Ti-foil was achieved with 40 mM of DPG, 60 % of loading volume of solvent and at an optimal growth temperature of 440 °C (SEM image in Figure A2.6 in Appendix 2.6). Nanowires directly grown on current collecting substrates do not require initial processing steps, such as decorating the substrate with metal nanoparticle seeds and the use of a binder or conductive additive. Additionally, Ti is very inert (unlike Cu foil) as a catalyst for Ge the self-seeded Ge nanowire growth at our growth temperatures, thus keeping the morphological and structural quality of the nanowires similar to that grown on Si substrates (see Figure A2.6 in Appendix 2.6).

C-Ge nanowires were cycled galvanostatically for 500 cycles at a rate of 0.2 C, in a voltage range of 1.50 to 0.01 V (vs Li/Li<sup>+</sup>). A selection of the resulting voltage profiles from the 1<sup>st</sup> to the 500<sup>th</sup> cycle is shown in Figure 2.4a, 2.4b and 2.4c. There was an initial rapid decrease from the open-circuit voltage of ~ 3.14 V down to ~ 0.4 V, during the 1<sup>st</sup> charge. This sharp voltage decrease may be associated with several processes, including the initial formation of an SEI layer, the irreversible decomposition of the electrolyte on the surface of the electrode material and the lithiation of crystalline Ge.<sup>56</sup>

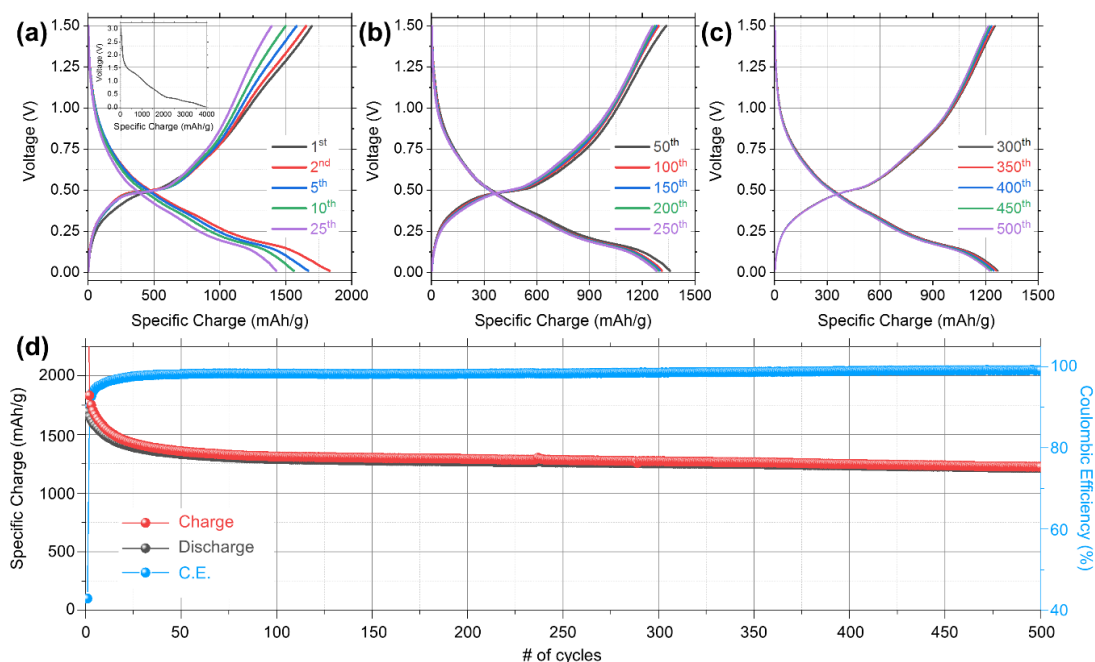


**Figure 2.4.** Voltage profiles for (a) the 1<sup>st</sup>, 2<sup>nd</sup>, 5<sup>th</sup>, 10<sup>th</sup> and 25<sup>th</sup> cycles, (b) the 50<sup>th</sup>, 100<sup>th</sup>, 150<sup>th</sup>, 200<sup>th</sup> and 250<sup>th</sup> cycles and (c) the 300<sup>th</sup>, 350<sup>th</sup>, 400<sup>th</sup>, 450<sup>th</sup> and 500<sup>th</sup> cycles for C-Ge nanowires at 0.2 C in a potential window of 1.50 - 0.01 V (vs Li/Li<sup>+</sup>). (d) Comparison of the specific charge values and Coulombic efficiency obtained for C-Ge nanowires over 500 cycles.

Three reduction plateau can be seen during the initial charge from  $\sim 0.35$  to  $0.25$  V,  $0.25$  to  $0.15$  V and from  $0.15$  to  $0.01$  V, which are attributed to the step-by-step lithiation of the Ge nanowires, leading to the formation of the  $c\text{-Li}_{15}\text{Ge}_4$  phase.<sup>57</sup> The oxidation plateau centred at  $\sim 0.49$  V during the first discharge is due to the delithiation of the Ge nanowires, and this plateau remains consistently at this potential for the remainder of the 500 cycles.<sup>58</sup> The initial charge and discharge specific charge values were  $\sim 3947$  and  $1692 \text{ mA h g}^{-1}$ , respectively, corresponding to an initial Coulombic efficiency (ICE) of 42.9 %. The large initial charge capacity is likely due to the formation of an SEI layer on the surface of the nanowires as well as the initial lithiation of C-Ge.<sup>59</sup> The ICE value obtained for our C-Ge nanowires is comparable to previously reported values for other Ge nanowire anodes.<sup>60,61</sup> Low

ICE is a common issue for alloying mode anode materials such as Ge and Si however, there are some reports which indicate that prelithiation of the anode material can improve the ICE. For example, Si-Carbon nanotubes anodes were prelithiated via mechanical pressing of stabilized lithium metal powder onto the working electrode, leading to an increase in ICE values.<sup>62</sup> Furthermore, the amorphous carbon coating may be contributing to the low ICE. The additional surface area provided by the carbon coating may contribute to the high inefficiency of the first cycle. Additional treatment of the C-Ge nanowires, such as heating to higher temperatures, may result in a more graphitized carbon, which could increase the efficiency of the first few cycles. Three sloping reduction plateau were observed from the second charge onwards from  $\sim 0.70$  to  $0.45$  V,  $0.45$  to  $0.3$  V and from  $0.3$  to  $0.01$  V, which are associated formation of a series of Li-Ge alloys ( $a\text{-Li}_x\text{Ge} \rightarrow a\text{-Li}_{15}\text{Ge}_4 \rightarrow c\text{-Li}_{15}\text{Ge}_4$ ).<sup>63</sup> The presence of this reduction plateau in the charge curves from the 2<sup>nd</sup> to the 500<sup>th</sup> cycle, as well as the consistency of the oxidation plateau, indicates that the formation of the various Li-Ge alloys is a highly reversible process.

The specific charge values obtained for C-Ge nanowires cycled at  $0.2$  C over 500 cycles and their related Coulombic efficiency (CE) values are shown in Figure 2.4d. It is clear that large specific charge values and excellent capacity retention can be obtained for C-Ge nanowires grown directly on Ti foil. The specific charge after the 2<sup>nd</sup> charge was  $\sim 1831$  mA h g<sup>-1</sup> and it decreases to  $1376$  mA h g<sup>-1</sup> after the 40<sup>th</sup> cycle. The CE from the 40<sup>th</sup> cycle onwards is  $> 98\%$  and continued above this value for the remainder of the 500 cycles (see Figure 2.4d). This level of CE stability is notable for Ge nanowires directly grown on a current collecting substrate with the absence of binders and conductive additives.

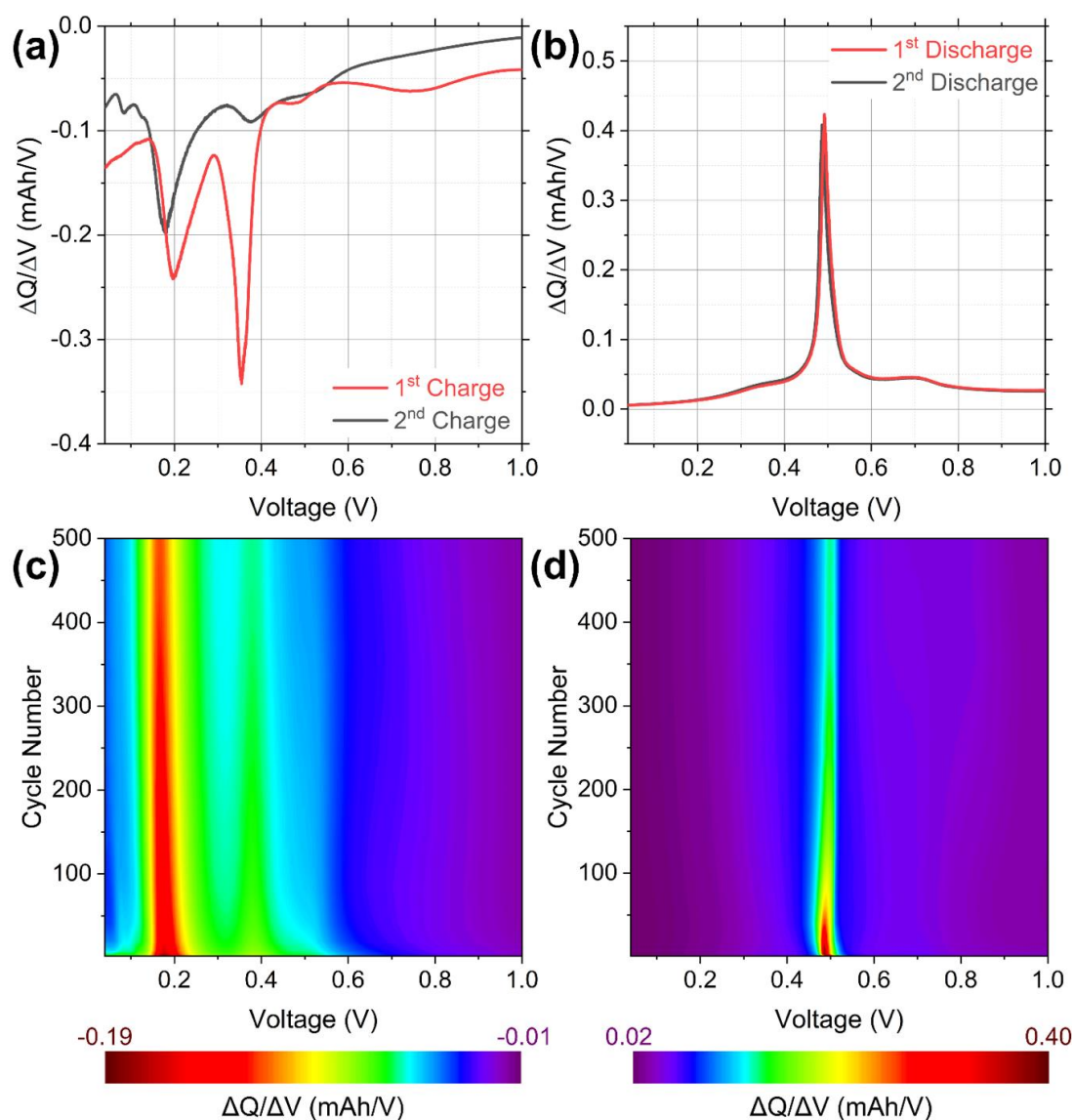


**Figure 2.5.** (a) Differential capacity curves calculated from the 1<sup>st</sup> and 2<sup>nd</sup> galvanostatic charges at 0.2 C. (b) Differential capacity contour plot calculated from differential charge curves from the 2<sup>nd</sup> to the 500<sup>th</sup> charge. (c) Differential capacity curves calculated from the 1<sup>st</sup> and 2<sup>nd</sup> galvanostatic discharges at 0.2 C. (d) Differential capacity contour plot calculated from differential discharge curves from the 2<sup>nd</sup> to the 500<sup>th</sup> discharge.

The specific charge retention from the 40<sup>th</sup> charge, once the CE stabilized above 98 %, to the 500<sup>th</sup> charge was ~ 89 %. This is an impressive level of specific charge retention over long term cycling. The mean capacity decay from the 2<sup>nd</sup> to the 500<sup>th</sup>

cycle was  $\sim 1.2 \text{ mA h g}^{-1}$  per cycle, which is a further indicator of the noteworthy stable cycling observed for the Ge nanowires.

Differential capacity plots (DCPs) were calculated from galvanostatic charge and discharge curves to investigate the charge storage mechanism of the C-Ge nanowires in more detail. The DCP from the first charge curve consisted of a series of reduction peaks as shown in Figure 2.5a. The weak band at  $\sim 0.76 \text{ V}$  may be associated with the formation of an SEI layer as it is only observed during the first cycle.<sup>23,64</sup> The strong, sharp peak at  $\sim 0.35 \text{ V}$  is associated with the initial lithiation of crystalline Ge and the intensity of this peak decreases significantly after the first charge. This indicates that the nanowires likely do not return to a fully delithiated, crystalline Ge phase after the initial lithiation of the nanowires. A similar decrease of this reduction peak after the first cycle has previously been reported for other Ge nanowire anodes.<sup>23,27</sup> The wide asymmetric reduction peak at  $\sim 0.20 \text{ V}$  is associated with the formation of a-Li<sub>15</sub>Ge<sub>4</sub> and c-Li<sub>15</sub>Ge<sub>4</sub> phases.<sup>65</sup> From the second charge onwards reduction peaks were observed at  $\sim 0.53, 0.38$  and  $0.18 \text{ V}$ , corresponding to the formation of a-Li<sub>x</sub>Ge, a-Li<sub>15</sub>Ge<sub>4</sub> and c-Li<sub>15</sub>Ge<sub>4</sub> phases, respectively.<sup>56,63</sup> The strong oxidation peak observed in the DCP of the first discharge, centred at  $\sim 0.49 \text{ V}$ , corresponds to the overlapping delithiation of the c-Li<sub>15</sub>Ge<sub>4</sub> and a-Li<sub>15</sub>Ge<sub>4</sub> phases.<sup>11,66</sup> There was no significant shifting of this peak in the DCP from the 2<sup>nd</sup> discharge. Differential capacity contour plots, calculated from charge and discharge voltage profiles, ranging from the 2<sup>nd</sup> to the 500<sup>th</sup> cycles are shown in Figure 2.5c and 2.5d. The two high-intensity regions observed in Figure 2.5c are associated with the reduction peaks for the formation of the a-Li<sub>15</sub>Ge<sub>4</sub> and c-Li<sub>15</sub>Ge<sub>4</sub> phases, which are centred at  $\sim 0.38$  and  $0.18 \text{ V}$ , respectively. The formation of these alloys is a highly



reversible process, as the potential of these reduction peaks remains consistent throughout the 500 cycles. Likewise, the oxidation peak at  $\sim 0.49$  V remains stable over 500 cycles as shown in Figure 2.5d. The consistency of these reduction and oxidation peaks may give rise to the stable capacity retention observed in Figure 2.4d.

The specific charge values obtained for our C-Ge nanowire anodes are higher or comparable to the previously reported results for Ge nanowire and C-Ge nanowire-based anodes as presented in Table A2.1 (Ge nanowire-based anodes) and Table A2.2 (C-Ge nanowire-based anodes) in Appendix 2.6. The C-Ge nanowire-based anode fabricated in this work shows the longest cycling stability up to 500 cycles together with the highest reversible capacity displayed at a 0.2 C cycling rate. Amorphous carbon coating in Ge nanowires can positively influence specific capacity and capacity retentivity. Amorphous carbon coating in Ge nanowires can drastically enhance the reaction kinetics during cycles by promoting electron transport, increasing electrical contact points, as well as providing more paths for charge carrier transfer, as demonstrated for C-Si nanowires by Liu et al.<sup>67</sup> They have also demonstrated a fast charging process and structural integrity of nanowires for amorphous carbon-coated nanowires compared to nanowire without any coating.

Ge nanowires and C-Ge nanowires for Li-ion battery applications are typically grown on substrates (directly on metal or on a semiconducting substrate) via chemical vapour deposition through the use of catalytic seed and/or with high boiling point solvents in a reflux set-up.<sup>25,68</sup> Our nanowires did not require any external seeding or the use of sophisticated precursors, solvents and set-up, and can be directly grown on metal Ti substrates. Some commonly used metal seeds, such as Au, form

irreversible alloys with Li during cycling and result in lower capacity values due to electrochemically inactive seeds.<sup>69</sup> Furthermore, it is worth noting that the impressive large specific charges and stable capacity retention of the C-Ge nanowires were achieved in the absence of any binders or conductive additives. The state-of-the-art electrochemical performance with a very high specific charge for the nanowires demonstrates their potential as advanced anode material for Li-ion batteries.

## 2.5. Conclusions

In summary, an alternative and simple synthetic method for the growth of Li-ion battery relevant C-Ge composite nanowires has been developed. This single-pot synthetic method does not require the use of any external metal catalysts, engineered precursors or templating agents. *In situ* polymerization of a simple germanium precursor at moderate growth temperatures in a supercritical batch setup leads to the growth of highly functional C-Ge nanocomposite anode material for Li-ion batteries. The Ge nanowire growth protocol postulated here could potentially be implemented for other carbonaceous nanomaterials such as Si, SiGe, *etc.* via *in situ* polymerization of the reaction by-products in a supercritical atmosphere. The C-Ge nanowires demonstrated exceptional performance as Li-ion battery anodes, capable of delivering impressively high specific charge values of  $> 1200 \text{ mA h g}^{-1}$  after 500 cycles at 0.2 C, with very low capacity decay. To our knowledge, the demonstrated electrochemical results represent some of the best electrochemical performances ever reported for Ge nanowires, therefore demonstrating the advantages of direct nanowire growth within a carbon-based matrix.

## 2.6. Appendix

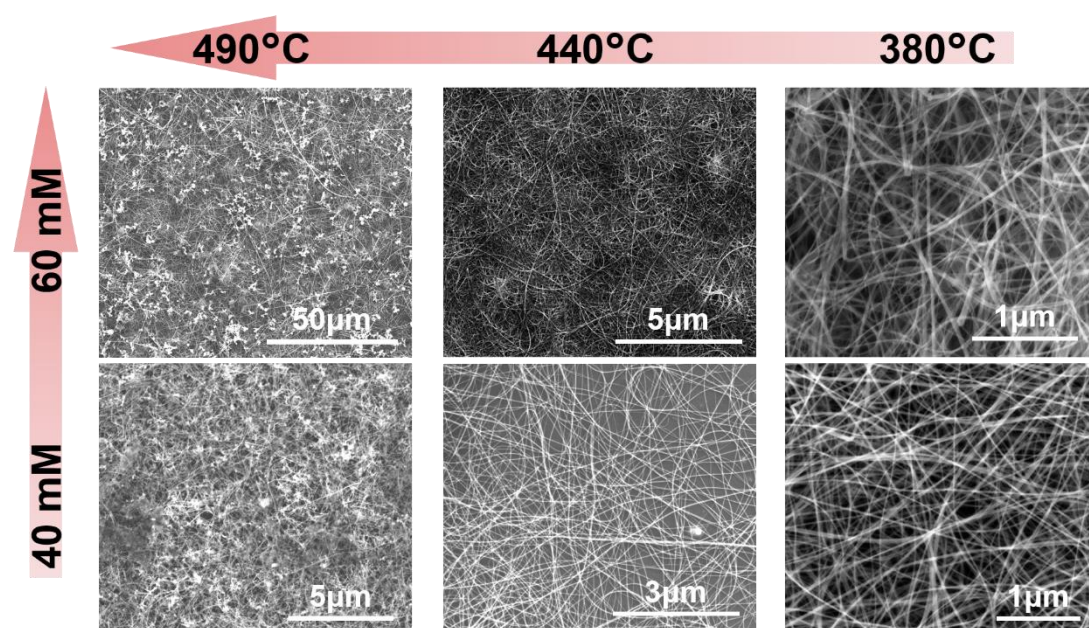


**Figure A2.1.** Representative SEM images of nanowires obtained at different temperatures and DPG concentrations.

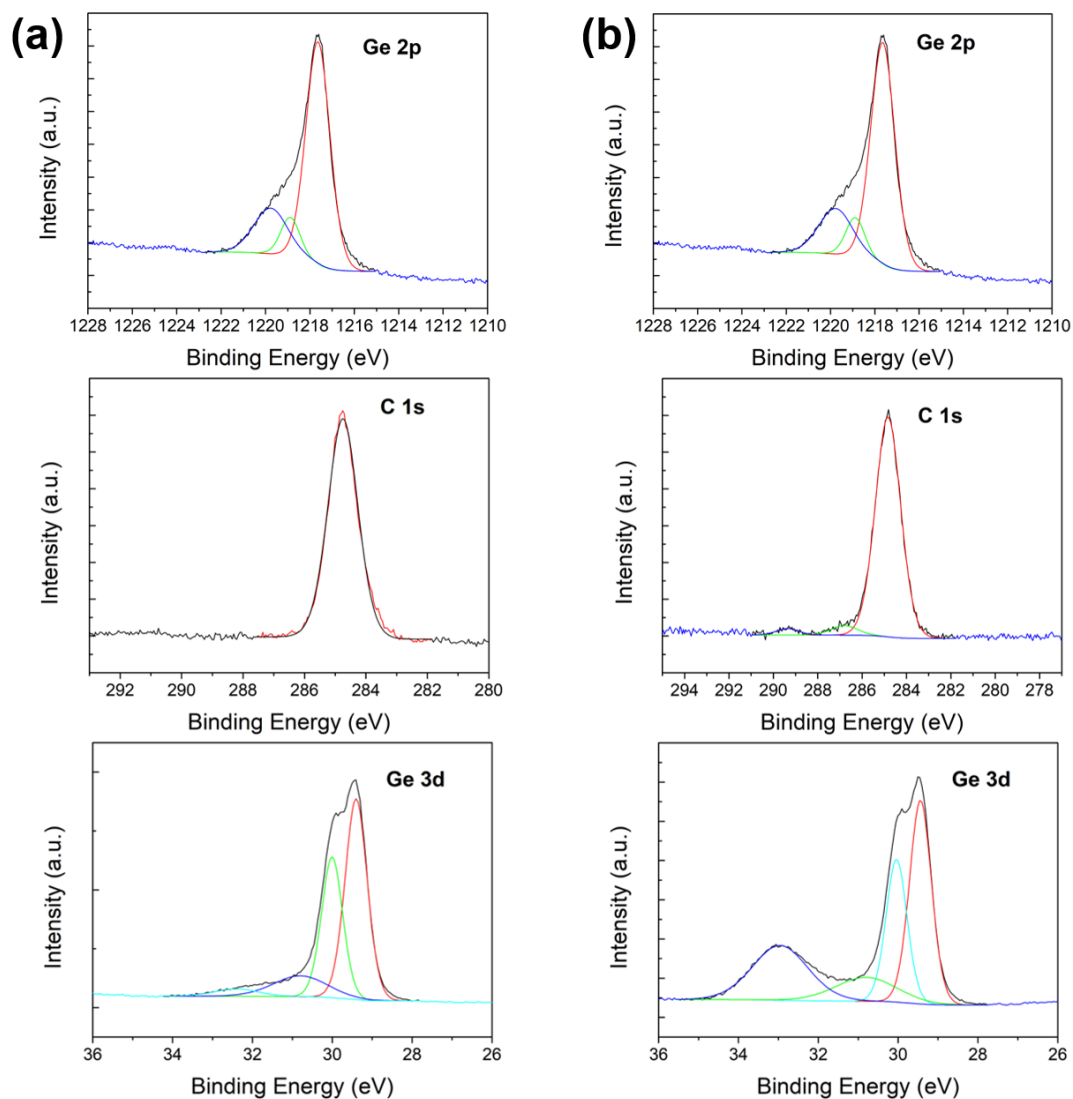


**Figure A2.2.** XPS spectra of Ge 3d, Ge 2p and C 1s sections from an (a) 60 mM solution at 380 °C, and (b) 60 mM solution at 440 °C.

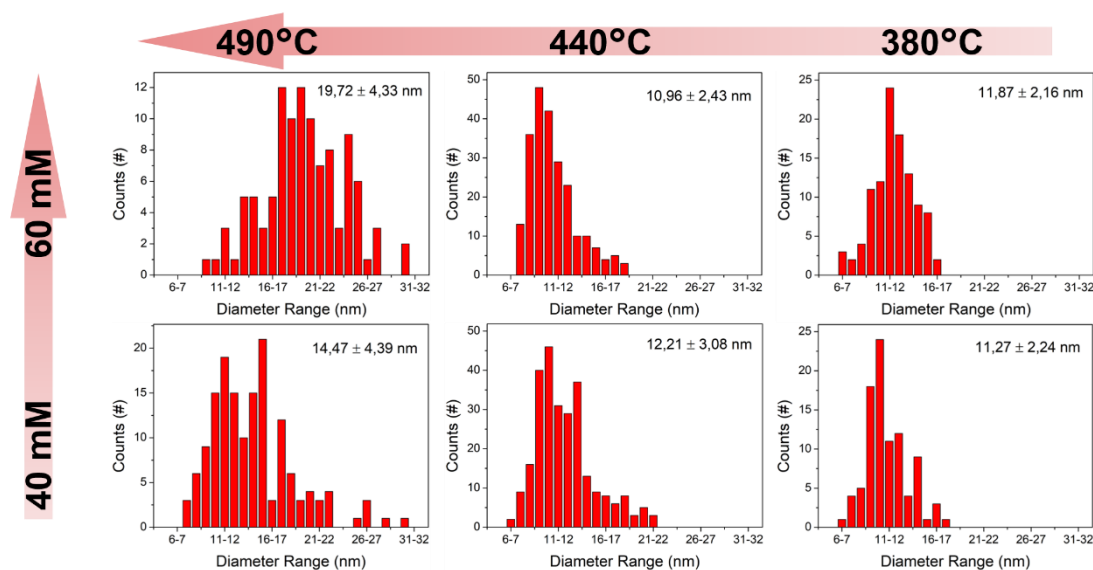


**Figure A2.3.** Diameter distribution of nanowires obtained at different temperatures and with different DPG concentrations. The average is noted along with its standard deviation.

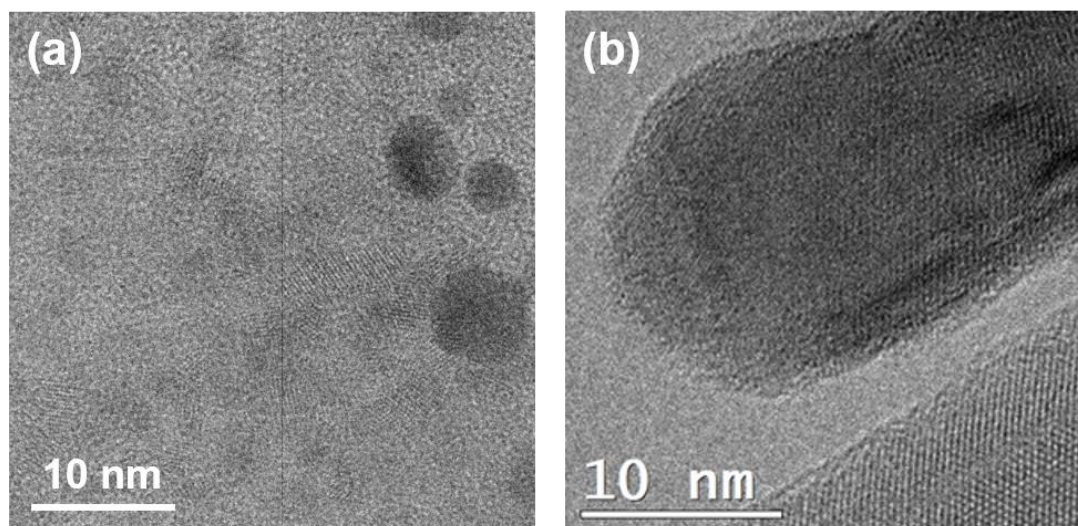


**Figure A2.4.** a) A TEM image of initial nanoparticle formation which acts as a nanowire seed. Sample obtained with a reaction at a temperature of 440 °C and a 20 % loading volume of the reactor. (b) TEM image of a regular seed at the tip of a carbonaceous Ge nanowire.

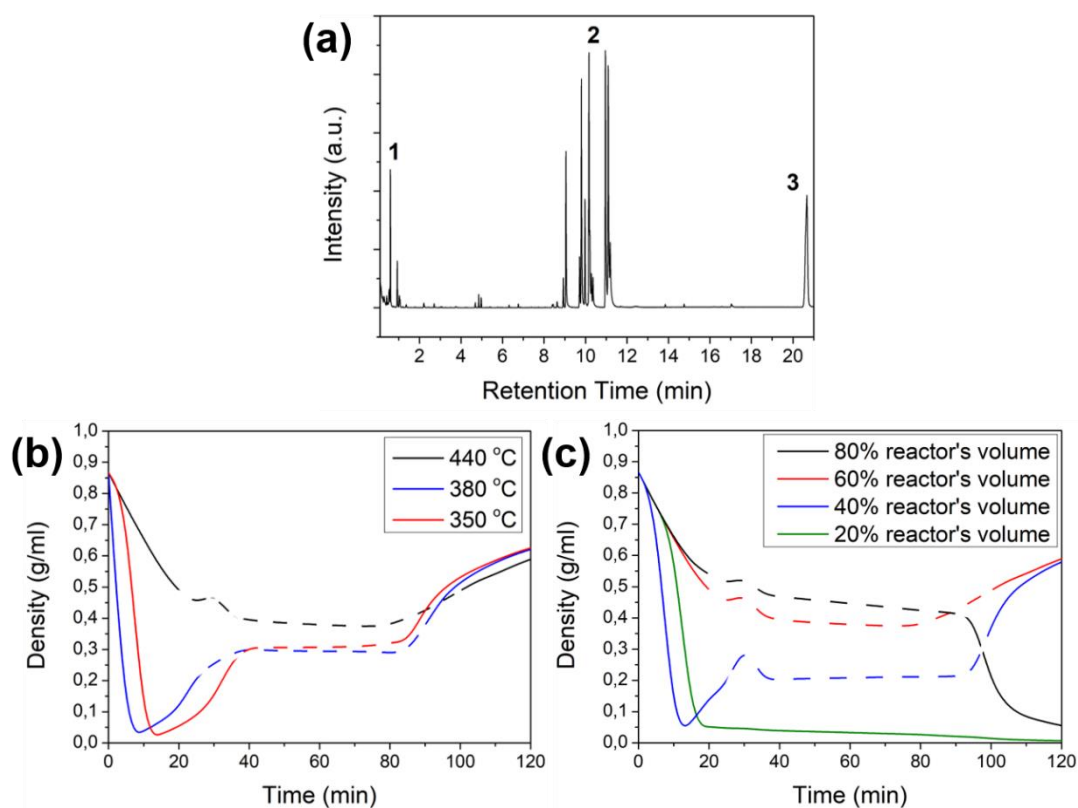


**Figure A2.5.** (a) Gas-chromatography spectra from the analysis of the residual liquid present in the reactor after the reaction. The spectrum presents three zones such as (1) Toluene-like structures and derivatives (*i.e.* ethylcyclohexane, ethylbenzene and *o*-xylene), (2) diphenylmethane and derivatives (*i.e.* 2,3'-dimethyl-1,1'-biphenyl, biphenyl or 1-methyl(4-phenylmethyl)benzene) and (3) tetraphenylgermane (QPG). (b) and (c) display calculated densities<sup>70</sup> of the solvent from pressure and temperatures measurement. Dashed areas indicate a supercritical state. (a) Density of the toluene at different temperatures with 60 % reactor's volume loading. (b) Density of the toluene with different volume loading into the reactor at 440 °C. All the measurements are independent of the Ge precursor concentration.

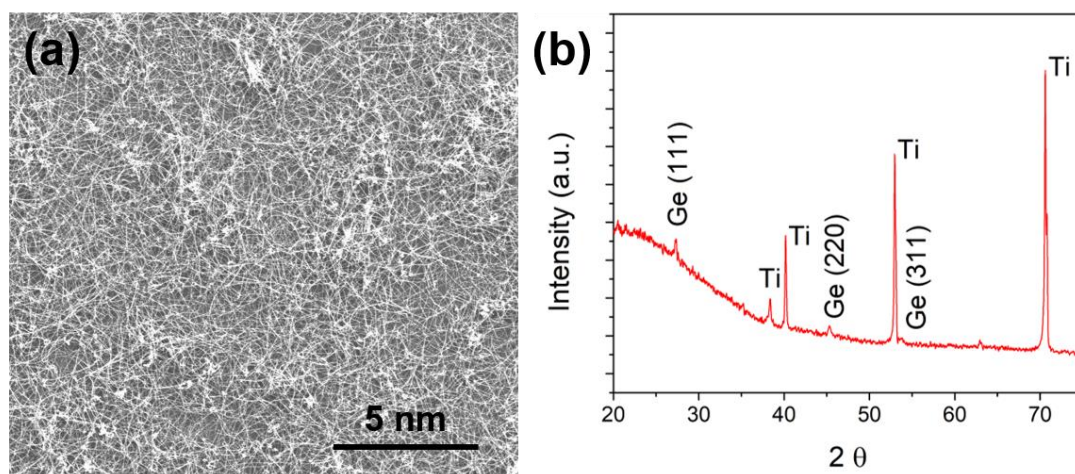


**Figure A2.6.** (a) SEM micrograph of C-Ge NWs grown over Ti substrate at 440 °C from 40 mM. (b) XRD pattern of a nanowire sample showing a diamond cubic structure of Ge crystals over a Ti substrate.



Table A2.1. Cycling performance of Ge nanostructures previously reported as anode electrodes.

<b>Ge nanowires and nanotubes</b>	<b>Preparation method</b>	<b>Electrochemical performance</b>	<b>Cycles tested</b>	<b>Electrode preparation</b>	<b>Ref.</b>
<b>Ge NWs and branched nanowires</b>	SLS and VLS	1072 mA h g <sup>-1</sup> at 0.5 C	50 cycles	As-synthesised (Stainless Steel)	71
<b>Ge nanowire cluster arrays</b>	Electrodeposition	~ 875 mA h g <sup>-1</sup> at 0.2 C	100 cycles	As-synthesised (Ni)	72
<b>Ge/inorganic nanowire bilayer mesh</b>	supercritical-fluid liquid solid growth	1092 mA h g <sup>-1</sup> at 0.1 C	100 cycles	Conductive mixture	73
<b>Ge nanowires</b>	Vapour-liquid-solid method	~ 1000 mA h g <sup>-1</sup> at 0.5 C	100 cycles	As-synthesised (Stainless Steel)	65
<b>Ge nanowires</b>	CVD	1408 mA h g <sup>-1</sup> at 0.1 C	100 cycles	As-synthesised (Stainless Steel)	74
<b>Ge nanowires</b>	Thermolytic decomposition	~ 1150 mA h g <sup>-1</sup> at 1 C	100 cycles	As-synthesised (Stainless Steel)	23
<b>Ge nanowires</b>	Electrodeposition	~ 1200 mA h g <sup>-1</sup> at 0.1 C	200 cycles	As-synthesised (Ni)	75
<b>Ge nanotube arrays</b>	Ionic liquid electrodeposition	~1000 mA h g <sup>-1</sup> at 0.2 C	250 cycles	As-synthesised (Cu)	76
<b>Nanoporous Ge nanofibers</b>	CVD	~1000 mA h g <sup>-1</sup> at 2 C	300 cycles	Conductive mixture	77

Table A2.2. Cycling performance of carbonaceous Ge nanostructures previously reported as anode electrodes.

<b>Carbonaceous Ge nanowires and nanotubes</b>	<b>Preparation method</b>	<b>Electrochemical performance</b>	<b>Cycles tested</b>	<b>Carbon content</b>	<b>Electrode preparation</b>	<b>Ref.</b>
<b>Graphene on a-Ge nanowires</b>	CVD	1210 mA h g <sup>-1</sup> at 0.5 C	200 cycles	≤ 4 graphene layers	Conductive mixture	22
<b>Alkanethiol-passivated Ge nanowires</b>	Dodecanethiol monolayer passivation	1130 mA h g <sup>-1</sup> at 0.1 C	100 cycles	~ 3 wt. %	Conductive mixture	78
<b>Ge/C nanowires</b>	Pyrolysis Ge/ethylenediamine nanowires	1200 mA h g <sup>-1</sup> at 0.2 C	50 cycles	~ 4 wt. %	Conductive mixture	79
<b>Ge@C nanocables</b>	Physical vapour deposition	1086 mA h g <sup>-1</sup> at 0.5 C	200 cycles	10 wt. %	Conductive mixture	80
<b>Ge nanowires on graphite nanofibers</b>	CVD	~ 1200 mA h g <sup>-1</sup> at 0.1 C	30 cycles	~ 18 wt. %	Conductive mixture	81
<b>Ge nanowires with carbon nanofibers coating</b>	Vapour-liquid-solid method	~ 1520 mA h g <sup>-1</sup> at 0.1 C	100 cycles	50 wt. %	As-synthesised	82
<b>Ge nanowire-in-Graphite Tubes</b>	CVD	1241 mA h g <sup>-1</sup> at 0.45 C	100 cycles	Undetermined	Conductive mixture	83

## 2.7. References

- (1) McNulty, D.; Lonergan, A.; O'Hanlon, S.; O'Dwyer, C. 3D Open-Worked Inverse Opal TiO<sub>2</sub> and GeO<sub>2</sub> Materials for Long Life, High Capacity Li-Ion Battery Anodes. *Solid State Ionics* **2018**, *314*, 195–203.
- (2) McNulty, D.; Noel Buckley, D.; O'Dwyer, C. NaV<sub>2</sub>O<sub>5</sub> from Sodium Ion-Exchanged Vanadium Oxide Nanotubes and Its Efficient Reversible Lithiation as a Li-Ion Anode Material. *ACS Appl. Energy Mater.* **2019**, *2* (1), 822–832.
- (3) Chu, S.; Majumdar, A. Opportunities and Challenges for a Sustainable Energy Future. *Nature* **2012**, *488* (7411), 294.
- (4) Yun, J. H.; Park, Y. C.; Kim, J.; Lee, H. J.; Anderson, W. A.; Park, J. Solution-Processed Germanium Nanowire-Positioned Schottky Solar Cells. *Nanoscale Res. Lett.* **2011**, *6* (1), 1–5.
- (5) Li, J.; Chen, Z.; Zhang, X.; Sun, Y.; Yang, J.; Pei, Y. Electronic Origin of the High Thermoelectric Performance of GeTe among the P-Type Group IV Monotellurides. *NPG Asia Mater.* **2017**, *9* (3), e353–e353.
- (6) Park, S. H.; King, P. J.; Tian, R.; Boland, C. S.; Coelho, J.; Zhang, C. (John); McBean, P.; McEvoy, N.; Kremer, M. P.; Daly, D.; Coleman, J. N.; Nicolosi, V. High Areal Capacity Battery Electrodes Enabled by Segregated Nanotube Networks. *Nat. Energy* **2019**, *4* (July), 560–567.
- (7) Chae, O. B.; Park, S.; Ku, J. H.; Ryu, J. H.; Oh, S. M. Nano-Scale Uniform Distribution of Ge/Cu<sub>3</sub>Ge Phase and Its Electrochemical Performance for Lithium-Ion Batteries. *Electrochim. Acta* **2010**, *55* (8), 2894–2900.
- (8) Xiao, X.; Li, X.; Zheng, S.; Shao, J.; Xue, H.; Pang, H. Nanostructured Germanium Anode Materials for Advanced Rechargeable Batteries. *Adv. Mater. Interfaces* **2017**, *4* (6), 1600798.
- (9) Park, C. M.; Kim, J. H.; Kim, H.; Sohn, H. J. Li-Alloy Based Anode Materials for Li Secondary Batteries. *Chem. Soc. Rev.* **2010**, *39* (8), 3115.
- (10) Graetz, J.; Ahn, C. C.; Yazami, R.; Fultz, B. Nanocrystalline and Thin Film Germanium Electrodes with High Lithium Capacity and High Rate Capabilities. *J. Electrochem. Soc.* **2004**, *151* (5), A698.
- (11) Yoon, S.; Park, C. M.; Sohn, H. J. Electrochemical Characterizations of Germanium and Carbon-Coated Germanium Composite Anode for Lithium-Ion Batteries. *Electrochem. Solid-State Lett.* **2008**, *11* (4), 42–45.

- (12) Wang, D.; Chang, Y.-L.; Wang, Q.; Cao, J.; Farmer, D. B.; Gordon, R. G.; Dai, H. Surface Chemistry and Electrical Properties of Germanium Nanowires. *J. Am. Chem. Soc.* **2004**, *126* (37), 11602–11611.
- (13) Liu, Y.; Vishniakou, S.; Yoo, J.; Dayeh, S. A. Engineering Heteromaterials to Control Lithium Ion Transport Pathways. *Sci. Rep.* **2015**, *5* (1), 18482.
- (14) Aghazadeh Meshgi, M.; Biswas, S.; McNulty, D.; O'Dwyer, C.; Alessio Verni, G.; O'Connell, J.; Davitt, F.; Letofsky-Papst, I.; Poelt, P.; Holmes, J. D.; Marschner, C. Rapid, Low-Temperature Synthesis of Germanium Nanowires from Oligosilylgermane Precursors. *Chem. Mater.* **2017**, *29* (10), 4351–4360.
- (15) McNulty, D.; Biswas, S.; Garvey, S.; O'Dwyer, C.; Holmes, J. D. Directly Grown Germanium Nanowires from Stainless Steel: High-Performing Anodes for Li-Ion Batteries. *ACS Appl. Energy Mater.* **2020**, *3* (12), 11811–11819.
- (16) Kennedy, T.; Brandon, M.; Ryan, K. M. Advances in the Application of Silicon and Germanium Nanowires for High-Performance Lithium-Ion Batteries. *Adv. Mater.* **2016**, *28*, 5696–5704.
- (17) Yang, Y.; Yuan, W.; Kang, W.; Ye, Y.; Pan, Q.; Zhang, X.; Ke, Y.; Wang, C.; Qiu, Z.; Tang, Y. A Review on Silicon Nanowire-Based Anodes for next-Generation High-Performance Lithium-Ion Batteries from a Material-Based Perspective. *Sustainable Energy and Fuels*. Royal Society of Chemistry April 1, 2020, pp 1577–1594.
- (18) Yu, Y.; Yan, C.; Gu, L.; Lang, X.; Tang, K.; Zhang, L.; Hou, Y.; Wang, Z.; Chen, M. W.; Schmidt, O. G.; Maier, J. Three-Dimensional (3D) Bicontinuous Au/Amorphous-Ge Thin Films as Fast and High-Capacity Anodes for Lithium-Ion Batteries. *Adv. Energy Mater.* **2013**, *3* (3), 281–285.
- (19) Doherty, J.; McNulty, D.; Biswas, S.; Moore, K.; Conroy, M.; Bangert, U.; O'Dwyer, C.; Holmes, J. D. Germanium Tin Alloy Nanowires as Anode Materials for High Performance Li-Ion Batteries. *Nanotechnology* **2020**, *31* (16), 165402.
- (20) Klavetter, K. C.; Pedro De Souza, J.; Heller, A.; Mullins, C. B. High Tap Density Microparticles of Selenium-Doped Germanium as a High Efficiency, Stable Cycling Lithium-Ion Battery Anode Material. *J. Mater. Chem. A* **2015**, *3* (11), 5829–5834.
- (21) Seng, K. H.; Park, M. H.; Guo, Z. P.; Liu, H. K.; Cho, J. Self-Assembled Germanium/Carbon Nanostructures as High-Power Anode Material for the

- Lithium-Ion Battery. *Angew. Chemie - Int. Ed.* **2012**, *51* (23), 5657–5661.
- (22) Kim, H.; Son, Y.; Park, C.; Cho, J.; Choi, H. C. Catalyst-Free Direct Growth of a Single to a Few Layers of Graphene on a Germanium Nanowire for the Anode Material of a Lithium Battery. *Angew. Chemie - Int. Ed.* **2013**, *52* (23), 5997–6001.
  - (23) Mullane, E.; Kennedy, T.; Geaney, H.; Ryan, K. M. A Rapid, Solvent-Free Protocol for the Synthesis of Germanium Nanowire Lithium-Ion Anodes with a Long Cycle Life and High Rate Capability. *ACS Appl. Mater. Interfaces* **2014**, *6* (21), 18800–18807.
  - (24) Zaitseva, N.; Harper, J.; Gerion, D.; Saw, C. Unseeded Growth of Germanium Nanowires by Vapor-Liquid-Solid Mechanism. *Appl. Phys. Lett.* **2005**, *86* (5), 1–3.
  - (25) Kang, K.; Kim, D. A.; Lee, H.; Kim, C.; Yang, J.; Jo, M. Low-Temperature Deterministic Growth of Ge Nanowires Using Cu Solid Catalysts. *Adv. Mater.* **2008**, *20* (24), 4684–4690.
  - (26) Chockla, A. M.; Korgel, B. A. Seeded Germanium Nanowire Synthesis in Solution. *J. Mater. Chem.* **2009**, *19* (7), 996–1001.
  - (27) Biswas, S.; Doherty, J.; Majumdar, D.; Ghoshal, T.; Rahme, K.; Conroy, M.; Singha, A.; Morris, M. A.; Holmes, J. D. Diameter-Controlled Germanium Nanowires with Lamellar Twinning and Polytypes. *Chem. Mater.* **2015**, *27* (9), 3408–3416.
  - (28) Allen, J. E.; Hemesath, E. R.; Perea, D. E.; Lensch-Falk, J. L.; Li, Z. Y.; Yin, F.; Gass, M. H.; Wang, P.; Bleloch, A. L.; Palmer, R. E.; Lauhon, L. J. High-Resolution Detection of Au Catalyst Atoms in Si Nanowires. *Nat. Nanotechnol.* **2008**, *3* (3), 168–173.
  - (29) Bootsma, G. A.; Gassen, H. J. A Quantitative Study on the Growth of Silicon Whiskers from Silane and Germanium Whiskers from Germane. *J. Cryst. Growth* **1971**, *10* (3), 223–234.
  - (30) Ge, M.; Liu, J. F.; Wu, H.; Yao, C.; Zeng, Y.; Fu, Z. D.; Zhang, S. L.; Jiang, J. Z. Synthesis of Germanium Nanowires. *J. Phys. Chem. C* **2007**, *111* (30), 11157–11160.
  - (31) Lotty, O.; Hobbs, R.; O'Regan, C.; Hlina, J.; Marschner, C.; O'Dwyer, C.; Petkov, N.; Holmes, J. D. Self-Seeded Growth of Germanium Nanowires: Coalescence and Ostwald Ripening. *Chem. Mater.* **2013**, *25* (2), 215–222.

- (32) Mo, R.; Lei, Z.; Rooney, D.; Sun, K. Three-Dimensional Double-Walled Ultrathin Graphite Tube Conductive Scaffold with Encapsulated Germanium Nanoparticles as a High-Areal-Capacity and Cycle-Stable Anode for Lithium-Ion Batteries. *ACS Nano* **2019**, *13*, 50.
- (33) Tan, L. P.; Lu, Z.; Tan, H. T.; Zhu, J.; Rui, X.; Yan, Q.; Hng, H. H. Germanium Nanowires-Based Carbon Composite as Anodes for Lithium-Ion Batteries. *J. Power Sources* **2012**, *206*, 253–258.
- (34) Pandres, E. P.; Olson, J. Z.; Schlenker, C. W.; Holmberg, V. C. Germanium Nanowire Battery Electrodes with Engineered Surface-Binder Interactions Exhibit Improved Cycle Life and High Energy Density without Fluorinated Additives. *ACS Appl. Energy Mater.* **2019**, *2* (9), 6200–6208.
- (35) Qiang, T.; Fang, J.; Song, Y.; Ma, Q.; Ye, M.; Fang, Z.; Geng, B. Ge@C Core-Shell Nanostructures for Improved Anode Rate Performance in Lithium-Ion Batteries. *RSC Adv.* **2015**, *5* (22), 17070–17075.
- (36) Zaitseva, N.; Dai, Z. R.; Grant, C. D.; Harper, J.; Saw, C. Germanium Nanocrystals Synthesized in High-Boiling-Point Organic Solvents. *Chem. Mater.* **2007**, *19* (21), 5174–5178.
- (37) Yang, H. J.; Tuan, H. Y. High-Yield, High-Throughput Synthesis of Germanium Nanowires by Metal-Organic Chemical Vapor Deposition and Their Functionalization and Applications. *J. Mater. Chem.* **2012**, *22* (5), 2215–2225.
- (38) Wang, Q.; Javey, A.; Tu, R.; Dai, H. Germanium Nanowire Field-Effect Transistors with SiO<sub>2</sub> and High-K HfO<sub>2</sub> Gate Dielectrics. *Appl. Phys. Lett.* **2003**, *83* (12), 2432–2434.
- (39) Lu, X.; Fanfair, D. D.; Johnston, K. P.; Korgel, B. A. High Yield Solution-Liquid-Solid Synthesis of Germanium Nanowires. *J. Am. Chem. Soc.* **2005**, *127* (45), 15718–15719.
- (40) Vadavalli, S.; Valligatla, S.; Neelamraju, B.; Dar, M. H.; Chiasera, A.; Ferrari, M.; Desai, N. R. Optical Properties of Germanium Nanoparticles Synthesized by Pulsed Laser Ablation in Acetone. *Front. Phys.* **2014**, *2*, 1–9.
- (41) Jalilian, R.; Sumanasekera, G. U.; Chandrasekharan, H.; Sunkara, M. K. Phonon Confinement and Laser Heating Effects in Germanium Nanowires. *Phys. Rev. B - Condens. Matter Mater. Phys.* **2006**, *74* (15), 155421.
- (42) Tyczkowski, J.; Kazimierski, P.; Hatanaka, Y.; Aoki, T. Excimer Laser Induced

Crystallization of Amorphous Hydrogenated Carbon-Germanium Films Fabricated by Plasma CVD. *Surf. Coatings Technol.* **2005**, *200* (1-4 SPEC. ISS.), 222–226.

- (43) Kazimierski, P.; Tyczkowski, J.; Kozanecki, M.; Hatanaka, Y.; Aoki, T. Transition from Amorphous Semiconductor to Amorphous Insulator in Hydrogenated Carbon-Germanium Films Investigated by Raman Spectroscopy. *Chem. Mater.* **2002**, *14* (11), 4694–4701.
- (44) Mariotto, G.; Vinegoni, C.; Jacobsohn, L. G.; Freire, F. L. Raman Spectroscopy and Scanning Electron Microscopy Investigation of Annealed Amorphous Carbon-Germanium Films Deposited by d.c. Magnetron Sputtering. *Diam. Relat. Mater.* **1999**, *8* (2–5), 668–672.
- (45) Kazimierski, P.; Jóźwiak. Transition from Amorphous Semiconductor to Amorphous Insulator in Hydrogenated Carbon-Germanium Films Investigated by IR Spectroscopy. *J. Non. Cryst. Solids* **2009**, *355* (4–5), 280–286.
- (46) Zhu, J. Q.; Jiang, C. Z.; Han, J. C.; Yu, H. L.; Wang, J. Z.; Jia, Z. C.; Chen, R. R. Optical and Electrical Properties of Nonstoichiometric A-Ge  $1-x$  C  $x$  Films Prepared by Magnetron Co-Sputtering. *Appl. Surf. Sci.* **2012**, *258* (8), 3877–3881.
- (47) Cardona, M. Vibrational Spectra of Hydrogen in Silicon and Germanium. *Phys. status solidi* **1983**, *118* (2), 463–481.
- (48) Gazicki, M. Plasma Deposition of Thin Carbon/Germanium Alloy Films from Organogermanium Compounds. *Chaos, solitons and fractals* **1999**, *10* (12), 1983–2017.
- (49) Scace, R. I.; Slack, G. A. Solubility of Carbon in Silicon and Germanium. *J. Chem. Phys.* **1959**, *30* (6), 1551–1555.
- (50) Park, K. H.; Lee, D.; Kim, J.; Song, J.; Lee, Y. M.; Kim, H. T.; Park, J. K. Defect-Free, Size-Tunable Graphene for High-Performance Lithium Ion Battery. *Nano Lett.* **2014**, *14* (8), 4306–4313.
- (51) Li, C.-P.; Lee, C.-S.; Ma, X.-L.; Wang, N.; Zhang, R.-Q.; Lee, S.-T. Growth Direction and Cross-Sectional Study of Silicon Nanowires. *Adv. Mater.* **2003**, *15* (78), 607–609.
- (52) Ma, D. D. D.; Lee, C. S.; Au, F. C. K.; Tong, S. Y.; Lee, S. T. Small-Diameter Silicon Nanowire Surfaces. *Science* **2003**, *299* (5614), 1874–1877.
- (53) Wu, Y. S.; Bagchi, S.; Garg, S.; Singh, N.; Tsai, T. Controlled Growth and

- Structures of Molecular-Scale Silicon Nanowires. *Nano Lett.* **2004**, *4* (3), 433–442.
- (54) Hanrath, T.; Korgel, B. A. Crystallography and Surface Faceting of Germanium Nanowires. *Small* **2005**, *1* (7), 717–721.
  - (55) Farrell, H. H.; Van Siclen, C. D. Binding Energy, Vapor Pressure, and Melting Point of Semiconductor Nanoparticles. *J. Vac. Sci. Technol. B Microelectron. Nanom. Struct.* **2007**, *25* (4), 1441–1447.
  - (56) Liu, X. H.; Huang, S.; Picraux, S. T.; Li, J.; Zhu, T.; Huang, J. Y. Reversible Nanopore Formation in Ge Nanowires during Lithiation–Delithiation Cycling: An In Situ Transmission Electron Microscopy Study. *Nano Lett* **2011**, *11*, 3991–3997.
  - (57) McNulty, D.; Geaney, H.; Buckley, D.; O'Dwyer, C. High Capacity Binder-Free Nanocrystalline GeO<sub>2</sub> Inverse Opal Anodes for Li-Ion Batteries with Long Cycle Life and Stable Cell Voltage. *Nano Energy* **2018**, *43*, 11–21.
  - (58) Dileo, R. A.; Frisco, S.; Ganter, M. J.; Rogers, R. E.; Raffaele, R. P.; Landi, B. J. Hybrid Germanium Nanoparticle-Single-Wall Carbon Nanotube Free-Standing Anodes for Lithium Ion Batteries. *J. Phys. Chem. C* **2011**, *115* (45), 22609–22614.
  - (59) Ngo, D. T.; Kalubarme, R. S.; Le, H. T. T.; Park, C. N.; Park, C. J. Conducting Additive-Free Amorphous GeO<sub>2</sub>/C Composite as a High Capacity and Long-Term Stability Anode for Lithium Ion Batteries. *Nanoscale* **2015**, *7* (6), 2552–2560.
  - (60) Kim, G. T.; Kennedy, T.; Brandon, M.; Geaney, H.; Ryan, K. M.; Passerini, S.; Appetecchi, G. B. Behavior of Germanium and Silicon Nanowire Anodes with Ionic Liquid Electrolytes. *ACS Nano* **2017**, *11* (6), 5933–5943.
  - (61) Chockla, A. M.; Klavetter, K. C.; Mullins, C. B.; Korgel, B. A. Solution-Grown Germanium Nanowire Anodes for Lithium-Ion Batteries. *ACS Appl. Mater. Interfaces* **2012**, *4* (9), 4658–4664.
  - (62) Forney, M. W.; Ganter, M. J.; Staub, J. W.; Ridgley, R. D.; Landi, B. J. Prelithiation of Silicon-Carbon Nanotube Anodes for Lithium Ion Batteries by Stabilized Lithium Metal Powder (SLMP). *Nano Lett.* **2013**, *13* (9), 4158–4163.
  - (63) Baggetto, L.; Notten, P. H. L. Lithium-Ion (De)Insertion Reaction of Germanium Thin-Film Electrodes: An Electrochemical and In Situ XRD Study. *J. Electrochem. Soc.* **2009**, *156* (3), A169.



- (64) Fang, S.; Shen, L.; Zheng, H.; Zhang, X. Ge-Graphene-Carbon Nanotube Composite Anode for High Performance Lithium-Ion Batteries. *J. Mater. Chem. A* **2015**, *3* (4), 1498–1503.
- (65) Kennedy, T.; Mullane, E.; Geaney, H.; Osiak, M.; O'Dwyer, C.; Ryan, K. M. High-Performance Germanium Nanowire-Based Lithium-Ion Battery Anodes Extending over 1000 Cycles through in Situ Formation of a Continuous Porous Network. *Nano Lett.* **2014**, *14* (2), 716–723.
- (66) Lim, L. Y.; Fan, S.; Hng, H. H.; Toney, M. F. Operando X-Ray Studies of Crystalline Ge Anodes with Different Conductive Additives. *J. Phys. Chem. C* **2015**, *119* (40), 22772–22777.
- (67) Liu, X. H.; Zhang, L. Q.; Zhong, L.; Liu, Y.; Zheng, H.; Wang, J. W.; Cho, J. H.; Dayeh, S. A.; Picraux, S. T.; Sullivan, J. P.; Mao, S. X.; Ye, Z. Z.; Huang, J. Y. Ultrafast Electrochemical Lithiation of Individual Si Nanowire Anodes. *Nano Lett.* **2011**, *11* (6), 2251–2258.
- (68) Mathur, S.; Shen, H.; Sivakov, V.; Werner, U. Germanium Nanowires and Core-Shell Nanostructures by Chemical Vapor Deposition of [Ge(C<sub>5</sub>H<sub>5</sub>)<sub>2</sub>]. *Chem. Mater.* **2004**, *16* (12), 2449–2456.
- (69) Chockla, A. M.; Bogart, T. D.; Hessel, C. M.; Klavetter, K. C.; Mullins, C. B.; Korgel, B. A. Influences of Gold, Binder and Electrolyte on Silicon Nanowire Performance in Li-Ion Batteries. *J. Phys. Chem. C* **2012**, *116* (34), 18079–18086.
- (70) NIST Chemistry WebBook <https://webbook.nist.gov/chemistry/> (accessed 2021 -05 -26).
- (71) Flynn, G.; Palaniappan, K.; Sheehan, M.; Kennedy, T.; Ryan, K. M. Solution Synthesis of Lead Seeded Germanium Nanowires and Branched Nanowire Networks and Their Application as Li-Ion Battery Anodes. *Nanotechnology* **2017**, *28* (25), 255603.
- (72) Chi, C.; Hao, J.; Liu, X.; Ma, X.; Yang, Y.; Liu, X.; Endres, F.; Zhao, J.; Li, Y. UV-Assisted, Template-Free Electrodeposition of Germanium Nanowire Cluster Arrays from an Ionic Liquid for Anodes in Lithium-Ion Batteries. *New J. Chem.* **2017**, *41* (24), 15210–15215.
- (73) Chang, W. C.; Kao, T. L.; Lin, Y.; Tuan, H. Y. A Flexible All Inorganic Nanowire Bilayer Mesh as a High-Performance Lithium-Ion Battery Anode. *J. Mater. Chem. A* **2017**, *5* (43), 22662–22671.

- (74) Farbod, B.; Cui, K.; Kupsta, M.; Kalisvaart, W. P.; Memarzadeh, E.; Kohandehghan, A.; Zahiri, B.; Mitlin, D. Array Geometry Dictates Electrochemical Performance of Ge Nanowire Lithium Ion Battery Anodes. *J. Mater. Chem. A* **2014**, 2 (39), 16770–16785.
- (75) Hao, J.; Yang, Y.; Zhao, J.; Liu, X.; Endres, F.; Chi, C.; Wang, B.; Liu, X.; Li, Y. Ionic Liquid Electrodeposition of Strain-Released Germanium Nanowires as Stable Anodes for Lithium Ion Batteries. *Nanoscale* **2017**, 9 (24), 8481–8488.
- (76) Liu, X.; Hao, J.; Liu, X.; Chi, C.; Li, N.; Endres, F.; Zhang, Y.; Li, Y.; Zhao, J. Preparation of Ge Nanotube Arrays from an Ionic Liquid for Lithium Ion Battery Anodes with Improved Cycling Stability. *Chem. Commun.* **2015**, 51 (11), 2064–2067.
- (77) Kim, C.; Song, G.; Luo, L.; Cheong, J. Y.; Cho, S.-H.; Kwon, D.; Choi, S.; Jung, J.-W.; Wang, C.-M.; Kim, I.-D.; Park, S. Stress-Tolerant Nanoporous Germanium Nanofibers for Long Cycle Life Lithium Storage with High Structural Stability. **2018**.
- (78) Yuan, F. W.; Yang, H. J.; Tuan, H. Y. Alkanethiol-Passivated Ge Nanowires as High-Performance Anode Materials for Lithium-Ion Batteries: The Role of Chemical Surface Functionalization. *ACS Nano* **2012**, 6 (11), 9932–9942.
- (79) Liu, J.; Song, K.; Zhu, C.; Chen, C. C.; Van Aken, P. A.; Maier, J.; Yu, Y. Ge/C Nanowires as High-Capacity and Long-Life Anode Materials for Li-Ion Batteries. *ACS Nano* **2014**, 8 (7), 7051–7059.
- (80) Yue, G. H.; Zhang, X. Q.; Zhao, Y. C.; Xie, Q. S.; Zhang, X. X.; Peng, D. L. High Performance of Ge@C Nanocables as the Anode for Lithium Ion Batteries. *RSC Adv.* **2014**, 4 (41), 21450–21455.
- (81) Woo, S.-H.; Choi, S. J.; Park, J.-H.; Yoon, W.-S.; Hwang, S. W.; Whang, D. Entangled Germanium Nanowires and Graphite Nanofibers for the Anode of Lithium-Ion Batteries. *J. Electrochem. Soc.* **2013**, 160 (1), A112–A116.
- (82) Li, W.; Li, M.; Yang, Z.; Xu, J.; Zhong, X.; Wang, J.; Zeng, L.; Liu, X.; Jiang, Y.; Wei, X.; Gu, L.; Yu, Y. Carbon-Coated Germanium Nanowires on Carbon Nanofibers as Self-Supported Electrodes for Flexible Lithium-Ion Batteries. *Small* **2015**, 11 (23), 2762–2767.
- (83) Sun, Y.; Jin, S.; Yang, G.; Wang, J.; Wang, C. Germanium Nanowires-in-Graphite Tubes via Self-Catalyzed Synergetic Confined Growth and Shell-Splitting Enhanced Li-Storage Performance. *ACS Nano* **2015**, 9 (4), 3479–3490.

# **Chapter 3**

## **Exploring the Tetragonal (ST12) Germanium Phase in One-dimensional (1D) Nanostructures**

Data from this chapter was submitted for publication in June 2021. Consequently, sections of the chapter such as the abstract and introduction may contain repeating concepts and paragraphs. I synthesised and performed the elemental and structural analysis of the nanowires reported in this chapter. I co-wrote the paper with SB and JDH and analysed Raman, TEM and photoluminescence data obtained from collaborators.

Garcia-Gil, A.; Biswas, S.; Roy, A.; Saladukh, D.; Raha, S.; Conroy, M.; Nicolosi, V.; Singha, A.; Holmes, J. D., 'Exploring the Tetragonal (ST12) Germanium Phase in One-dimensional (1D) Nanostructures'. Submitted June 2021.

### 3.1. Abstract

New semiconducting materials, such as state-of-the-art alloys, engineered composites and allotropes of well-established materials can demonstrate unique physical properties and generate wide possibilities for a vast range of applications. Here we demonstrate, for the first time, the fabrication of tetragonal germanium (ST12-Ge) nanowires via a one-step bottom-up synthetic process. One-dimensional (1D) nanostructures of ST12-Ge were grown in supercritical toluene at temperatures ranging between 290-330 °C at a pressure of  $\leq 48$  bar. Nanowire growth was achieved via a self-seeded vapour-liquid-solid (VLS)-like paradigm, with the aid of an *in situ* formed amorphous carbonaceous layer. The crystalline phase and structure of the ST12-Ge nanowires were confirmed by X-ray diffraction (XRD), high-resolution transmission electron microscopy (HRTEM) and Raman spectroscopy. The nanowires produced displayed a high-aspect-ratio, with a very narrow mean diameter of  $9.04 \pm 1.44$  nm and lengths beyond 4  $\mu\text{m}$ . The growth of the ST12 phase of Ge nanowires is governed by the formation of the carbonaceous structure on the surface of the nanowires and the creation of Ge-C bonding on the surface. The ST12-Ge nanowire allotrope was found to have a profound effect on the intensity of the light emission and on the directness of the bandgap, as confirmed by a temperature-dependent photoluminescence study.

### 3.2. Introduction

Group IV elements such as carbon, silicon, germanium and tin can present extensive polymorphism to form many uncommon allotropes, besides graphite and diamond cubic (dc) crystallographic structures. These allotropes have drawn great attention because of their interesting characteristics, *e.g.* high packing densities<sup>1</sup>, insulator/semiconductor behaviour<sup>2</sup>, metallicity<sup>3</sup> and superconductivity<sup>2,3</sup>, and their wide range of potential applications, such as in solar cells,<sup>4,5</sup> gate-all-around transistors<sup>6</sup>, and superconducting devices<sup>4,7,8</sup>. In particular, germanium polymorphs exhibit attractive electronic and optical properties, especially good electrical conductivity<sup>1</sup> and a direct and narrow bandgap.<sup>2,3</sup>

Over the years, considerable effort has been made to synthesise and characterise different polymorphs of Ge, some of which are predicted to possess better energetic stabilities in comparison with the diamond cubic Ge (dc-Ge) phase.<sup>9–11</sup> To date, allotropes of Ge have typically been obtained and characterised at very high pressures (in the range of from 100 to 1600 bar), both upon compression and decompression.<sup>12</sup> When amorphous or dc-Ge is placed under high pressure (above 10 GPa in bulk, and 17 GPa for nanoscale), a new metallic  $\beta$ -Sn structure (I4<sub>1</sub>/amd) is formed due to a phase transformation.<sup>13</sup> However, upon release of the pressure at room temperature,  $\beta$ -Sn Ge does not reverse to dc-Ge form, but transform to different metastable phases, such as the tetragonal phase (ST12-Ge or Ge-III), the body centred-cubic structure (BC8) or the rhombohedral R8 phase, and sometimes metastable phases mixed with dc-Ge.<sup>1,14</sup>

Among all the possible crystalline Ge allotropes, most of them are thermodynamically unstable at room temperature and ambient pressure. However, ST12-Ge has become the most commonly studied Ge allotrope because of its kinetical stability at ambient conditions.<sup>15</sup> ST12-Ge is based on a tetrahedral structure with 12 atoms per unit cell arranged to form fivefold, sixfold and sevenfold rings. Hence, ST12-Ge is expected to be semiconducting and has attracted special attention due to its potential use in electronic and energy storage applications.<sup>16,17</sup> Also, comparisons with theoretical calculations carried out for ST12-silicon suggest that doped ST12-Ge may act as a superconductor at low temperatures.<sup>7</sup> The initial characterisation of the optical properties of ST12-Ge, primarily theoretical, have produced contradictory results, especially in regards to its electronic band structure.<sup>15,18,19</sup> Recent density-functional theory (DFT)-based calculations reported an indirect fundamental bandgap of 0.54 eV<sup>2</sup> and 0.70 eV<sup>1</sup> for the ST12-Ge structure, with a direct non-fundamental bandgap of 0.56 eV<sup>2</sup> and 0.72 eV<sup>1</sup>. A very small separation ( $\sim 20$  meV) between the indirect (L) and direct ( $\Gamma$ ) valleys potentially permits a direct bandgap transition in ST12-Ge through the application of external strain. Experimental reports on determining the bandgap of single-crystalline ST12-Ge are limited. A bandgap of 1.5 eV has been reported for nanocrystalline grains (3-4 nm) of ST12-Ge deposited via cluster-beam evaporation.<sup>20</sup> Very recently, Zhao *et al.*<sup>1</sup> reported an indirect bandgap of 0.59 eV and a direct optical transition of 0.74 eV for single-crystalline bulk ST12-Ge via optical absorbance and Tauc plot analysis.

Besides the traditional high-pressure laboratory synthesis, a few techniques at ambient pressure, like plasma-enhanced severe plastic deformation (SPD)<sup>21</sup> and indentation techniques<sup>22</sup> have also been utilised to obtain ST12-Ge in bulk form. Although there

have been attempts to grow ST12-Ge in bulk form, there have been no reports on synthesising one dimensional tetragonal Ge nanostructures, to keep track of the miniaturisation of Si-based nanoelectronics and to take advantage of their 1D geometry for new age field-effect transistor (FET) devices, *e.g.* finFET, gate-all-around (GAA) FET *etc.* Additionally, nanostructures of tetragonal Ge could be highly advantageous for solar power conversion and in energy storage devices such as Li-ion batteries.<sup>5,16</sup> The formation of ST12-Ge nanocrystals have previously been synthesised at atmospheric pressure,<sup>22–24</sup> but not in a one-dimensional nanoform. Although different deposition-based techniques, such as chemical vapour deposition (CVD)<sup>25</sup> and ionised cluster beam deposition<sup>26,27</sup>, have been useful in obtaining ST12-Ge crystals with small nanograins, true nanocrystalline samples (nanoparticles of diameter  $\sim 6$  nm) have only been obtained by thermal annealing of amorphous nanophase Ge by the naphthalide-mediated reduction of  $\text{GeCl}_4$ .<sup>28</sup> Subsequent research has also been directed towards the thermal stability<sup>17,29</sup> of the nanograin allotrope, with little consensus on the results obtained.

Here we report for the first time the synthesis of single-crystalline ST12-Ge 1D nanostructures using a simple and scalable bottom-up synthetic method. The ST12-Ge nanowires were grown using a single-step batch synthesis method, without the addition of a metal or metalloid growth catalyst, at mild temperatures. The crystalline phase of the ST12-Ge nanowires was analysed by X-ray diffraction (XRD), high-resolution transmission electron microscopy (HRTEM) and Raman spectroscopy. A direct bandgap for the ST12-Ge nanowires was obtained via photoluminescence (PL) spectroscopy.

### 3.3. Experimental

**Synthesis of ST12-Ge nanowires.** Anhydrous toluene 99.8 % was purchased from Sigma-Aldrich Co. and diphenylgermane (DPG) 95 % was purchased from Fluorochem. All chemicals were stored and used in a nitrogen glovebox ( $O_2 < 0.1$  ppm,  $H_2O < 0.5$  ppm).

ST12-Ge nanowire synthesis was carried out in a 5 mL stainless steel reaction cell from High-Pressure Equipment Company. Before synthesis, the reaction cell and connectors were dried under vacuum at 125 °C for 12 h. Reactions were performed at temperatures between 290 to 440 °C on Si (100) with dimensions of 0.5 cm × 1.5 cm. The native oxide was not removed from the surface of the Si substrates prior to reaction. The reaction temperature was monitored by a thermocouple connected to the reaction vessel and the pressure was monitored via a pressure gauge, connected to one end of the reaction cell. In a typical reaction, 3 ml of a DPG/toluene solution was added to a 5 ml reaction cell which was heated to the desired temperature in a tube furnace for 60 min. The DPG concentration was varied between 40 and 60 mM. The filling volume of the reactant solution, *i.e.* filling fraction, was 60 % of the total reactor's volume (5 ml). The reaction cell was cooled to room temperature after the reaction and disassembled to access the growth substrate. Growth substrates were washed with dry toluene and dried under  $N_2$  for further characterisation.

**Characterisation.** The as-grown samples were imaged using an FEI Quanta FEG 650 scanning electron microscope (SEM) operated at 15 kV. High-resolution transmission electron microscopy (HRTEM) and high resolution scanning transmission electron



microscopy (HRSTEM) imaging were performed on a JEOL 2100 electron microscope operated at 200 kV, an FEI Titan electron microscope (operating at 300 kV) and a Titan Themis double-corrected and monochromated transmission electron microscope at 300 kV. High-angle annular-dark-field scanning-transmission-electron-microscopy (HAADF-STEM) was performed on the FEI Titan electron microscope operated at 300 kV. X-ray Photoelectron Spectroscopy (XPS) spectra were acquired on an Oxford Applied Research Escabase XPS system, equipped with a CLASS VM 100-mm-mean-radius hemispherical electron-energy-analyser with a five-channel detector arrangement in an analysis chamber with a base pressure of  $10 \times 10^{-10}$  mbar. Raman experiments were carried out in a Horiba Yuvon micro-Raman spectrometer equipped with 1800 lines/mm grating and a Peltier cooled charge-coupled device (CCD) camera. An Ar ion laser of wavelength 488 nm was used to excite the sample and a  $100 \times$  objective lens was used to focus the sample as well as collect the data in backscattering geometry. The crystal structure of the product was confirmed by XRD using a Philips X'pert Pro MPD, equipped with a Panalytical Empyrean Cu X-ray tube and a Philips X'celerator detector. Fourier-transform infrared spectroscopy (FTIR) spectra were recorded on an infrared spectrometer (IR 660, Varian) over a wavenumber range between 400 and  $4000 \text{ cm}^{-1}$ . EDX mapping was performed on a Titan Themis double-corrected and monochromated transmission electron microscope at 300 kV with a Bruker Super X detector. Software used for imaging and EDS mapping was FEI Velox. Photoluminescence (PL) data were obtained using a Ti:Sa pulsed laser as the excitation source, tuned to a wavelength of 700 nm and an 80 MHz repetition rate, a 300 fs pulse width and a mean power of 0.2 W. The laser spot was focused on a  $9 \text{ }\mu\text{m}$  spot, providing a pump power density of  $200 \text{ kW cm}^{-2}$ . Samples were cooled to 10 K using a Helium cryostat. PL was

detected using liquid nitrogen chilled InAs detector with a sensitivity range from 0.9  $\mu\text{m}$  to 3  $\mu\text{m}$  ( $\sim 0.41 - 1.338 \text{ eV}$ ).

### 3.4. Results and Discussion

Tetragonal (ST12) Ge nanowires were grown at relatively mild temperatures, between 290-330  $^{\circ}\text{C}$ , in a batch reactor using low boiling point solvents, *e.g.* toluene and DPG. The supercritical toluene environment created in the closed-cell reactors provided ideal conditions for fast precursor decomposition and *in situ* carbonaceous polymer formation, which was crucial for the self-seeded growth of the ST12-Ge nanowires. Figure 3.1a and 3.1b show SEM images of ST12-Ge nanowires grown on a Si (100) substrate at a reaction temperature of 330  $^{\circ}\text{C}$  from a 60 and 40 mM solution of DPG in toluene, respectively. Figure 3.1a shows the formation of a three-dimensional (3D) sponge-like porous structure, like a matrix, from the micron long reticulated nanowires. The Ge nanowires assemble together to form a uniform Ge film over the Si substrates. The SEM images (see Figure 3.1 and Figure A3.1 in Appendix 3.6) clearly show the formation of a 3D porous network from the interweaving nanowires, consisting of bundles of individual nanowires. Significantly, nanowire growth was also achieved at temperatures as low as 290  $^{\circ}\text{C}$  (see Figure A3.1 in Appendix 3.6). The yield of nanowires varied from 0.36 to 0.51  $\mu\text{g mm}^{-2}$ , depending on the growth temperature and precursor concentration. Of note, no spherical (or hemispherical) growth seeds were detected at the tips of the nanowires, which is typically observed with catalytic bottom-up nanowire growth.

***Crystalline phase and structural analysis of Ge nanowires.*** As the primary objective of this work was to fabricate the crystalline tetragonal ST12-Ge nanowire, XRD

analysis on the as-grown samples was used to determine the phase purity and crystal structure of the nanowires. Figure 3.1c shows the XRD profile from a nanowire sample grown from a 60 mM DPG/toluene solution at a reaction temperature of 330 °C. After subtracting the reflection peaks from the Si substrate, the nanowire sample exhibited a sharp peak at 33.29°, which matches well with the calculated and experimental XRD pattern of ST12-Ge (JCPDS No. 72-1425,  $a = 5.93 \text{ \AA}$  and  $c = 6.98 \text{ \AA}$ ).<sup>1,16,27</sup> We have assigned the peak in the XRD pattern to the reflection from the {112} plane as this is the closest match with the  $2\theta$  value. However, previous XRD characterisation of bulk polycrystalline tetragonal Ge samples has depicted three reflections at  $2\theta \sim 33^\circ$ , *i.e.* 32.791°, 33.376° and 33.771°, corresponding to the diffractions from the {201}, {112} and {210} planes of the ST12-Ge respectively (JCPDS 72-1089 and 72-1425).<sup>30</sup> Thus, the experimental peak observed at 33.29° could be the reflection from any one of these planes, as a change in the lattice parameters is expected for single-crystalline nanoscale materials such as ST12-Ge nanowires. All the as-grown nanowire samples characterised by XRD presented the characteristic peak at  $\sim 33^\circ$  associated with the {112} crystallographic plane of the ST12-Ge structure. The single peak observed in the XRD corresponds to the strongest (112) reflection from the ST12-Ge sample. Peaks corresponding to other impurity phases such as dc-Ge or crystalline GeO<sub>2</sub> were not detected by the XRD. Although phase pure tetragonal ST12-Ge nanowires were achieved at temperatures of 330 and 290 °C, increasing the growth temperature resulted in the formation of nanowires of mixed ST12-Ge and dc-Ge phase (at 350 °C) (see Figure A3.2 in Appendix 3.6) and phase pure dc-Ge (at 380 and 440°C) (see Figures A3.3a and A3.3b in Appendix 3.6).

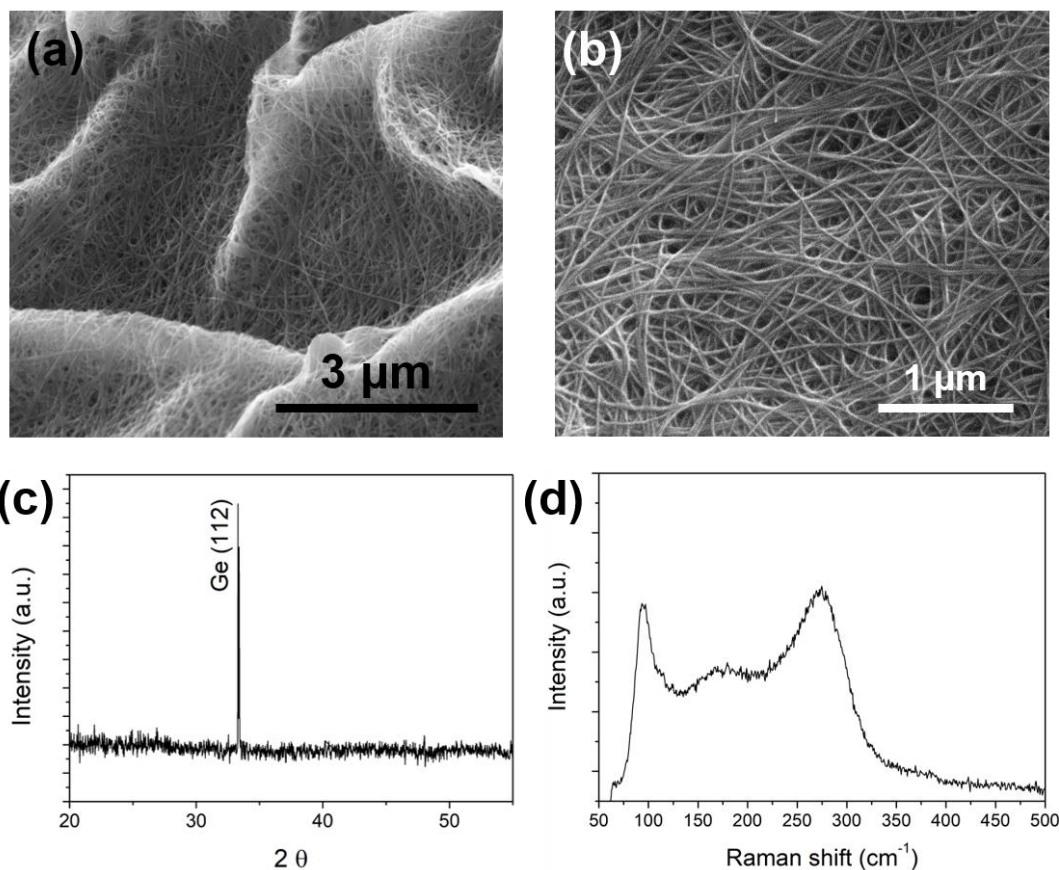


**Figure 3.1.** (a), (b) SEM micrographs of Ge nanowires grown at a temperature of 330 °C from a 40 and 60 mM DPG/toluene solution, respectively. (c) XRD pattern of a nanowire sample showing the formation of ST12-Ge crystal structure. (d) Raman spectrum of ST12-Ge nanowires.

Raman Spectroscopy, a powerful and non-destructive tool, was used to further confirm the phase of the Ge nanowires. Figure 3.1d shows room temperature Raman spectra recorded from the Ge nanowires between wavenumbers of 50 to 500 range. The measurements were performed at a low laser power (0.18 mW) to avoid laser-induced heating. The ST12 phase of Ge has a  $P4_32_12$  crystal structure and group theory analysis suggests that this phase has  $4A_1 + 5B_1 + 4B_2 + 8E$  Raman active optical phonon modes, while the dc-Ge phase only has one Raman active mode ( $E_{2g}$ ); which originates from a doubly degenerate LO-TO phonon. The Raman spectra, from an ST12-Ge nanowire sample, synthesized at 330 °C, displayed several peaks below

300  $\text{cm}^{-1}$ . These peaks are in general agreement with the previously reported Raman data for ST12-Ge.<sup>1,31</sup> No peaks corresponding to dc-Ge further demonstrates the formation of phase-pure ST12-Ge nanowires. The broadness of the Raman peaks was possibly caused by phonon confinement present in the nanowires. The magnified view of the peaks in the region around 1500  $\text{cm}^{-1}$  are shown in the inset of Figure 3.1d. The sharp peak around 1580  $\text{cm}^{-1}$  corresponds to the C-C G-band and indicates the presence of a carbonaceous structure in the nanowire samples.

***Chemical analysis of ST12-Ge nanowires.*** The chemical purity of the Ge nanowires was further characterised by EDX analysis, which confirmed that the bulk of the nanowires was solely comprised of Ge atoms (see Figure A3.4 in Appendix 3.6). The pure Ge composition was consistent throughout the nanowire body; as verified by EDX elemental mapping. EDX mapping also revealed the presence of oxygen on the surface of the nanowires due to the oxidation caused by air exposure of the sample.

The carbonaceous layer surrounding the Ge nanowires, as shown in the SEM images of Figures 3.1a and 3.1b, was analysed by FTIR absorption spectroscopy and XPS. Characterisation of the ST12-Ge nanowire samples via FTIR spectroscopy revealed the presence and interaction between the Ge nanowires and certain carbonaceous structures. FTIR spectra taken from nanowires samples showed absorption bands at  $\sim 2350$ ,  $\sim 970$ ,  $\sim 890$  and  $\sim 819 \text{ cm}^{-1}$  (see Figure 3.2a). These bands have previously been reported and,  $\sim 2350$  and  $890 \text{ cm}^{-1}$  in particular, correspond to the vibration modes of  $\text{C}=\text{C}$ <sup>32</sup>. The other bands,  $\sim 970$  and  $\sim 819 \text{ cm}^{-1}$  are consistent with the  $\text{CO}_2$  vibration and  $\text{Ge-CH}_3$  rocking vibrations, respectively.<sup>33</sup> FTIR analysis, therefore, confirms the formation of carbonaceous material in the nanowire samples.

Absorption bands at  $\sim 560$ ,  $\sim 615$  and  $\sim 740\text{ cm}^{-1}$  have been also observed in the FTIR spectra which can be assigned to the stretching modes of C-Ge-C<sup>32</sup>, Ge-C<sup>34</sup> bonds and Ge-H wagging mode<sup>35</sup>, respectively. These data not only confirm the presence of a carbonaceous matrix within the Ge nanowire sample but also suggest the interaction of this layer with the surface of the nanowires.

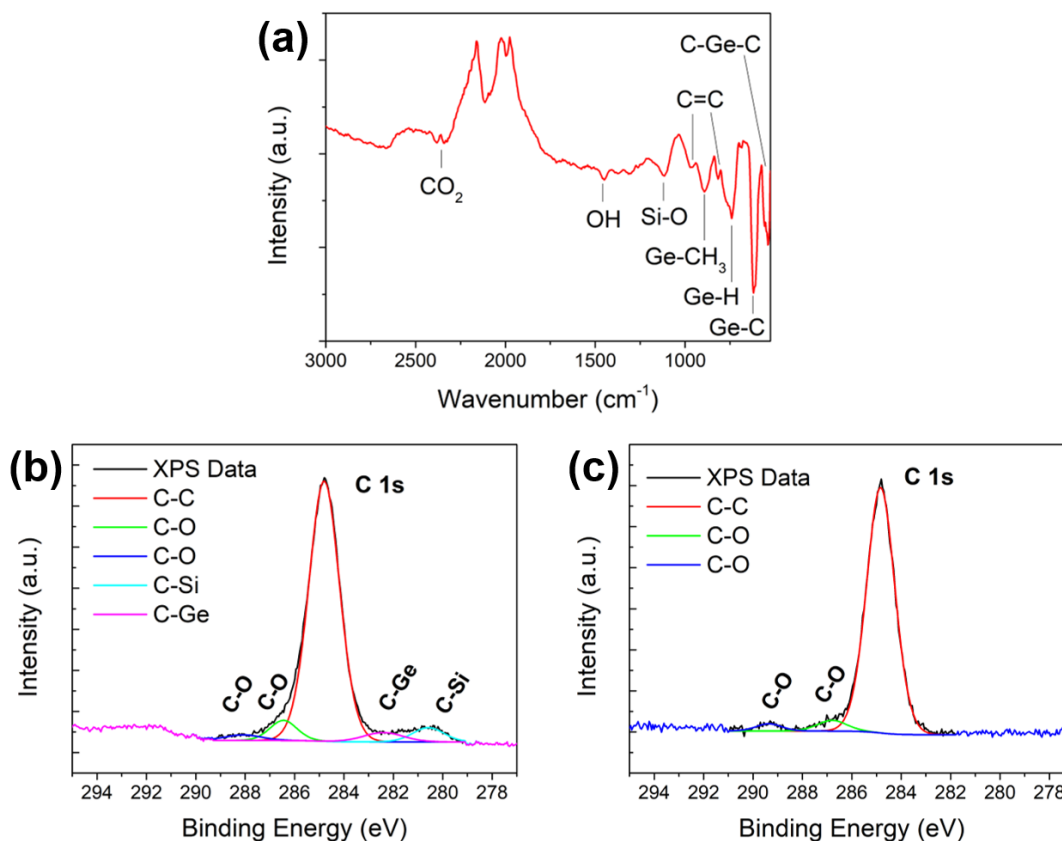


**Figure 3.2.** (a) FT-IR spectrum of cleaned Ge nanowires (with no carbonaceous matrix) and deposited on a Si substrate. XPS spectrum of C 1s peaks from nanowires grown at (b) a reaction temperature of 330 °C and DPG concentration of 60 mM (ST12-Ge nanowires) and (c) at a reaction temperature of 440 °C and a DPG concentration of 60 mM (dc-Ge nanowires).

XPS analysis was also performed on a representative nanowire sample grown at 330 °C and a DPG concentration of 60 mM, to further study the interaction between the Ge nanowires and the as described carbonaceous structure. XPS spectra of the

tetragonal ST12-Ge nanowires was compared with XPS data obtained from dc-Ge nanowires grown under similar growth condition but at the higher growth temperature of 440 °C (see Figures 3.2b and 3.2c). The C 1s peak of the XPS spectrum (see Figure 3.2b) of ST12-Ge and dc-Ge nanowires highlights a different interaction between the carbonaceous structures and the two Ge nanowire crystal phases. The peak at ~ 283.9 eV was only present in the XPS spectrum of ST12-Ge and can be assigned to a strong interaction (covalent bonding) between carbon and the surface of the ST12-Ge nanowire as Ge-C (see Figure 3.2b). This observation validates the FTIR data which suggests that an interaction exists between the carbonaceous matrix and the ST12-Ge nanowires (see Figure 3.2a). No analogous peak was found in the XPS spectrum of dc-Ge nanowires (see Figure 3.2c). C-C, C=C, C-O and CO<sub>3</sub> bonds were present in the C1s spectrum for both samples. Germanium oxide formation was also found (see Figure A3.5 in Appendix 3.6) due to air exposure of the samples when stored in an ambient atmosphere. Thus, the carbonaceous compounds bonded to the nanowire surface do not act as a passivation layer to protect the Ge nanowires from oxidation. Both FT-IR and XPS evaluations confirm carbonaceous compound formation in the samples and interaction between this carbonaceous matrix with the surface of the ST12-Ge nanowires.

***Structural and crystal quality analysis of ST12-Ge nanowires.*** The surface interaction of the Ge nanowires with the carbonaceous matrix can potentially induce strain and crystal deformation, such as the formation of twins and stacking faults. HAADF-STEM, HRTEM and Selected area electron diffraction (SAED) were used to further confirm the formation of the ST12-Ge crystalline phase and structural quality of the nanowires. Figures 3.3a and 3.3b show HAADF-STEM data from an ST12-Ge

nanowire sample grown at 330 °C from a 60mM DPG/toluene solution. The nanowire exhibited uniform structural quality and a crystalline nature, analogous to the other nanowires formed under similar growth conditions. The ST12-Ge structure had a distorted tetrahedral arrangement with a packing density about 11 % greater than that of dc-Ge.<sup>15</sup> The nanowires presented a high instability under the TEM electron beam and, consequently, a transformation to the dc-Ge was repeatedly observed. This behaviour can be explained by the metastability of the ST12-Ge<sup>29</sup> phase which, upon external perturbation such as heating or high energy electron beam exposure, transform back into the stable dc-Ge form.<sup>20</sup> HAADF-STEM of the Ge nanowires showed the stacking of {110} planes along the nanowire growth direction (see Figure 3.3a). The <110> nanowire growth direction is the most common growth direction for diamond cubic Si and Ge nanowires of this dimension<sup>36–38</sup> and seems also valid for the ST12-Ge nanowires. As the stacking of some of the (112) crystal planes in the family of {112} plane is perpendicular to the {110} plane for the tetragonal crystal, a strong {112} reflection is justified in the XRD pattern (see Figure 3.1c).

A more detailed examination of the nanowire crystal is depicted in the HRSTEM image (see Figure 3.3b), oriented along the <110> zone axis, and recorded from the core of a crystalline ST12-Ge nanowire. HRSTEM imaging reveals an interplanar spacing ( $d$ ) of 0.21 nm (see Figure 3.3b) along with the nanowire growth axis, corresponding to the {220} plane of an ST12-Ge crystal. All the interplanar spacings for other planes match well with the ST12-Ge (JCPDS 072-1425). SAED measurements on the single nanowire could only be indexed to the ST12-Ge structure (see Figure 3.3c) and the reflections were assigned to the high-order Laue zone diffraction of {002}, {111} and {220} planes of ST12-Ge (JCPDS 072-1425).



Additionally, the interplanar angles of  $\sim 31^\circ$ ,  $\sim 59^\circ$  and  $\sim 90^\circ$  were measured between (111) and (220), (002) and (111), and (002) and (220), respectively. These interplanar angles match well with the tetragonal Ge crystal and are particularly useful in assigning the lattices with closely matched spacings. SAED patterns recorded from the nanowire also corresponds to ST12-Ge (JCPDS 72-1425) and confirms the single-crystalline nature of the nanowires.

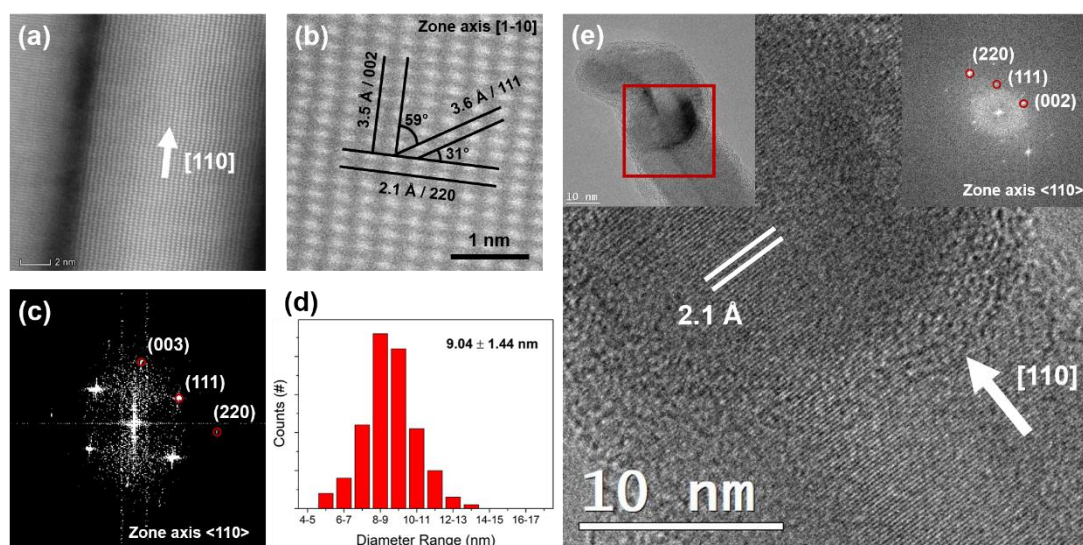


**Figure 3.3.** (a) HRSTEM image of ST12-Ge nanowires with the stacking of (110) plane along the nanowire growth axis. (b) Latticed-resolved HRSTEM image of an ST12-Ge nanowire. (c) SAED pattern recorded from a representative ST12-Ge nanowire which confirms the ST12 structure. (d) Diameter distributions of Ge nanowires obtained at 330 °C from a 60mM DPG/toluene solution. (e) HRTEM image of a Ge seed and nanowire interface (shown by the red box on the top-left inset) confirms the self-seeded growth. Top-right inset shows an FFT of the seed area.

The presence of the amorphous carbon on the surface of the nanowires was observed by TEM to be a discontinuous and uneven coating along the length of the nanowires (see Figure A3.6 in Appendix 3.6). Figure 3.3d shows a diameter distribution analysis of a nanowire sample grown at 330 °C with a mean diameter of 9.0 ( $\pm 1.4$ ) nm. The mean diameter of the Ge nanowires was found to be uniform for

all growth conditions. Most of the nanowires exceeded a measurable length over 4  $\mu\text{m}$  and very few displayed kinking at growth temperatures employed. Tapered nanowires were also not observed under any growth conditions investigated.

The presence of hemispherical seed and the seed-nanowire interface was further examined by HRTEM (see Figure 3.3e). A low-magnification TEM image of a Ge nanowire with a growth seed can be seen in the inset of Figure 3.3e (top-left) which confirms the participation of a seeded, bottom-up growth mechanism. Figure 3.3e shows a high-magnification TEM image recorded with  $\langle 110 \rangle$  zone axis alignment, from the same nanowire. A smooth interface is observed between the nanowire and the nanoparticle seed with no crystallographic difference. The crystal structure in both the nanoparticle and the nanowire segments correspond to ST12-Ge. Fast Fourier Transform (FFT), in the top-right inset of Figure 3.3e, of the seed region also confirms the formation of crystalline ST12-Ge. The apparent continuity of the similar lattice from the seed to the nanowire confirms self-seeding of the nanowires, *i.e.* seeded from *in situ* formed Ge nanoparticles.<sup>39–41</sup>

***Growth mechanism of ST12-Ge Nanowires.*** The growth of the self-seeded ST12-Ge nanowires likely occurs via a triple-phase (source-seed-nanowire) bottom-up growth which is aided by the formation of the carbonaceous matrix. The formation of Ge seeds and their participation in nanowire growth (self-seeded) is evident from the presence of Ge nanoparticles at the tips of the nanowires (see Figure 3.3e). In self-catalytic growth temperature and pressure are key factors associated with the Ge precursor decomposition and nanowire growth. In our experiments, ST12-Ge nanowires were only synthesised under certain temperatures (290 and 330 °C) and

pressure (an *in situ* generated pressure of  $\leq 48$  bar) conditions, close to the critical point of pure toluene (318.6 °C and 41.3 bar). These reaction conditions give the necessary environment to generate ST12-Ge nanoparticles which act as the catalytic seed for ST12-Ge nanowire growth (see Figure 3.3e). The formation of the nanoparticle phase (see Figure A3.3c in Appendix 3.6) takes place when the Ge precursor (DPG) decomposes to form Ge adatoms, liberating very reactive phenyl groups.<sup>42</sup> The formation of Ge nanoparticles seeds for nanowire growth can be described as a spontaneous phenomenon. Simultaneously, the carbonaceous material forms via polymerisation of the phenyl compounds. At this point, available Ge adatoms, via decomposition of DPG, aggregate and dissolve into the carbonaceous matrix to form the Ge nanoparticles. The as-formed organic structures limit the capacity of aggregation and Ostwald ripening of the Ge nanoparticles and thus the formation of larger spherical particles. The Ge nanoparticles placed at the outer surface of the polymer are exposed for the attachment of Ge adatoms for the growth of Ge nanowires. Self-seeded growth of Ge nanowires from *in situ* generated nanoparticles has previously been proposed via “pseudo” vapour-liquid-solid (VLS) like growth.<sup>40,43</sup> In our particular case, the initial formation of Ge nanoparticles in the carbonaceous template (analogous to the dc-Ge nanoparticles we can observe in Figure A3.3c in Appendix 3.6) and the presence of these nanoparticles at the tips of the nanowires, indicates the participation of nanoparticle seeds in the growth of the ST12-Ge nanowires.

The formation of the carbonaceous structure on the Ge nanostructures and its interaction with the Ge is key to the observation of ST12-Ge over dc-Ge crystalline structure under certain growth conditions. In nanowires, due to the high surface to

volume ratio, surface energy plays a crucial role in the formation and stability of the metastable nanostructure, particularly in the case of small radii. The nanowire diameter and its specific sidewall facets have been often pointed out as key factors determining the crystal phase of nanowires.<sup>44</sup> The energy difference between dc-Ge and ST12-Ge structures gets significantly small for nanostructures with small dimensions.<sup>45,46</sup> The energy difference between the two phases further decreases with the change in the surface properties, *e.g.* reconstructed surface, of the nanostructures.<sup>46</sup> The chemical interaction at the surface plays a key role in the stability of the ST12 phase in nanostructures.<sup>46</sup> The formation of metastable tetragonal clusters is possible by trapping amorphous Ge nanoparticles with carbon resulting in unsaturated and reconstructed surfaces at low temperatures. Thus, along with the nanowire diameter (diameter of ~ 9 nm for ST12-Ge nanowires), the formation of singular carbonaceous-structure compositions and their interaction with the available Ge surface (both for nanoparticles in the initial stage of the growth and for nanowires) could be crucial in determining the phase and the stability of the ST12-Ge nanowire phase. As the cubic and ST12-Ge nanostructures have comparable lattice energies, their nucleation is likely dependent on local environmental factors such as growth temperature and pressure.

Surface tension could also be a key contributor to the persistence of the ST12 phase in Ge nanostructures. Kim *et al.*<sup>28</sup> suggested that the addition of the sterically hindered organometallic reagent t-BuMgCl promotes the nucleation of ST12 structures in Ge nanoparticles by imparting surface strain onto nascent amorphous Ge nanoclusters. This results in a metastable surface with a high degree of unsaturation that leads to an ST12-Ge structure. In our case, ST12-Ge nanowires are only obtained at growth

temperatures between 290 and 330 °C, whereas dc-Ge was obtained at high temperatures. An interaction between the Ge and the carbonaceous compound was only observed, with the formation of the Ge-C bond, for the ST12-Ge nanowires (see Figure 3.2b). Osten *et al.*<sup>47</sup> have previously postulated that a small amount of isoelectronic carbon (< 2 at.%) can induce strain in the SiGe lattice for a tetragonal distortion. The formation of the Ge-C bond at the surface of the Ge nanowires can therefore potentially induce strain in the Ge lattice due to the change in the bonding environment, the bond length of Ge-C 1.98 Å and Ge-Ge 2.46 Å. This strain can change the Ge-Ge bond length and angular distortion in the lattice and create a tetragonal symmetry in the nanowires. Additionally, the surface stress, which can be induced by the carbonaceous matrix, can act as the driving force by creating a compressive strain in a certain crystal direction, *e.g.* [001], for the phase transformation.<sup>48</sup> The presence of the carbonaceous matrix and the Ge-C bond formation at the surface of the Ge nanowire plays a crucial role in the formation of the ST12 phase. This is confirmed by the removal of the carbonaceous compound (by sonication in ethanol), which transformed the ST12 nanowires to dc-Ge nanowire (see Figures A3.7a and A3.7b in Appendix 3.6).

***Photoluminescence of ST12-Ge Nanowires.*** Photoluminescence (PL) is a primary technique to determine the nature of the bandgap in nanoscale systems. PL peak positions, intensity and linewidths can be used to determine the nature of an electronic band transition. Previous attempts to obtain detectable PL signals in the near-infrared (NIR) region of the spectrum from the ST12-Ge crystal structure were not successful for both room temperature and low-temperature measurements.<sup>27,28</sup> To examine the nature of the band transition in ST12 nanowires, low-temperature PL studies were

carried out using a liquid helium cryostat. A PL spectrum recorded from ST12-Ge nanowires recorded at 10 K using a Ti:Sa laser with an excitation wavelength of 700 nm is depicted in Figure 3.4a. The PL spectrum shows an intense PL peak centred at 1938 nm, which equates to bandgap energy of 0.64 eV. Another low-intensity small shoulder peak was also observed at a higher wavelength of 2343 nm ( $\sim 0.53$  eV). By fitting the spectra to the Gauss function, the full width half maximum (FWHM) of the peak was obtained. The primary emission peak has a relatively narrow linewidth of 322 nm. The very strong main peak at 0.64 eV can be assigned to direct bandgap emission and the weak shoulder peak centred at around 0.53 eV is ascribed to indirect bandgap related emission. The PL peak position of the ST12-Ge (0.64 eV) reported here matches well with the theoretically calculated bandgap for ST12-Ge.<sup>1,49</sup> Zhao *et. al.*<sup>1</sup> and Malone *et. al.*<sup>2</sup> have calculated, by DFT calculations using a hybrid functional approach, the fundamental bandgap to be indirect with values of 0.70 and 0.54 eV respectively. However, their calculation also predicted a relatively "weak" indirect bandgap for ST12-Ge, in the sense that the direct bandgap is only  $\sim 20$  meV larger than the indirect bandgap. Experimental determination of the bandgap of ST12-Ge is rarely reported. A bandgap of 1.5 eV was reported for cluster beam deposited Ge nanograins through optical absorption measurements,<sup>20</sup> whereas optical absorbance and reflectivity measurements of bulk ST12-Ge and Tauc plot analysis showed a fundamental indirect bandgap of 0.59 eV and a direct transition at 0.74 eV.<sup>1</sup>

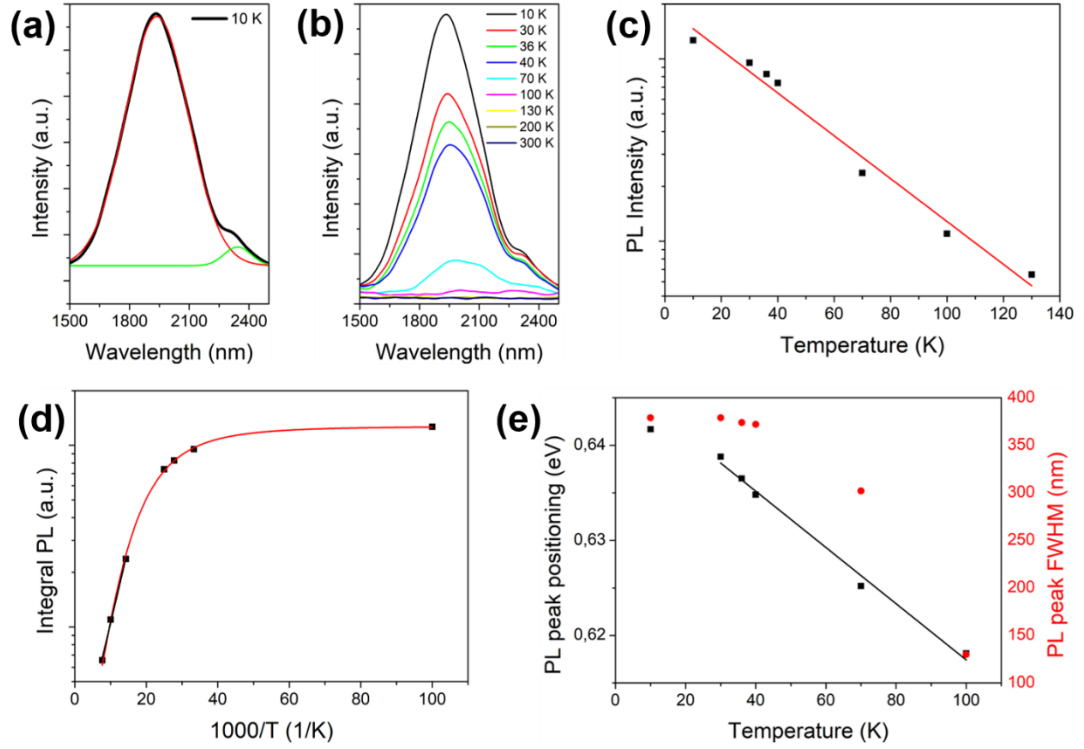


**Figure 3.4.** (a) PL spectra of ST12-Ge nanowires obtained at 10 K. (b) Temperature-dependent PL spectrum obtained from ST12-Ge nanowires at temperatures between 10 to 300 K. (c) Lineal fit plot of the integral PL intensity vs temperature of the peak at  $\sim 1940$  nm from 10 to 100 K with the coefficient of determination close to unity ( $R^2 = 0.9908$ ). (d) The Arrhenius relation of the integral PL intensity vs temperature of the peak at  $\sim 1940$  nm from 10 to 100 K with the coefficient of determination close to unity ( $R^2 = 0.9967$ ). (e) Lineal fit plot (black) of the PL peak position vs temperature of the peak at  $\sim 1940$  nm from 10 to 100 K with the coefficient of determination close to unity ( $R^2 = 0.9926$ ). Red dot plot corresponds to the PL peak FWHM at the different temperatures.

Temperature-dependent PL studies are invaluable for probing the nature of the fundamental bandgap of a material.<sup>50,51</sup> Temperature-dependent PL studies have previously been used to probe the direct/indirect nature of the fundamental gap in 1D nanoscale materials.<sup>52–54</sup> The nature of the bandgap for ST12-Ge nanowires was verified by temperature-dependent studies between 10 - 300 K. PL spectra recorded as a function of temperatures are plotted in Figure 3.4b and to the best of our

knowledge, is the first reported experimental observation of a PL-determined bandgap from any ST12-Ge structure. The primary PL emission (at  $\sim 0.64$  eV) from ST12 nanowires monotonously decreases in intensity with increasing temperature (see Figure 3.4b), which can be attributed to a reduced transfer of electrons from the  $\Gamma$  to L valleys by thermal activation, thus a higher electron population in the  $\Gamma$  valley. A monotonical decrease (see Figure 3.4c) in the PL intensity with increasing temperature, which is typical behaviour of a direct bandgap semiconductor,<sup>50,54–56</sup> confirms the direct bandgap nature of the ST12-Ge nanowires. With increasing temperature, the fast diffusion of photocarriers toward surfaces and interfaces leads to non-radiative surface and interface recombination respectively, reducing the radiative transition rate, along with the activation energy  $E_A$ . An Arrhenius plot, depicting integrated photoluminescence intensity as a function of inverted temperature is shown in Figure 3.4d. Arrhenius plots have been fitted with a single exponential function with a coefficient of determination ( $R^2$ ) close to unity ( $R^2 = 0.9989$ ). The activation energy ( $E_A$ ) for the non-radiative processes from the Arrhenius plots was calculated to be 83 meV from the first three displayed points. The high activation energy for the non-radiative process at higher temperature indicates a direct bandgap material, although the calculated value may appear on the higher limit due to the particular data available. Furthermore, narrow linewidth deviation, determined by the FWHM when fitted with a Gaussian function, of the PL emission at low temperatures (between 360 to 300 nm for temperature between 10 to 70 K) is indicative of a single channel of recombination and thus indicates a direct bandgap transition.<sup>50</sup>

The effect of temperature on the peak position is displayed in Figure 3.4e. The temperature dependence of the PL peak position shows an increase in bandgap energy



for a decrease in temperature from 100 to 10 K. The bandgap is blue-shifted from 0.61 to 0.64 eV with the decrease in temperature. The temperature dependence of the PL peak energy can provide information on the carrier distribution within electronic bands or localised states. The monotonic decrease of the direct bandgap with temperature follows the bandgap (Varshni law) and carrier distribution variation in a semiconductor,<sup>57</sup> similar to previous observations for Ge and GeSn alloys.<sup>50-52</sup> We have only selected the last 5 points in the linear fitting due to the usual flat behaviour at the lowest temperatures.<sup>58</sup> However, the apparent redshift of the PL peak position with temperature can also be caused by laser-induced heating and subsequent heat-trapping within the dense nanowires array.<sup>59,60</sup> The weak peak at 0.54 eV at 10 K is associated with the indirect transition. The PL intensity of this indirect emission decreases continuously as T increases from 10 to 100 K, and then the peak disappears at room temperature. At a temperature  $\geq 100$  K, the phonon-assisted indirect L-valley to valence band transition (2275 nm) is almost as intense as the direct bandgap transition (2005 nm) (see Figure A3.8 in Appendix 3.6), indicating the availability of enough phonons at higher temperatures, which are essential for the momentum conservation in the transition process. The temperature-dependent PL observation indicates a higher probability of the direct transition below 100 K, compared to the phonon-assisted indirect transition, for ST12-Ge nanowires. A dominant direct bandgap transition is observed, especially at low temperatures (below 100 K). The nature of the bandgap in the ST12-Ge nanowires has therefore changed significantly from the reported cubic Ge bandgap or the calculated bandgap for ST12-Ge bulk crystals. This might be due to the presence of carbonaceous structures on the surface of the nanowires and the formation of Ge-C bonds at the surface samples. The very narrow diameter of the nanowires ( $\sim 9$  nm) and quantum confinement effects

associated with this dimension could be responsible for the observation of a fundamental direct bandgap in the ST12-Ge nanowires. Although the steady-state PL measurements gave an indication on the nature of the bandgap for ST12-Ge nanowires, direct measurements of the carrier lifetimes are required to precisely resolve the directness of the electronic band structure.

### 3.5. Conclusions

In summary, an alternative and simple synthetic method for growing ST12-Ge 1D nanostructures has been developed. ST12 nanowire growth was achieved at moderate temperatures and a much lower pressure compared to previously synthesised ST12-Ge bulk crystals. *In situ* polymerisation of a simple Ge precursor and the formation of carbonaceous compounds on the surface of the nanowires, in a batch setup, leads to the growth of this novel allotrope (ST12) of Ge in 1-D nanoform. Three-phase bottom-up growth, via *in situ* formed Ge growth catalysts, is liable for the 1D growth. This method opens a new window of fast and accessible procedures for obtaining crystalline zero-dimensional (0D) and 1D nanostructures. Further engineering of the ST12 nanostructures, *e.g.* through doping, heterostructure formation, to tune the physical properties of this novel material could also be achieved via this bottom-up growth approach. PL studies suggest that the ST12-Ge nanowires possess a bandgap with direct character  $\sim 0.64$  eV, which is in contrast to the previous theoretical suggestion that bulk ST12-Ge is an indirect semiconductor. Overall, we have demonstrated that bottom-up grown ST12-Ge nanowires represent a low-cost approach to meet the growing demand for direct-gap group-IV optoelectronic materials suitable for monolithic integration on Si.

### 3.6. Appendix

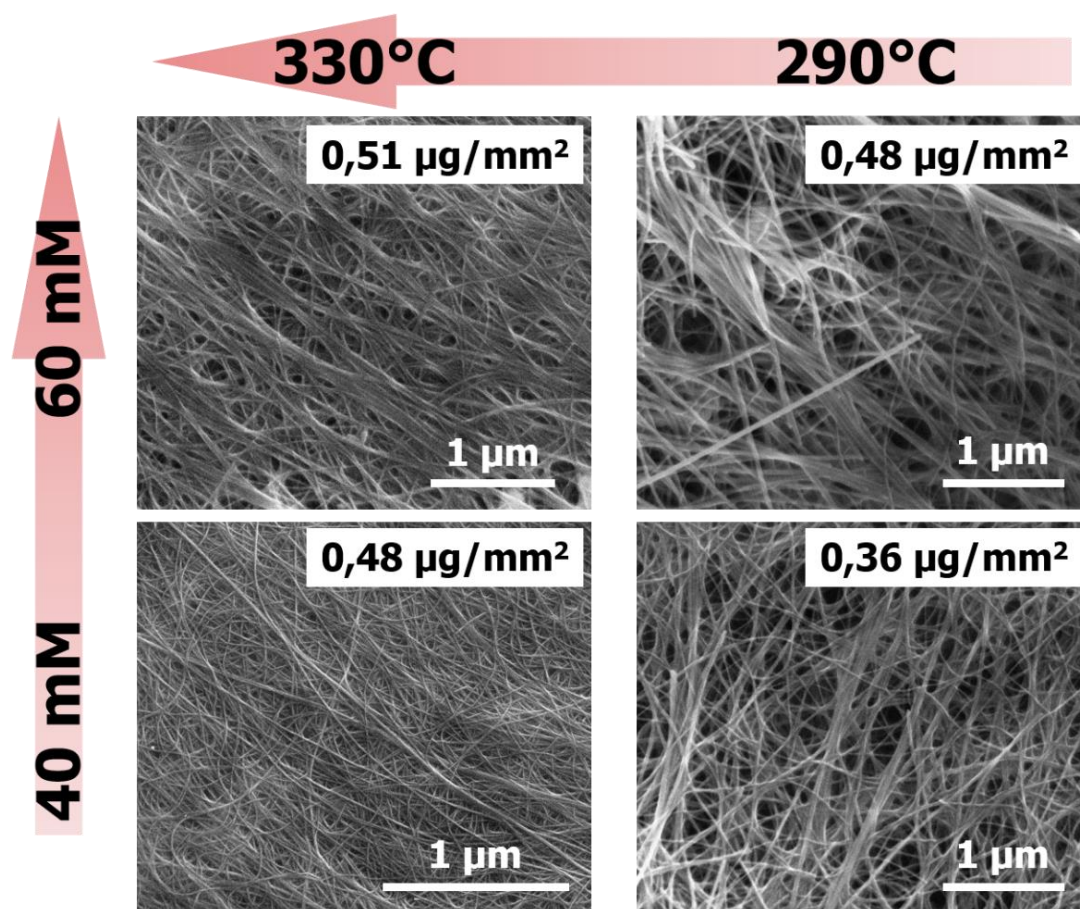


**Figure A3.1.** SEM images of ST12-Ge nanowires obtained as a function of reaction temperature and precursor (DPG) concentration. Corresponding yield of every reaction condition on top-right of SEM images.

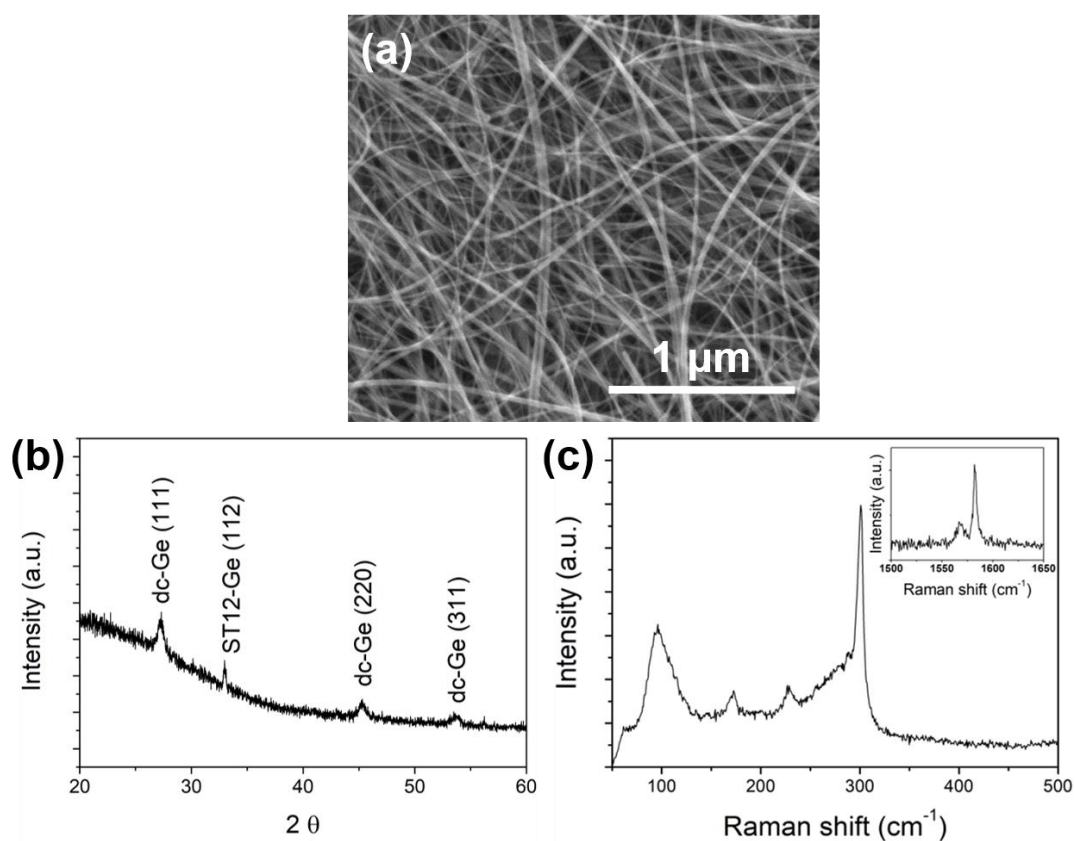


**Figure A3.2.** (a) SEM micrographs of mixed phase of dc-Ge and ST12-Ge nanowires grown at a temperature of 350 °C from a 60 mM DPG/toluene solution and a filling volume of 60 % of the total reactor's volume. (b) XRD pattern of a nanowire sample showing the formation of both dc-Ge and ST12-Ge crystal structures. (c) Raman spectrum of the mixture of dc-Ge and ST12-Ge nanowires. Inset of (c) depicts a detailed view of the C-C G-band area.

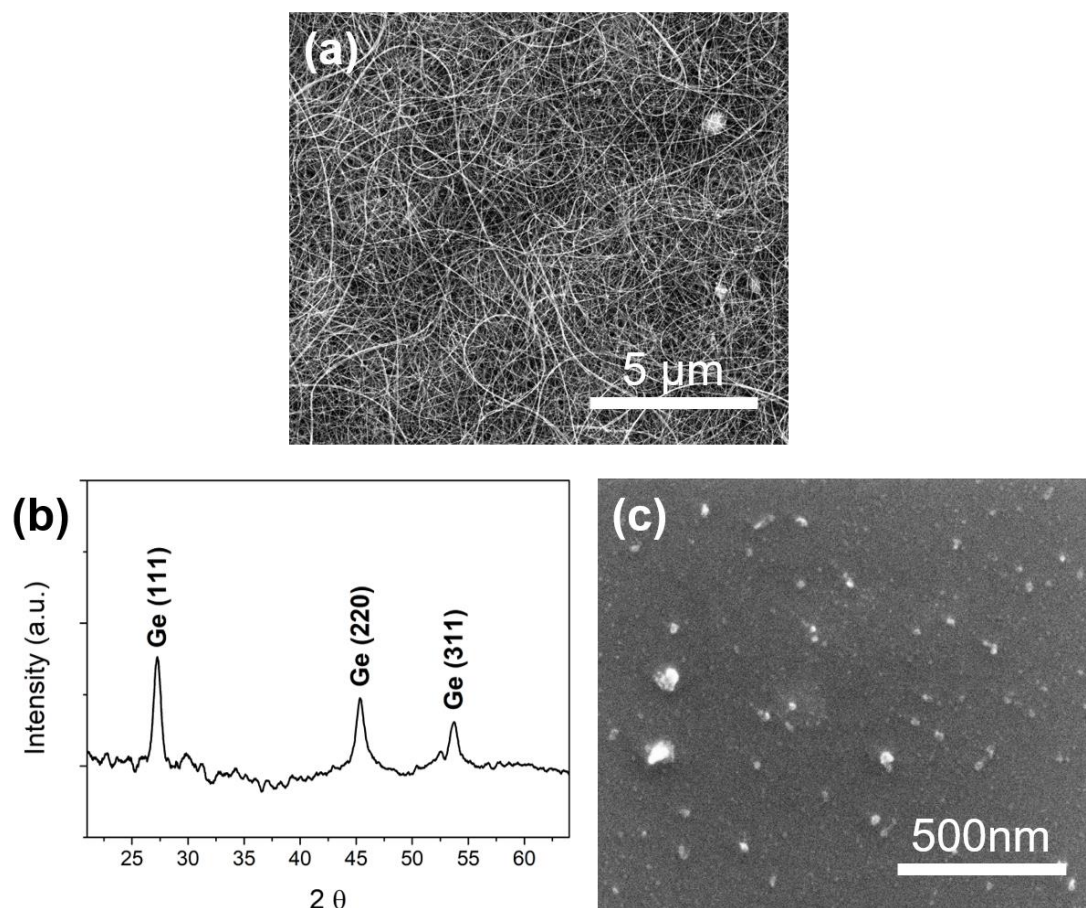


**Figure A3.3.** (a) SEM micrographs of dc-Ge nanowires grown at a temperature of 440 °C from a 60 mM DPG/toluene solution and a filling volume of 60 % of the total reactor's volume. (b) XRD pattern of a nanowire sample showing the formation of dc-Ge crystal structure. (c) SEM micrographs of dc-Ge nanoparticles grown at a temperature of 440 °C from a 20 mM DPG/toluene solution and a filling volume of 20 % of the total reactor's volume.

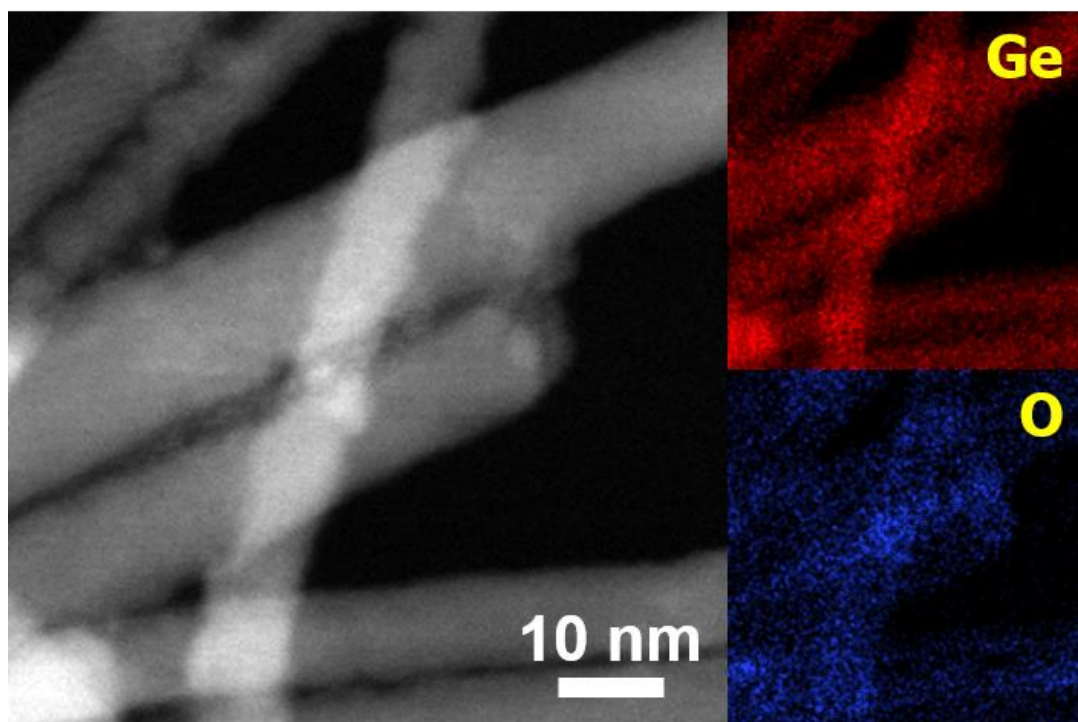


**Figure A3.4.** EDX spectrum recorded from the body of several ST12-Ge nanowires showing the sole presence of Ge and native O.

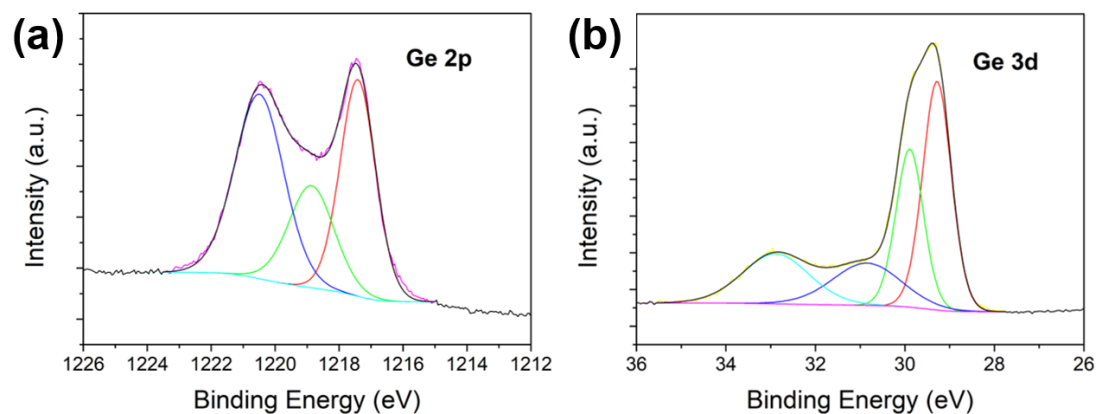


**Figure A3.5.** XPS spectra from ST12-Ge nanowires of the (a) Ge 2p and (b) Ge 3d regions. Oxidation peaks can be appreciated on a sample exposed to air during a year.



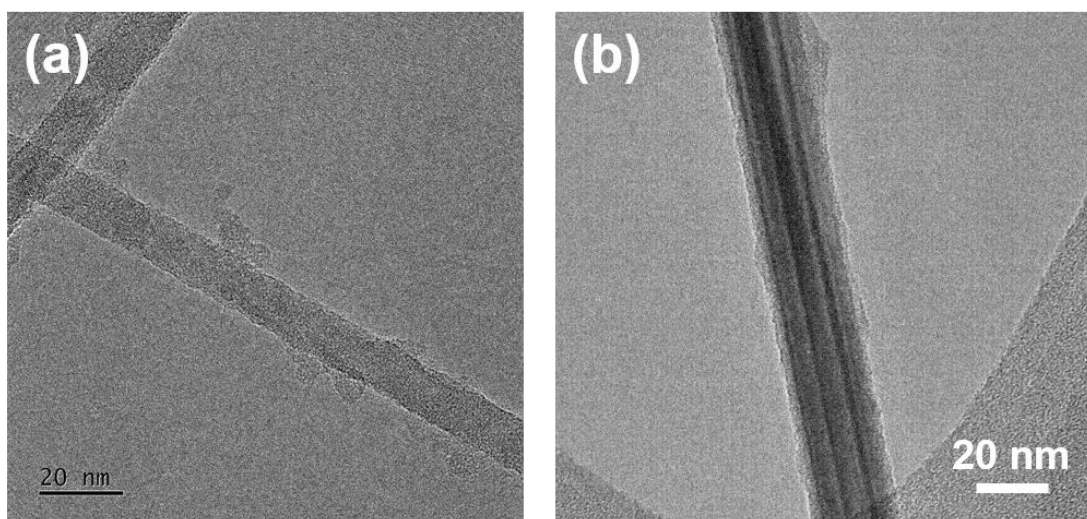


**Figure A3.6.** (a), (b) HRSTEM images of ST12-Ge nanowires where the discontinuous uneven amorphous carbonaceous coating can be observed along the lengths of the nanowires.



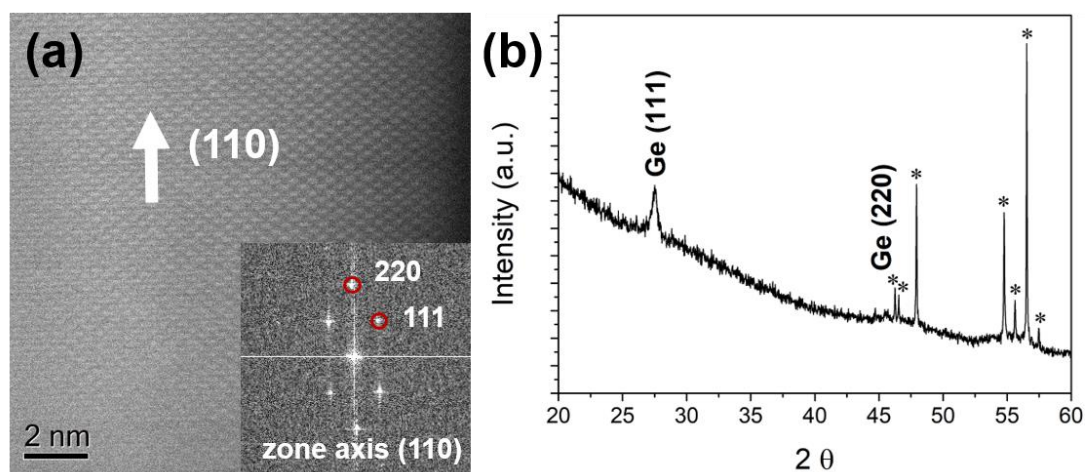


**Figure A3.7.** (a) HRSTEM image of originally ST12-Ge nanowires, restructured into dc-Ge nanowires once the carbonaceous coating was removed, with the stacking of (110) plane along the nanowire growth axis. Inset shows the FFT pattern from the displayed dc-Ge nanowire. (b) XRD pattern of a nanowire sample showing the formation of dc-Ge crystal structure. Stars depict peaks corresponding to Si substrate.

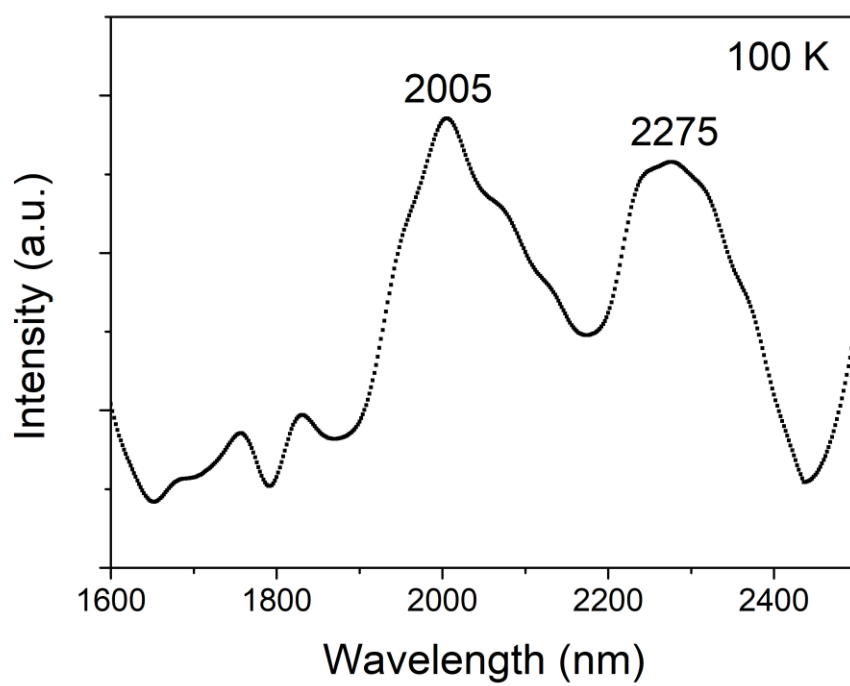


**Figure A3.8.** NIR PL spectra of ST12-Ge nanowires obtained at 100 K.

### 3.7. References

- (1) Zhao, Z.; Zhang, H.; Kim, D. Y.; Hu, W.; Bullock, E. S.; Strobel, T. A. Properties of the Exotic Metastable ST12 Germanium Allotrope. *Nat. Commun.* **2017**, *8*, 1–8.
- (2) Malone, B. D.; Cohen, M. L. Electronic Structure, Equation of State, and Lattice Dynamics of Low-Pressure Ge Polymorphs. *Phys. Rev. B - Condens. Matter Mater. Phys.* **2012**, *86* (5), 1–7.
- (3) Selli, D.; Baburin, I. A.; Martoňák, R.; Leoni, S. Novel Metastable Metallic and Semiconducting Germaniums. *Sci. Rep.* **2013**, *3* (1), 1466.
- (4) Malone, B. D.; Sau, J. D.; Cohen, M. L. Ab Initio Study of the Optical Properties of Si-XII. *Phys. Rev. B - Condens. Matter Mater. Phys.* **2008**, *78* (16), 161202.
- (5) Vörös, M.; Wippermann, S.; Somogyi, B.; Gali, A.; Rocca, D.; Galli, G.; Zimanyi, G. T. Germanium Nanoparticles with Non-Diamond Core Structures for Solar Energy Conversion. *J. Mater. Chem. A* **2014**, *2* (25), 9820–9827.
- (6) Yeo, K. H.; Suk, S. D.; Li, M.; Yeoh, Y. Y.; Cho, K. H.; Hong, K. H.; Yun, S. K.; Lee, M. S.; Cho, N.; Lee, K.; Hwang, D.; Park, B.; Kim, D. W.; Park, D.; Ryu, B. II. Gate-All-around (GAA) Twin Silicon Nanowire MOSFET (TSNWFET) with 15 Nm Length Gate and 4 Nm Radius Nanowires. In *Technical Digest - International Electron Devices Meeting, IEDM*; 2006.
- (7) Malone, B. D.; Sau, J. D.; Cohen, M. L. Ab Initio Survey of the Electronic Structure of Tetrahedrally Bonded Phases of Silicon. *Phys. Rev. B - Condens. Matter Mater. Phys.* **2008**, *78* (3), 035210.
- (8) Weill, G.; Mansot, J. L.; Sagon, G.; Carlone, C.; Besson, J. M. Characterisation of Si III and Si IV, Metastable Forms of Silicon at Ambient Pressure. *Semicond. Sci. Technol.* **1989**, *4* (4), 280–282.
- (9) Mujica, A.; Pickard, C. J.; Needs, R. J. Low-Energy Tetrahedral Polymorphs of Carbon, Silicon, and Germanium. *Phys. Rev. B - Condens. Matter Mater. Phys.* **2015**, *91* (21), 214104.
- (10) Zhao, Z.; Tian, F.; Dong, X.; Li, Q.; Wang, Q.; Wang, H.; Zhong, X.; Xu, B.; Yu, D.; He, J.; Wang, H. T.; Ma, Y.; Tian, Y. Tetragonal Allotrope of Group 14 Elements. *J. Am. Chem. Soc.* **2012**, *134* (30), 12362–12365.
- (11) Pickard, C. J.; Needs, R. J. Hypothetical Low-Energy Chiral Framework

- Structure of Group 14 Elements. *Phys. Rev. B - Condens. Matter Mater. Phys.* **2010**, *81* (1), 014106.
- (12) Mujica, A.; Rubio, A.; Muñoz, A.; Needs, R. J. High-Pressure Phases of Group-IV, III-V, and II-VI Compounds. *Rev. Mod. Phys.* **2003**, *75* (3), 863–912.
  - (13) Sapelkin, A. V.; Karavanskii, V. A.; Kartopu, G.; Es-Souni, M.; Luklinska, Z. Raman Study of Nano-Crystalline Ge under High Pressure. *Phys. status solidi* **2007**, *244* (4), 1376–1380.
  - (14) Coppari, F.; Chervin, J. C.; Congeduti, A.; Lazzeri, M.; Polian, A.; Principi, E.; Di Cicco, A. Pressure-Induced Phase Transitions in Amorphous and Metastable Crystalline Germanium by Raman Scattering, x-Ray Spectroscopy, and Ab Initio Calculations. *Phys. Rev. B - Condens. Matter Mater. Phys.* **2009**, *80* (11), 1–9.
  - (15) Bundy, F. P.; Kasper, J. S. A New Dense Form of Solid Germanium. *Science* **1963**, *139* (3552), 340–341.
  - (16) Cho, Y. J.; Im, H. S.; Kim, H. S.; Myung, Y.; Back, S. H.; Lim, Y. R.; Jung, C. S.; Jang, D. M.; Park, J.; Cha, E. H.; Cho, W. Il; Shojaei, F.; Kang, H. S. Tetragonal Phase Germanium Nanocrystals in Lithium Ion Batteries. *ACS Nano* **2013**, *7* (10), 9075–9084.
  - (17) Ikoma, Y.; Toyota, T.; Ejiri, Y.; Saito, K.; Guo, Q.; Horita, Z. Allotropic Phase Transformation and Photoluminescence of Germanium Nanograins Processed by High-Pressure Torsion. *J. Mater. Sci.* **2015**, *51* (1), 138–143.
  - (18) Mujica, A.; Needs, R. J. First-Principles Calculations of the Structural Properties, Stability, and Band Structure of Complex Tetrahedral Phases of Germanium: ST12 and BC8. *Phys. Rev. B* **1993**, *48* (23), 17010–17017.
  - (19) Joannopoulos, J. D.; Cohen, M. L. Electronic Properties of Complex Crystalline and Amorphous Phases of Ge and Si. I. Density of States and Band Structures. *Phys. Rev. B* **1973**, *7* (6), 2644–2657.
  - (20) Sato, S.; Nozaki, S.; Morisaki, H. Density of States of the Tetragonal-Phase Germanium Nanocrystals Using x-Ray Photoelectron Spectroscopy. *Appl. Phys. Lett.* **1998**, *72* (19), 2460–2462.
  - (21) Islamgaliev, R. K.; Kuzel, R.; Obraztsova, E. D.; Burianek, J.; Chmelik, F.; Valiev, R. Z. TEM, XRD and Raman Scattering of Germanium Processed by Severe Deformation. *Mater. Sci. Eng. A* **1998**, *249* (1–2), 152–157.
  - (22) Jang, J. Il; Lance, M. J.; Wen, S.; Pharr, G. M. Evidence for Nanoindentation-

- Induced Phase Transformations in Germanium. *Appl. Phys. Lett.* **2005**, *86* (13), 1–3.
- (23) Chiu, H. W.; Kauzlarich, S. M. Investigation of Reaction Conditions for Optimal Germanium Nanoparticle Production by a Simple Reduction Route. *Chem. Mater.* **2006**, *18* (4), 1023–1028.
  - (24) Bradby, J. E.; Williams, J. S.; Wong-Leung, J.; Swain, M. V.; Munroe, P. Nanoindentation-Induced Deformation of Ge. *Appl. Phys. Lett.* **2002**, *80* (15), 2651–2653.
  - (25) Jiang, J.; Chen, K.; Huang, X.; Li, Z.; Feng, D. New Crystalline Structure for Nanometer-Sized Ge Microcrystallites Prepared by Plasma Enhanced Chemical Vapor Deposition. *Appl. Phys. Lett.* **1994**, *65* (14), 1799–1801.
  - (26) Sato, S.; Nozaki, S.; Morisaki, H. Photo-Oxidation of Germanium Nanostructures Deposited by the Cluster-Beam Evaporation Technique. *J. Appl. Phys.* **1997**, *81* (3), 1518–1521.
  - (27) Sato, S.; Nozaki, S.; Morisaki, H.; Iwase, M. Tetragonal Germanium Films Deposited by the Cluster-Beam Evaporation Technique. *Appl. Phys. Lett.* **1995**, *66* (23), 3176.
  - (28) Kim, S. J.; Quy, O. K.; Chang, L. S.; Stach, E. A.; Handwerker, C. A.; Wei, A. Formation of the ST12 Phase in Nanocrystalline Ge at Ambient Pressure. *J. Mater. Chem.* **2010**, *20* (2), 331–337.
  - (29) Huston, L. Q.; Johnson, B. C.; Haberl, B.; Wong, S.; Williams, J. S.; Bradby, J. E. Thermal Stability of Simple Tetragonal and Hexagonal Diamond Germanium. *J. Appl. Phys.* **2017**, *122* (17), 175108.
  - (30) Kasper, J. S.; Richards, S. M. The Crystal Structures of New Forms of Silicon and Germanium. *Acta Crystallogr.* **1964**, *17* (6), 752–755.
  - (31) Winer, K.; Wooten, F. Vibrational Properties of Metastable Phases of Si and Ge. *Phys. status solidi* **1986**, *136* (2), 519–527.
  - (32) Kazimierski, P.; Jóźwiak. Transition from Amorphous Semiconductor to Amorphous Insulator in Hydrogenated Carbon-Germanium Films Investigated by IR Spectroscopy. *J. Non. Cryst. Solids* **2009**, *355* (4–5), 280–286.
  - (33) Gazicki, M. Plasma Deposition of Thin Carbon/Germanium Alloy Films from Organogermanium Compounds. *Chaos, solitons and fractals* **1999**, *10* (12), 1983–2017.
  - (34) Zhu, J. Q.; Jiang, C. Z.; Han, J. C.; Yu, H. L.; Wang, J. Z.; Jia, Z. C.; Chen, R.

- R. Optical and Electrical Properties of Nonstoichiometric A-Ge  $1-x$  C  $x$  Films Prepared by Magnetron Co-Sputtering. *Appl. Surf. Sci.* **2012**, 258 (8), 3877–3881.
- (35) Cardona, M. Vibrational Spectra of Hydrogen in Silicon and Germanium. *Phys. status solidi* **1983**, 118 (2), 463–481.
  - (36) Li, C.-P.; Lee, C.-S.; Ma, X.-L.; Wang, N.; Zhang, R.-Q.; Lee, S.-T. Growth Direction and Cross-Sectional Study of Silicon Nanowires. *Adv. Mater.* **2003**, 15 (78), 607–609.
  - (37) Ma, D. D. D.; Lee, C. S.; Au, F. C. K.; Tong, S. Y.; Lee, S. T. Small-Diameter Silicon Nanowire Surfaces. *Science* **2003**, 299 (5614), 1874–1877.
  - (38) Wu, Y. S.; Bagchi, S.; Garg, S.; Singh, N.; Tsai, T. Controlled Growth and Structures of Molecular-Scale Silicon Nanowires. *Nano Lett.* **2004**, 4 (3), 433–442.
  - (39) Hobbs, R. G.; Barth, S.; Petkov, N.; Zirngast, M.; Marschner, C.; Morris, M. A.; Holmes, J. D. Seedless Growth of Sub-10 Nm Germanium Nanowires. *J. Am. Chem. Soc.* **2010**, 132 (39), 13742–13749.
  - (40) Lotty, O.; Hobbs, R.; O'Regan, C.; Hlina, J.; Marschner, C.; O'Dwyer, C.; Petkov, N.; Holmes, J. D. Self-Seeded Growth of Germanium Nanowires: Coalescence and Ostwald Ripening. *Chem. Mater.* **2013**, 25 (2), 215–222.
  - (41) Connaughton, S.; Hobbs, R.; Lotty, O.; Holmes, J. D.; Krstić, V. Variation of Self-Seeded Germanium Nanowire Electronic Device Functionality Due to Synthesis Condition Determined Surface States. *Adv. Mater. Interfaces* **2015**, 2 (5), 1400469.
  - (42) Chockla, A. M.; Korgel, B. A. Seeded Germanium Nanowire Synthesis in Solution. *J. Mater. Chem.* **2009**, 19 (7), 996–1001.
  - (43) Zaitseva, N.; Harper, J.; Gerion, D.; Saw, C. Unseeded Growth of Germanium Nanowires by Vapor-Liquid-Solid Mechanism. *Appl. Phys. Lett.* **2005**, 86 (5), 1–3.
  - (44) Yu, J.; Zhang, C.; Wu, W.; Cai, Y.; Zhang, Y. Nodes-Connected Silicon-Carbon Nanofibrous Hybrids Anodes for Lithium-Ion Batteries. *Appl. Surf. Sci.* **2021**, 548, 148944.
  - (45) Chiu, H. W.; Chervin, C. N.; Kauzlarich, S. M. Phase Changes in Ge Nanoparticles. *Chem. Mater.* **2005**, 17 (19), 4858–4864.
  - (46) Pizzagalli, L.; Klepeis, J. E.; Gygi, F. Structure and Stability of Germanium

- Nanoparticles. *Phys. Rev. B - Condens. Matter Mater. Phys.* **2001**, *63* (16), 165324.
- (47) Osten, H. J.; Bugiel, E.; Zaumseil, P. Growth of an Inverse Tetragonal Distorted SiGe Layer on Si(001) by Adding Small Amounts of Carbon. *Appl. Phys. Lett.* **1994**, *64* (25), 3440–3442.
  - (48) Diao, J.; Gall, K.; Dunn, M. L. Surface-Stress-Induced Phase Transformation in Metal Nanowires. *Nat. Mater.* **2003**, *2* (10), 656–660.
  - (49) Khazaei, M.; Liang, Y.; Venkataramanan, N. S.; Kawazoe, Y. Polymerization of Cyanoacetylene under Pressure: Formation of Carbon Nitride Polymers and Bulk Structures. *Phys. Rev. B - Condens. Matter Mater. Phys.* **2012**, *85* (5), 054101.
  - (50) Stange, D.; Wirths, S.; Von Den Driesch, N.; Mussler, G.; Stoica, T.; Ikonik, Z.; Hartmann, J. M.; Mantl, S.; Grützmacher, D.; Buca, D. Optical Transitions in Direct-Bandgap Ge<sub>1</sub>-XSn<sub>x</sub>Alloys. *ACS Photonics* **2015**, *2* (11), 1539–1545.
  - (51) Ryu, M. Y.; Harris, T. R.; Yeo, Y. K.; Beeler, R. T.; Kouvetakis, J. Temperature-Dependent Photoluminescence of Ge/Si and Ge<sub>1</sub>-YSn<sub>y</sub>/Si, Indicating Possible Indirect-to-Direct Bandgap Transition at Lower Sn Content. *Appl. Phys. Lett.* **2013**, *102* (17), 1–5.
  - (52) Manna, S.; Katiyar, A.; Aluguri, R.; Ray, S. K. Temperature Dependent Photoluminescence and Electroluminescence Characteristics of Core-Shell Ge-GeO<sub>2</sub> Nanowires. *J. Phys. D: Appl. Phys.* **2015**, *48* (21), 215103.
  - (53) Doherty, J.; Biswas, S.; Saladukha, D.; Ramasse, Q.; Bhattacharya, T. S.; Singha, A.; Ochalski, T. J.; Holmes, J. D. Influence of Growth Kinetics on Sn Incorporation in Direct Band Gap Ge<sub>1-x</sub>Sn<sub>x</sub> Nanowires. *J. Mater. Chem. C* **2018**, *6*, 8738–8750.
  - (54) Biswas, S.; Doherty, J.; Saladukha, D.; Ramasse, Q.; Majumdar, D.; Upmanyu, M.; Singha, A.; Ochalski, T.; Morris, M. A.; Holmes, J. D. Non-Equilibrium Induction of Tin in Germanium: Towards Direct Bandgap Ge<sub>1</sub>-XSn<sub>x</sub> Nanowires. *Nat. Commun.* **2016**, *7*, 114005.
  - (55) Lezama, I. G.; Arora, A.; Ubaldini, A.; Barreateau, C.; Giannini, E.; Potemski, M.; Morpurgo, A. F. Indirect-to-Direct Band Gap Crossover in Few-Layer MoTe<sub>2</sub>. *Nano Lett.* **2015**, *15* (4), 2336–2342.
  - (56) Wirths, S.; Geiger, R.; Von Den Driesch, N.; Mussler, G.; Stoica, T.; Mantl, S.; Ikonik, Z.; Luysberg, M.; Chiussi, S.; Hartmann, J. M.; Sigg, H.; Faist, J.; Buca,

- D.; Grützmacher, D. Lasing in Direct-Bandgap GeSn Alloy Grown on Si. *Nat. Photonics* **2015**, 9 (2), 88–92.
- (57) Varshni, Y. P. Temperature Dependence of the Energy Gap in Semiconductors. *Physica* **1967**, 34 (1), 149–154.
- (58) Julsgaard, B.; Pedersen, C.; Buca, D.; Driesch, N. von den; Tidemand-Lichtenberg, P.; Ikonik, Z.; Buca, D. Carrier Lifetime of GeSn Measured by Spectrally Resolved Picosecond Photoluminescence Spectroscopy. *Photonics Res. Vol. 8, Issue 6, pp. 788-798* **2020**, 8 (6), 788–798.
- (59) Lautenschlager, P.; Allen, P. B.; Cardona, M. Temperature Dependence of Band Gaps in Si and Ge. *Phys. Rev. B* **1985**, 31 (4), 2163–2171.
- (60) Allen, P. B.; Cardona, M. Temperature Dependence of the Direct Gap of Si and Ge. *Phys. Rev. B* **1983**, 27 (8), 4760–4769.



# **Chapter 4**

## **Batch-produced self-seeded Germanium-Tin Alloy Nanowires as Highly Efficient Li-Ion Battery Anodes**

Data from this chapter is currently in preparation for publication. Consequently, sections of the chapter such as the abstract and introduction may contain repeating concepts and paragraphs. I synthesised and performed the elemental and structural analysis of the nanowires reported in this chapter. I co-wrote the paper with SB and JDH and analysed Raman, TEM and electrochemical data obtained from collaborators.

Garcia-Gil, A.; Biswas, S.; McNulty, D.; Roy, A.; Ryan, K.M.; Nicolosi, V.; Holmes, J. D., 'Batch-produced self-seeded Germanium-Tin Alloy Nanowires as Highly Efficient Li-Ion Battery Anodes'. Submitted August 2021.

#### 4.1. Abstract

Ge<sub>1-x</sub>Sn<sub>x</sub> nanomaterials have potential applications in optical, electronic and energy storage devices. Considerable research has recently been undertaken on Ge<sub>1-x</sub>Sn<sub>x</sub> nanostructures, including Ge<sub>1-x</sub>Sn<sub>x</sub> nanowires. However, many Ge<sub>1-x</sub>Sn<sub>x</sub> nanowires synthesised to date are thick and short with low aspect ratios (< 50) and have tapered morphologies. Here, we report the fabrication of a high aspect ratio (> 440) Ge<sub>1-x</sub>Sn<sub>x</sub> nanowires with super-thin (~ 9 nm) diameter using a simple solvothermal-like growth method under supercritical toluene conditions at a reaction temperature of 440 °C. Ge<sub>1-x</sub>Sn<sub>x</sub> nanowires were grown with varying amounts of Sn in Ge lattice, between 3.1 to 10.2 at.%. The growth of the Ge<sub>1-x</sub>Sn<sub>x</sub> alloy nanowires follows a vapour-liquid-solid (VLS) paradigm, where nanowires are directly formed on titanium substrates for electrical testing as potential Li-ion anodes. No additional catalytic seeds were required for the growth of the nanowires. The electrochemical performance of the Ge<sub>1-x</sub>Sn<sub>x</sub> nanowires as an anode material for Li-ion batteries was investigated via galvanostatic cycling and detailed analysis of differential capacity plots. The dimensions of the nanowires, and the amount of Sn in Ge, was critical to achieve a high specific capacity and capacity retention. Ge<sub>1-x</sub>Sn<sub>x</sub> nanowires with the highest aspect ratios and with the lowest Sn content (3.1. at.%) demonstrated exceptional capacity retention of ~ 90 and 86 % from the 10<sup>th</sup> to the 100<sup>th</sup> and 150<sup>th</sup> cycles respectively, while maintaining a specific capacity value of 1176 mA h g<sup>-1</sup> and 1127 mA h g<sup>-1</sup> after the 100 cycles and 150 cycles respectively.

## 4.2. Introduction

Over the past two decades, the growth and properties of  $\text{Ge}_{1-x}\text{Sn}_x$  alloy, mainly in thin-film form, have been extensively studied.<sup>1</sup> Theoretical and experimental studies have depicted a series of interesting features about  $\text{Ge}_{1-x}\text{Sn}_x$  alloys, such as (i) higher carrier mobility (proportional to Sn content)<sup>2</sup> compared to  $\text{Si}^3$  and  $\text{Ge}^4$  individually, (ii) a tunable bandgap,<sup>5</sup> (iii) a narrow direct bandgap structure (with  $> 6.5$  at.% Sn)<sup>6,7</sup> and (iv) a low-synthesis temperature (eutectic point at  $231.1^\circ\text{C}$ ) compared to Si and Ge<sup>8</sup>.  $\text{Ge}_{1-x}\text{Sn}_x$  alloys are also deemed to be very versatile and a Si-friendly technology, *i.e.* compatible with industrial Si processing. Specifically, the direct bandgap of  $\text{Ge}_{1-x}\text{Sn}_x$  alloys makes them an ideal material for photonics and optoelectronics, *e.g.* infrared lasers<sup>9–11</sup> and photodectors<sup>12,13</sup>, light-emitting diodes<sup>14–16</sup>, whereas their high electronic conductivity makes them ideal for high-speed field-effect transistors<sup>17,18</sup> and energy storage devices, *e.g.* Li-ion batteries<sup>19,20</sup>.

Li-ion batteries, in particular, claim a suitable replacement for graphite as an anode material to satisfy the increasing demands for batteries with high power and energy densities.<sup>21,22</sup> Ge and Sn, display higher theoretical capacities than graphite ( $1620\text{ mA h g}^{-1}$ ,  $991\text{ mA h g}^{-1}$  and  $372\text{ mA h g}^{-1}$ , respectively)<sup>23,24</sup> and, as consequence, Ge and  $\text{Ge}_{1-x}\text{Sn}_x$  alloys have been put forward as an alternative to graphite for high specific capacity commercial cells.<sup>19,25,26</sup> Ge also exhibit a high electrical conductivity (two orders of magnitude higher than Si) and high Li-ion diffusion at room temperature ( $\sim 400$  times greater than that of Li ions in Si).<sup>23,27</sup> The combination of two active Li-ion materials, Ge and Sn, can result in improved conduction paths with high capacity retention, due to the different levels of expansion of Ge and Sn components in the alloy upon lithiation.  $\text{Ge}_{1-x}\text{Sn}_x$  alloy nanostructures have shown

improved conduction paths with higher capacity retention and enhanced cycling performance, in comparison with their individual components.<sup>26,28–30</sup> Further to this, the relative cost of the Ge anode materials could be also reduced by alloying it with cheaper and more abundant elements, such as Sn.

However, the main drawback when using Ge and  $\text{Ge}_{1-x}\text{Sn}_x$  in Li-ion battery anode is the large volume changes encountered upon lithiation/delithiation, which leads to structural cracking and pulverisation, resulting in capacity fading and poor cycling life. Among other solutions, nanostructuring (microflowers,<sup>31</sup> nanoparticles,<sup>32</sup> branched nanostructures,<sup>33</sup> nanowires,<sup>20</sup> nanotubes,<sup>34</sup> *etc.*) of anode materials has been screened to mitigate this obstacle. Specifically, the many benefits of using nanowires as anode materials in Li-ion batteries include high interfacial area, short Li-ion diffusion path lengths, good electrical conductivity along their lengths and the unique ability to convert from crystalline to amorphous phases while preserving their structural stability over many cycles. Nanowire structure is particularly suitable to accommodate high Sn incorporation due to a series of advantages such as strain accommodation due to nanoscale dimensions, growth at lower reaction temperatures *etc.* At the same time nanowire structure has attracted much attention for Li-ion batteries due to its advantages in providing one-dimensional conductive path, large specific surface area, short diffusion path of charge carriers (especially thin nanowires), more space to buffer volume change and high crack resistance.<sup>35</sup> Developing new, simpler and scalable fabrication methods to tune Sn incorporation in the  $\text{Ge}_{1-x}\text{Sn}_x$  nanostructure and for the generation of long and thinner nanowire morphologies for superior electrochemical performances is key for the development of Li-ion battery anodes based on GeSn alloys.<sup>35</sup>

Low-temperature chemical vapour deposition (CVD) and solution-based methods have been employed to synthesise  $\text{Ge}_{1-x}\text{Sn}_x$  nanowires with a Sn incorporation far in excess ( $x \geq 0.10$ ) of the equilibrium concentration of Sn in Ge.<sup>8,36,37</sup> Typically, bottom-up growth processes employing metal catalysts are used for synthesising  $\text{Ge}_{1-x}\text{Sn}_x$  nanowires.<sup>25,38</sup> The use of external catalysts can enhance Sn incorporation in Ge nanowires, but can also lead to impurity incorporation from the metallic seeds into the nanowire structure; which can influence the mechanical and electrical properties of the nanowires and potentially the charge capacity of Li-ion cells. Also, the application of  $\text{Ge}_{1-x}\text{Sn}_x$  alloy nanowires in Li-ion batteries is seriously hindered by the tendency for Sn to segregate at high concentrations and the short and tapered morphologies of  $\text{Ge}_{1-x}\text{Sn}_x$  nanowires synthesised, not suitable for high capacity anodes with large capacity retentions.<sup>8,28,36,38</sup> Additionally, the necessity for scalability of  $\text{Ge}_{1-x}\text{Sn}_x$  nanowires have placed a different set of demands on synthetic protocols. For Li-ion anodes, the synthesis of long, high-density nanowires grown without any additional catalyst and directly onto the conducting substrates via a simple and scalable method is ideal.<sup>39</sup>

Here we report, the fabrication of  $\text{Ge}_{1-x}\text{Sn}_x$  ( $x = 0.03, 0.08$  and  $0.10$ ) alloy nanowires using a simple, single-step batch synthesis method, without the need for additional catalysts (metal or metalloid) or templates.  $\text{Ge}_{1-x}\text{Sn}_x$  nanowires were synthesised in supercritical toluene atmosphere directly onto Ti metal disc, used as current collectors for Li-ion battery. This direct growth eliminates the requirement for conductive slurries and binders. The electrochemical performance of the nanowires as Li-ion battery anode was evaluated via long-term galvanostatic cycling. The  $\text{Ge}_{1-x}\text{Sn}_x$  ( $x = 0.03$ ) nanowires exhibited impressive electrochemical performance in terms of

specific capacity retention, demonstrating a reversible capacity of  $> 1120 \text{ mA h g}^{-1}$  after the 150 cycles, which is close to the theoretical capacity of Ge and outperforming  $\text{Ge}_{1-x}\text{Sn}_x$  nanostructure and most Ge nanowire anodes reported to date.

### 4.3. Experimental

Anhydrous toluene (99.8 %) was purchased from Sigma-Aldrich Co, diphenylgermane (DPG) 95 % was purchased from Fluorochem and tetraethyltin (TET) 97 % was purchased from Alpha Aesar. All chemicals were stored and used under  $\text{N}_2$  in a glovebox ( $\text{O}_2 < 0.1 \text{ ppm}$ ,  $\text{H}_2\text{O} < 0.5 \text{ ppm}$ ).

$\text{Ge}_{1-x}\text{Sn}_x$  nanowire synthesis was carried out in a 1 mL stainless steel reaction cell. Prior to synthesis, the reaction cell and connectors were dried under vacuum at  $125^\circ\text{C}$  for 12 h. Reactions were performed at a temperature of  $440^\circ\text{C}$  on Ti foil disk substrates (0.6 cm in diameter, native oxide present). The reaction temperature was monitored using a thermocouple connected to the reaction vessel and the pressure was monitored via a pressure gauge, connected to one end of the reaction cell. In general, 0.6 ml of a DPG/TET/toluene solution was added to the 1 ml reaction cell and the cell was heated to the desired temperature in a tube furnace for 60 min. The DPG/TET concentration was varied between 20/1 mM, 20/2 mM, 20/4 mM and 20/7 mM, which correspond to mole ratios of 95:5, 90:10, 85:15 and 75:25. The filling volume of the reactant solution, *i.e.* filling fraction, was 60 % of the total reactor's volume (1 ml). The reaction cell was cooled to room temperature after the reaction and disassembled to access the growth substrate. Growth substrates were washed with dry toluene and dried under a  $\text{N}_2$  flow for further characterisation.

***Structural and chemical characterisation.*** Samples were imaged using a FEI Quanta FEG 650 scanning electron microscope (SEM) operated at 15 kV. High-resolution transmission electron microscopy (HRTEM) and high resolution scanning transmission electron microscopy (HRSTEM) imaging were performed on a JEOL 2100 electron microscope operated at 200 kV and an FEI Titan electron microscope, operating at 300 kV. High-angle annular-dark-field scanning-transmission-electron-microscopy (HAADF-STEM) was performed on the FEI Titan electron microscope operated at 300 kV. Raman scattering analysis was performed using a Lab RAM HR (Jobin Yvon) spectrometer equipped with a 488 nm laser source and a CCD detector. The laser was focused on the sample using a 100× objective lens. The laser power was maintained at 0.18 mW throughout the measurement, the spot size used was 660  $\mu\text{m}$  (which corresponds to an intensity of 526  $\text{W m}^{-2}$ ) and the data acquisition time was 50 s. Raman scattering analysis was performed on the nanowires at low power (0.18 mW); to avoid laser-induced heating which can cause structural changes in the nanowires and a red-shift in the Ge-Ge phonon vibration. Raman spectra for the nanowires were recorded over a wavenumber range between 200 - 400  $\text{cm}^{-1}$ . Fourier-transform infrared spectroscopy (FTIR) spectra were recorded on Varian IR 660 infrared spectrometer between the wavelength range of 400 to 4000  $\text{cm}^{-1}$ .

The electrochemical properties of  $\text{Ge}_{1-x}\text{Sn}_x$  nanowire anodes were investigated in two electrode Swagelok cells assembled in an Ar filled glovebox.  $\text{Ge}_{1-x}\text{Sn}_x$  nanowire anodes were cycled against pure Li metal counter electrodes. Electrochemical tests were performed using a BioLogic VSP Potentiostat/Galvanostat. The electrolyte was a 1  $\text{mol dm}^{-3}$  solution of  $\text{LiPF}_6$  in a 1:1 (v/v) mixture of ethylene carbonate in dimethyl carbonate with 3 wt.% vinylene carbonate; 200  $\mu\text{L}$  of electrolyte was used in each

cell. The separator used in all electrochemical tests was Celgard 2400 (diameter: 13 mm, thickness: 25  $\mu\text{m}$ ). A Mettler Toledo XP2U ultra microbalance was used to determine the mass of  $\text{Ge}_{1-x}\text{Sn}_x$  nanowires on the Ti foil substrates. The size of the Ti foil substrates was  $0.5 \times 1.0$  cm, therefore the areal mass loading of the  $\text{Ge}_{1-x}\text{Sn}_x$  nanowires on the stainless-steel current collectors was  $3.45 \mu\text{g mm}^{-2}$ . Cyclic voltammetry was performed at a scan rate of 0.1 mV/s in a potential window of 1.5 - 0.01 V (vs Li/Li<sup>+</sup>). Galvanostatic cycling was performed at 0.2 C in a potential window of 1.5 - 0.01 V (vs Li/Li<sup>+</sup>).

#### 4.4. Results and Discussion

For the application of nanomaterials as Li-ion battery anodes, it is key to develop a simple and cost-effective growth process to produce high-yields of nanomaterials. The growth of  $\text{Ge}_{1-x}\text{Sn}_x$  alloy nanowires was achieved via a single-step solvothermal-like synthesis method, solely in the presence of Ge and Sn precursors under a supercritical toluene atmosphere, *i.e.* without any additional catalytic metal seeds or growth directing templates. Novel self-seeded growth of  $\text{Ge}_{1-x}\text{Sn}_x$  nanostructures was also achieved directly on Ti substrates, which also acted as current collectors for Li-ion anodes. Closed-cell nanowire growth in a supercritical toluene atmosphere provided ideal conditions for fast precursor decomposition and the formation of high-aspect-ratio nanostructures.

Figure 4.1a shows a high magnification SEM image of  $\text{Ge}_{1-x}\text{Sn}_x$  nanowires grown on a Ti substrate at a temperature of 440 °C from a DPG/TET (95:5 molar ratio) solution in toluene. Figures 4.1a and 4.1b highlight the formation of high-aspect-ratio nanowires with uniform radial dimensions along their lengths, with lengths of several



micrometres ( $> 4 \mu\text{m}$ ). The STEM image shown in Figure 4.1b highlights the detailed nature of the  $\text{Ge}_{1-x}\text{Sn}_x$  nanowires, which display moderate bends and kinks along their lengths. The  $\text{Ge}_{1-x}\text{Sn}_x$  nanowires exhibited a mean diameter of  $9.3 (\pm 0.2) \text{ nm}$ , evaluation of  $> 100$  nanowires, and most of the nanowires exceeded a measurable length over  $4 \mu\text{m}$  (see Figure 4.1c); giving an aspect ratio of  $> 4 \times 10^2$ . This is the first report of  $\text{Ge}_{1-x}\text{Sn}_x$  nanowire with diameter below the Bohr radius (which is the preferred separation distance between the electron and hole probability distributions in an exciton) of Ge and with the aspect ratio of  $> 100$ .<sup>1,40</sup> EDX elemental mapping was performed on  $\text{Ge}_{1-x}\text{Sn}_x$  nanowires to confirm the presence of Sn and the uniformity of Sn dissolution in Ge (see Figure 4.1d). EDX maps ruled out the formation of any Sn clusters or aggregates in the core or on the surfaces of the nanowires. The uniformity of Sn dissolution in the alloy nanowires was further confirmed by evaluating over 30 nanowires through EDX point scans at different positions along the lengths of the nanowires, obtaining a mean Sn concentration of  $3.1 (\pm 1.0) \text{ at.}\%$ . Additionally, contrary to the previous  $\text{Ge}_{1-x}\text{Sn}_x$  nanowire growth,<sup>40</sup> no spherical (or hemispherical) growth seeds at the tips of the nanowires were observed, which is typical for catalytic bottom-up growth. The dark-field STEM image shown in Figure 4.1b confirms the morphology of the nanowires and highlights the absence of growth seeds at the tip of the nanowires.

An increase in the Sn concentration in the nanowires and radically different nanowire morphologies were observed when the Ge:Sn precursor mole ratio was varied from 95:5 to 85:15 (in the reaction solution), keeping the amount (moles) of Ge precursor constant. Average Sn incorporation increased from  $3.1 (\pm 1.0) \text{ at.}\%$  to  $7.9 (\pm 2.0)$  and

10.2 ( $\pm 2.5$ ) at.% with the increase of Sn precursor concentration in the initial solution to 90:10 and 85:15 respectively (see Figure A4.1a in Appendix 4.6).

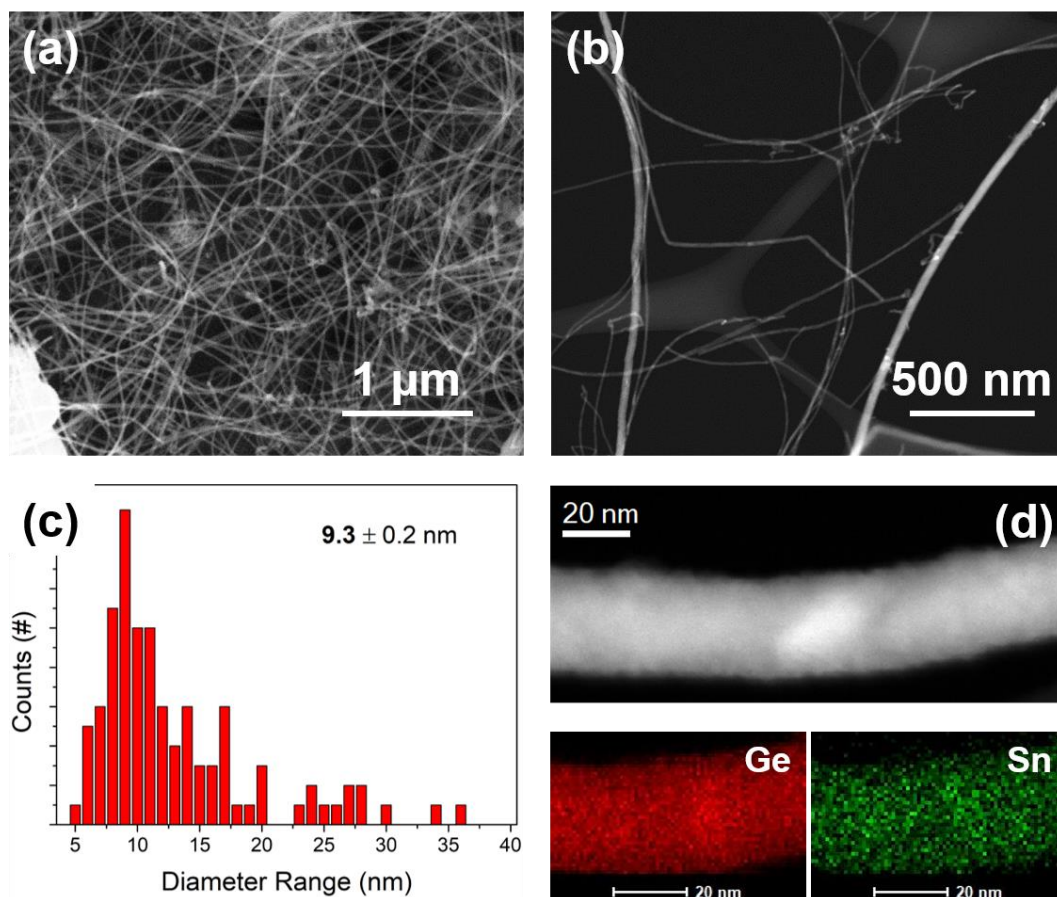


**Figure 4.1.** (a) SEM image of  $\text{Ge}_{1-x}\text{Sn}_x$  nanowires grown on a Ti substrate from a 95:5 mole ratio of DPG/TET initial solution in toluene at a temperature of 440 °C with a mean Sn content of 3.1 at.%. (b) A STEM image of the same batch of nanowires as shown in part (a). (c) Diameter distribution of the nanowires; showing the mean diameter of 9.3 nm and standard deviation of 0.2. (d) HAADF-STEM image and corresponding Ge and Sn EDX maps of a single  $\text{Ge}_{1-x}\text{Sn}_x$  nanowire.

Tin distribution and incorporation was also evaluated in high-Sn content nanowires via EDX line-scans and mapping (see Figure A4.2 in Appendix 4.6). Sn was found to be homogeneously distributed in nanowires with high Sn contents, *i.e.* 7.9 and 10.2 at.%, without any Sn segregation. Line-scans and mapping EDX provide atomic

percentage quantification only when considering the exact thickness of the studied nanowire, data observed on these images (see Figure A4.2 in Appendix 4.6) corresponds to indicative elemental proportions. These nanowires also displayed Sn-rich alloy seeds at their tip, suggesting growth through a vapour-liquid-solid (VLS) growth mechanism.

While nanowires grown with a 95:5 (Ge:Sn) mole ratio reaction solution displayed long, thin nanowires with no spherical seeds at their tips (see Figures 4.1a and 4.1b), nanowires grown from 90:10 and 85:15 (Ge:Sn) solution are 5 to 10 times thicker (mean diameters of  $48.3 (\pm 2.0)$  and  $108.8 (\pm 2.4)$  nm) than  $\text{Ge}_{1-x}\text{Sn}_x$  nanowires grown from 95:5 (Ge:Sn) solution. Spherical seeds, typical for catalytic bottom-up growth, were also observed at the tips of these nanowires (see Figure A4.1b in Appendix 4.6). These nanowires also revealed appreciable inverse tapering along their lengths (see Figure A4.1b in Appendix 4.6); up to 100 nm diameter difference along the length of a given nanowire.  $\text{Ge}_{1-x}\text{Sn}_x$  nanowires generated from the 90:10 solution exhibited a mixed morphology of long and uniform nanowires, with the presence of inverse tapered and short nanowires. The amount of inverse tapered nanowires increased and more pronounced tapering was observed in  $\text{Ge}_{1-x}\text{Sn}_x$  nanowires generated from 85:15  $\text{Ge}_{1-x}\text{Sn}_x$  solution. Tapered nanowires were measured at the base of the seed as a reference diameter value. A radical change in the nanowire morphology with Sn concentrations suggests a very different growth setting with a higher amount of Sn in the initial reaction solution.

***Chemical & structural analysis of  $\text{Ge}_{1-x}\text{Sn}_x$  nanowires.*** Raman spectroscopy was also used to quantify the Sn inclusion in the  $\text{Ge}_{1-x}\text{Sn}_x$  nanowires. Figure 4.2a shows

Raman spectra from  $\text{Ge}_{1-x}\text{Sn}_x$  alloy nanowires with different Sn concentrations. The Ge-Ge LO Raman mode recorded from the nanowires was observed to gradually redshift from bulk Ge<sup>40,41</sup> ( $303\text{ cm}^{-1}$ ), with the LO peak at  $298$  to  $293\text{ cm}^{-1}$  for  $\text{Ge}_{1-x}\text{Sn}_x$  nanowires with 3.1 and 10.2 at.% Sn, respectively. A subtle redshift ( $< 5\text{ cm}^{-1}$ ) in the Ge-Ge LO mode has previously been reported for phase pure Ge nanowires with diameters  $< 50\text{ nm}$ , in comparison with bulk Ge, due to the phonon confinement effect.<sup>19,41</sup> The Raman shift towards the lower wavenumbers in the  $\text{Ge}_{1-x}\text{Sn}_x$  nanowires could therefore be due to both an alloying effect (e.g. mass disorder, bond distortion) and phonon confinement (especially for  $\text{Ge}_{1-x}\text{Sn}_x$  ( $x = 0.03$ ) nanowires with  $9.3\text{ nm}$  average diameter); where phonon confinement can also result in the peak broadening. As all Raman measurements were performed at room temperature and at low laser power, the peak shift and broadening observed for the  $\text{Ge}_{1-x}\text{Sn}_x$  nanowires was not due to sample heating. The largest Raman shift was observed for the thickest nanowires (mean diameter of  $108.8\text{ nm}$ ) with the highest Sn incorporation (10.2 at.%) along with the maximum broadening (FWHM of  $14.2\text{ cm}^{-1}$ ). The presence of any compressive or tensile strain in the nanowires is unlikely, as strain is efficiently released in high surface area structures.<sup>42</sup> While comparison with pure Ge nanowires might be advantageous, similar growth conditions without Sn incorporation yielded Ge nanowires with completely different sizes and morphologies. Additionally, an asymmetry in the lower energy side of the Ge-Ge LO mode was observed in the spectra (especially for the nanowires with higher Sn content) due to the development of a Ge-Sn couple vibrational mode with increasing Sn concentration.<sup>43</sup>

Li et al.<sup>43</sup> introduced a linear expression ( $\omega(x) = \omega_0 + \Delta\omega x$ ) for  $\text{Ge}_{1-x}\text{Sn}_x$  alloy to correlate Sn concentration with the Raman peak shift, obtaining a value of

$\Delta\omega = -68 (\pm 5) \text{ cm}^{-1}$ , while describing the characterized films as completely strain-free. When fitting the Raman peak shift against Sn composition (see Figure 4.2b) the obtained value for  $\Delta\omega$  was found to be  $-(69.8 \pm 2.2) \text{ cm}^{-1}$ , consistent with the previously reported value for strain-free thin film. This linear correlation in the alloy nanowires corroborates the Sn content determined by EDX in the  $\text{Ge}_{1-x}\text{Sn}_x$  nanowires.

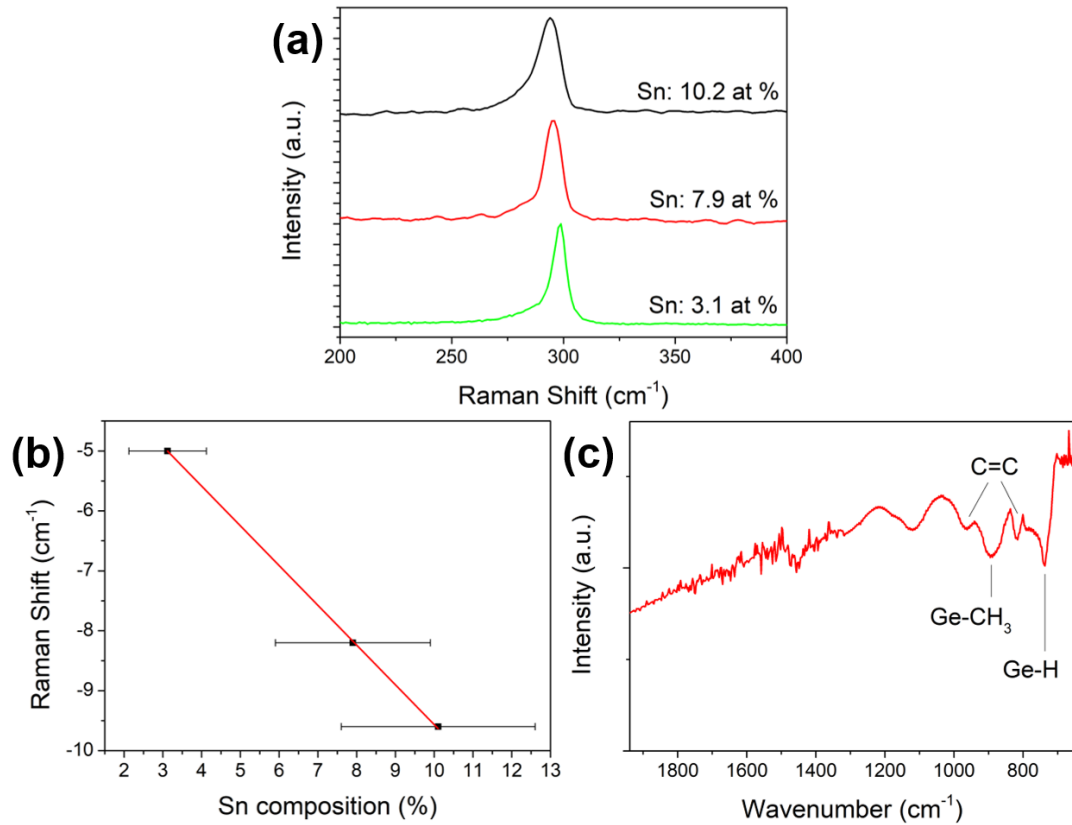


**Figure 4.2.** (a) Raman spectra of  $\text{Ge}_{1-x}\text{Sn}_x$  nanowires as a function of the average Sn content (at.%), within the wavenumber range of 200-400  $\text{cm}^{-1}$ . (b) Plotting of the downshift of Ge-Ge LO mode as a function of Sn percentage. Experimental data are represented with dots which fits (straight line with  $R^2 = 0.9999$ ) well with the linear expression,  $\omega(x) = \omega_0 + \Delta\omega x$ . (c) FT-IR spectra of the  $\text{Ge}_{1-x}\text{Sn}_x$  nanowires deposited on a Si substrate.

An FTIR spectra taken from  $\text{Ge}_{1-x}\text{Sn}_x$  ( $x = 0.03$ ) nanowires show absorption bands at  $\sim 750$  and  $\sim 890 \text{ cm}^{-1}$  (see Figure 4.2c). This spectrum is representative of all other

Ge<sub>1-x</sub>Sn<sub>x</sub> nanowires with different Sn content. These bands have previously been assigned to the wagging mode of Ge-H<sup>44</sup> and Ge-CH<sub>3</sub> rocking vibrations<sup>45,46</sup>, respectively. These data suggest the formation of a carbonaceous structure around the crystalline nanowires due to the presence of peaks at ~ 963 and ~ 815 cm<sup>-1</sup>, corresponding to C=C,<sup>45</sup> as well as ~ 963 cm<sup>-1</sup> which is associated with the presence of Ge-C-C<sup>45,47</sup>. These data also suggest a definite interaction of the carbonaceous matrix within the Ge nanowire surfaces. The binary phase diagram of C and Ge alloys implies that the formation of solid solutions of carbonaceous Ge (C-Ge) is unlikely at the growth temperature in this study.<sup>48</sup> The carbon content detected in the samples arises from the omnipresent adventitious carbon and carbonaceous structures generated during the reaction.

***Structural characterisation of nanowires via STEM and HRTEM analysis.*** To determine the crystal quality of the nanowires, their morphologies were investigated by HRTEM, HAADF-STEM and selected area electron diffraction (SAED) (see Figure 4.3 and Figure A4.3 in Appendix 4.6). Figure 4.3a shows HAADF-STEM of representative Ge<sub>1-x</sub>Sn<sub>x</sub> nanowires grown with an initial Ge:Sn mole ratio of 95:5. The nanowire imaged displayed uniform structural quality and a crystalline nature, without any crystal defects such as stacking faults and twinning. Defect-free materials are typically better as Li-ion battery anode materials due to their long life cycles.<sup>49</sup> HRTEM imaging of the nanowires (mean diameter 9.3 nm) revealed an interplanar spacing (*d*) of 0.33 nm (see Figure 4.3a) along with a <111> growth direction. The interplanar spacing is marginally larger than the *d* value reported for bulk diamond cubic Ge (dc-Ge) (0.326 nm from the JCPDS 04-0545), corresponding to (111) planes of Ge diamond cubic crystal structure. Fast Fourier Transform (FFT) analysis of a

HAADF-STEM image on a single nanowire could only be indexed to the dc-Ge structure (inset of Figure 4.3a) and the spot pattern indicates that the Ge nanowires are single-crystalline. Further analysis of the FFT data (insert of Figure 4.3a) also confirmed the formation of dc-Ge crystal structure and the reflections were assigned to the high-order Laue zone diffraction of two  $\{111\}$  and  $\{200\}$  planes of dc-Ge.<sup>50</sup>

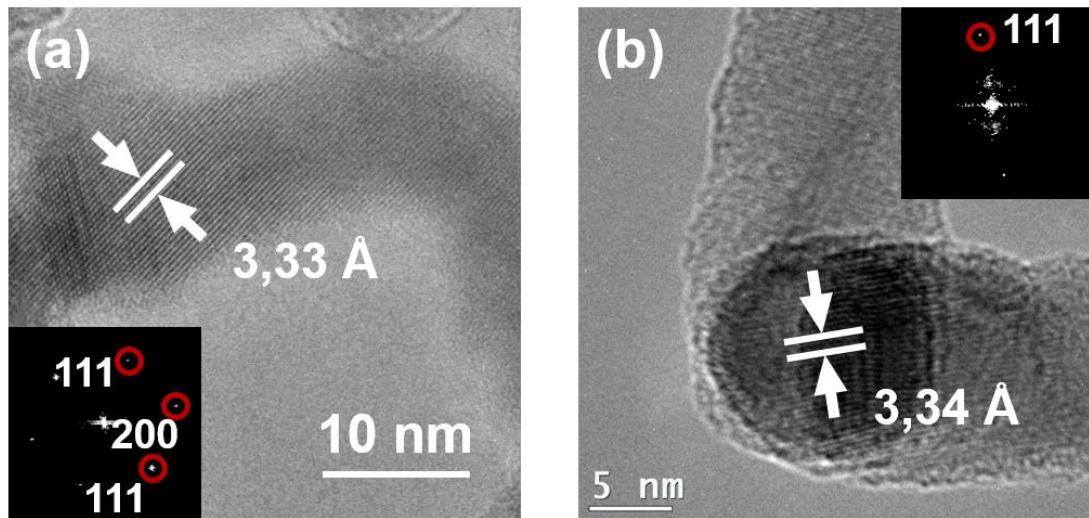


**Figure 4.3.** (a) Lattice-resolved HRTEM image of a  $\text{Ge}_{1-x}\text{Sn}_x$  nanowire with a mean Sn content of 3.1 at.%, revealing an interspace  $d$  value of 0.333 nm corresponding to the dc-Ge crystal structure. Bottom-left inset shows an FFT of the full image with a corresponding pattern of a representative dc-Ge structure. (b) HRTEM image of a Ge/Sn seed. The top-right inset shows an FFT of the full image.

Growth seeds were not readily observed at the tips of the alloy nanowires with the lowest Sn content (3.1 at.%). The presence of any observable seeds was further examined by HRTEM (see Figure 4.3b). Growth seeds with different shapes and nature in comparison to those formed by a conventional VLS process were observed in few instances for these nanowires. Figure 4.3b shows an HRTEM image of overlapping growth seeds at the tips of two  $\text{Ge}_{1-x}\text{Sn}_x$  nanowires (3.1 at.%), confirming the participation of seeded bottom-up growth. The HRTEM image revealed an

interplanar spacing ( $d$ ) of 0.34 nm, corresponding to  $\langle 111 \rangle$  planes of the dc-Ge crystal. No crystallographic differences, and a smooth interface, were observed between the “seed” and the nanowire segments. This apparent continuity of the lattice from the seed to the nanowire confirms a VLS-like nanowire growth mechanism, catalysed from *in situ* formed Ge nanoparticles. The FFT pattern of the HRTEM image, in the top-right inset of Figure 4.3b, of the seed region (corresponding to the red-squared area highlighted on the main image) also confirms the formation of the dc-Ge. FFT analysis was recorded from the same nanowire with  $\langle 110 \rangle$  zone axis alignment. The observation of Ge-rich seeds for low Sn content nanowires is contrary to the observation of Sn-rich ( $> 90$  at.%) seeds for  $\text{Ge}_{1-x}\text{Sn}_x$  nanowires with a high Sn content, *i.e.* 7.9 and 10.2 at.% (see Figure A4.2 in Appendix 4.6). The observation of Sn rich seeds is similar to previously reported CVD-grown  $\text{Ge}_{1-x}\text{Sn}_x$  nanowires.<sup>40,41</sup> Shorter and tapered  $\text{Ge}_{1-x}\text{Sn}_x$  nanowires (see Figure A4.1b in Appendix 4.6) with a mean Sn content of 7.9 and 10.2 at.% clearly display spherical nanoparticle seeds at their tips (see Figure A4.3a and Figure A4.2a in Appendix 4.6). This further suggests two very different growth mechanisms for low and high Sn-content alloy nanowires. High Sn-content (7.9 and 10.2 at.%)  $\text{Ge}_{1-x}\text{Sn}_x$  nanowires also depicted a dc-Ge crystal structure, as confirmed by HRSTEM and SAED (see Figure A4.3b in Appendix 4.6).

***Growth mechanism of  $\text{Ge}_{1-x}\text{Sn}_x$  Nanowires.*** The growth of  $\text{Ge}_{1-x}\text{Sn}_x$  nanowires is believed to occur through a self-seeded supercritical fluid-liquid-solid (SFLS) growth mechanism. The incorporation of Sn in the growing nanowires likely occurs through a solute trapping mechanism.<sup>51</sup> We propose two different growth scenarios for the  $\text{Ge}_{1-x}\text{Sn}_x$  nanowires with low- (3.1 at.%) and high-Sn (7.9 and 10.1 at.%) content. With low ratios of the Sn precursor in the initial solution  $\text{Ge}_{1-x}\text{Sn}_x$  nanowire growth



was initiated by Ge nanoparticle seeds, depicted in the HRTEM image in Figure 4.3b (see Figure 4.4a). These Ge nanoparticle seeds were formed by DPG decomposition and stabilized by carbonaceous compounds (formation of carbonaceous structure is confirmed from FTIR in Figure 4.2c), formed via polymerization of phenyl molecules (liberated as a by-product of DPG decomposition) in supercritical toluene atmosphere. These results in  $\text{Ge}_{1-x}\text{Sn}_x$  nanowires with a very thin diameter (9.3 nm) with narrow diameter distribution. Formation of Ge nanoparticle seeds from DPG decomposition seems kinetically favoured for the nanowire growth reaction with 95:5 (Ge:Sn) initial solution.

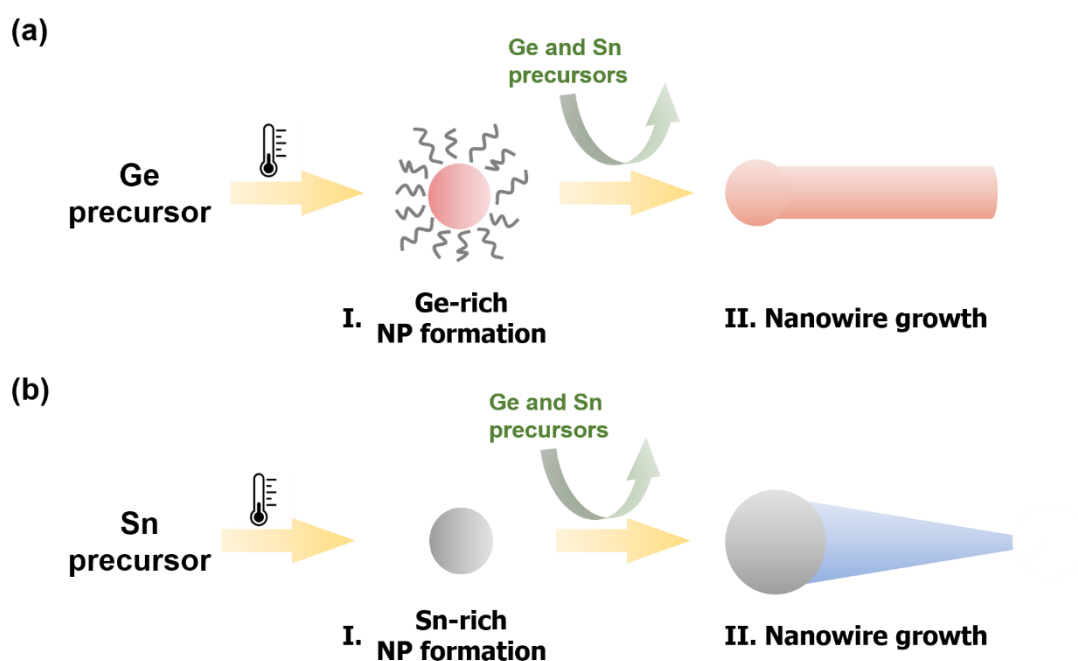


**Figure 4.4.** Illustration of the two proposed nanowire growth mechanisms. (a) Corresponds to the nanowires (3.1 at.% Sn incorporation) grown from an initial solution of 95:5 (Ge:Sn precursors) which generated Ge nanoparticle seed. (b) Corresponds to the nanowires (7.9 and 10.1 at.% Sn incorporation) grown from initial solutions of 90:10 and 85:15 (Ge:Sn precursors) respectively generating Sn seeds.

For the growth of  $\text{Ge}_{1-x}\text{Sn}_x$  nanowires with high Sn, high mole ratios of Sn precursor (TET) in the reaction solution favours homogenous nucleation of Sn and the formation of larger Sn nanoparticle seeds (see Figure 4.4b). The formation of Sn nanoparticles occurs during the Sn precursor decomposition, forming catalytic seed for nanowire growth. A lack of stabilization of Sn nanoparticles, contrary to the Ge-rich nanoparticle seeds, resulted in thicker nanowires ( $d = 48.3$  and  $108.8$  nm) with tapered morphology. The inverted and tapered nature of the  $\text{Ge}_{1-x}\text{Sn}_x$  ( $x = 0.08, 0.10$ ) nanowires grown from an initial solution of 90:10 and 85:15 (Ge:Sn precursors) is caused by the continuous incorporation of Sn adatoms into the catalyst seeds during nanowire growth. A schematic of both growth scenarios is presented in Figure 4.4.

During the nanowire growth, Sn is incorporated into the nanowire structure at the seed/nanowire interphase.<sup>52</sup> The non-equilibrium incorporation of Sn in the nanowire can be attributed to solute trapping, a kinetically driven process. The difference in atomic concentration of Sn in different phases influences the trapping of Sn adatoms at the triple-phase interface, as previously described.<sup>40,41,51</sup> For the high Sn content nanowire with Sn seed, a large difference in the Sn concentration between the Sn-rich liquid eutectic seed and nanowire can result in the solute trapping of Sn. Additionally, as discussed by Wen *et al.*,<sup>53</sup> large diameter nanowires have higher step velocities (growth at the atomic level by step flow) compared to their smaller diameter counterparts, which is also related to a faster impurity trapping rate in the growing nanowires. This higher step velocity in nanowires with larger diameters ( $d = 48.3$  and  $108.8$  nm) can result in increased Sn% incorporation (7.9 and 10.1 at.%).

***Electrochemical analysis of  $\text{Ge}_{1-x}\text{Sn}_x$  Nanowires.*** The morphology and crystal structure of nanowires are tightly related with several Li-ion battery variables like the contact area between active material and electrolyte, the diffusion length for Li-ions, and the area of the solid electrolyte interface (SEI) film, which will influence the electrochemical properties.<sup>54</sup> The motivation to integrate functional materials with high surface areas make super-thin 3.1 at.% Sn containing alloy nanowires good candidates for Li-ion batteries. Besides, as previously shown,  $\text{Ge}_{1-x}\text{Sn}_x$  nanocrystals with high Sn incorporation ( $\sim 10$  at.%) resulted in a decrease in specific capacity due to the tendency of metallic Sn to segregate, leading to significant side reactions.<sup>26</sup> Therefore, the electrochemical performance of  $\text{Ge}_{1-x}\text{Sn}_x$  nanowires as anodes for Li-ion batteries (LIB) was tested for the super-thin nanowires with a mean Sn content of 3.1 at.%.

The electrochemical properties of  $\text{Ge}_{1-x}\text{Sn}_x$  nanowires with a mean Sn loading of 3.1 at.% were initially investigated by cyclic voltammetry (CV). The first anodic scan (lithiation), (see Figure 4.5a), consisted of a weak reduction peak at  $\sim 0.5$  V, associated with the initial lithiation of crystalline Ge and two strong reduction peaks at  $\sim 0.20$  and  $0.09$  V, corresponding to the formation of amorphous (a) and crystalline (c)  $\text{Li}_{15}\text{Ge}_4$  alloys, respectively.<sup>21,55</sup> After this initial lithiation, there is a distinct change in the profile of the reduction peaks observed from the second cycle onwards. Three reduction peaks were observed at  $\sim 0.47$ ,  $0.33$  and  $0.12$  V (see Figure 4.5b), corresponding to the stepwise formation of different Li–Ge alloys ( $\text{a-Li}_x\text{Ge} \rightarrow \text{a-Li}_{15}\text{Ge}_4 \rightarrow \text{c-Li}_{15}\text{Ge}_4$ ).<sup>56</sup> One sharp asymmetric oxidation peak was observed in the cathodic (delithiation) CV scans. The asymmetric nature of this peak indicates that it

is a convolution of peaks associated with the delithiation of c-Li<sub>15</sub>Ge<sub>4</sub> and a-Li<sub>15</sub>Ge<sub>4</sub> phases.

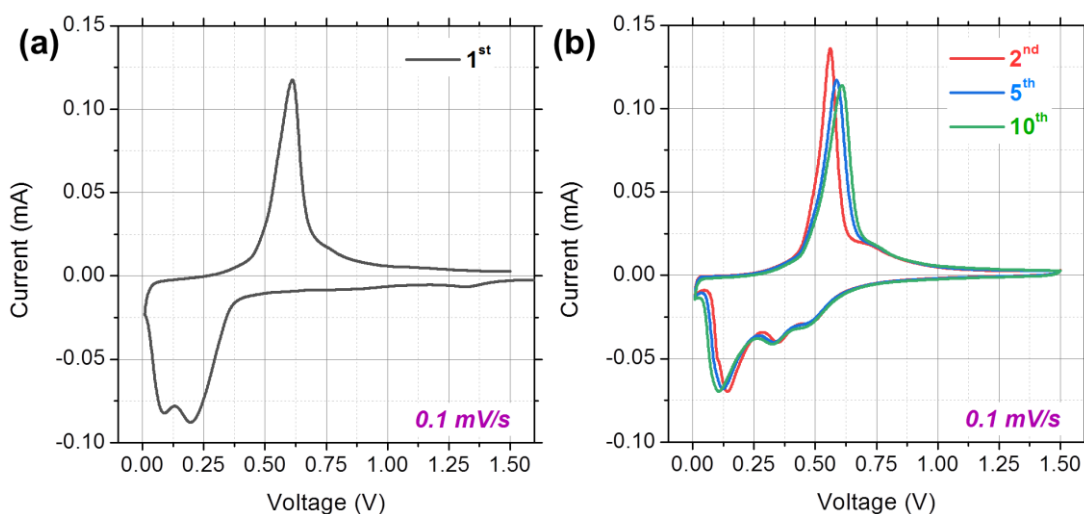


**Figure 4.5.** Cyclic voltammograms of Ge<sub>1-x</sub>Sn<sub>x</sub> nanowires with a mean Sn content of 3.1 at.% showing (a) the 1<sup>st</sup> and (b) the 2<sup>nd</sup>, 5<sup>th</sup> and 10<sup>th</sup> cycles; cycled at 0.1 mV/s in a potential window from 1.5 - 0.01 V.

Galvanostatic cycling of Ge<sub>1-x</sub>Sn<sub>x</sub> nanowires with a Sn content of 3.1. at.% was performed to determine the specific capacity values they can deliver and to examine their capacity retention ability. Voltage profiles, observed during galvanostatic cycling at C/5 in a voltage window of 1.5 – 0.01 V (vs Li/Li<sup>+</sup>), are shown in Figure 4.6. During the first charge curve (lithiation), the voltage decreased quickly until the initial lithiation of crystalline Ge commenced at ~ 0.5 V, followed by a more gradual decrease to the low voltage limit of 0.01 V, due to the formation of a-Li<sub>15</sub>Ge<sub>4</sub> and c-Li<sub>15</sub>Ge<sub>4</sub> alloys (inset of Figure 4.6a). A plateau was observed at ~ 0.53 V during the first discharge process (delithiation), corresponding to the dealloying of the nanowires.<sup>19</sup> The specific capacities after the first lithiation and delithiation were 2438 and 1165 mA h g<sup>-1</sup>, respectively, resulting in an initial Coulombic efficiency (ICE) of ~ 47.8 %. Low ICE values are commonly reported for alloying mode anode materials

and can be attributed to a combination of different factors including, the initial formation of an SEI layer on the surface of the NWs, electrolyte decomposition and the as well as the formation of quasi reversible  $\text{Li}_2\text{O}$ .<sup>57–60</sup> There was no significant change in the trend of the voltage profiles from the 2<sup>nd</sup> to the 150<sup>th</sup> cycle, which indicates that the lithiation of the nanowires is a highly reversible process from the second cycle onwards.

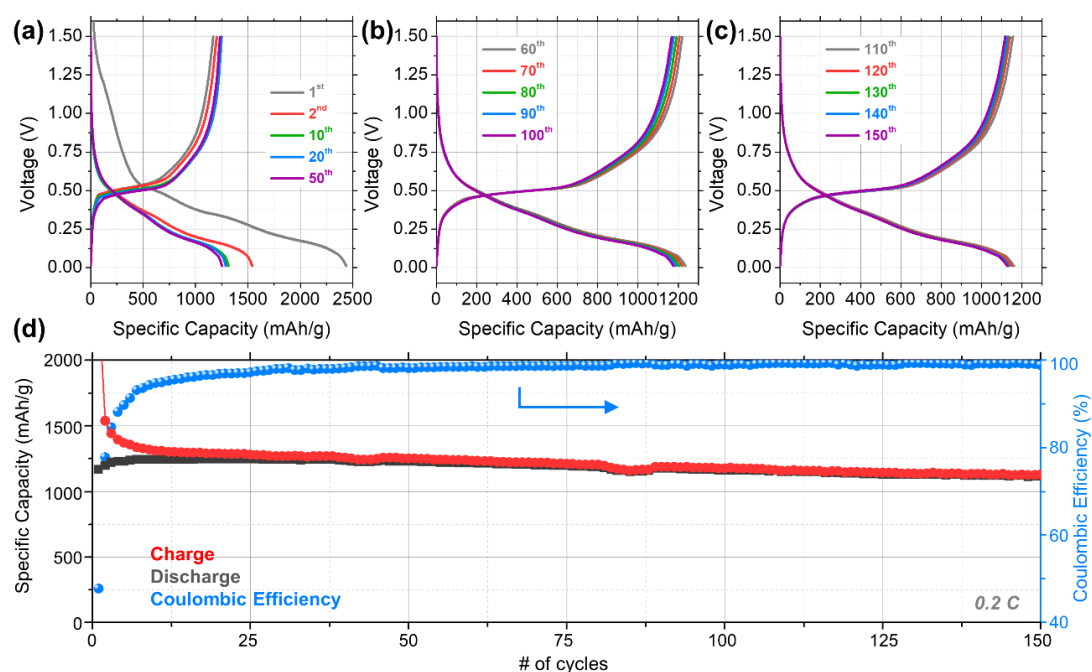


**Figure 4.6.** Voltage profiles for (a) the 1<sup>st</sup>, 2<sup>nd</sup>, 10<sup>th</sup>, 20<sup>th</sup> and 50<sup>th</sup> cycles, (b) the 60<sup>th</sup>, 70<sup>th</sup>, 80<sup>th</sup>, 90<sup>th</sup> and 100<sup>th</sup> cycles and (c) the 110<sup>th</sup>, 120<sup>th</sup>, 130<sup>th</sup>, 140<sup>th</sup> and 150<sup>th</sup> cycles for  $\text{Ge}_{1-x}\text{Sn}_x$  nanowires, with a mean Sn content of 3.1 at.%, at 0.2 C in a potential window of 1.50 – 0.01 V (vs Li/Li<sup>+</sup>). (d) Specific capacity and Coulombic efficiency values obtained for the same nanowires.

The specific capacity values measured for the nanowires during 150 cycles at 0.2 C, and the corresponding CEs, are shown in Figure 4.6d. The nanowires demonstrated a high level of capacity retention. The specific capacity after the 10<sup>th</sup> charge was 1312 mA h g<sup>-1</sup> and this value decreased gradually to 1176 mA h g<sup>-1</sup> after the 100<sup>th</sup>

charge and  $1127 \text{ mA h g}^{-1}$  after the 150<sup>th</sup> charge. This change corresponds to a capacity retention of  $\sim 90$  and  $86 \%$  from the 10<sup>th</sup> to the 100<sup>th</sup> and 150<sup>th</sup> cycles respectively. The mean capacity decay per cycle from the 2<sup>nd</sup> cycle onwards was  $\sim 2.8 \text{ mA h g}^{-1}$ . The impressive capacity retention of the  $\text{Ge}_{1-x}\text{Sn}_x$  nanowires was also demonstrated in the CE values. After the first 10 cycles, the CE values were  $> 95 \%$  and they remained above this value for the remainder of the 150 cycles.

The redox properties of  $\text{Ge}_{1-x}\text{Sn}_x$  nanowires were further examined through analysis of differential charge plots (DCPs), which were calculated from galvanostatic cycling curves. The DCP for the first charge (lithiation) consisted of three reduction peaks (see Figure 4.7a), which is in good agreement with the first anodic scan in the CV curves (see Figure 4.5a). The intensity of the sharp reduction peak associated with the initial lithiation of crystalline Ge, significantly decreased from the second cycle onwards, indicating that after the initial lithiation process, the  $\text{Ge}_{1-x}\text{Sn}_x$  nanowires may not return to a fully delithiated crystalline Ge phase. A similar observation has been reported for other  $\text{Ge}_{1-x}\text{Sn}_x$  nanowires anodes.<sup>25,33</sup> The strong reduction peaks observed at  $\sim 0.35$  and  $0.18 \text{ V}$  can be attributed to the formation of  $\alpha\text{-Li}_{15}\text{Ge}_4$  and  $\text{c-Li}_{15}\text{Ge}_4$  alloys, respectively.<sup>55</sup> The DCP for the first charge (delithiation) consisted of one broad, asymmetric peak which is associated with the delithiation of the  $\text{c-Li}_{15}\text{Ge}_4$  and  $\alpha\text{-Li}_{15}\text{Ge}_4$  phases.

Contour plots were calculated from the DCPs acquired from the 2<sup>nd</sup> to the 150<sup>th</sup> cycles (see Figures 4.7c and 4.7d). These contour plots allow visualisation of changes in the intensities of the redox peaks during galvanostatic cycling. The contour plot for the lithiation process (see Figure 4.7a) demonstrates three reduction peaks at  $\sim 0.50, 0.35$

and 0.17 V, corresponding to the formation of amorphous Li-Ge alloys ( $a\text{-Li}_x\text{Ge}$  and  $a\text{-Li}_{15}\text{Ge}_4$ ), and a crystalline Li-Ge alloy ( $c\text{-Li}_{15}\text{Ge}_4$ ), respectively.<sup>61</sup> The intensity of the reduction peak associated with  $a\text{-Li}_x\text{Ge}$  decreases sharply during initial cycling, suggesting that as cycling progresses, less and less of the overall charge stored is due to the formation of this amorphous alloy. The reduction peak associated with the  $a\text{-Li}_{15}\text{Ge}_4$  alloy is observed throughout the 150 cycles, however, the intensity of this peak gradually fades as cycling progressed. Figure 4.7a shows that the reduction process, which consistently contributes the most towards the overall charge stored, is due to the formation of the  $c\text{-Li}_{15}\text{Ge}_4$  phase. The delithiation contour plot (see Figure 4.7d) consists of one wide band, centred at  $\sim 0.50$  V, which is attributed to the overlapping delithiation of the  $a\text{-Li}_{15}\text{Ge}_4$  and  $c\text{-Li}_{15}\text{Ge}_4$  alloys. Of note, there was no significant shift of the potentials at which the redox process occur during 150 cycles; this stability may contribute towards the capacity retention demonstrated in Figure 4.6d.

With the aim to compare the performance displayed by  $\text{Ge}_{1-x}\text{Sn}_x$  nanowires ( $x = 0.03$ ) nanowires with the higher Sn content nanowires, the specific capacity values obtained for the  $\text{Ge}_{1-x}\text{Sn}_x$  nanowires with a mean Sn content of 7.9 at.% were measured during 100 cycles at 0.2 C, and the corresponding CEs, are shown in Figure A4.4 in Appendix 4.6. The specific capacity after the 150th charge was  $780 \text{ mA h g}^{-1}$ . These nanowires also demonstrated a high level of capacity retention of  $\sim 86 \%$  from the 10th to the 150th cycles and a CE after the first 10 cycles  $> 95 \%$  which remained above this value for the remainder of the 150 cycles. This nanowire sample (7.9 at.% of mean Sn content) displayed a significantly lower specific capacity ( $780 \text{ mA h g}^{-1}$  after 150 cycles) in comparison with the sample with a 3.1 at.% of mean Sn content ( $1127 \text{ mA h g}^{-1}$  after 150 cycles) while exhibiting comparable columbic efficiencies.

The contrasting battery performance displayed might be associated with each particular morphology and Sn content exhibited.

The electrochemical results demonstrated here for  $\text{Ge}_{1-x}\text{Sn}_x$  nanowires are comparable to and, in many cases, greater than previously reported capacities for  $\text{Ge}_{1-x}\text{Sn}_x$  alloy-based anodes (Table A1 in Appendix 4.6). The  $\text{Ge}_{1-x}\text{Sn}_x$  nanowire-based anode fabricated in this work (mean Sn content of 3.1 at.%) shows the longest cycling stability up to 150 cycles together with the highest reversible capacity displayed at 0.2 C cycling rate. There are several factors which contribute towards the impressive specific capacity values and stable capacity retention observed. The growth of the  $\text{Ge}_{1-x}\text{Sn}_x$  (3.1 at.%) nanowires was catalysed via a self-seeded approach (i.e. Ge nanoparticle catalyst). The formation of Li-Sn alloys has previously been observed for  $\text{Ge}_{1-x}\text{Sn}_x$  nanowires which were synthesized with Sn seeds, however, we do not see any contribution from Sn in the DCPs.<sup>55</sup> This is because the 3.1 at.% Sn incorporated  $\text{Ge}_{1-x}\text{Sn}_x$  nanowires are predominantly seeded by Ge (see Figure 4.3b). A low amount of Sn presence in the nanowire bulk and no apparent presence of Sn nanoparticles in the nanowire sample suggests that the formation of any Li-Sn alloys has a negligible contribution towards the overall charge stored. Very thin nanowire morphology for 3.1 at.% Sn incorporated nanowires could also contribute to stable and high capacity, as previously reported for Si nanowires.<sup>62</sup> This could be due to the shorter diffusion pathway for lithium in thin  $\text{Ge}_{1-x}\text{Sn}_x$  nanowires, ensuring a fast and homogeneous lithiation. Additionally, our  $\text{Ge}_{1-x}\text{Sn}_x$  nanowires are grown directly on a Ti substrate, ensuring that the nanowires are in intimate contact with the current collector. Growing  $\text{Ge}_{1-x}\text{Sn}_x$  nanowires directly on a current collector also negates the need to prepare a traditional slurry with a conductive additive and binder. The stable capacity retention



shown in Figure 4.6d is impressive as it was achieved without the need to prepare slurry-based electrodes.

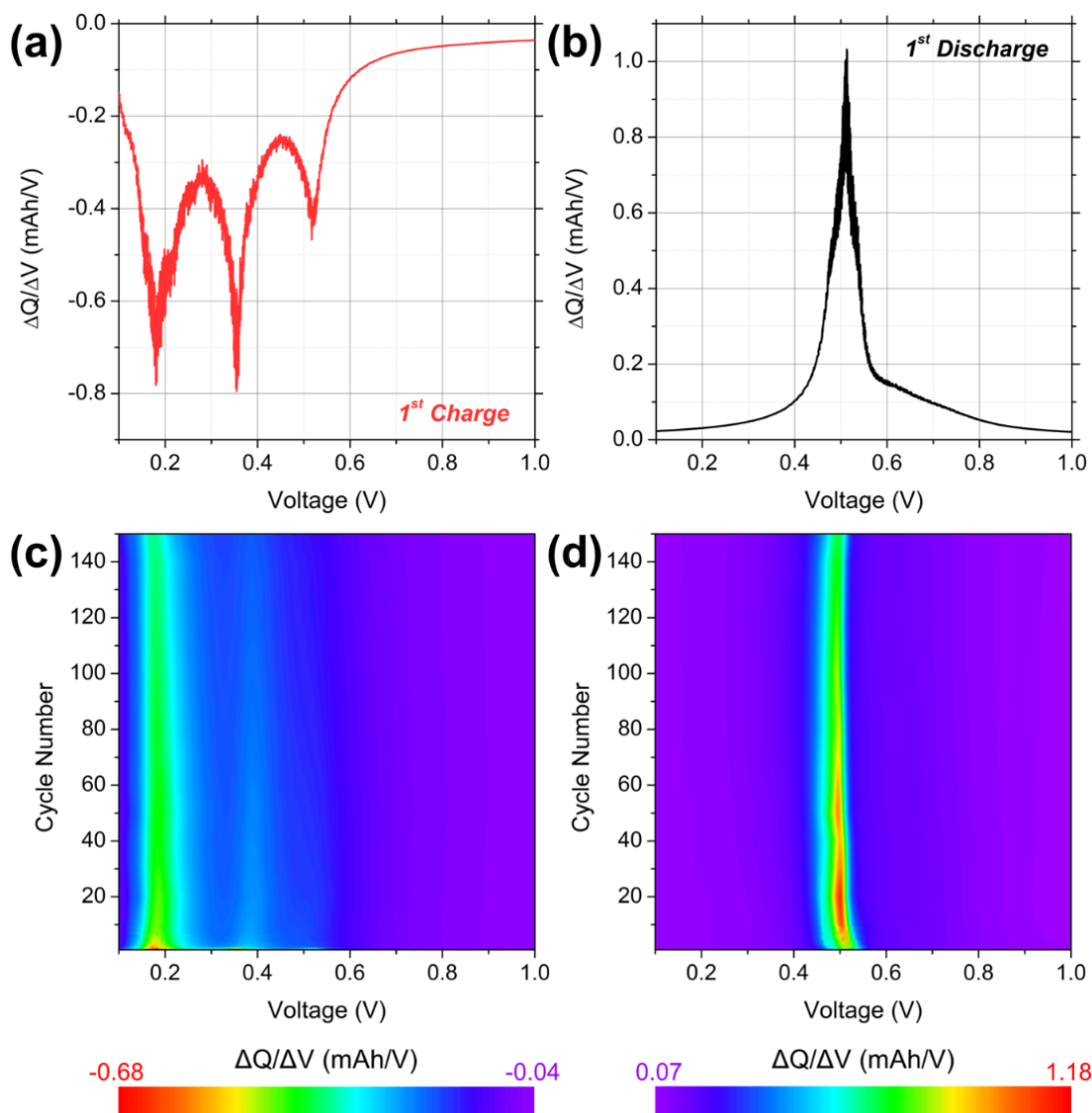


**Figure 4.7.** Differential charge plots (DCPs) of  $\text{Ge}_{1-x}\text{Sn}_x$  nanowires (mean Sn content of 3.1 at.%) calculated from (a) the 1<sup>st</sup> charge and (b) the 1<sup>st</sup> discharges at 0.2 C. (c) Contour DCP calculated from differential charge curves from the 2<sup>nd</sup> to the 150<sup>th</sup> charge. (d) Contour DCP calculated from differential discharge curves from the 2<sup>nd</sup> to the 150<sup>th</sup> discharge.

#### 4.5. Conclusions

In summary, an alternative and simple bottom-up method was developed for the growth  $\text{Ge}_{1-x}\text{Sn}_x$  nanowires that could potentially be used as an anode material in Li-ion batteries. These alloy nanowires were successfully grown directly on titanium substrates, which act as anode current collectors, eliminating the need for conductive slurry and binders. The simple and versatile solvothermal-like growth method does not require any catalyst metal seeds, templates, designer precursors or high boiling point solvents. Sn incorporation into the Ge lattice was achieved between 3.1 to 10.2 at.%. A distinct change in the morphology of the nanowires and growth seeds was observed for  $\text{Ge}_{1-x}\text{Sn}_x$  nanowires with different Sn content.  $\text{Ge}_{1-x}\text{Sn}_x$  nanowires with 3.1 at.% Sn incorporation are very thin (mean diameter of 9.3 nm) and long, whereas thicker, shorter and tapered (mean diameter of 48.3 and 108.8 nm) nanowires were observed for larger (~ 8 - 10 at.%) Sn incorporation.

$\text{Ge}_{1-x}\text{Sn}_x$  nanowires with a mean Sn content of 3.1 at.% demonstrated good performance as Li-ion battery anodes. The nanowires exhibited a high level of capacity retention, with a reversible specific capacity of 1127 mA h g<sup>-1</sup> after the 150<sup>th</sup> charge, when cycled at 0.2 C. The impressive capacity retention of the nanowires was highlighted by the mean capacity decay per cycle of just ~ 2.8 mA h g<sup>-1</sup> from the 2<sup>nd</sup> to the 150<sup>th</sup> cycle. Analysis of differential charge plots revealed that the formation of a-Li<sub>15</sub>Ge<sub>4</sub> and c-Li<sub>15</sub>Ge<sub>4</sub> alloys are highly reversible and that the majority of charge stored is due to the reduction process associated with the development of the c-Li<sub>15</sub>Ge<sub>4</sub> phase. The impressive stable cycling performance of the nanowires was achieved without the presence of conductive additives or binders, as the nanowires were grown directly on current collecting substrates. The high specific capacity

values obtained for the nanowires surpassed previously reported values for other Ge based anodes. The impressive electrochemical performance of the nanowires in terms of specific capacities, Coulombic efficiency and voltage stability demonstrates that they are a promising anode material for advanced Li-ion batteries.

## 4.6. Appendix

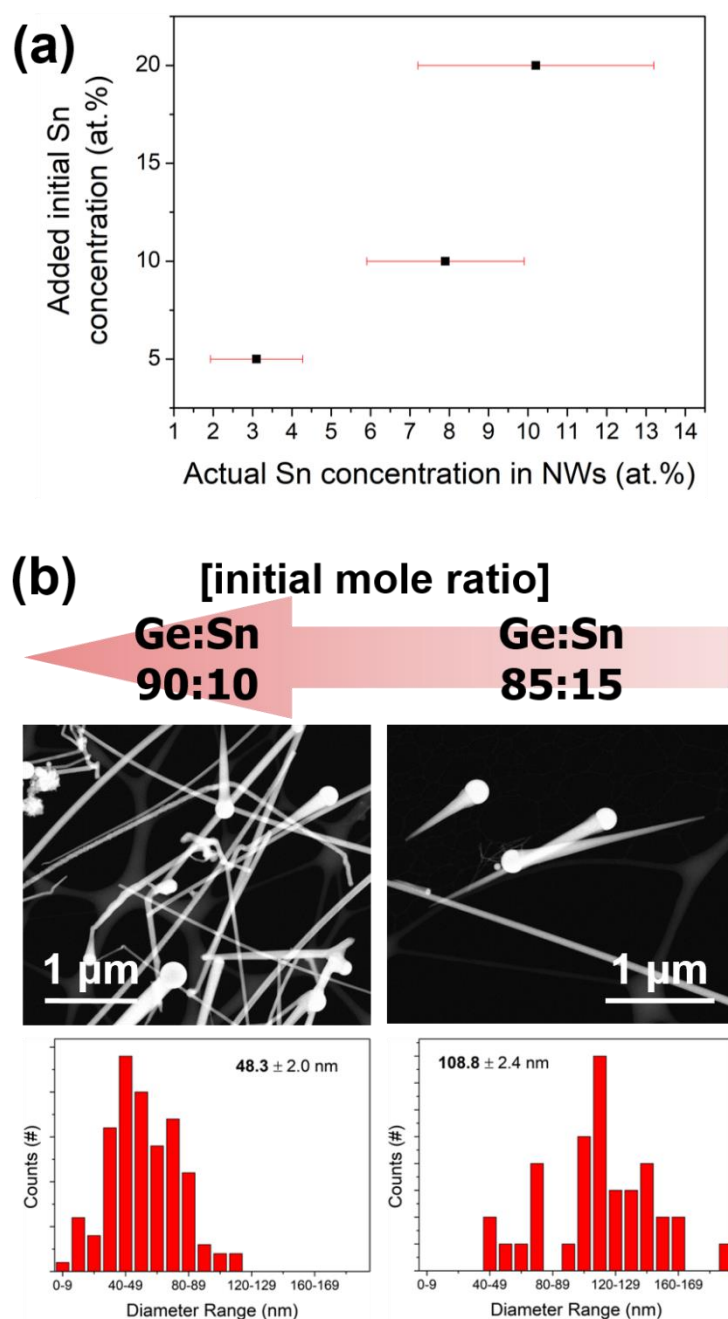


**Figure A4.1.** (a) A plot showing the variations in Sn concentration for  $\text{Ge}_{1-x}\text{Sn}_x$  nanowires under different growth conditions. (b) STEM images and diameter distributions of the  $\text{Ge}_{1-x}\text{Sn}_x$  nanowires grown from 90:10 and 85:15 Ge:Sn mole ratio solutions. Inserts shows mean diameters and standard deviations.

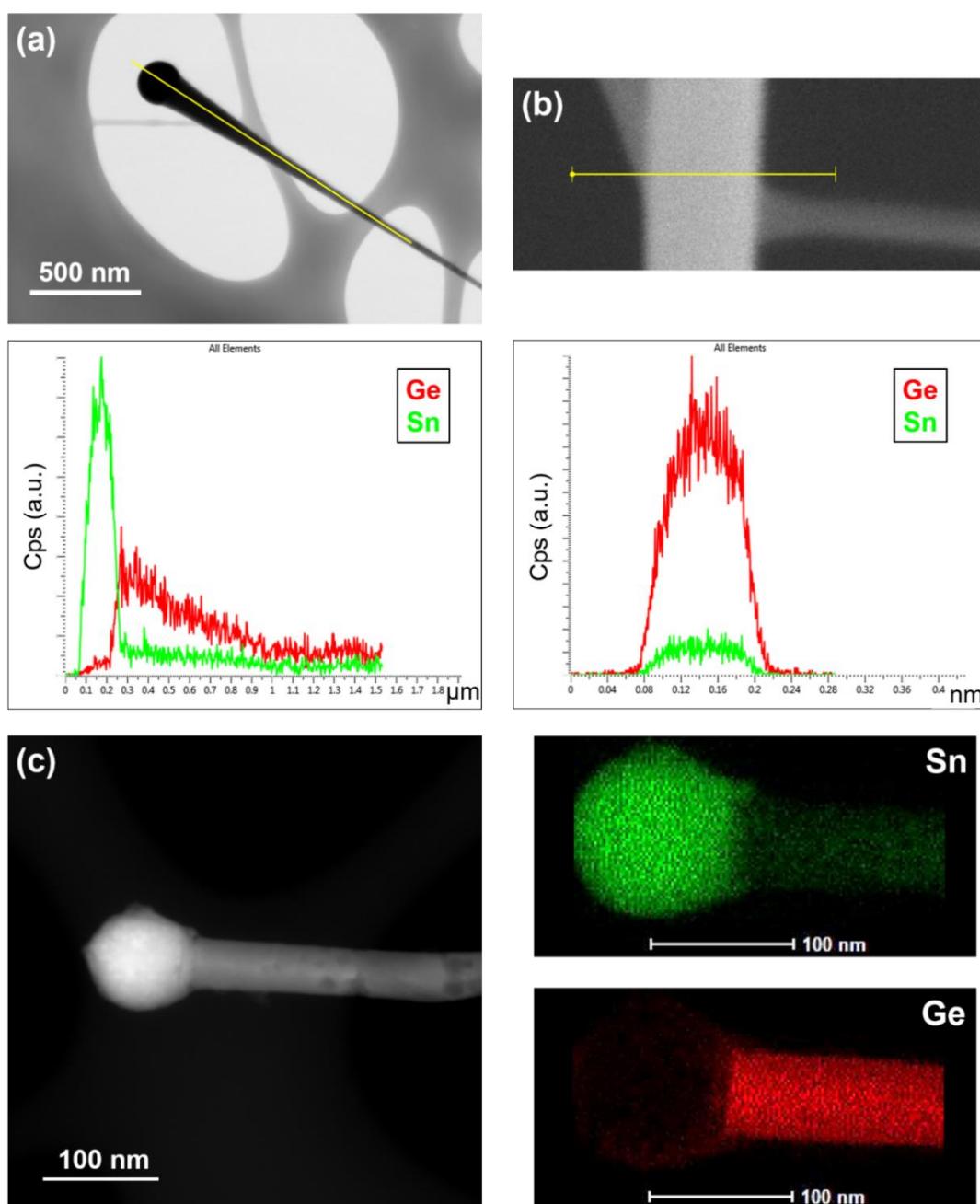


**Figure A4.2.** (a) EDX linear concentration profile of Ge and Sn from a  $\text{Ge}_{1-x}\text{Sn}_x$  nanowire; grown on Ti substrate from a DPG/TET mole ratio of 85:15 in toluene at a temperature of 440 °C (~ 10.2 at.% Sn incorporation). (b) EDX radial scan of a  $\text{Ge}_{1-x}\text{Sn}_x$  nanowire from the same samples as in (a). (c) EDX seed-region mapping of Ge and Sn from a  $\text{Ge}_{1-x}\text{Sn}_x$  nanowire grown on Ti substrate from a DPG/TET mole ratio of 90:10 mole at a temperature of 440 °C (~ 7.9 at.% Sn incorporation). EDX profiles show no segregation of Sn at or near the nanowire surface.

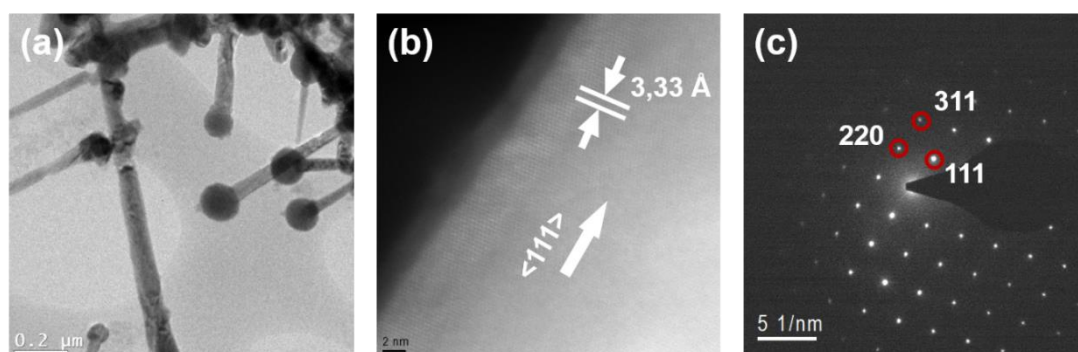


**Figure A4.3.** (a) TEM image of  $\text{Ge}_{1-x}\text{Sn}_x$  nanowire grown on Ti substrate from a DPG/TET mole ratio of 90:10 in toluene at a temperature of 440 °C; showing the spherical nature of the nanoparticle seeds present at the tips of the nanowires. (b) Latticed-resolved HRSTEM image shows a nanowire with a  $\langle 111 \rangle$  growth direction and the displayed interplanar spacing. (c) SAED pattern of the same nanowire with a corresponding pattern of a representative dc-Ge structure.

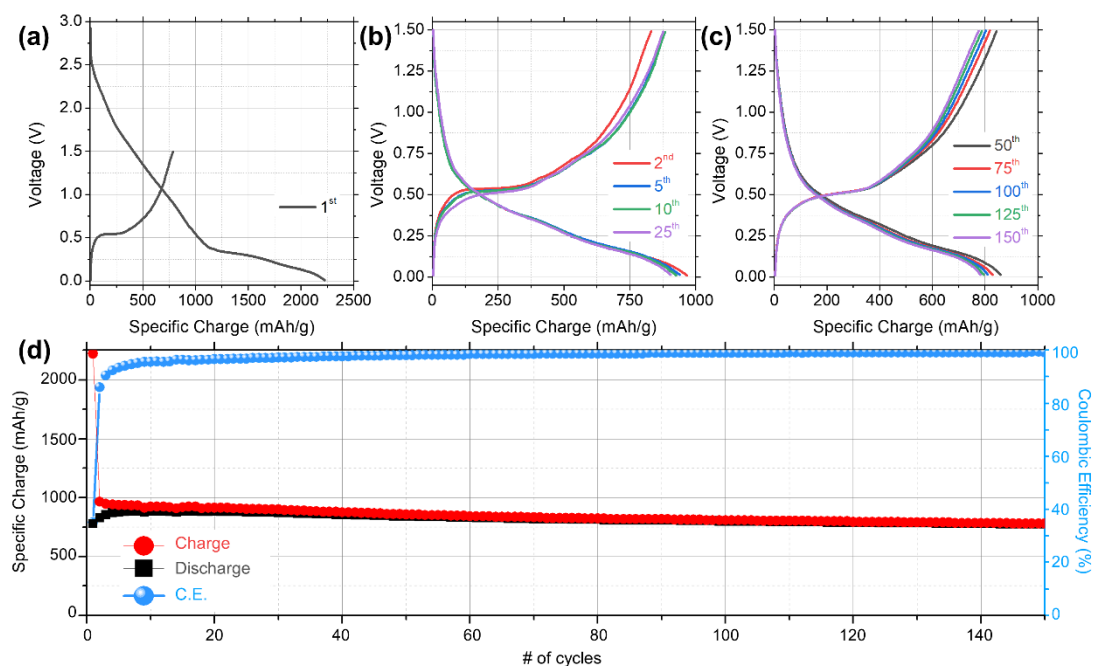


**Figure A4.4.** Voltage profiles for (a) the 1<sup>st</sup> cycle, (b) the 2<sup>nd</sup>, 5<sup>th</sup>, 10<sup>th</sup> and 25<sup>th</sup> cycles and (c) the 50<sup>th</sup>, 75<sup>th</sup>, 100<sup>th</sup>, 125<sup>th</sup> and 150<sup>th</sup> cycles for  $\text{Ge}_{1-x}\text{Sn}_x$  nanowires, with a mean Sn content of 7.9 at.%, at 0.2 C in a potential window of 1.50 - 0.01 V (vs Li/Li<sup>+</sup>). (d) Specific capacity and Coulombic efficiency values obtained for the same nanowires.

**Table A1.** Cycling performance of Ge<sub>1-x</sub>Sn<sub>x</sub> nanostructures previously reported as anode electrodes.

GeSn nano-structures	Preparation method	Sn incorporation	Cycling performance	Number of cycles	Electrode preparation	Ref.
<b>GeSn Alloy Nanowires</b>	Liquid-injection chemical vapour deposition	4.8 at. %	~ 921 mA h g <sup>-1</sup> at 0.2 C	100 cycles	As-synthesised (Stainless Steel)	25
<b>GeSn nanocrystals</b>	Gas-phase laser photolysis	5 at. %	1010 mA h g <sup>-1</sup> at 0.1 C	50 cycles	Conductive mixture	26
<b>GeSn Branched Nanowires</b>	Liquid-injection chemical vapour deposition	~ 8 at. % in the branches	1040 mA h g <sup>-1</sup> at 0.2 C	25 cycles	As-synthesised (Stainless Steel)	33
<b>Crystalline GeSn nanograins</b>	Melt spinning process	20 at. %	~ 1000 mA h g <sup>-1</sup> at 0.1 C	60 cycles	Conductive mixture	63
<b>Nano-composite of Amorphous Ge gels and SnP<sub>0.94</sub></b>	Vacuum annealing	59 at. %	~ 700 mA h g <sup>-1</sup> at 0.2 C	50 cycles	Conductive mixture	29
<b>GeSn@Carbon Core-Shell Nanowires</b>	Thermal annealing	78 at. %	1050 mA h g <sup>-1</sup> at 0.3 C	45 cycles	Conductive mixture	28



#### 4.7. References

- (1) Doherty, J.; Biswas, S.; Galluccio, E.; Broderick, C. A.; Garcia-Gil, A.; Duffy, R.; O'Reilly, E. P.; Holmes, J. D. Progress on Germanium-Tin Nanoscale Alloys. *Chem. Mater.* **2020**, *32* (11), 4383–4408.
- (2) Uchida, N.; Maeda, T.; Lieten, R. R.; Okajima, S.; Ohishi, Y.; Takase, R.; Ishimaru, M.; Locquet, J. P. Carrier and Heat Transport Properties of Polycrystalline GeSn Films on SiO<sub>2</sub>. *Appl. Phys. Lett.* **2015**, *107* (23), 232105.
- (3) Sau, J. D.; Cohen, M. L. Possibility of Increased Mobility in Ge-Sn Alloy System. *Phys. Rev. B - Condens. Matter Mater. Phys.* **2007**, *75* (4), 1–7.
- (4) Lieten, R. R.; Maeda, T.; Jevasuwan, W.; Hattori, H.; Uchida, N.; Miura, S.; Tanaka, M.; Locquet, J. P. Tensile-Strained GeSn Metal-Oxide-Semiconductor Field-Effect Transistor Devices on Si(111) Using Solid Phase Epitaxy. *Appl. Phys. Express* **2013**, *6* (10), 101301.
- (5) Cong, H.; Yang, F.; Xue, C.; Yu, K.; Zhou, L.; Wang, N.; Cheng, B.; Wang, Q. Multilayer Graphene-GeSn Quantum Well Heterostructure SWIR Light Source. *Small* **2018**, *14* (17), 1704414.
- (6) Yin, W. J.; Gong, X. G.; Wei, S. H. Origin of the Unusually Large Band-Gap Bowing and the Breakdown of the Band-Edge Distribution Rule in the Sn<sub>x</sub>Ge<sub>1-x</sub> Alloys. *Phys. Rev. B - Condens. Matter Mater. Phys.* **2008**, *78* (16), 1–4.
- (7) Chen, R.; Lin, H.; Huo, Y.; Hitzman, C.; Kamins, T. I.; Harris, J. S. Increased Photoluminescence of Strain-Reduced, High-Sn Composition Ge<sub>1-x</sub>Sn<sub>x</sub> Alloys Grown by Molecular Beam Epitaxy. *Appl. Phys. Lett.* **2011**, *99* (18), 181125.
- (8) Azrak, E.; Chen, W.; Moldovan, S.; Gao, S.; Duguay, S.; Pareige, P.; Roca I Cabarrocas, P. Growth of In-Plane Ge<sub>1-x</sub>Sn<sub>x</sub> Nanowires with 22 at. % Sn Using a Solid-Liquid-Solid Mechanism. *J. Phys. Chem. C* **2018**, *122* (45), 26236–26242.
- (9) Wirths, S.; Geiger, R.; Von Den Driesch, N.; Mussler, G.; Stoica, T.; Mantl, S.; Ikonik, Z.; Luysberg, M.; Chiussi, S.; Hartmann, J. M.; Sigg, H.; Faist, J.; Buca, D.; Grützmacher, D. Lasing in Direct-Bandgap GeSn Alloy Grown on Si. *Nat. Photonics* **2015**, *9* (2), 88–92.
- (10) Stange, D.; Wirths, S.; Geiger, R.; Schulte-Braucks, C.; Marzban, B.; Driesch,

- N. V. Den; Mussler, G.; Zabel, T.; Stoica, T.; Hartmann, J. M.; Mantl, S.; Ikonc, Z.; Grützmacher, D.; Sigg, H.; Witzens, J.; Buca, D. Optically Pumped GeSn Microdisk Lasers on Si. *ACS Photonics* **2016**, *3* (7), 1279–1285.
- (11) Al-Kabi, S.; Ghetmiri, S. A.; Margetis, J.; Pham, T.; Zhou, Y.; Dou, W.; Collier, B.; Quinde, R.; Du, W.; Mosleh, A.; Liu, J.; Sun, G.; Soref, R. A.; Tolle, J.; Li, B.; Mortazavi, M.; Naseem, H. A.; Yu, S. Q. An Optically Pumped 2.5  $\mu\text{m}$  GeSn Laser on Si Operating at 110 K. *Appl. Phys. Lett.* **2016**, *109*, 171105.
  - (12) Conley, B. R.; Margetis, J.; Du, W.; Tran, H.; Mosleh, A.; Ghetmiri, S. A.; Tolle, J.; Sun, G.; Soref, R.; Li, B.; Naseem, H. A.; Yu, S. Q. Si Based GeSn Photoconductors with a 1.63 A/W Peak Responsivity and a 2.4  $\mu\text{m}$  Long-Wavelength Cutoff. *Appl. Phys. Lett.* **2014**, *105*, 221117.
  - (13) Pham, T. N.; Du, W.; Conley, B. R.; Margetis, J.; Sun, G.; Soref, R. A.; Tolle, J.; Li, B.; Yu, S. Q. Si-Based Ge<sub>0.9</sub>Sn<sub>0.1</sub> Photodetector with Peak Responsivity of 2.85 A/W and Longwave Cutoff at 2.4  $\mu\text{m}$ . *Electron. Lett.* **2015**, *51* (11), 854–856.
  - (14) Tseng, H. H.; Wu, K. Y.; Li, H.; Mashanov, V.; Cheng, H. H.; Sun, G.; Soref, R. A. Mid-Infrared Electroluminescence from a Ge/Ge<sub>0.922</sub>Sn<sub>0.078</sub>/Ge Double Heterostructure p-i-n Diode on a Si Substrate. *Appl. Phys. Lett.* **2013**, *102* (18), 182106.
  - (15) Gupta, J. P.; Bhargava, N.; Kim, S.; Adam, T.; Kolodzey, J. Infrared Electroluminescence from GeSn Heterojunction Diodes Grown by Molecular Beam Epitaxy. *Appl. Phys. Lett.* **2013**, *102* (25), 251117.
  - (16) Chang, C.; Chang, T. W.; Li, H.; Cheng, H. H.; Soref, R.; Sun, G.; Hendrickson, J. R. Room-Temperature 2-  $\mu\text{m}$  GeSn P-I-N Homojunction Light-Emitting Diode for Inplane Coupling to Group-IV Waveguides. *Appl. Phys. Lett.* **2017**, *111* (14), 141105.
  - (17) Ionescu, A. M.; Riel, H. Tunnel Field-Effect Transistors as Energy-Efficient Electronic Switches. *Nature* **2011**, *479* (7373), 329–337.
  - (18) Zhao, Q. T.; Richter, S.; Schulte-Braucks, C.; Knoll, L.; Blaeser, S.; Luong, G. V.; Trellenkamp, S.; Schafer, A.; Tiedemann, A.; Hartmann, J. M.; Bourdelle, K.; Mantl, S. Strained Si and SiGe Nanowire Tunnel FETs for Logic and Analog Applications. *IEEE J. Electron Devices Soc.* **2015**, *3* (3), 103–114.
  - (19) McNulty, D.; Biswas, S.; Garvey, S.; O'Dwyer, C.; Holmes, J. D. Directly Grown Germanium Nanowires from Stainless Steel: High-Performing Anodes

- for Li-Ion Batteries. *ACS Appl. Energy Mater.* **2020**, *3* (12), 11811–11819.
- (20) Mullane, E.; Kennedy, T.; Geaney, H.; Dickinson, C.; Ryan, K. M. Synthesis of Tin Catalyzed Silicon and Germanium Nanowires in a Solvent-Vapor System and Optimization of the Seed/Nanowire Interface for Dual Lithium Cycling. *Chem. Mater.* **2013**, *25* (9), 1816–1822.
  - (21) Mullane, E.; Kennedy, T.; Geaney, H.; Ryan, K. M. A Rapid, Solvent-Free Protocol for the Synthesis of Germanium Nanowire Lithium-Ion Anodes with a Long Cycle Life and High Rate Capability. *ACS Appl. Mater. Interfaces* **2014**, *6* (21), 18800–18807.
  - (22) Liu, X.; Wu, X. Y.; Chang, B.; Wang, K. X. Recent Progress on Germanium-Based Anodes for Lithium Ion Batteries: Efficient Lithiation Strategies and Mechanisms. *Energy Storage Mater.* **2020**, *30*, 146–169.
  - (23) Tian, H.; Xin, F.; Wang, X.; He, W.; Han, W. High Capacity Group-IV Elements (Si, Ge, Sn) Based Anodes for Lithium-Ion Batteries. *J. Mater.* **2015**, *1* (3), 153–169.
  - (24) Chu, S.; Majumdar, A. Opportunities and Challenges for a Sustainable Energy Future. *Nature* **2012**, *488* (7411), 294.
  - (25) Doherty, J.; McNulty, D.; Biswas, S.; Moore, K.; Conroy, M.; Bangert, U.; O'Dwyer, C.; Holmes, J. D. Germanium Tin Alloy Nanowires as Anode Materials for High Performance Li-Ion Batteries. *Nanotechnology* **2020**, *31* (16), 165402.
  - (26) Cho, Y. J.; Kim, C. H.; Im, H. S.; Myung, Y.; Kim, H. S.; Back, S. H.; Lim, Y. R.; Jung, C. S.; Jang, D. M.; Park, J.; Lim, S. H.; Cha, E. H.; Bae, K. Y.; Song, M. S.; Cho, W. Il. Germanium-Tin Alloy Nanocrystals for High-Performance Lithium Ion Batteries. *Phys. Chem. Chem. Phys.* **2013**, *15* (28), 11691–11695.
  - (27) Yoon, S.; Park, C. M.; Sohn, H. J. Electrochemical Characterizations of Germanium and Carbon-Coated Germanium Composite Anode for Lithium-Ion Batteries. *Electrochem. Solid-State Lett.* **2008**, *11* (4), 42–45.
  - (28) Lee, H.; Cho, J. Sn<sub>78</sub>Ge<sub>22</sub>@carbon Core-Shell Nanowires as Fast and High-Capacity Lithium Storage Media. *Nano Lett.* **2007**, *7* (9), 2638–2641.
  - (29) Kim, M. G.; Cho, J. Nanocomposite of Amorphous Ge and Sn Nanoparticles as an Anode Material for Li Secondary Battery. *J. Electrochem. Soc.* **2009**, *156* (4), A277.
  - (30) Chou, C. Y.; Kim, H.; Hwang, G. S. A Comparative First-Principles Study of

- the Structure, Energetics, and Properties of Li-M (M = Si, Ge, Sn) Alloys. *J. Phys. Chem. C* **2011**, *115* (40), 20018–20026.
- (31) Lee, G. H.; Kwon, S. J.; Park, K. S.; Kang, J. G.; Park, J. G.; Lee, S.; Kim, J. C.; Shim, H. W.; Kim, D. W. Germanium Microflower-on-Nanostem as a High-Performance Lithium Ion Battery Electrode. *Sci. Rep.* **2014**, *4* (1), 1–9.
  - (32) Lee, H.; Kim, M. G.; Choi, C. H.; Sun, Y. K.; Yoon, C. S.; Cho, J. Surface-Stabilized Amorphous Germanium Nanoparticles for Lithium-Storage Material. *J. Phys. Chem. B* **2005**, *109* (44), 20719–20723.
  - (33) Doherty, J.; Biswas, S.; McNulty, D.; Downing, C.; Raha, S.; Regan, C. O.; Singha, A.; Dwyer, C. O.; Holmes, J. D. One-Step Fabrication of GeSn Branched Nanowires. *Chem. Mater.* **2019**, *31*, 4016–4024.
  - (34) Park, M. H.; Cho, Y.; Kim, K.; Kim, J.; Liu, M.; Cho, J. Germanium Nanotubes Prepared by Using the Kirkendall Effect as Anodes for High-Rate Lithium Batteries. *Angew. Chemie - Int. Ed.* **2011**, *50* (41), 9647–9650.
  - (35) Zamfir, M. R.; Nguyen, H. T.; Moyen, E.; Lee, Y. H.; Pribat, D. Silicon Nanowires for Li-Based Battery Anodes: A Review. *J. Mater. Chem. A* **2013**, *1* (34), 9566–9586.
  - (36) Seifner, M. S.; Hernandez, S.; Bernardi, J.; Romano-Rodriguez, A.; Barth, S. Pushing the Composition Limit of Anisotropic Ge<sub>1-x</sub>Sn<sub>x</sub> Nanostructures and Determination of Their Thermal Stability. *Chem. Mater.* **2017**, *29*, 9802–9813.
  - (37) Barth, S.; Seifner, S.; Bernardi, J. Microwave-Assisted Solution–Liquid–Solid Growth of Ge<sub>1-x</sub>Sn<sub>x</sub> Nanowires with High Tin Content. *Chem. Commun.* **2015**, *51* (61), 12282–12285.
  - (38) Sun, Y. L.; Matsumura, R.; Jevasuwan, W.; Fukata, N. Au-Sn Catalyzed Growth of Ge<sub>1-x</sub>Sn<sub>x</sub> Nanowires: Growth Direction, Crystallinity, and Sn Incorporation. *Nano Lett.* **2019**, *19* (9), 6270–6277.
  - (39) Yuan, F. W.; Yang, H. J.; Tuan, H. Y. Seeded Silicon Nanowire Growth Catalyzed by Commercially Available Bulk Metals: Broad Selection of Metal Catalysts, Superior Field Emission Performance, and Versatile Nanowire/Metal Architectures. *J. Mater. Chem.* **2011**, *21* (36), 13793–13800.
  - (40) Biswas, S.; Doherty, J.; Saladukha, D.; Ramasse, Q.; Majumdar, D.; Upmanyu, M.; Singha, A.; Ochalski, T.; Morris, M. A.; Holmes, J. D. Non-Equilibrium Induction of Tin in Germanium: Towards Direct Bandgap Ge<sub>1-x</sub>Sn<sub>x</sub> Nanowires. *Nat. Commun.* **2016**, *7*, 114005.

- (41) Doherty, J.; Biswas, S.; Saladukha, D.; Ramasse, Q.; Bhattacharya, T. S.; Singha, A.; Ochalski, T. J.; Holmes, J. D. Influence of Growth Kinetics on Sn Incorporation in Direct Band Gap Ge  $1-x$  Sn  $x$  Nanowires. *J. Mater. Chem. C* **2018**, *6*, 8738–8750.
- (42) Su, S.; Wang, W.; Cheng, B.; Hu, W.; Zhang, G.; Xue, C.; Zuo, Y.; Wang, Q. The Contributions of Composition and Strain to the Phonon Shift in Ge  $1-x$  Sn  $x$  Alloys. *Solid State Commun.* **2011**, *151* (8), 647–650.
- (43) Li, S. F.; Bauer, M. R.; Menéndez, J.; Kouvetakis, J. Scaling Law for the Compositional Dependence of Raman Frequencies in SnGe and GeSi Alloys. *Appl. Phys. Lett.* **2004**, *84* (6), 867–869.
- (44) Cardona, M. Vibrational Spectra of Hydrogen in Silicon and Germanium. *Phys. status solidi* **1983**, *118* (2), 463–481.
- (45) Kazimierski, P.; Jóźwiak. Transition from Amorphous Semiconductor to Amorphous Insulator in Hydrogenated Carbon-Germanium Films Investigated by IR Spectroscopy. *J. Non. Cryst. Solids* **2009**, *355* (4–5), 280–286.
- (46) Gazicki, M. Plasma Deposition of Thin Carbon/Germanium Alloy Films from Organogermanium Compounds. *Chaos, solitons and fractals* **1999**, *10* (12), 1983–2017.
- (47) Tyczkowski, J.; Kazimierski, P.; Szymanowski, H. Correlations between Process Parameters, Chemical Structure and Electronic Properties of Amorphous Hydrogenated Ge $x$ C $1-x$  Films Prepared by Plasma-Enhanced Chemical Vapour Deposition in a Three-Electrode Reactor. *Thin Solid Films* **1994**, *241* (1–2), 291–294.
- (48) Scace, R. I.; Slack, G. A. Solubility of Carbon in Silicon and Germanium. *J. Chem. Phys.* **1959**, *30* (6), 1551–1555.
- (49) Park, K. H.; Lee, D.; Kim, J.; Song, J.; Lee, Y. M.; Kim, H. T.; Park, J. K. Defect-Free, Size-Tunable Graphene for High-Performance Lithium Ion Battery. *Nano Lett.* **2014**, *14* (8), 4306–4313.
- (50) Bell, D. C.; Wu, Y.; Barrelet, C. J.; Gradeč Ak, S.; Xiang, J.; Timko, B. P.; Lieber, C. M. Imaging and Analysis of Nanowires. *Microsc. Res. Tech* **2004**, *64*, 373–389.
- (51) Moutanabbir, O.; Isheim, D.; Blumtritt, H.; Senz, S.; Pippel, E.; Seidman, D. N. Colossal Injection of Catalyst Atoms into Silicon Nanowires. *Nature* **2013**, *496* (7443), 78–82.

- (52) Wacaser, B. A.; Dick, K. A.; Johansson, J.; Borgström, M. T.; Deppert, K.; Samuelson, L. Preferential Interface Nucleation: An Expansion of the VLS Growth Mechanism for Nanowires. *Adv. Mater.* **2009**, *21* (2), 153–165.
- (53) Wen, C. Y.; Tersoff, J.; Reuter, M. C.; Stach, E. A.; Ross, F. M. Step-Flow Kinetics in Nanowire Growth. *Phys. Rev. Lett.* **2010**, *105* (19), 195502.
- (54) Xiang, J. Y.; Tu, J. P.; Zhang, L.; Zhou, Y.; Wang, X. L.; Shi, S. J. Self-Assembled Synthesis of Hierarchical Nanostructured CuO with Various Morphologies and Their Application as Anodes for Lithium Ion Batteries. *J. Power Sources* **2010**, *195* (1), 313–319.
- (55) Kennedy, T.; Mullane, E.; Geaney, H.; Osiak, M.; O'Dwyer, C.; Ryan, K. M. High-Performance Germanium Nanowire-Based Lithium-Ion Battery Anodes Extending over 1000 Cycles through in Situ Formation of a Continuous Porous Network. *Nano Lett.* **2014**, *14* (2), 716–723.
- (56) Baggetto, L.; Notten, P. H. L. Lithium-Ion (De)Insertion Reaction of Germanium Thin-Film Electrodes: An Electrochemical and In Situ XRD Study. *J. Electrochem. Soc.* **2009**, *156* (3), A169.
- (57) Kim, G. T.; Kennedy, T.; Brandon, M.; Geaney, H.; Ryan, K. M.; Passerini, S.; Appetecchi, G. B. reco of Germanium and Silicon Nanowire Anodes with Ionic Liquid Electrolytes. *ACS Nano* **2017**, *11* (6), 5933–5943.
- (58) Chockla, A. M.; Klavetter, K. C.; Mullins, C. B.; Korgel, B. A. Solution-Grown Germanium Nanowire Anodes for Lithium-Ion Batteries. *ACS Appl. Mater. Interfaces* **2012**, *4* (9), 4658–4664.
- (59) McNulty, D.; Geaney, H.; Ramasse, Q.; O'Dwyer, C. Long Cycle Life, Highly Ordered SnO<sub>2</sub>/GeO<sub>2</sub> Nanocomposite Inverse Opal Anode Materials for Li-Ion Batteries. *Adv. Funct. Mater.* **2020**, *30* (51), 2005073.
- (60) McNulty, D.; Geaney, H.; Buckley, D.; O'Dwyer, C. High Capacity Binder-Free Nanocrystalline GeO<sub>2</sub> Inverse Opal Anodes for Li-Ion Batteries with Long Cycle Life and Stable Cell Voltage. *Nano Energy* **2018**, *43*, 11–21.
- (61) Liu, X. H.; Huang, S.; Picraux, S. T.; Li, J.; Zhu, T.; Huang, J. Y. Reversible Nanopore Formation in Ge Nanowires during Lithiation–Delithiation Cycling: An In Situ Transmission Electron Microscopy Study. *Nano Lett* **2011**, *11*, 3991–3997.
- (62) Gohier, A.; Laïk, B.; Pereira-Ramos, J. P.; Cojocaru, C. S.; Tran-Van, P. Influence of the Diameter Distribution on the Rate Capability of Silicon

- Nanowires for Lithium-Ion Batteries. *J. Power Sources* **2012**, *203*, 135–139.
- (63) Fan, S.; Lim, L. Y.; Tay, Y. Y.; Pramana, S. S.; Rui, X.; Samani, M. K.; Yan, Q.; Tay, B. K.; Toney, M. F.; Hng, H. H. Rapid Fabrication of a Novel Sn-Ge Alloy: Structure-Property Relationship and Its Enhanced Lithium Storage Properties. *J. Mater. Chem. A* **2013**, *1* (46), 14577–14585.

# **Chapter 5**

## **Conclusions and Future Outlook**



Progress achieved in the last two decades has fueled the possibility of self-seeded Ge nanowires integration in a broad diversity of applications. Although nowadays Si still prevails over any other material for the microelectronics industry as well as graphite (carbon) does the same in the LIB industry, the demands of the industry will soon require new materials to fulfil the new demands from the consumers. Germanium, and Ge nanowires, in particular, offers a unique alternative in many application fields due to the particular advantages that presents in each of them. Self-seeded Ge nanowires is a contrasted material which can overcome issues associated with widely tested materials such as the impurity issues associated with metal-catalysed Ge nanowires. At the same time, it can provide unique and competitive features *i.e.* nanowire growth rates, narrow-diameter distributions and analogous morphologies.

A considerable number of quite distinct growth methods were described in the last few decades. However, the usual doubt arises about the method that suits best, but it mainly depends on the application. In this thesis, an alternative and simple synthetic method for the growth of group IV semiconductor nanowires has been developed which may be useful for a broad number of applications. This single-pot synthetic method favours the formation of self-seeded nanowires, without the use of metal catalysts or templating agents. This approach can be used to grow highly crystalline Ge, with different polymorphs, and GeSn nanowires from simple and commercially available precursors, at moderate reaction temperatures between 330 and 490 °C. Different reaction constraints such as growth time, temperature, volume fraction, precursor type and concentration were screened to obtain optimal growth conditions for Ge and GeSn nanowires. However, alternative growth conditions such as lower and higher initial concentrations, alternative metalorganic precursors, longer or shorter

reaction times, *etc.* remain to be explored. At the same time, industrial large scale production may have a preference for the nanowires production in a flow-through setup, thus, alternative laboratory setups may be explored.

Both Ge and GeSn nanowires with diameters as small as 9 nm, surrounded by a thin carbonaceous matrix, could be generated in high yields using the supercritical fluid assisted batch method. Yields discussed along this thesis were compared with the obtained results by the gold-seeded CVD method using the same amount of Ge and GeSn precursors. Results were revealed to be significantly higher when using the supercritical fluid assisted batch method. FTIR and XPS techniques were used to confirm the presence and nature of the carbon in the surrounding carbonaceous shell and TEM analysis further confirmed the amorphous nature, inhomogeneity and irregularity of the shell. The amount of these carbonaceous structures found in the Ge nanowire samples decreased with the growth temperature (from 490 to 290 °C), with GeSn nanowires having a significantly lower carbon shell content compared to Ge nanowires under the same growth temperature (at 440 °C). The metastable tetragonal ST12 Ge polymorph was also successfully formed for the first time in the 1D nanoform. Photoluminescence studies of the ST12-Ge nanowires suggested a direct bandgap for the tetragonal nanowires with a fundamental direct bandgap of ~ 0.64 eV.

Generally, as in our case, bottom-up nanowire synthetic approaches produce meshes of entangled nanowires. This means that successive steps of positioning and assembly step for device integration may be required in some application fields. The lack of in-place fabrication methods, that is, the synthesis of nanowires at specific positions on a substrate is still a great challenge which needs to be addressed. Success in this field

would allow the bottom-up growth approaches to directly challenge the top-down fabrication methods that dominate in the industry. This would mean significant progress in terms of growth control, large scale method reliability and nanowire size variability and tunability.

Studies, both experimental and computational, about the self-seeded growth of Ge nanowires growth mechanisms are still necessary for this process to be understood in detail. Yet, some connections have been discussed between the different approaches reported in the literature. Solution-phase methods (including supercritical-phase methods) share many points in common, such as the presence of organic ligands (carbonaceous structures) and their decomposition pathways. These structures, at the same time, seem to play a key role in the growth of self-seeded Ge nanowires. In this thesis, a self-seeded nanowire growth process was put forward as the mechanism for Ge nanowire growth; also including an interpretation for the growth of the small-diameter GeSn nanowires. *In situ* formation of Ge seeds and their participation in nanowire growth was evident from their presence at the tips of synthesised nanowires. Spontaneous *in situ* polymerisation of the organic ligands present in the Ge precursor, *i.e.* diphenylgermane, is a crucial and distinctive step for the formation of carbonaceous compounds and stabilisation of the catalytic nanoparticle seeds. These carbonaceous materials also precipitated onto the sidewalls of the nanowires to create a ‘carbon shell’ around them. Temperature and pressure were found to be crucial factors for the initial decomposition of diphenylgermane and the formation of the carbonaceous material.

Both cubic carbonaceous Ge (C-Ge) and GeSn nanowires were evaluated as potential anodes for LIBs. For this purpose nanowires were grown directly onto metallic substrates, *i.e.* Ti discs. Both the dc-Ge and GeSn nanowires demonstrated exceptional promise as Li-ion battery anodes, capable of delivering impressively high specific charge values ( $> 1200 \text{ mA h g}^{-1}$  after 500 cycles at 0.2 C for dc-Ge nanowires and  $1127 \text{ mA h g}^{-1}$  after 150 cycles at 0.2 C for GeSn nanowires), with very low-capacity decay. The small mean diameter of the C-Ge and GeSn nanowires and the presence of the carbonaceous shell around C-Ge nanowires were crucial to achieve a high specific capacity and capacity retention. The impressive electrochemical performance of the Ge and GeSn nanowires demonstrates an advantage of directly growing nanowires on metallic anode current collectors and of having a carbon shell surrounding the nanowires.

The nanowire synthesis process described in this thesis represents a low-cost method to meet the growing demand for group-IV semiconducting nanomaterials for electronic, optoelectronic and portable energy storage devices. The synthesis of high-quality nanowires without the need for any external metal catalysts, or templates, could potentially be used to other group IV nanowires, *e.g.* Si and SiGe. Growth constraints could be employed to synthesise group IV alloys that are often difficult to obtain difficult in nanowire form, *e.g.* SiGeSn. Also, this growth method could be used to grow III-V and II-VI nanowires, as an alternative approach to catalyst-assisted CVD or template-mediated solvothermal growth.

A more in-depth exploration of the nucleation and crystallisation mechanisms involved in the self-seeded growth of Ge-based nanowires is also required to provide a more detailed understanding of precursor decomposition kinetics and possible

fragment polymerisation, the influence of solvent on nanowire growth and stabilisation and the role of the carbonaceous structures play in nanowire formation. This knowledge will permit better control over the morphologies, crystal structure and surfaces of the nanowires. The simplicity of this method allows the exploration of initial solution mixtures with a certain complexity. However, the initial solution is only composed of the metalorganic precursor and the organic solvent. The possibility of using different precursors or certain additives (*i.e.* secondary ligands), such as thiols, could lead to not only new nanostructured morphologies, such as 2D nanoflakes but also new properties and features which may make them suitable for other application fields. My research has only investigated the application of the Ge and GeSn nanowires synthesised as anode materials for Li-ion batteries. However, their unique characteristics, *e.g.* the presence of the carbonaceous shell, their small diameters, may also makes them promising materials for use in other fields such as photocatalysis, and nanoscale electrical sensors.

